Optimisation and Modelling of the Spiral Jet Mill

Ruaidhri (Rory) Forbes William MacDonald

School of Chemical Engineering and Advanced Materials, Newcastle University

A thesis submitted for the degree of

Engineering Doctorate

February 2017

This page is left intentionally blank.

Abstract

The spiral jet mill is a widely applied and robust apparatus for reduction of mean particle size to less than 10 microns. Despite the spiral jet mill being a well established technology, there are no proven scale up methodologies and many commercial mill designs are not optimised for energy efficiency.

Within this thesis a novel analytical derivation is presented for spiral jet mill cut size as a function of micronisation settings, gas thermodynamic properties and empirically derived constants for the material and mill. The derivation is corroborated by experimental evidence for a number of products owned by GlaxoSmithKline (GSK) and previously reported data in the academic literature. This equation provides an insight into the interaction between aerodynamic particle classification and fine grinding for the spiral jet mill, and brings great advancement to the level of understanding in the academic literature on the control of particle size with a spiral jet mill. The constants within the equation can be determined empirically for a given material and mill, leading to a better prediction across a design space than standard empirical models. A scale up methodology is proposed for a high value material by using a small scale mill to determine the material specific constants of the high value material and a cheaper surrogate material to determine mill specific parameters at increased scale.

In addition to a novel analytical derivation, this thesis presents the first ever Computational Fluid Dynamics (CFD) based optimisation of a combined spiral jet mill and cyclone. Some combined spiral jet mill and cyclone designs have poor cyclonic separation yields, and this thesis presents the CFD and experimental investigation which led to an optimised mill and cyclone that significantly improved yield while maintaining similarity of particle size.

Acknowledgements

GlaxoSmithKline (GSK) must be acknowledged for allowing the opportunity to perform experiments with commercial equipment and API, perform optimisation experiments with novel mill designs, use their particle size analysers and allowing access to some of their development data. David Rowe is acknowledged for his support as an industrial supervisor and reviewer. Elaine Martin of Leeds University, Jonathan Lee of Newcastle University and Lee Gorringe, Jeremy Clarke, Warren Eagles and Peter Clements of GSK are acknowledged for their support in reviewing some aspects of this thesis. My wife Deborah and three children (Finlay, Elizabeth and Isabelle) are thanked for their support and patience. The Engineering and Physical Sciences Research Council (EPSRC, EP/G037620/1) must also be acknowledged for providing the funding for this research project.

This page is left intentionally blank.

CONTENTS

List of Tables and Figures

Chapter 1. Introduction

1.1 Micronisation in Context

Particle size reduction is one of oldest and most essential unit operations known to humanity. Micronisation is the process of particle size reduction to the micrometer scale, and as early as 105,000 years ago ancient humans were grinding starch grains of wild grasses in Mozambique with stone pestles down to particle sizes of 5 to 25 μm (Mercader 2009). By 23,000 years ago wild oats were being reduced to particle sizes as small as 4 to 10 μm (Nadel *et al.* 2012). Since the dawn of humanity, we have understood that by reducing the particle size of a material it is possible to change its characteristics. The increase in bioavailability of starches from grains is an example of how milling technology has changed the course of human history.

The understanding that reduction in particle size can change the medicinal effect of a substance is also ancient as it is an essential step in Babylonian natural remedies from over 3000 years ago (Geller 2010), and, given how long humans have been crushing food, could date back even further. Particle size reduction is even more important now than it was then for medicinal formulations. GlaxoSmithKline (GSK) perform micronisation with a spiral jet mill to prepare particles primarily in the 0.5 to 5 μm size range for use in a wide variety of dose forms and products. For nasal sprays, creams, ointments and OSD products, micronisation is performed to increase the bioavailability of poorly soluble materials. In the case of respiratory APIs, the particle size dictates where in the lungs the particles are delivered and the subsequent clinical effect of the formulation (Brodka-Pfeiffer 2003). For this reason, control of API particle size is particularly crucial for respiratory products.

This doctoral thesis will initially discuss particle size control by aerodynamic particle classification and the mechanistic basis for relationships between milling parameters for a spiral jet mill. Aerodynamic particle classification is then optimised for a combined spiral jet mill and cyclone so as to improve the yield for a respiratory product while maintaining similarity of particle size.

1.2 The Spiral Jet Mill

The spiral jet mill is a popular apparatus for micronisation of powders as it has no moving parts, making it easy to clean as well as a robust and dependable technology. Size reduction is achieved as a result of particle collisions caused by high velocity gas exiting a series of nozzles situated around a grind chamber as per Figure 1.1 which shows a side view and Figure 1.2 which shows the plan view and process description. The grind chamber is typically cylindrical but may also be elliptical in shape. Input material is introduced into the grind chamber by a feed nozzle and typically a Venturi from either a tangential entrance as per Figure 1.2 or in other cases by a top entrance. The grind nozzles are angled such that gas and particles circulate at high velocity around a central exit, resulting in centrifugal force which retains particles in the grind chamber until micronised. Most spiral jet mills have a classifier at the grind chamber exit as shown in Figure 1.1 which prevents the escape of large particles along the walls of the chamber where there is less centrifugal force due to lower gas tangential velocity. The spiral jet mill is generally operated at steady state as a semi-continuous process with a controlled solids feed rate and gas mass flow rate. Gas mass flow rate is often controlled by maintaining a constant pressure behind the nozzles, referred to as the "grind pressure". When the solids feed rate and gas mass flow rate are controlled, the spiral jet mill delivers a consistent output Particle Size Distribution (PSD) as the classifier dynamics remain controlled. Micronised output can be collected by a combined vane-less axial entry reverse flow cyclonic separator (bottom discharge system) or other means such as filter socks or separate tangential entry cyclone (top discharge system).

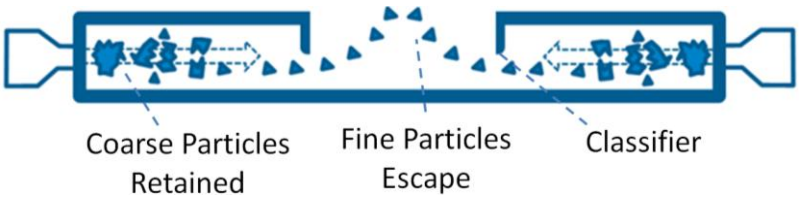

Figure 1.1 Spiral Jet Mill Grind Chamber (Side View)

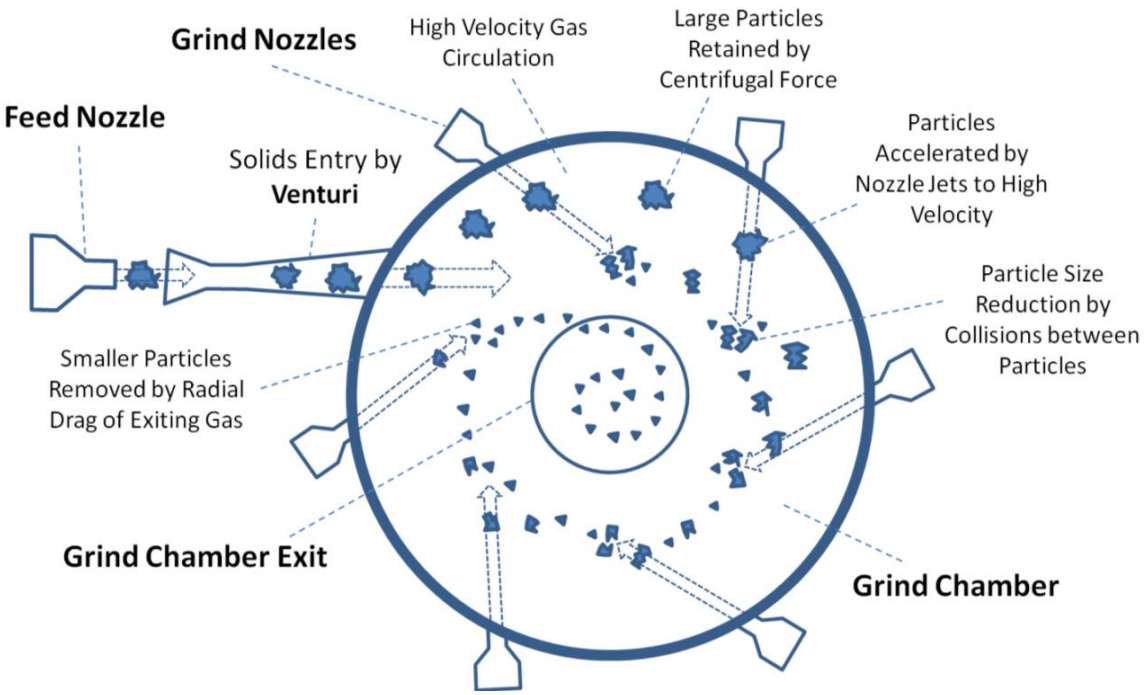

Figure 1.2 Spiral Jet Mill Grind Chamber (Plan View)

1.3 Industrial Problem Statements

Despite micronisation being a process steeped in history, the underpinning physical processes governing output particle size from a spiral jet mill are still under investigation. As a given spiral jet mill can in most occasions robustly deliver a desired output PSD for a controlled solids feed rate and gas mass flow rate, understanding the interaction between milling parameters (gas mass flow rate and solids feed rate) with mill geometry (classifier dimensions, mill scale, nozzle angle *etc.*) has not been required so long as there is enough time and material available to experimentally identify the correct parameters for a given mill and material to achieve a desired particle size.

However, with some APIs being more expensive than gold, there is a driver to minimise industrial scale experimentation and ensure yields are as high as possible. This doctoral thesis will address two problem statements faced by GSK and the wider academic and industrial community:

1) Lack of mechanistic process understanding for the spiral jet mill
2) Low cyclonic separation yield for some materials

1.3.1 Lack of Mechanistic Process Understanding

For some materials there are working empirical correlations between Specific Energy Consumption (E_{sp}) and output particle size for a given mill as discussed in Chapter 2. These correlations allow process parameters (gas mass flow rate and solids feed rate) to be modified to maintain similarity of particle size when increasing or decreasing throughput for a given material and mill. The mechanistic basis for these correlations is not understood or documented in academic literature.

For other materials the interaction between solids feed rate and gas flow rate is more complicated, making estimation of required changes in process parameters to maintain similarity of particle size with an E_{sp} correlation impossible (Chapter 4). The reason why some APIs do not adhere to E_{sp} was not understood or documented in academic literature prior to the research detailed in this thesis.

Different spiral jet mill designs also lead to different output particle sizes for the same combination of gas flow rate and solids feed rate. The correlations between mill geometry and output particle size are not understood or documented in academic literature.

GSK requires a robust mechanistic model on which to base scale up and platform transfer. There is a gap in academic literature regarding mechanistic process understanding of the interactions between aerodynamic particle classification and the fine grinding process. This thesis, and its corresponding journal publication, address this problem statement and contribute to the current body of knowledge on the spiral jet mill.

1.3.2 Low Cyclonic Separation Yield

Some materials are not easily separated from the micronisation gas with the current combined spiral jet mill and cyclonic separator design used with Product A as per Figure 1.3.

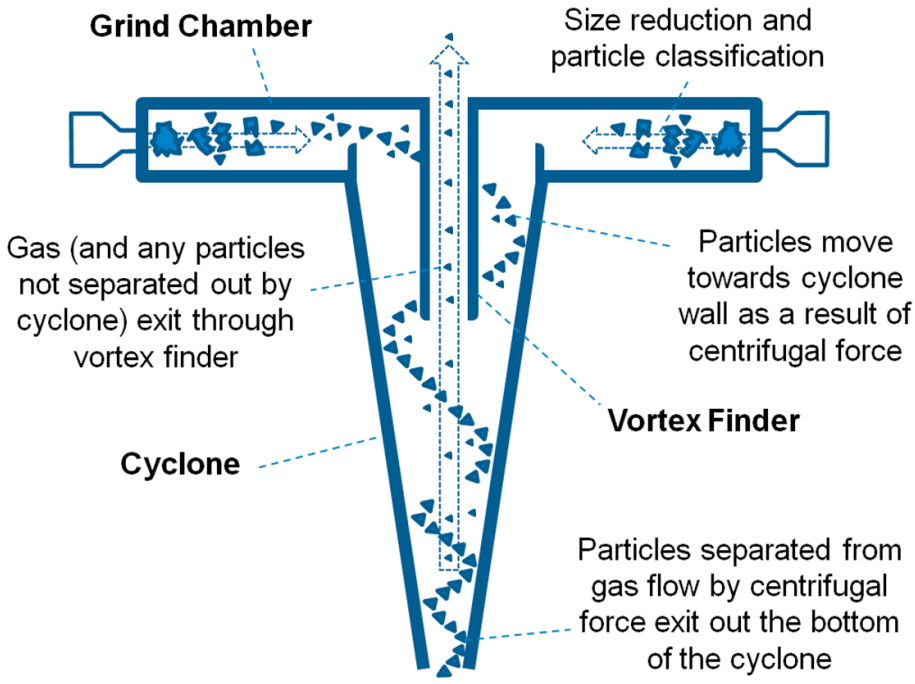

Figure 1.3 Combined Spiral Jet Mill and Vaneless Axial Entry Reverse Flow Cyclonic Separator (Bottom Discharge Spiral Jet Mill)

The yield for micronisation of a commercial respiratory asset (referred to as Product A for confidentiality reasons) is currently 89% due to poor cyclonic separation (Chapter 8). If the cyclonic separation yield were to increase without any change to the micronisation process or if the filter fines and collected product were to be blended post micronisation, there would be an increase in the fraction of very fine particles present as the 11% lost during cyclonic separation is finer than the 89% collected as product. The solids feed rates and grind pressures used for Product A and other similar products are restricted to a narrow range as per the current manufacturing process, and so cannot be changed to maintain similarity of particle size following a change to the cyclone performance. Therefore the classifier of the spiral jet mill must be modified to adjust the size of particles entering the cyclone to maintain similarity of particle size for the collected product.

GSK requires the design of the cyclone and classifier for Product A to be simultaneously modified to increase yield while maintaining similarity of particle size. There is a gap in academic literature regarding geometry optimisation of a bottom discharge spiral jet mill. This thesis addresses an industry need by developing an optimised mill and cyclone geometry which increases yield while maintaining similarity of particle size, and in doing so contributes to the body of knowledge on bottom discharge spiral jet mills.

Chapter 2. Spiral Jet Mill Literature Review

2.1 Invention

The mortar and pestle discussed in Chapter 1 eventually developed into sophisticated mechanically driven grind stones, such as water wheel driven flour mills, capable of industrial scale continuous grinding of grain (Lucas 2006). Particle size reduction by crushing and grinding between two surfaces became ever more advanced with the invention of the ball mill (Walker 1847), which eventually developed into industrial planetary (Herzfeld 1896) and cascading (Ostwald 1912) balls mills capable of grinding some materials down to the nano scale.

Although the jet mill may not be capable of reducing the mean particle size to the order of nanometers, it represents a step change in the method of particle size reduction. Rather than crushing or grinding against the mill surfaces, the jet mill allows the material to be micronised against itself. The opposed jet mill was originally patented in 1881 by Frederic A. Luckenbach and John Wolfenden as per Figure 2.1 (Luckenbach and Wolfenden 1881).

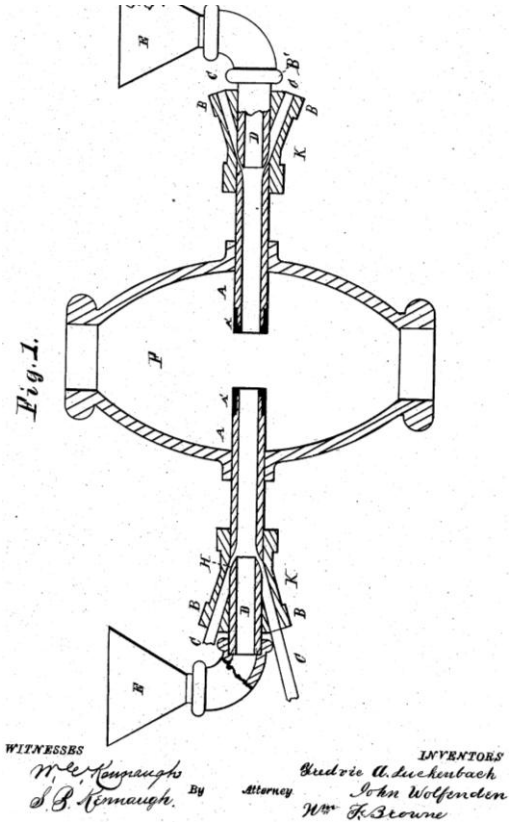

Figure 2.1 Opposed Jet Mill (Luckenbach and Wolfenden 1881)

In terms of the size reduction process, the opposed jet mill maximises the momentum that can be exchanged between particles by opposing the jets such that primarily head on collisions occur. However, the opposed jet mill has no size classification process, and as such must be either operated as a batch process for given periods of time or coupled with an air classifier which recycles coarse particles back to the nozzles. By micronising a material against itself rather than against the mill surfaces, the jet mill can be used for applications where very high purity of the milled product is required.

The spiral jet mill marks the next advancement in jet milling technology as it combines fine grinding and aerodynamic particle classification in one unit operation, allowing for continuous processing. An extensive patent (Andrews 1936) was filed by Norwood H. Andrews which details the basic principles of operation of several mill designs that incorporate jet milling, particle classification and cyclonic separation in one apparatus. Some diagrams from Andrews' patent are shown in Figure 2.2.

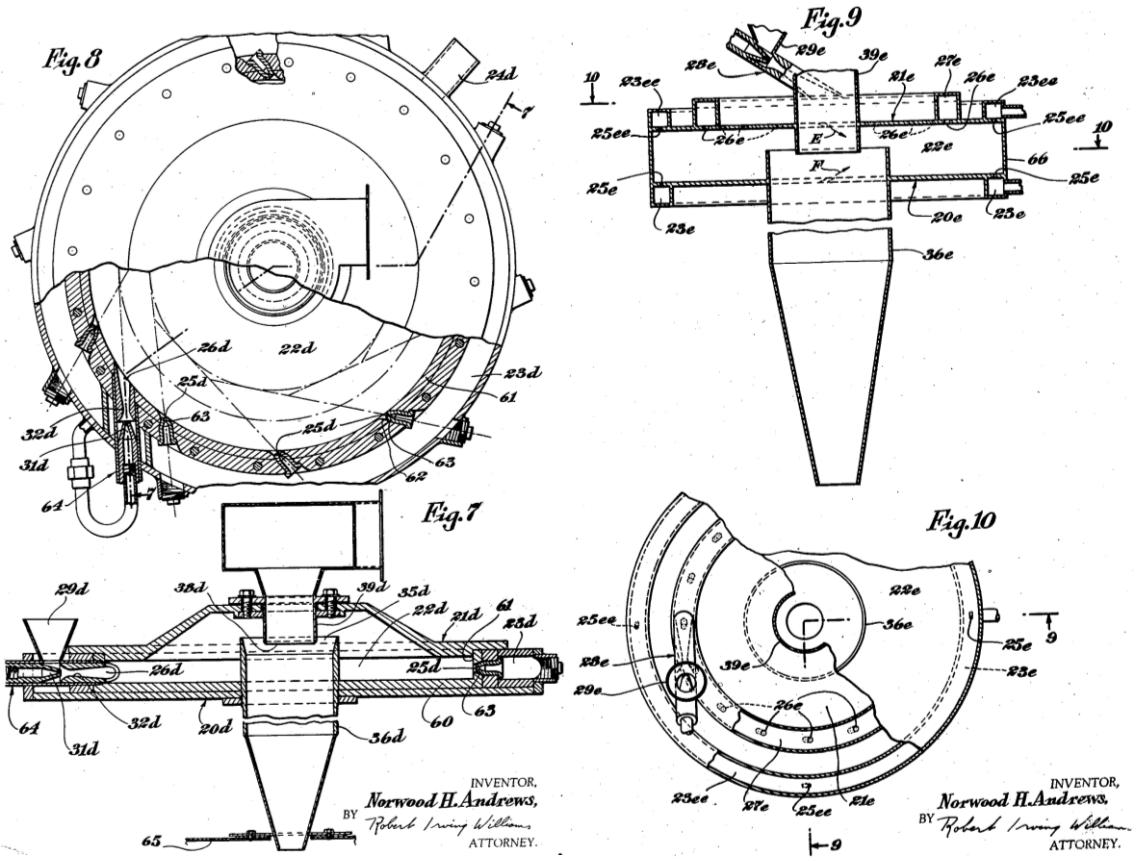

Figure 2.2 The Spiral Jet Mill (Andrews 1936)

The spiral jet mill has changed very little since the original 1936 patent as can be seen by comparing Figure 1.3 to Figure 2.2.

2.2 Early Theoretical Basis

The first clear description of the principles of operation of the spiral jet mill or "micronizer" may be found in a paper by Berry (1946). His description of the operation of a spiral jet mill is so succinct that it bears repeating:

- "Size reduction and classification take place simultaneously in the same chamber, which is essentially a cylinder of low axial height."
- "High velocity fluid jets issuing from orifices in the wall of the cylinder are directed so as to set up a rapid rotation of the gas-solids suspension in the chamber."
- "Centrifugal force resulting from this rotation tends to hold the coarse solids in a path following the cylindrical wall."
- "The size reduction is accomplished by the impact of particle upon particle and shearing effects as the high speed fluid jets intersect the path of the rotating suspension."
- "The classifying action is obtained by balancing the centrifugal force on a particle, due to its circular path, against the entraining force of the expanded gases which leave the size reduction chamber near its axis."
- "A barrier is created in which the particles larger than a certain size are rejected to the periphery of the chamber for further size reduction, while particles smaller than this size are swept from the size reduction chamber."
- "The micronizer product size is basically dependent on the rotational speed, fluid flow rate, internal size, and proportions of the size reduction chamber. Control of the first and second factors is usually accomplished by controlling the rate of solid feed and the fluid pressure at the orifices."
- "The size and shape of the chamber are determined for best performance during initial experimental work with a particular material".

Berry, 1946

The most crucial observation that Berry makes is that the output particle size is a function of the centrifugal to drag force balance, which is discussed in detail in Chapter 3. Dobson and Rothwell (1969) further develop on the concept of aerodynamic classification. They are able to replicate the performance of a spiral jet mill by using an external impact chamber and cyclone with the coarse fraction of the cyclone being recycled to the external impact chamber. They also showed that a force balance on a particle at the classifier (using tangential velocity of nozzle jets) gave an estimated cut size of 3 μm, which is close to the experimentally determined particle size of 6 to 9 μm. It was however noted that the force balance

alone is not capable of accounting for differences in particle size with varying feed rate and input material mechanical properties.

The effect of increasing the input material feed rate on output particle size was initially measured and discussed by Dotson (1962). Dotson claimed for the loop jet mill that an initial increase in grinding efficiency is observed with an increase in feed rate due to a greater chance of particle-particle collisions followed by a decrease in efficiency as the distance a particle can accelerate before a collision is reduced as the particle population increases. Despite working on the loop jet mill, Dotson's work is worth noting as his explanation for differences in grinding efficiency with varying feed rate is the earliest account in academic literature of this effect. Although the loop and spiral jet mill appear very different as per Figure 2.3, they both simultaneously micronise and aerodynamically classify particles.

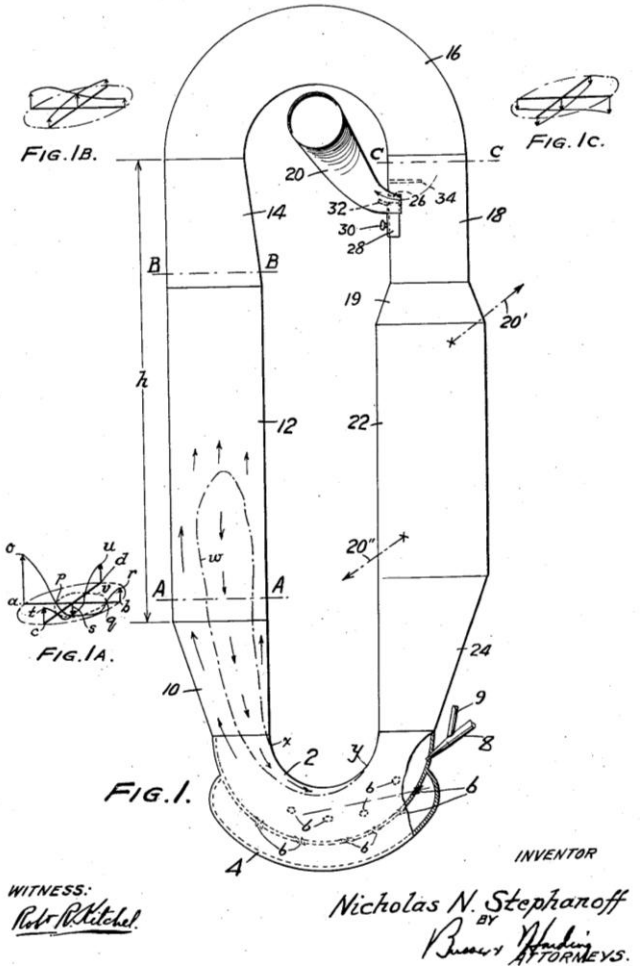

Figure 2.3 The Loop Jet Mill (Stephanoff 1938)

Tanaka (1972) attempted to develop a theoretical basis for scale up of the spiral jet mill. The scale up approach centred around maintaining similarity of particle

size by ensuring similarity of the centrifugal to drag force balance on a particle at the grind chamber exit. This was primarily done by making assumptions regarding how velocity will change with geometry for the spiral jet mill, and then determining what relationships between dimensions must exist to maintain similarity in the ratios of velocities. This required the assumption that at a given flow rate an Archimedes spiral flow with constant tangential velocity develops around the grind chamber exit extending to the interface with the tips of the nozzle jets. Tanaka however provided no experimental evidence that this scale up approach works other than the observed increase in efficiency with scale matching the predictions of his equation. Tanaka's scale up approach also did not look at design features, such as a classifier ring at the grind chamber exit or the effect of material properties or feed rate on the classifier cut off point. Additionally, Tanaka assumed a laminar flow regime of gas across a particle at the grind chamber exit, whereas the flow regime is typically transitional ($Re > 0.2$) and in most cases the Reynolds number (Re) will exceed the values where laminar drag correlations can be applied. Stokes' law typically cannot be applied when $Re > 2$, and for air at 25 ^{o}C this occurs at approximately 6.3 $m.s^{-1}$ for a 5 micron sphere or 32 $m.s^{-1}$ for a 1 micron sphere. Radial velocities at the classifier can typically exceed 30 $m.s^{-1}$ and therefore Tanaka's assumption of laminar drag may result in his scale up approach being incorrect as he was maintaining the wrong ratio of radial to tangential velocity.

2.3 Experimental Investigation (Particle Size)

Early studies regarding size reduction were concerned with the energy required for the process and how this related to the size of the input compared to the output for materials of differing mechanical properties. Rittinger developed an empirical law of comminution which stated that the work required for size reduction is proportional to the new surface area created. Kick proposed that the energy is proportional to the size reduction ratio. Bond claimed that the work is proportional to the difference in the inverse of the square root of the diameter of the input and output. Austin (1972) performed a mathematical analysis of these laws and concluded that Rittinger's and Bond's laws could both be applied to the same data set with approximately similar validity as both are empirical in nature. Rumpf (1973) performed a detailed study of comminution and showed through

dimensional analysis that assuming similarity of fracturing across scales leads to Rittinger's law while also developing methodologies to account for dissimilarity in fracturing with scale due to reduction in the number of flaws within a particle with its size.

Detailed investigations into the size reduction process in a spiral jet mill were first performed by Kürten and Rumpf (1966). They were able to visualise where grinding occurs in a tangential entry spiral jet mill by using a glass cover plate, camera and tribo-luminescent materials as shown in Figure 2.4.

Figure 2.4 Collision Visualisation in a Spiral Jet Mill (Kürten and Rumpf 1966)

Kürten *et al.* (1970) latterly investigated jet milling in more detail by using individual opposed jets and varying their angle, distance and powder loading rather than further studying the spiral jet mill. It was shown that the collision energy, as defined by angle and velocity, is the critical factor in determining the smallest fragments generated. It was also shown that the particle concentration, and time allowed for acceleration in a nozzle jet prior to collision, define the particle velocity at point of collision.

Ramanujam and Venkateswarlu (1969) published a detailed study on the influence of solids feed rate, solids size, gas pressure and nozzle diameter for the loop jet mill. It was noted that increasing pressure, increasing nozzle diameter and reducing the solids feed rate are means of reducing output particle size. It was also noted that output particle size is relatively insensitive to input particle size for micronisation of calcium carbonate. As part of their study they were able to

investigate the amount of hold up within the loop jet mill and the mean residence time (estimated by dividing the hold up by the feed rate). Importantly it was noted that the level of hold up increases with both feed rate (x axis) and gas pressure (indicated by differently shaped markers) as per Figure 2.5.

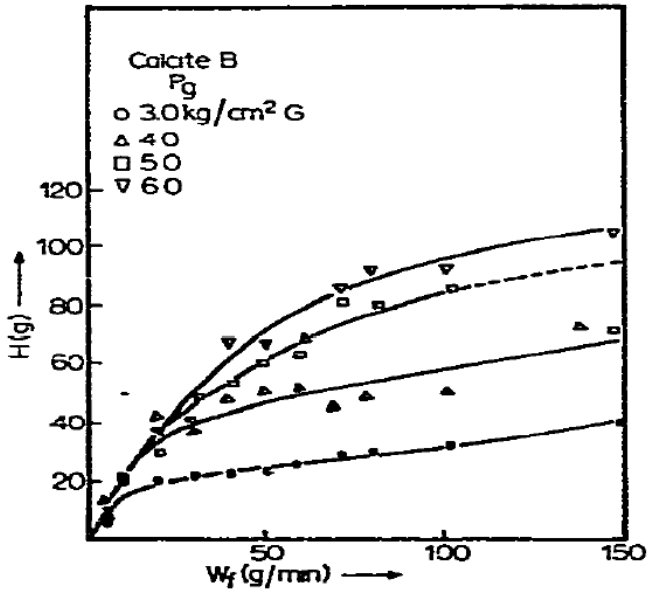

Figure 2.5 Feed Rate against Hold Up (Ramanujam *et al.* 1969)

Mohanty and Narasimhan (1982) published a further investigation into micronisation of different materials with the loop jet mill. An equation was derived according to Rittinger's law (the energy for new surface creation is proportional to the area of surface created) to phrase output particle size as a function of input particle size, solids feed rate and material specific constants. The experimental data was then fitted according to the equation to determine the material specific constants. Unfortunately their equation does not account for the known variation in particle size with gas flow rate and also does not match other experimental data where the output particle size is shown to be relatively insensitive to input particle size (Ramanujam *et al.* 1969). However there is an important observation to be made from their experimental data, which is that the transition point from "starving" through to normal operation occurs at different feed rates for different materials as per Figure 2.6. The "starving" condition relates to a low particle concentration such that particle collisions are so infrequent that increases in feed rate lead to a reduction in particle size as a result of an increase in the collision rate.

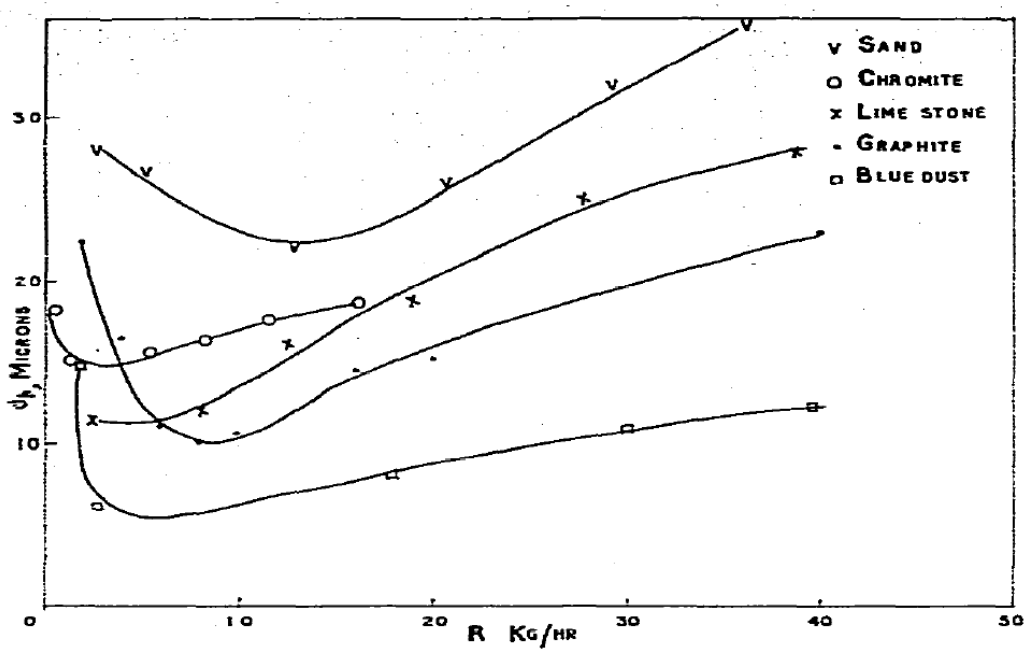

Figure 2.6 Particle Size against Feed Rate (Mohanty *et al.* 1982)

Yoon (1993) showed that a scale up approach based on a publication by Ito (1987) worked approximately for scaling a pilot plant spiral jet mill with a throughput of 20 kg.hr^{-1} to an industrial scale mill with a throughput of 500 kg.hr^{-1}. Unfortunately, modification was required to several indices of the scale up equations to get them to fit his experimental data. Additionally, Yoon only showed his modified indices to work with the data he used to determine them. Yoon also explained the reduction in particle size with increasing grind pressure to be a result of an increase in individual collision energies, rather than an increase in residence time and total number of collisions as a result of a change to the classification process (Chapter 3). Interestingly however, Yoon also showed that the addition of deflector plates to increase the number and intensity of particle-wall collisions could decrease the particle size obtained.

Müller *et al.* (1996) published a detailed study and showed an excellent understanding of the physical processes governing particle size in a spiral jet mill. Müller *et al.* claim that the amount of material retained in the grind chamber, or hold up, for a given mill depends on the physical properties of the material, solids feed rate and gas mass flow rate and that the hold up has an effect on the cut size by influencing the circumferential, or tangential, speed. However, their paper either contained a mistake or typographical error with respect to defining the force balance as the units on either side of their equation do not balance.

Additionally they appear to use the mill diameter instead of particle diameter in the length scale for the Reynolds number and their dimensional analysis, which is incorrect if as per their commentary they are looking at the radial flow of gas past a particle in the grind chamber. Despite Müller *et al.*'s error in their force balance and dimensional analysis, their dimensionless number is claimed to work for scale up of spiral jet mills at BASF (Müller *et al.* 1996).

Tuunila and Nyström (1998) shared the results of an investigation into the effect of varying the feed rate, gas flow rate and classifier height (grind chamber exit slit width). The variation in particle size with feed rate and gas flow rate was similar to previously reported data. Importantly, they showed that increasing the classifier height (reducing the exit slit width) led to coarser product for the range investigated.

Katz and Kalman (2007) published a detailed investigation into varying geometrical parameters. They showed similar results to other researchers for variation in particle size with solids feed rate and gas mass flow rate. They also confirmed Ramanujam *et al.*'s observation (1969) that the output particle size is relatively insensitive to input particle size. Katz and Kalman investigated three geometrical parameters; nozzle angle, nozzle diameter and grind chamber height. Their lowest investigated angle of 45^{o} resulted in the finest material, and increasing the angle such that the nozzles are further from tangential resulted in coarser material. They also showed that increasing the nozzle diameter for a constant gas flow rate results in coarser output, whereas maintaining constant gas pressure to increase the flow rate with increased nozzle diameter results in minimal change to the particle size. However, at the low gas flow rates investigated by Katz and Kalman the increase in nozzle diameter from 1.0 mm to 2.0 mm at constant gas mass flow rate (approximately 36 $kg.hr^{-1}$) for 12 nozzles could have led to sub-sonic nozzle exit velocities and reduction in collision energy. It was also shown that changes in grind chamber height, and therefore volume, do not result in any significant change to particle size. The observation of no change in particle size with grind chamber height for a zero classifier height is discussed in more detail in Chapter 6.

Further experimental investigations were published by Nair and Ramanujam (1991) and Nair (1999) for the circular loop jet mill. Their work centred on

empirically fitting data to classification and breakage parameters to build a model of their milling performance. Despite their models being very specific to their equipment, one key observation was made; particle breakage rates follow first order kinetics with respect to particle concentration.

Djokić *et al.* (2014) performed a detailed factorial Design of Experiments (DoE) for micronisation of an API, and generated data which concurred with other observations in the literature such as reduction in particle size with increased nozzle diameter and gas pressure. It was noted that the distance between the feed gas injection nozzle and the milling chamber had a negligible impact on particle size.

2.4 Changes in Physical Properties by Micronisation with a Spiral Jet Mill

Micronisation not only changes the particle size of a material and its specific surface area, but also its surface properties. Grimsey *et al.* (2002) summarise the findings of several researchers regarding changes to surface energetics as a result of milling. During the particle fragmentation process, crystals will preferentially cleave along the weakest planes of the crystal habit. This preferential fragmentation results in a change to the surface energetics of the powder as a whole as these cleavage planes and their surface chemistry will become more prevalent. Inverse Gas Chromatography (IGC) of substances (Lloyd *et al.* 1989) before and after micronisation often shows a clear change in the surface chemistry of a powder (Heng *et al.* 2006). These newly exposed surfaces are typically more hydrophobic as functional groups with this surface chemistry are normally more prevalent along the weaker planes of a crystal habit (Heng *et al.* 2006).

In addition to changing bulk surface chemistry by preferential cleaving of crystals, micronisation can also result in a breakdown of crystalline structure and the generation of amorphous material. Brodka-Pfeifer *et al.* (2003) showed for micronisation of salbutamol sulphate that although the particle size did not vary significantly with grind pressures above 6 bar, the amorphous content continued to increase. It is thought that the increase in grind pressure beyond 6 bar leads to more unsuccessful collisions causing breakdown of the crystalline structure of salbutamol sulphate rather than causing further fragmentation. Vemuri *et al.* (2003) developed a patented technique of humidified micronisation to reduce the

formation of amorphous material, but could not explain why their invention reduced the generation of amorphous material. It is known that water sorption and increased temperatures can induce a transition from amorphous to crystalline in many materials (Burnett *et al.* 2004), and it may be the case that the humidified gas rapidly repaired amorphous regions rather than prevent them from being formed during the micronisation process.

2.5 The Influence of Input Material Mechanical Properties

Input material mechanical properties have a direct influence on the output particle size following micronisation. Berry (1946) had noted that rubbery materials (low Young's modulus and high yield stress) are challenging to micronise with a spiral jet mill and that for successful performance the input material must be capable of shattering.

Analysis of attrition and comminution has Ghadiri and Zhang (2002) developed a theoretical relationship between the fractional loss in mass during collision with input material mechanical properties and impact velocity for a cubic crystal due to chipping from an impact on one of its corners:

$$\xi = \alpha\eta \qquad (2.1)$$

where ξ is the fractional loss per impact, α is a proportionality constant and η is a dimensionless attrition propensity parameter given by:

$$\eta = \frac{\rho v^2 l H}{K_c^2} \qquad (2.2)$$

where ρ is the particle density, v is the particle velocity, l is the length dimension of the cubic particle, H is the hardness of the particle and K_c is the fracture toughness. As can be seen from Equation 2.2, materials with a greater hardness (H) undergo a greater loss of mass in the event an impact for the same particle size, fracture toughness and velocity. Zhang and Ghadiri (2002) were able to demonstrate the validity of their analytically derived equations with experimental evidence using a single particle impact device. Equation 2.2 clearly demonstrates that the attrition propensity and amount of mass lost from a collision event will change with the size of the particle and its mechanical properties.

Zügner *et al.* (2006) published a detailed paper relating the nanomechanical properties of crystals to their micronisation performance in a spiral jet mill. Nanoindentation (Fischer-Cripps 2000) is generally required for APIs as the crystals are so small prior to micronisation that traditional mechanical testing is challenging. It was shown that harder and less elastic materials actually result in smaller output particle sizes than softer and more elastic materials. This is a result of collisions between hard and brittle particles being more likely to result in successful fragmentation and chipping than collisions between elastic particles which will simply bounce apart, or soft/ductile materials which will plastically deform rather than shatter. The results of Zügner *et al.* (2006) further confirm previous analysis by Ghadiri and Zhang (2002) that harder materials shatter better.

Bonakdar *et al.* (2016) developed a technique which uses a commercially available dry disperser (Scirocco) and particle sizing apparatus (Malvern Mastersizer 2000) to determine $\alpha H/K_c^2$ (combination of parameters from Equations 2.1 and 2.2 which define grinding characteristics). The results obtained with the Scirocco correlated well with those from the single particle impact device used by Zhang and Ghadiri (2002). This technique is particularly important for industrial application as although there are no commercially available particle impact devices, many manufacturing and research facilities are equipped with a Scirocco and Malvern Mastersizer 2000.

2.6 Specific Energy Consumption Correlations

The concept of Specific Energy Consumption (E_{sp}) was initially proposed by Schurr and Zhao (1994). It is an important concept as it allows the micronisation settings of solids feed rate ($\dot{m}_s$) and gas mass flow rate ($\dot{m}_g$) to be grouped into one parameter (E_{sp}) which can be correlated with particle size. It is a powerful tool as for some materials it allows the required change to settings to be determined to maintain similarity of particle size while changing throughput on a given spiral jet mill.

E_{sp} is defined as the ratio of kinetic energy delivery rate to solids feed rate, to give the total amount of energy consumed by the microniser per unit weight of powder:

$$E_{sp} = \frac{\dot{E_k}}{\dot{m}_s} \tag{2.3}$$

where $\dot{m}_s$ is the solids feed rate to the microniser and $\dot{E_k}$ is the kinetic energy delivery rate. The kinetic energy delivery rate is defined by:

$$\dot{E_k} = \frac{1}{2}\dot{m}_g v_{sonic}^2 \tag{2.4}$$

where $\dot{m}_g$ is the gas mass flow rate and v_{sonic} is the gas sonic velocity. Sonic velocity is defined for an ideal gas by:

$$v_{sonic} = \sqrt{\frac{kRT_{throat}}{M_W}} \tag{2.5}$$

where k is the ratio of specific heat capacities, R is the specific gas constant, T_{throat} is the temperature at the nozzle throat ($2T/k + 1$) and M_W is the gas molecular weight. It must be noted that Schurr and Zhao (1994) did not explicitly account for temperature reduction at the nozzle throat with pressure reduction, and as such may have overestimated the actual grinding energy by overestimating the sonic velocity. For non ideal gases the compressibility factor, z, can be included so that $v_{sonic} = \sqrt{zkRT_{throat}/M_W}$.

Empirical correlations for a given material between particle size and E_{sp} are shown to work well for similar spiral jet mills by Midoux *et al.* (1999). These correlations allow a prediction of particle size to be made for a given combination of material, solids feed rate and gas mass flow rate. If an increase in powder throughput is desired for a given material, it is possible to predict the gas pressure or nozzle diameter increase required to maintain similarity of particle size.

Midoux *et al.* showed that the change in Specific Surface Area (SSA) of a material, as a result of micronisation, correlates with E_{sp} for different gas molecular weights and at different scales as per Figure 2.7.

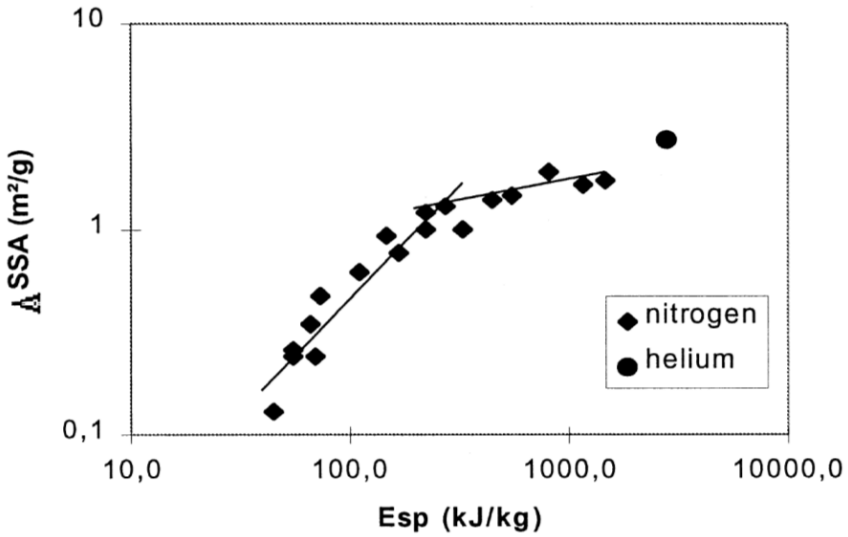

Figure 2.7 Change in SSA against E_{sp} (Midoux *et al.* 1999)

The concept of a critical value of E_{sp} is described by Midoux *et al.* to be where the two trend lines shown in Figure 2.7 intersect. It is claimed that at energies below this point, particle fragmentation with large changes in specific surface area occur, whereas above this transition point increases in energy only result in modest increases in specific surface area as a result of attrition occurring instead of fragmentation.

Zhao and Schurr (2002) presented some insightful data for micronisation with gases of differing molecular weight. To interpret their results it is necessary to introduce the concept of the grinding limit. The grinding limit is the smallest mean particle size that can be attained by micronisation with a spiral jet mill. This grinding limit will typically be much greater than the minimum achievable particle size for most crystalline materials (1-10 nm) but may be similar in size to the minimum achievable size for some polymers (1-10 μm). The grinding limit for the spiral jet mill relates to the smallest achievable aerodynamic cut size, as it will not be possible to reduce the mean particle size much below this, whereas the minimum achievable particle size relates to the physical properties of the particle and is the size at which it will no longer be possible to initiate a crack within the particle (Peukert 2004).

The grinding limit for a material in a spiral jet mill may be approached by feed rate reduction, increasing gas mass flow rate or re-passing ground material such that the powder hold up tends towards zero. Zhao and Schurr found that the grinding

limit varied for gases of differing molecular weights as shown in Figure 2.8, with lighter gases giving smaller particle size as the specific energy tends towards infinity.

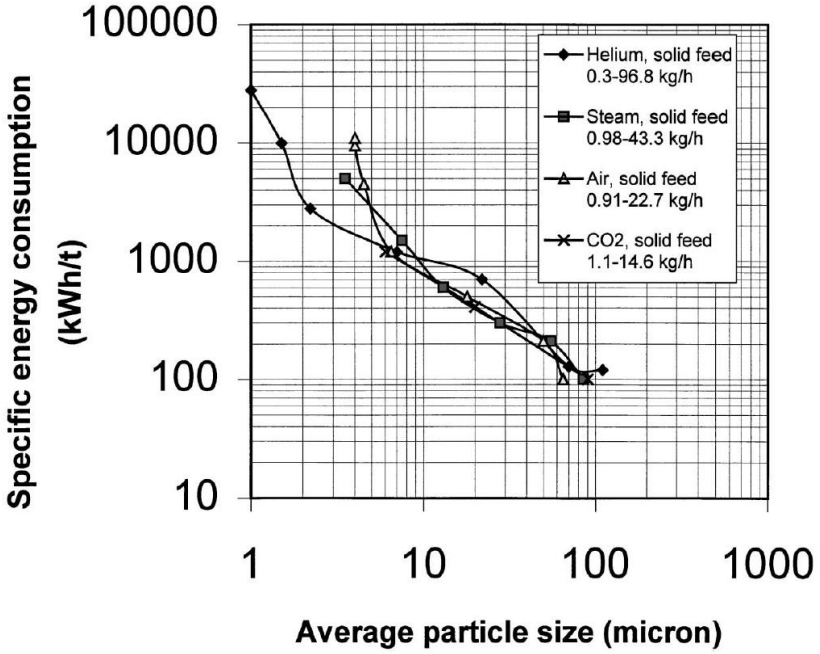

Figure 2.8 E_{sp} **against Particle Size (Zhao and Schurr 2002)**

Importantly, Zhao and Schurr also found that at low E_{sp} values, gases of a lower molecular weight give a coarser output rather than finer. It is claimed that the reduction in grinding limit with reduced molecular weight is a result of increased energy due to increased sonic velocity. This claim however directly contradicts the presumption that E_{sp} correlates with particle size as a result of the average energy imparted to the material, as it would be expected that regardless of gas molecular weight the same particle size should be obtained for a given E_{sp} value.

2.7 Numerical Simulation

The basis for simulation of the grinding process was first developed in academic literature by Brown (1941). A breakage distribution function $B(x, y)$ is defined as the mass fraction of fragments below size x when particles of original size y are broken once. Brown (1941) assumed the following empirical relationship for the breakage distribution function of coal:

$$B(x,y) = \frac{1-\exp(-x)}{1-\exp(-\frac{y}{m})} \qquad (2.6)$$

Where m is a constant for given type of coal and impact energy. A breakage function similar to this and Equation 2.1 is applied to the spiral jet mill in Chapter 3. Epstein (1948) used this breakage function to show that after a number of steps the resultant population of particles from such a function is logarithmico-normal. As the PSD following a particle size reduction process is generally logarithmico-normal, it confirms that it may be possible to use such a breakage distribution function to numerically simulate milling.

A number of papers were then published by researchers proposing various means of modelling the particle breakage process between 1948 and 1970 which were summarised, critiqued and further developed by Austin (1971). This work eventually led to the population balance model developed by Herbst and Fuerstenau (1980). Venkataraman and Fuerstenau (1984) further developed these equations and performed their own experiments to test the predictions of such a population balance model. Although these experiments involved measuring the output particle size of a ball mill operated for varying lengths of time, the verification of the breakage equation and population balance model is relevant as it forms the basis of subsequent models for jet mills.

Vogel and Peukert (2003a) performed extensive experimental investigation, leading to a means of estimating the milling properties of a material from single particle impact tests. This can then be used to build a population balance model (Vogel and Peukert 2003b) based on material properties, rather than fitting the constants in a population balance model to experimental data.

The first reported application of the population balance model to the jet mill is a paper by Berthiaux and Dodds (1999) on the fluidised bed opposed jet mill. Their results for batch milling showed that a single breakage equation did not apply to the entire particle size range, and that to fit experimental data it was necessary to consider that the breakage function would be different for smaller particles. Berthiaux *et al.* (1999) then used their population balance model to simulate continuous grinding based on removal of particles for a specified gas flow rate and revolutions per minute (RPM) by a mechanical classifier. Their numerical model required details of the grade efficiency of their mechanical classifier, which were experimentally determined. Their numerical model closely matched their

experimental data, however this may be a result of their experimentally determined grade efficiency curve.

The population balance was further developed as a stochastic model and verified with experimental data by Teng *et al.* (2010). However again, the close agreement between experimental and theoretical found by Teng *et al.* was a result of setting the classification size in their model to that of their experimental data set.

Computational Fluid Dynamics (CFD) is required to determine classification dynamics of a spiral jet mill, or indeed any other form of jet mill and aerodynamic particle classifier. CFD allows fluid flows to be simulated numerically for a given geometry and set of boundary conditions. CFD is necessary as measurement of gas velocity and visualisation of flow patterns within a spiral jet mill is not feasible, and CFD allows detailed information to be gathered on gas flow that would otherwise be impossible to obtain from experimentation. Studies primarily investigating gas flow were published by Kozawa *et al.* (2011) and Rodnianski *et al.* (2013). Kozawa *et al.* showed that the introduction of a classifier (Figure 1.1) could prevent large particles escaping along the grind chamber wall closest to the central exit, but also that classifier heights of greater than 4 mm resulted in a coarsened output due to increased drag forces. The CFD results obtained by Kozawa *et al.* confirm the experimental results of Tuunila and Nyström (1998) where increases in classifier height led to increased particle size. Rodnianski *et al.* also confirmed that higher classifier heights result in greater exit velocities. Rodnianski *et al.* showed that the spin ratio (ratio of tangential velocity to radial velocity) remained approximately constant in the grind chamber for varying gas mass flow rates as both components of velocity change proportionally with each other up until the classifier where the proportionality breaks down. This observation of an approximately constant spin ratio within the spiral jet mill for various gas mass flow rates is important for Chapter 3 and is investigated in detail in Chapter 5.

The spiral jet mill involves complicated interactions between gas and particles, and as such cannot be simulated by CFD alone. An early example for modelling both gas and particle dynamics for the spiral jet mill can be found in a publication by Eskin *et al.* (1999). Eskin *et al.* showed that the interaction between gas and solids is likely to be significant, but were not able to fully simulate the milling process. Han

et al. (2002) published the first results of combined CFD-Discrete Element Method (CFD-DEM) study for the spiral jet mill. CFD-DEM allows the particle breakage process to be modelled according to mechanical properties and for the interactions between gas and particles to be thoroughly simulated. Due to computational limitations at the time of the publication, the simulation by Han *et al.* was restricted to two dimensions. Teng *et al.* (2011) were able to perform three dimensional CFD-DEM for a simplistic two nozzle spiral jet mill by not simulating particle breakage. Despite not investigating fragmentation, their study provided useful information about the location of collisions and their corresponding energies.

Brosh *et al.* (2013) developed CFD-DEM code which is capable of performing much faster simulations in three dimensions by detaching the DEM grid from the CFD grid, increasing the time step and removing collision fragments from the simulation when below 10 µm. Even with improved code to speed up their simulation, the results of a three dimensional CFD-DEM simulation of a spiral jet mill published by Brosh *et al.* (2014) took "a couple of months" to solve. Their simulation results appear similar to experimental as per Figure 2.9, however this is likely to be a result of the simulation being designed to remove particles of below 10 µm in diameter and the experimental data being mostly below 10 µm.

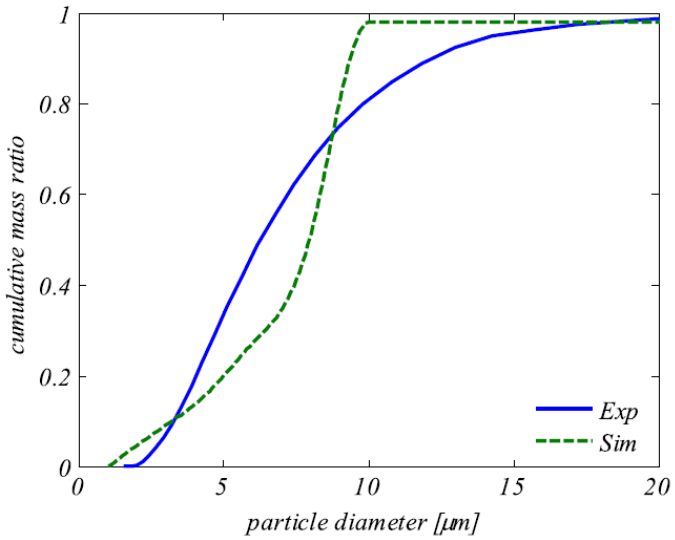

Figure 2.9 Numerical and Experimental Cumulative Undersize Distribution (Brosh *et al.* 2014)

2.8 Summary of Key Facts

- Particle size reduction is primarily a result of particle-particle collisions for mills with intersecting nozzle paths (Berry 1946, Kürten *et al.* 1970, Han *et al.* 2002, Brosh *et al.* 2014).
- Output particle size (cut size) is defined by a centrifugal to drag force balance at the grind chamber exit (Berry 1946, Dobson and Rothwell 1969, Müller *et al.* 1996, Rodnianski *et al.* 2013).
    - Modifications to the grind chamber and classifier can change the cut size (Tuunila and Nyström 1998, Katz and Kalman 2007).
    - Retention of particles until micronised to below the cut size leads to hold up of particles within the grind chamber (Berry 1946, Müller *et al.* 1996).
    - Hold up of particles leads to a reduction in gas tangential velocity and a change to the cut size by reduction in centrifugal force (Müller *et al.* 1996).
    - Changes to gas mass flow rate, solids feed rate and solids mechanical properties can change the amount of hold up and therefore cut size (Müller *et al.* 1996).
- The grinding limit can be defined as the cut size for zero hold up, and may be approached by feed rate reduction, gas mass flow rate increase or repassing ground material (Müller *et al.* 1996, Zhao and Schurr 2002).
    - The grinding limit of gas of a lower molecular weight is smaller than those of a greater molecular weight (Zhao and Schurr 2002).
- The surface chemistry of a material can change following micronisation as a result of preferential cleaving along weaker planes within the crystal habit (Grimsey 2002).
- Micronisation can result in a breakdown of crystallinity and produce amorphous materials (Brodka-Pfeiffer 2003).
- Hard and brittle materials micronise to small sizes with a spiral jet mill, as they shatter easily, whereas elastic or soft materials have larger cut sizes as a result of collisions between particles being less successful (Ghadiri and Zhang 2002, Zügner *et al.* 2006).
- Output particle size is generally insensitive to input particle size (Ramanujam *et al.* 1969, Katz and Kalman 2007).

- Particle breakage may be modelled by a breakage function which assumes that for a given collision energy and input particle size, the fraction of fragments below a given size will be constant (Brown 1941, Ghadiri and Zhang 2002, Vogel and Peukert 2003a).
- CFD has shown that the spin ratio remains constant with varying gas mass flow rates (Rodnianski *et al.* 2013).

Chapter 3. Spiral Jet Mill Cut Size Equation

3.1 Rationale

Empirical correlations for a given material between particle size and E_{sp} have been shown to work well for identical spiral jet mills as per Chapter 2. These correlations allow a relatively accurate prediction of particle size to be made for a given combination of material, solids feed rate and gas mass flow rate. If an increase in powder throughput is desired for a given material, it is possible to predict the gas pressure or nozzle diameter increase required to maintain similarity of particle size. Both Midoux *et al.* (1999) and Zhao and Schurr (2002) suggest that E_{sp} could be used for scale up without presenting supporting evidence.

Industrial experience at GlaxoSmithKline (GSK) detailed in Chapter 4 and 6 suggests that E_{sp}-particle size correlations do not work for all materials. Additionally, Tuunila and Nyström (1998) and Katz and Kalman (2007) showed that by varying geometrical parameters, differences in particle size can occur for identical combinations of gas flow rate and solids feed rate.

The spiral jet mill currently lacks a mechanistic basis for the correlation between E_{sp} and cut size for a given material and mill, as well as the reason for different cut sizes being obtained for different mill geometries. An analytical derivation of the relationship between particle size, mill geometry, gas mass flow rate, gas physical properties, solids feed rate and solids physical properties could lead to a reduction in time and material required for scale up. Such an analytical derivation is presented in this chapter.

The approach taken for the derivation of the cut size equation was to populate a force balance with terms from grind chamber geometry and an energy balance between the gas only single phase system and gas and powder two phase system. The force balance was then solved for cut size to produce a general equation. Assumptions were then made about the system so that cut size could be phrased as a function of gas mass flow rate and solids feed rate.

3.2 Force Balance

The underlying physics governing particle size obtained from a spiral jet mill were initially discussed by Dobson and Rothwell (1969) who noted that output particle size could be estimated by opposing centrifugal and radial drag forces on a particle at the grind chamber exit. Theoretically, the spiral jet mill has a size of particle (d_{cut}) that will remain balanced at the grind chamber exit with equal drag and centrifugal force as per Figure 3.1

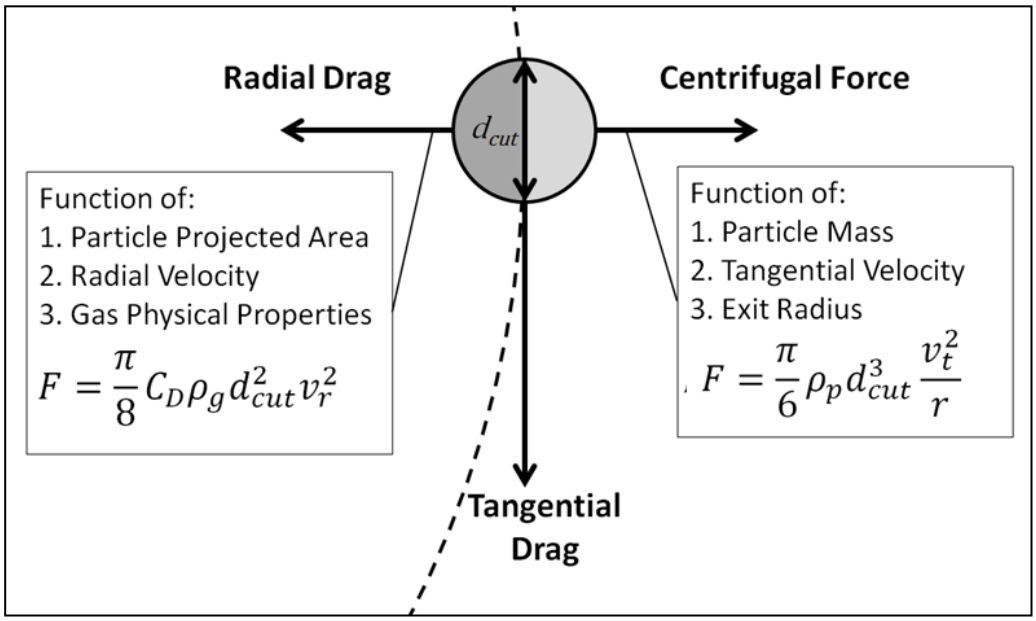

Figure 3.1 Spiral Jet Mill Particle Force Balance (MacDonald *et al.* 2016)

The force balance was solved in the radial direction for cut size (d_{cut}):

$$d_{cut} = k_1 \frac{v_r^2}{v_t^2} \qquad (3.1)$$

where $k_1 = 3C_D\rho_g r/4\rho_p$, C_D is the drag coefficient of the particle, ρ_g is the gas density, ρ_p is the particle true density, r is the radial position of the particle, v_r is the gas radial velocity and v_t is the tangential velocity of the particle. The drag coefficient, C_D, is known to vary with gas velocity, particle diameter and particle shape and is considered in detail in Section 3.5 of this chapter.

Rodnianksi *et al.* (2013) performed a CFD investigation of the flow fields in a spiral jet mill and their dependence on geometry and gas throughput. It was shown that the spin ratio (v_t/v_r) does not vary significantly across a range of gas mass flow rates for a gas only system. This is corroborated by a CFD investigation with

varying motive gases in Chapter 5. Rodnianski *et al.* had also noted as part of their analysis that the actual particle tangential velocity may be less than the gas tangential velocity due to the slip velocity between the particle and gas, and proposed to modify the particle tangential velocity:

$$v_{t(particle)} = v_{t(gas)}(1 - 0.0638 \cdot d_{cut}^{0.3} \cdot \rho_p^{0.5}) \qquad (3.2)$$

Equation 3.2 was however developed empirically by Konno and Saito (1969) for particles of greater than 120 µm in diameter and for velocities of less than 20 m.s^{-1}. A more recent study by Rautiainen *et al.* (1999) using 64 µm particles showed that at low levels of mass flux for increasing gas velocity, the slip velocity tends towards the terminal velocity of the particles as per Figure 3.2.

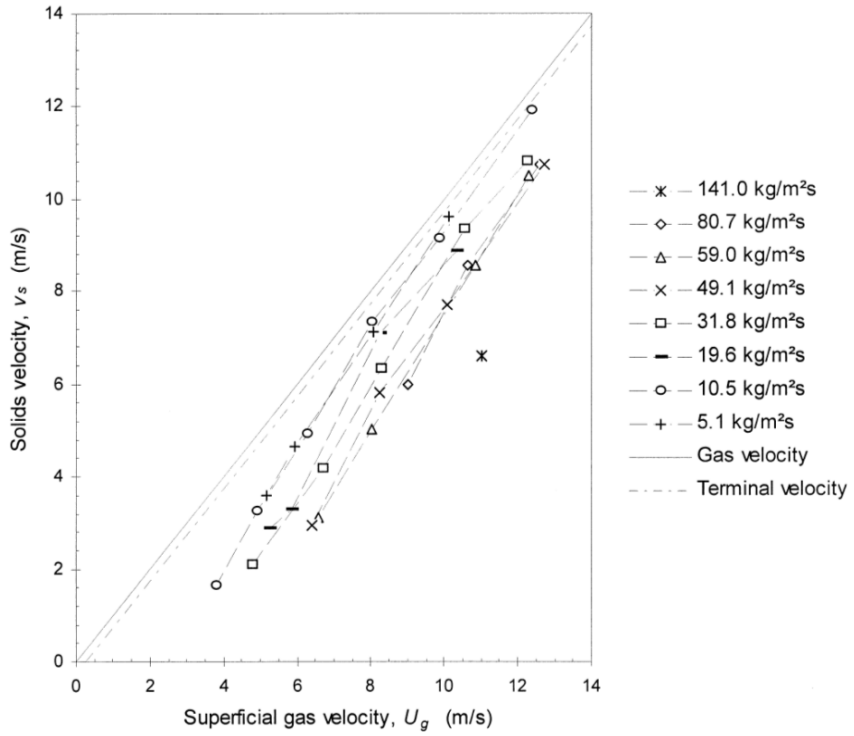

Figure 3.2 Superficial Gas Velocity against Solids Velocity (Rautiainen *et al.* 1999)

As can be seen from Table 3.1 the mass flux is relatively low for the experimental data presented by Rodnianksi *et al.* (2013) for sodium chloride micronisation compared to the mass fluxes shown in Figure 3.2. It must be noted that the input material feed rates in Table 3.1 are quite high for the scale of mill used, meaning these are quite high levels of mass flux for powder exiting a spiral jet mill.

Solids Feed Rate ($kg.hr^{-1}$)	Solids Feed Rate ($g.s^{-1}$)	Mass Flux ($kg.m^{-2}s^{-1}$)
3.6	1	1.2
18	5	6.2
25.2	7	8.7

Table 3.1 Mass Flux Exiting Grind Chamber ($D_{exit} = 32$ mm, $H_{exit} = 8$ mm)

Therefore, based on Figure 3.2 and Table 3.1 it would be expected that, for the tangential velocities in excess of 100 $m.s^{-1}$ found in a spiral jet mill and the range of mass fluxes, the particle terminal velocity would be a more appropriate slip velocity. Spherical particle terminal velocities in air for sodium chloride as per Stokes' law can be found in Table 3.2.

Particle Diameter (μm)	Terminal Velocity ($m.s^{-1}$)
1	0.00006
5	0.00158
9.7	0.00596
50	0.15837
100	0.63348

Table 3.2 Spherical NaCl Particle Terminal Velocities in Air at 25 °C Calculated According to Stokes' Law

As can be seen from Table 3.2, the terminal velocity of micronised particles below or at the cut size is insignificant in relation to even the most modest of tangential velocities. Even for particles above the cut size (50 and 100 μm) the terminal velocity is almost negligible when compared to the expected tangential velocities in a spiral jet mill of in excess of 100 $m.s^{-1}$. From Figure 3.2 and Tables 3.1 and 3.2 it can be concluded that the assumption that the particle tangential velocity is equal to the gas tangential velocity is valid.

Rautiainen *et al.* (1999) and Konno and Saito (1969) measured the slip velocity for vertical flow of gas. It logically follows that the slip velocity would tend towards terminal velocity as the particles are subjected to the force of gravity in the opposite direction to flow. With respect to flow in a spiral jet mill, the actual slip velocity as a result of gravity will be in a perpendicular direction to the gas flow

and may have no impact at all other than pulling particles towards to bottom of the grind chamber.

Considering again that the theoretical cut size is for the case where a particle is balanced by radial drag and centrifugal force, this is analogous to the case of terminal velocity where a particle is balanced by axial drag and gravitational force. In this analogy it can be considered that with respect to the total gas velocity there is a considerable slip velocity in the radial component of velocity as a result of centrifugal force from gas and particle tangential velocity. Regardless of how it is considered, it is unlikely that there is any notable slip between the particle and gas in the tangential component of velocity.

With regards to aerodynamic particle classification in a spiral jet mill with different gases, for very small particles with low Reynolds numbers that are not subject to turbulent drag, it may be worth considering the Cunningham slip correction factor (Rader 1990). When the particle size nears the mean free path of molecules of gas, the amount of drag force that can be exerted by gas molecules reduces. This correction factor may be important when modelling the path of the smallest collision fragments out of a spiral jet mill, but not for trying to model the largest particle that can escape the grind chamber.

Despite the tangential slip velocity assumption being invalid, a crucial observation was made by Rodnianski *et al.* (2013) that as a particle travels towards the grind chamber exit it gains momentum that may allow it to escape the grind chamber despite being greater in size than the theoretical cut size derived from a static force balance. With knowledge of the tangential and radial velocity profiles as a function of radial position it may be possible to numerically determine an adjusted theoretical cut size that considers the momentum a particle can develop while exiting the grind chamber. However, for the sake of an analytical derivation of a general cut size equation, only the static particle force balance as given by Equation 3.1 will be considered.

3.3 Geometry and Velocity

To determine the cut size equation in terms of specific energy consumption (E_{sp}), gas velocities may be phrased in terms of gas kinetic energy delivery rate. It is

possible to define the gas kinetic energy delivery rate in terms of gas volumetric flow rate in the grind chamber by combining Equation 2.4 and Equation 2.5:

$$\dot{E}_k = \frac{1}{2}\dot{m}_g \frac{kRT_{throat}}{M_W} \quad (3.3)$$

Assuming ideal gas behaviour, $\dot{m}_g$ can be phrased in terms of volumetric flow rate through the grind chamber:

$$\dot{m}_g = \dot{V}\frac{PM_W}{RT} \quad (3.4)$$

where P is the pressure in the grind chamber, T is the temperature in the grind chamber and $\dot{V}$ is the volumetric flow rate through the grind chamber. Combining Equation 3.3 and Equation 3.4 yields:

$$\dot{E}_k = \frac{T_{throat}}{2T} kP\dot{V} \quad (3.5)$$

From Equation 3.5 it can be deduced that for gases with similar ratios of specific heat capacity there will be similarity of volumetric flow rate for the same kinetic energy delivery rate, regardless of their molecular weight. It should be noted that in this analysis the gas volumetric flow rate ($\dot{V}$), mass flow rate ($\dot{m}_g$) and kinetic energy delivery rate ($\dot{E}_k$) refer to the sum of the grinding gas, feed gas and entrained gas. Additionally, although the total gas flow rate is being considered in this derivation, the constant spin ratio assumption (Rodnianski *et al.* 2013) is only likely to hold when the ratio of grinding gas, feed gas and entrained gas is constant, as the CFD simulations it is based on did not cover variation in feed gas or entrained gas.

The grind chamber exit geometry can be defined in three parameters (r, h_1 and h_2 which are the classifier radius, exit gap and grind chamber height respectively) as shown in Figure 3.3 which shows the side view of a grind chamber with a "classifier" at its exit and the various parameters. Many spiral jet mills have a classifier that results in a different gap size for gas flow at the grind chamber exit compared to the rest of the grind chamber. The purpose of the classifier is to prevent the escape of larger particles which can travel along the walls of the grind chamber where the radial velocity is higher and radial drag dominates over centrifugal forces. In this case, a flat grind chamber geometry has been presented

where the height of the entire grind chamber is h_2. This derivation should also apply to elliptical plates (both symmetrical and asymmetrical), however it should be noted that changing the plate shape will potentially impact on both the collision kinetics and the spin ratio. Although only a single classifier has been shown in Figure 3.3, the dimensions refer to the gap for gas flow rather than classifier height and as such could also be applied to a spiral jet mill with a double classifier.

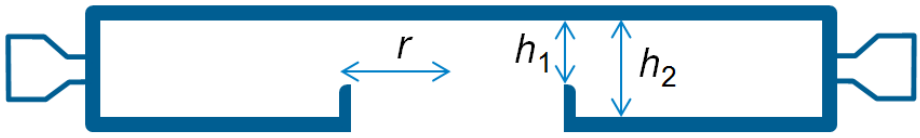

Figure 3.3 Grind Chamber Exit Geometry (MacDonald *et al.* 2016)

The general gas radial velocity at a point in a cylinder with gas flowing radially towards the centre, $v_{r\,(general)}$, can be phrased in terms of gas volumetric flow rate:

$$v_{r\,(general)} = \frac{\dot{V}}{2\pi r h} \tag{3.6}$$

where h is the height of the gap through which gas flows and r is the radial position. The radial velocity will vary across h (Kozawa 2012, Rodnianski *et al.* 2013), however to realise the subsequent analysis of the system as a whole, Equation 3.6 assumes that the radial velocity is constant across the height of the grind chamber.

Equation 3.6 can be combined with Equation 3.5 and solved for the radial velocity at the grind chamber exit, v_r:

$$v_r = \frac{k_2 \dot{E_k}}{h_1} \tag{3.7}$$

where $k_2 = \frac{T}{T_{throat} \pi r k P}$.

The constant spin ratio assumption (Rodnianski *et al.* 2013) can be combined with Equation 3.6 and 3.5 to define the tangential velocity at the grind chamber exit for the zero hold up system, $v_{t\,(gas\ only)}$:

$$v_{t\,(gas\ only)} = \frac{k_2 k_3 \dot{E_k}}{h_2} \tag{3.8}$$

where k_3 is the spin ratio (v_t/v_r) for the zero hold up system. The height h_2 has been used instead of h_1 in Equation 3.8 as Rodnianski *et al.* (2013) showed that the constant spin ratio assumption only holds for changes in grind chamber height, and not variation in classifier height.

The force balance can be defined for a particle at the interface between the classifier and the grind chamber where it is subjected to the tangential velocity of the grind chamber and the radial exit velocity of the classifier. Figure 3.4 shows the force balance for a particle at the interface between the grind chamber and classifier.

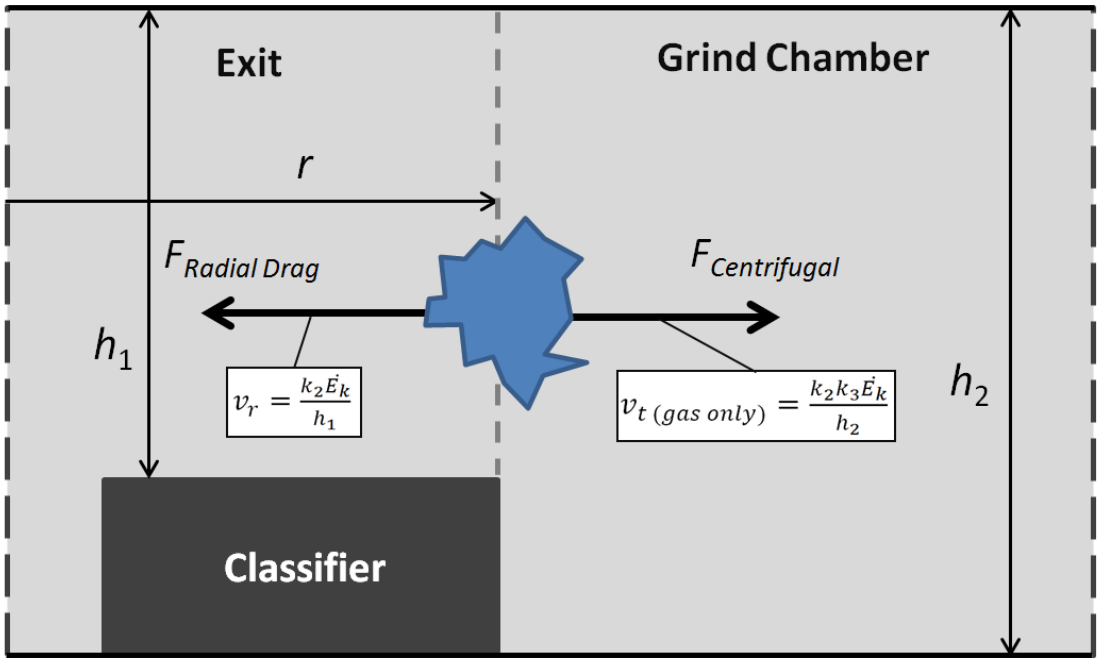

Figure 3.4 Classifier to Grind Chamber Interface (MacDonald *et al.* 2016)

Although Figure 3.4 suggests that for increasing classifier height (reduction in h_1) there would be an increase in radial drag force and cut size, whilst for a reduction in classifier height (increase in h_1), the radial drag force and cut size would be reduced, this does not apply to all classifier heights (Kozawa *et al.* 2012). Where there is no classifier, the output is expected to be coarser as there is a shortcut route for large particles to escape along the grind chamber wall, and therefore the initial introduction of the classifier will result in a finer output.

3.4 Force and Energy Balance

Prior to performing a balance between the gas only and gas and powder systems with respect to the rate of kinetic energy consumption at the grind chamber exit, the effect of suspended powder hold up on tangential velocity must be considered. This analysis only considers the effect of suspended solids on gas velocity, and does not consider the effect of changing mill dimensions associated with excessive build up on mill surfaces. Once the system has reached a steady state of dynamic equilibrium, there will be a constant mass of suspended solids held up (m_h) in the grind chamber volume (V_{grind}):

$$\frac{m_h}{V_{grind}} = constant \tag{3.9}$$

Assuming a constant solids concentration and no slip between the solids and gas, there will be an equivalent solids hold up rate associated with the gas volumetric flow rate to maintain the solids concentration:

$$\frac{m_h}{V_{grind}} = \frac{\dot{m}_h}{\dot{V}} \tag{3.10}$$

where $\dot{m}_h$ is the equivalent rate of powder hold up. It should be noted that $\dot{m}_h$ refers to the sum of both the retained particles and particles flowing through the system ($\dot{m}_s$). The equivalent rate of powder hold up is an important concept with regards to energy consumption, as maintaining hold up in rotation will consume energy at a given rate.

A balance can subsequently be performed on the rate of kinetic energy consumption at the grind chamber exit based on the assumption that the solids concentration is uniform and that the radial and tangential components of velocity do not change with position. Although it is known that the radial and tangential components will change with position and that the solids concentration is not uniform, they were assumed to be constant as this simplification allows the behaviour of the system to be approximated analytically. It is also assumed that axial movement of the gas and powder is negligible. The energy balance is performed by considering a unit volume (dV) in the grind chamber for the gas only and also the gas and powder systems. Figure 3.5 illustrates the energy balance by considering a unit volume for the gas only system on the left, and the gas and

powder system on the right. The rate of consumption of kinetic energy from the gas only system is a function of the gas radial and tangential velocity at the grind chamber exit, whereas the rate of consumption of kinetic energy for the gas and powder system is a function of the gas and powder radial and tangential velocities and additional frictional energy losses associated with particle collisions. As the gas radial velocity is fixed by geometry and volumetric flow rate this does not change when moving to the gas and powder system. However, the gas tangential velocity reduces with powder hold up as maintaining this hold up in circulation consumes energy.

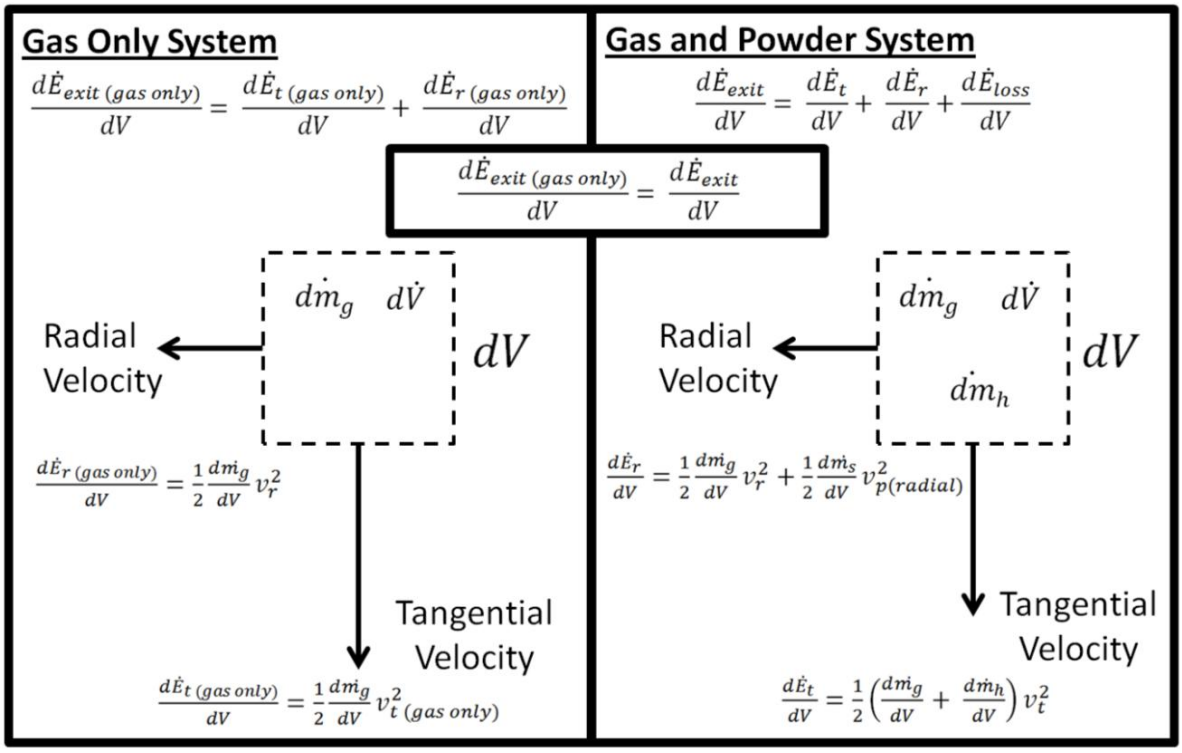

Figure 3.5 Energy Rate Balance on a Unit Volume at the Grind Chamber Exit (MacDonald *et al.* 2016)

The kinetic energy consumption rates can be integrated across the volume for the gas only system, Equation 3.11 and Equation 3.12, and for the gas and powder system, Equation 3.13 and Equation 3.14:

$$\dot{E}_{exit\ (gas\ only)} = \int \left(\frac{1}{2}\frac{d\dot{m}_g}{dV} v_{t\ (gas\ only)}^2 + \frac{1}{2}\frac{d\dot{m}_g}{dV} v_r^2\right) dV \qquad (3.11)$$

$$\dot{E}_{exit\ (gas\ only)} = \frac{1}{2}\dot{m}_g v_{t\ (gas\ only)}^2 + \frac{1}{2}\dot{m}_g v_r^2 \qquad (3.12)$$

$$\dot{E}_{exit} = \int(\frac{1}{2}\left(\frac{d\dot{m}_g}{dV} + \frac{d\dot{m}_h}{dV}\right)v_t^2 + \frac{1}{2}\frac{d\dot{m}_g}{dV}v_r^2 + \frac{1}{2}\frac{d\dot{m}_s}{dV}v_{p(radial)}^2 + \frac{d\dot{E}_{loss}}{dV})dV \quad (3.13)$$

$$\dot{E}_{exit} = \frac{1}{2}\left(\dot{m}_g + \dot{m}_h\right)v_t^2 + \frac{1}{2}\dot{m}_g v_r^2 + \frac{1}{2}\dot{m}_s v_{p(radial)}^2 + \dot{E}_{loss} \quad (3.14)$$

where $\dot{E}_{loss}$ is the rate of energy loss associated with friction, particle acceleration and collisions and $v_{p(radial)}$ is the particle radial velocity on exit from the grind chamber. The kinetic energy consumption rates at the grind chamber exit may be balanced for the gas only and gas and powder systems and solved for v_t^2 as follows:

$$v_t^2 = \frac{\dot{m}_g v_{t\,(gas\ only)}^2 - \dot{m}_s v_{p(radial)}^2 - 2\dot{E}_{loss}}{\dot{m}_g + \dot{m}_h} \quad (3.15)$$

By combining Equation 3.1, Equation 3.7 and Equation 3.15 a general equation for spiral jet mill cut size can be derived:

$$d_{cut} = \frac{k_1(h_2 k_2 \dot{E}_k)^2(\dot{m}_g + \dot{m}_h)}{\dot{m}_g(h_1 k_2 k_3 \dot{E}_k)^2 - 2\dot{E}_{loss} - \dot{m}_s v_{p(radial)}^2} \quad (3.16)$$

However, Equation 3.16 in its current form cannot be used to determine cut size as a number of the parameters are unknown for the system, including the drag coefficient and response of solids hold up to solids feed rate and gas mass flow rate.

3.5 Variation in Drag Coefficient

As previously discussed in Chapter 2, the flow regime of radial drag past a particle near the classifier is transitional and cannot be estimated using Stokes' law (Re>2). The drag coefficient reduces with increasing Reynolds number towards a constant value, C_1, for turbulent conditions depending on the particle shape as per Figure 3.6 by Haider and Levenspiel (1989).

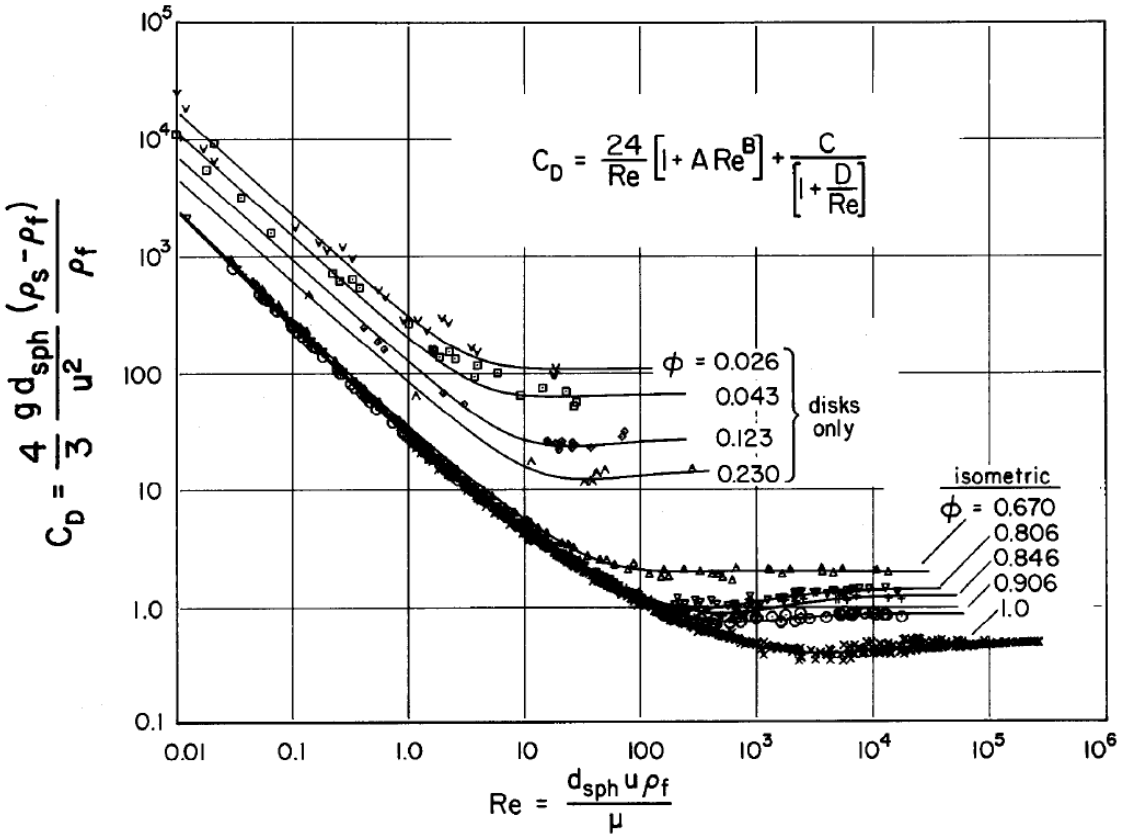

Figure 3.6 Drag Coefficient for Varying Particle Sphericities (Haider and Levenspiel 1989)

To approximate the drag coefficient, the following simplified equation is proposed:

$$C_D = \frac{24}{Re} + C_1 \qquad (3.17)$$

where C_1 is the drag coefficient as the Reynolds number tends towards infinity and is defined for a given sphericity as per Figure 3.6. The basis for this simplification is that it combines the inverse proportionality between the Reynolds number and drag coefficient expected by Stokes' Law with the crucial observation from empirical correlations that the drag coefficient tends towards a constant value as the Reynolds number is increased (Haider and Levenspiel 1989). Equation 3.17 can then be combined with the definition of the Reynolds number and Equation 3.7 to obtain Equation 3.18 for the drag coefficient of a particle at the grind chamber exit:

$$C_D = \frac{24\mu k_4 h_1}{\rho_g k_2 d_{Reynolds} \dot{m}_g} + C_1 \qquad (3.18)$$

where μ is the gas viscosity, $d_{Reynolds}$ is the Reynolds length scale and $k_4 = 2/v_{sonic}^2$. Although equivalent to cut size, $d_{Reynolds}$, will be assumed to be constant in the

subsequent analysis as variation in cut size is generally small when compared to variation in solids feed rate or gas mass flow rate. This can be observed in Figure 4.2 a plot of variation in cut size for Product A discussed in Chapter 4, where doubling the gas mass flow rate reduced the cut size by less than 25%.

This estimation of the drag coefficient may then be combined with the definition of k_1 giving:

$$k_1 = \frac{x_1 k_4}{d_{Reynolds} \dot{m}_g} + C_2 \qquad (3.19)$$

where $x_1 = 18\mu h_1 r/\rho_p k_2$ and $C_2 = 3C_1\rho_g r/4\rho_p$. It should be noted that k_1 is now a function of the Reynolds length scale and gas mass flow rate. As the cut size (Reynolds length scale) is reduced, the dependence of k_1 on gas mass flow rate will increase. Similarly as cut size increases k_1 will tend towards C_2.

3.6 Collision Kinetics

As the rate of generation of small fragments is dependent on collisions occurring between particles, it may be possible to analyse the particle size reduction process in a similar manner to collision kinetics and reaction chemistry. Similar to reaction kinetics, two or more particles must collide with sufficient activation energy to result in fragmentation such that particles below the cut size are generated. If a parallel were to be drawn between collision kinetics and reaction chemistry, a second order relationship for collision rate with respect to powder concentration would be expected:

$$\dot{m}_{collide} \propto \left(\frac{m_h}{V_{grind}}\right)^2 \qquad (3.20)$$

However, the collision process in a spiral jet mill differs in principle to typical bimolecular reactions where the rate limiting step is a collision event between two randomly moving molecules in three dimensions. In the case of a spiral jet mill, highly energetic collisions primarily occur at the intersection of the nozzle jets and the rest of the grind chamber. Prior to collision, particles must be transported from the grind chamber to the grind nozzles, leading to a two stage process for particle collisions. Transport of particles to the nozzles can be defined as:

$$\dot{m}_{nozzles} = D\left(\frac{m_h}{V_{grind}}\right) \qquad (3.21)$$

where D is the transfer coefficient in $m^3.s^{-1}$ which will be specific to the transport properties of the particles being micronised, the gas physical properties and the flow conditions in the grind chamber. The mass transfer coefficient relates to the volume of gas-solids mixture intersecting with the nozzles per second. The rate of collisions is thus expected to be second order:

$$\dot{m}_{collide} = K\left(\frac{\dot{m}_{nozzles}}{\dot{V}}\right)^2 \qquad (3.22)$$

where K is a rate constant in $m^6.kg^{-1}.s^{-1}$ for a collision between two particles that will vary depending on the solids concentration, particle velocities and particle cross sectional area.

The angled configuration of grind nozzles is designed to result in particle collisions with enough energy to cause them to fragment. The most likely collision scenario, and the scenario resulting in the greatest momentum exchange (Kürten *et al.* 1970), is where a particle (1) accelerated by the nozzle jets collides with another particle (2) and whose path coincides with the nozzle jet as illustrated in Figure 3.7. Although subdivided into the particles accelerated by the nozzle jets (1) and particles colliding with them (2), this is one collision scenario. A second collision scenario (3) exists where two particles, both accelerated by different nozzle jets, collide with each other. This would be more likely to occur for either closely spaced nozzles or low solids concentrations.

It is expected that for both of these scenarios there will be a wide range of types of collisions between particles depending on the mass, velocity, angular velocity and mechanical properties of the particles. Particularly energetic collisions between large particles are likely to result in particle breakage (body crushing), whereas lower energy collisions between smaller particles are more likely to result in chipping (surface grinding) or fatigue as demonstrated with CFD-DEM (Han *et al.* 2002, Brosh *et al.* 2014).

The third collision scenario (4) involves collisions between a particle and the mill surfaces. These could involve a particle being pulled by centrifugal force to the edge of the grind chamber and colliding with the periphery of the chamber, particles colliding with the classifier or particles hitting the top or bottom of the chamber. This third scenario may account for a significant amount of attrition in mill designs with fewer nozzles such that the nozzle jets do not intersect. Teng *et*

al. (2011) reported a numerical simulation utilising CFD-DEM for a spiral jet mill design consisting of two nozzles which did not intersect and were angled approximately tangentially in the direction of the mill chamber walls. This particular mill design (Teng *et al.* 2011) led to an increased prevalence of the third collision scenario compared to the first two. Particle-mill collisions may also be more likely for particularly large input particles where centrifugal forces are very high or for low solids concentrations where particle-particle collisions are less likely than particle-mill collisions. As most spiral jet mills have nozzle jets which intersect with each other, the first two scenarios as per Figure 3.7 are considered to be the most frequent. As the third scenario also requires mass transport to the nozzles for the most energetic wall collisions, the derivation in this paper also applies to this attrition mechanism.

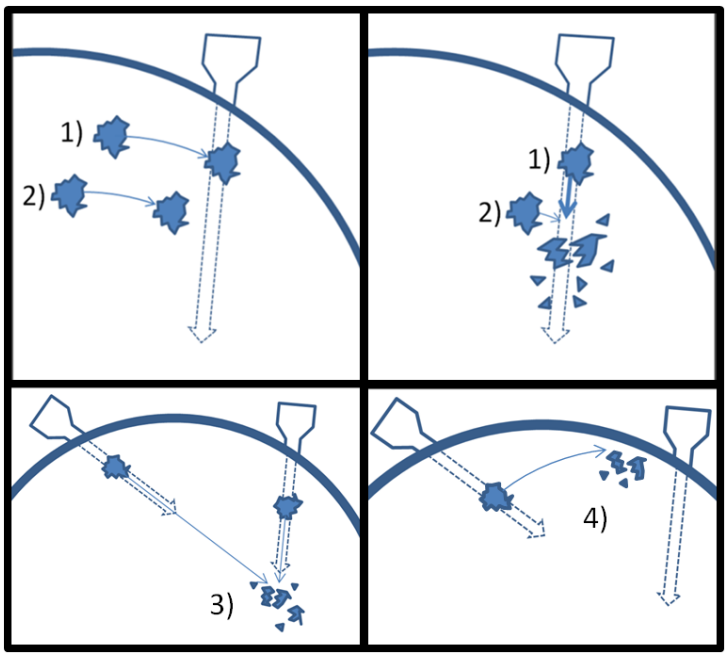

Figure 3.7 Particle Collision Scenarios (MacDonald *et al.* 2016)

Drawing on an analogy with reaction kinetics, the overall reaction order will be defined by the rate limiting step. It is assumed that mass transport to the nozzles is the rate limiting step in the particle fragmentation process. This assumption has been made as the angled configuration of grind nozzles is such that once a particle intersects with a nozzle jet it is likely to undergo a subsequent collision, making this process faster than mass transport to the nozzles. Therefore, it is possible to deduce Equation 3.23 for the rate of collisions:

$$\dot{m}_{collide} = D\left(\frac{m_h}{V_{grind}}\right) = D\left(\frac{\dot{m}_h}{\dot{V}}\right) \quad (3.23)$$

By drawing a parallel with reaction chemistry it should be noted that as the nozzle jet velocity is limited to sonic velocity for choked flow, it can be assumed that the maximum collision energy will be similar for a fixed grind angle across a wide range of grind pressures. Similarity in maximum collision velocity will be maintained for grind pressures in the choked flow regime where the ratio of pressure in the mill chamber to the grind pressure is less than $(2/k{+}1)^{k/k\text{-}1}$ where k is the heat capacity ratio of the gas. Therefore, the collision energy remains approximately constant for a given nozzle jet velocity and collision angle. By applying the similarity of fracturing law / constant attrition propensity (Rumpf 1973 / Ghadiri and Zhang 2002) and assuming that variation in cut size is small with respect to overall size reduction, it is possible to assume that the mass fraction of collision fragments below the cut size is constant for a given spiral jet mill across a range of gas pressures and flow rates. This then allows the rate of generation of particles below the cut size ($\dot{m}_{below\ cut\ size}$) to be defined by the time averaged mass fraction of collision fragments below the cut size (b):

$$\dot{m}_{below\ cut\ size} = b\dot{m}_{collide} \quad (3.24)$$

Kürten *et al.* (1970) showed for opposed jets with a nozzle pressure difference of 4 bar, that increasing the solids feed rate from 6 g.min^{-1} to 800 g.min^{-1} resulted in a reduction in collision velocity from 142 m.s^{-1} to 83 m.s^{-1} as the time available for acceleration in the nozzle jet reduces with increases in powder concentration and collision probability. It would therefore be expected that for changes in powder concentration greater than an order of magnitude the mass fraction of collision fragments, b, will decrease with a reduction in acceleration time and collision energy. The assumption of b remaining constant is expected to be valid for changes of powder concentration within an order of magnitude as the collision velocities and energies will be approximately similar.

The collision energy and attrition propensity may vary with particle size as large primary particles will be able to retain their velocity following exit from a nozzle jet, whereas smaller particles will quickly lose their velocity due to fluid forces. The velocity retention and subsequent higher collision energies in addition to the larger size having greater attrition propensity may result in a greater value for b

when hold up has a greater mass fraction of large particles, and a lower b value for when hold up has a greater mass fraction of fine particles. For a given material, output PSD can vary with feed material PSD, potentially as a consequence of differing values of b. Determining the effect of feed material PSD and mechanical properties on b analytically is not considered in this derivation, however experimentation with different sizes of particles with contrasting mechanical properties could provide an empirical relationship. The experimental evidence for output particle size being relatively insensitive to input particle size may be a result of the overall distribution of partially micronised particles held up in the grind chamber being relatively insensitive to the size of the primary particles.

It is proposed that the mass fraction of collision fragments below the cut size, b, could be determined experimentally at laboratory scale with a 4" or 2" diameter spiral jet mill for a material and used to model behaviour at pilot or industrial scale. It may also be possible to estimate b by following a similar approach to that proposed by Vogel and Peukert (Vogel and Peukert 2003, Peukert 2004) or Zhang and Ghadiri (2002), using a single particle impact device and then estimating the collision conditions in the spiral jet mill. The mass fraction of collision fragments below the cut size should theoretically correlate with $\alpha H/K_c^2$ which can be experimentally determined with a Scirocco and Malvern Mastersizer 2000 (Bonakdar *et al.* 2016).

Upon delivery of a given solids feed rate to the grind chamber ($\dot{m}_s$), the equivalent rate of powder hold up ($\dot{m}_h$) will continue to increase until the rate of generation of collision fragments below the cut size ($\dot{m}_{below\ cut\ size}$) equals the rate of powder delivery ($\dot{m}_s$). This allows the rate of powder hold up ($\dot{m}_h$) to be defined in terms of the solids feed rate ($\dot{m}_s$) and gas mass flow rate ($\dot{m}_g$) for steady state:

$$\dot{m}_h = \frac{\dot{m}_g \dot{m}_s}{x_2} \tag{3.25}$$

where $x_2 = DbPM_w/RT$ assuming the gas in the grind chamber is ideal.

3.7 Equation Solution

Due to the unknown rate of energy loss, Equation 3.16 is difficult to solve. However, if it is assumed that the rate of unknown energy loss ($\dot{E}_{loss}$) and particle

radial velocity energy loss ($\frac{1}{2}\dot{m}_s v_{p(radial)}^2$) are negligible with respect to the energy losses associated with maintaining powder hold up in circulation, Equation 3.16 can be simplified:

$$d_{cut} = \left(\frac{h_2}{h_1}\right)^2 \left(\frac{k_1}{k_3^2} + \frac{k_1}{k_3^2}\frac{\dot{m}_h}{\dot{m}_g}\right) \tag{3.26}$$

It is known that energy losses associated with particle collisions are not completely negligible, as the size reduction process requires energy and must be a result of energy transfer from the grind nozzles to the particles and then from the particles to other particles. However it is known that collision energy losses will be less than those associated with maintaining hold up in circulation as long as the rate of particles intersecting with the grind nozzles ($\dot{m}_{nozzles}$) is less than the rate of powder hold up ($\dot{m}_h$). The rate of particles intersecting with the nozzles is a small fraction of the hold up rate due to the low nozzle intersection volume compared to total grind chamber volume. As the rate of particles intersecting the nozzles is by definition a small fraction of the rate of hold up, the hold up will always consume more energy, making this assumption valid.

Additionally, the rate of particles intersecting the grind nozzles should be directly proportional to the solids concentration, hence the associated energy loss will be directly proportional to that for hold up. If the constants in the cut size equation were to be determined empirically, the energy losses associated with particle acceleration for collisions would be accounted for by an increase in the magnitude of constants associated with hold up. It is thus possible to combine Equation 3.19, Equation 3.25 and Equation 3.26 giving:

$$d_{cut} = \left(\frac{h_2}{h_1}\right)^2 \left(\frac{C_2}{{k_3}^2} + \frac{x_1 k_4}{{k_3}^2 d_{Reynolds}\dot{m}_g} + \frac{C_2\dot{m}_s}{{k_3}^2 x_2} + \frac{x_1}{{k_3}^2 d_{Reynolds} x_2}\frac{1}{E_{sp}}\right) \tag{3.27}$$

This equation not only shows that cut size can be defined with specific energy (E_{sp}) as a variable with constants describing the system, but also that for different combinations of $\dot{m}_s$ and $\dot{m}_g$, differences in cut size could potentially be observed for the same specific energy. This derivation also indicates that different spiral jet mill geometries will result in different particle sizes for the same value of E_{sp}.

The grinding limit, d_{limit}, or cut size for zero hold up, is of particular interest as it can be determined experimentally. The grinding limit can be approached by allowing the gas mass flow rate to tend towards infinity, or letting the solids feed rate tend towards zero. According to Equation 3.27 the grinding limit should differ depending on how it is approached. If the solids feed rate tends towards zero for a constant gas mass flow rate, the grinding limit is given by:

$$d_{limit} = \left(\frac{h_2}{h_1}\right)^2 \left(\frac{C_2}{{k_3}^2} + \frac{x_1 k_4}{{k_3}^2 d_{Reynolds} \dot{m}_g}\right) \tag{3.28}$$

However, if the grinding limit is approached by increasing the gas mass flow rate to infinity for a constant feed rate the grinding limit is as follows:

$$d_{limit} = \left(\frac{h_2}{h_1}\right)^2 \left(\frac{C_2}{{k_3}^2} + \frac{C_2 \dot{m}_s}{{k_3}^2 x_2}\right) \tag{3.29}$$

Assuming that changes in d_{cut} and $d_{Reynolds}$ are less than an order of magnitude, it would be expected that a plot of cut size against $1/E_{sp}$ would produce a straight line if either solids feed rate or gas mass flow rate is kept constant. The gradient and intercepts of the lines for the constant solids feed rate and the constant gas mass flow rate will differ as indicated in Equation 3.27 with the intercepts for a constant gas mass flow rate and the solids feed rate defined by Equation 3.28 and Equation 3.29 respectively. This behaviour has been observed for Product A as shown in Chapter 4.

For studies involving difficult to micronise materials where x_2 is small, or studies at very high solids feed rates such that E_{sp} is small, it is expected that the response of cut size to varying gas mass flow rate and solids feed rate could be approximated by Equation 3.30 as the final term in Equation 3.27 becomes large compared to the other terms:

$$d_{cut} = \left(\frac{h_2}{h_1}\right)^2 \left(\frac{C_2}{{k_3}^2} + \frac{x_1}{{k_3}^2 d_{Reynolds} x_2} \frac{1}{E_{sp}}\right) \tag{3.30}$$

It is important to note that Equation 3.30, if x_2 is assumed constant, is solely a function of specific energy for a fixed geometry. For investigations with difficult to micronise materials, or very high solids feed rates such that E_{sp} or x_2 is small, it is likely that the results will conform to Equation 3.30. This may explain why the

relationship between particle size and specific energy has been a valid observation in previously reported data.

3.8 Discussion

Equation 3.27, the spiral jet mill cut size equation:

$$d_{cut} = \left(\frac{h_2}{h_1}\right)^2 \left(\frac{C_2}{{k_3}^2} + \frac{x_1 k_4}{{k_3}^2 d_{Reynolds} \dot{m}_g} + \frac{C_2 \dot{m}_s}{{k_3}^2 x_2} + \frac{x_1}{{k_3}^2 d_{Reynolds} x_2} \frac{1}{E_{sp}} \right) \qquad (3.27)$$

provides a mechanistic explanation for the variation in particle size with changes in process parameters such as gas mass flow rate ($\dot{m}_g$) and solids feed rate ($\dot{m}_s$) and their combined parameter of specific energy ($\dot{m}_g / k_4 \dot{m}_s = E_{sp}$). The equation may have applicability to scale up as it contains a material specific breakage parameter (b, x_2 =f(b, D)) while also being capable of explaining variation in particle size with changes to constants such as gas physical properties, solids aerodynamic properties, classifier geometry and mill geometry (x_1, k_4, C_2, k_3, h_1, h_2). As will be shown in Chapter 6, good agreement is observed with data reported in the academic literature and robust explanations are provided for the observed phenomena of the asymptotic approach to the grinding limit and variation in particle size with different motive gases.

Many of the parameters in Equation 3.27 are by definition mill specific, and could be determined by data generated from several materials micronised on a number of mills. The parameter C_1 is a function of particle shape, and therefore should remain similar for a given material micronised by different spiral jet mills so long as the fragmentation process results in similarly shaped particles. It may be possible to consider x_2 as material specific if the transport parameter, D, and mass fraction of collision fragments below the cut size, b, remain similar during scale up. The parameter D is likely to be mill specific as it relates to the transfer of particles to the grind nozzles, whereas b is likely to be both material and mill specific as it relates to both the collision energy and the fragmentation/attrition process for a given material. Micronisation of a number of materials across several spiral jet mills should be able to show whether D and/or b may be assumed constant or not. A detailed scale up methodology is proposed in Chapter 6.

The cut size equation can be used for more than just process modelling and scale up; it also provides insight into the limitations of the process from an energy

efficiency perspective. Four key observations can be made from the cut size equation with regards to possible improvements in energy efficiency:

i. Some mill geometries will be more efficient than others with regards to particle classification. It could be possible to optimise the classifier height and radius such that C_2 and $\left(\frac{h_2}{h_1}\right)^2$ are minimised and optimise the grind angle and grind chamber shape such that $k_3$is maximised.
ii. Higher gas mass flow rates and reduced gas molecular weight will tend to be more efficient and for a given specific energy will give a finer powder as a result of improved particle classification.
iii. The nozzle angle and nozzle separation distance will influence the mass fraction of collision fragments below the cut size, *b*, and could be optimised to increase the momentum exchanged during collisions.
iv. The greatest consumption of energy within a spiral jet mill is keeping hold up in circulation around the grind chamber. Any changes that increase the mass transport of particles to the grind nozzles, *D*, should lead to increased energy efficiency.

Some of the changes to increase efficiency may contradict each other, for example the collision angle to maximise momentum exchange during collisions may result in a reduced spin ratio, k_3. As such experimentation may be required to find the optimal balance between milling and classification. The energy delivered to a spiral jet mill is primarily consumed by maintaining hold up in circulation, and as such any change to reduce the hold up to solids feed rate ratio without detriment to the aerodynamic particle classification characteristics could lead to increased efficiency.

3.9 Conclusion

A novel model has been presented that describes the cut size of a spiral jet mill as a function of operational parameters, mill specific constants and material specific constants. The cut size equation can allow modelling of cut size for operational parameters for a given mill and material, has potential for scale up and provides insights that could lead to improved energy efficiency. Assumptions of this derivation, particularly regarding the grinding limit, are tested experimentally in Chapter 4.

Chapter 4. Experimental Investigation with Product A

4.1 Materials and Methods

To test the assumptions of the cut size equation, experiments were performed using an Active Pharmaceutical Ingredient (API) referred to for confidentiality reasons as Product A in this doctoral thesis.

Product A is relatively coarse (x50 = 191 μm, x90 = 358 μm) with a high Specific Surface Area (SSA) (>10 $m^2.g^{-1}$) and is particularly friable as it produces finer particles at lower energy settings than some of GSK's products. It is used in this study as an example material that does not fit well with standard correlations between cut size and E_{sp}. The response of Product A to varying grind pressures and feed rates was investigated for a fixed geometry. Additionally, h_2/h_1 was also varied at a fixed feed rate and grind pressure by modification to h_1.

A single input batch of Product A was micronised with nitrogen on an industrial 8" spiral jet mill with tangential powder entry and eight grinding nozzles. The precise dimensions of the mill cannot be disclosed for confidentiality reasons. The feed and grind gas pressures were controlled to a set point and the gas mass flow rate was measured by a coriolis flow meter. The feed and grind gas absolute pressures were maintained at a constant ratio (5:4) as per Table A1.1 of Appendix 1 so that the ratio of feed and grind gas mass flow rates is approximately constant throughout the experiment. The screw speed was set for a volumetric feeder and the average solids feed rate was determined by measurement of the input mass and the time taken for the feeder to fully discharge.

The feed and grind gas pressures were controlled to $\pm$ 0.1 barg and the volumetric feeder screw speed to $\pm$ 1 RPM. The input mass of powder was recorded to $\pm$ 0.001 kg and the time taken for the powder to discharge was recorded to $\pm$ 2 seconds. The accuracy of the time measurement means that faster feed rate runs (lower energy) have a comparatively larger error due to the impact of the absolute measurement accuracy on a reduced time reading. The gas mass flow rates and gas temperatures were recorded to $\pm$ 0.1 $kg.hr^{-1}$ and $\pm$ 0.1 ^oC respectively for every second throughout the course of each experiment. The mean, maximum and minimum values for the gas process data are then reported and used in

subsequent analysis. The reported experimental data may be found in Table A1.1 of Appendix 1. As the calibration of the mass flow meter and temperature probe were to $\pm$ 1 kg.hr^{-1} and $\pm$ 1 ^{o}C respectively, this error had to be recorded in Table A1.1 and applied to the subsequent analysis, however any error would be systematic across the data set rather than a randomised instrumentation readability error.

Micronised powder was collected by a vaneless axial entry reverse flow cyclonic separator that is attached directly below the grind chamber exit. As it was not possible to sample from a moving stream during micronisation with the available equipment, the total collected powder was tumbled within its container prior to sampling so as to minimise the impact of segregation and variation in solids feed rate. Two 1 g samples were taken for each experiment from six different random locations within the container to ensure that the sub-sample was representative of the bulk material. An initially clean container was used for each experiment.

The following Malvern Mastersizer 2000 sampling preparation and analysis method was performed: Each 1 g sample was tumbled prior to taking two smaller 35.0 mg aliquots. Tumbling is performed to reduce the effect of particle size segregation within the 1 g sample on both 35.0 mg aliquots. The aliquots are mixed with a 0.05% lecithin in iso-octane solution, and added drop-wise to more 0.05% lecithin in iso-octane solution in a Hydro 2000S sample handling unit to a target obscuration of 8-12%. The suspension is then sonicated using the Hydro 2000S internal sonic probe. Each aliquot was then subject to duplicate particle size analysis with a Malvern Mastersizer 2000.

The Malvern Mastersizer 2000 is typically capable of measuring x50 and x90 with a repeatability of $\pm$ 1%, however the actual repeatability that is observed during experimentation depends on the material in question and the analytical method. For these experiments the validated Quality Assurance (QA) release method for Product A particle size was used. The mean, maximum and minimum values obtained from duplicate analysis of two aliquots per sample is then recorded and used in subsequent analysis. The reported experimental data may be found in Appendix 1.

The investigation included a repetition at four separate gas pressure and feeder screw speed settings to assess the repeatability of the experimental process and involved 32 separate micronisation runs in total. A comparison of the repeatability of the experimental process compared to the repeatability of the particle size measurement process may be found in Table 4.1.

Measure of Variability	Between Aliquots from the Same Experiment		Between Aliquots from Experimental Repetitions	
	x50	x90	x50	x90
Average Discrepancy between Mean and Maximum and Minimum (%)	1.0	1.5	2.1	4.0
Maximum Discrepancy between Mean and Maximum or Minimum (%)	3.4	8.8	3.0	10.2
Minimum Discrepancy between Mean and Maximum or Minimum (%)	0.3	0.2	1.1	1.5
Standard Deviation for Discrepancy between Mean and Maximum or Minimum (%)	0.6	2.0	0.5	2.9

Table 4.1 Comparison of Measurement Variability to Experimental Variability

As can be seen from Table 4.1, there is an observed variability of between $\pm 0.2\%$ and $\pm$ 8.8% associated with the x90 measurement process which then increases to between $\pm 1.1\%$ and $\pm$ 10.2% when the experimental repeatability and particle size measurement variability are both considered. Given that this experimental data set consists of 32 separate experiments with x90 values ranging from 3.0 μm to 5.9 μm, the demonstrated repeatability is acceptable for the subsequent analysis.

4.2 Results

4.2.1 Particle Size Distribution (PSD) Analysis

By convention x50 (particle diameter for which 50% of the volume of assumed spherical particles are smaller) has been used as the basis of the discussion for milled materials and has been compared to E_{sp}. Additionally, when discussing the cut size of a cyclone, x50 is again typically reported. However, some materials produce a significant quantity of very fine particles during micronisation regardless of the solids feed rate or gas pressure as the collision energy is fixed by sonic velocity. This is observed in the Particle Size Distribution (PSD) plots in Figure 4.1 for Product A (x50 = 191 μm, x90 = 358 μm) where it can be seen that,

at a low specific energy (1140 kJ.kg^{-1}), there is a significant "fine shoulder" of particles of less than a micron in diameter. The impact of this fine shoulder on the distribution is that the x50 only changes from 2.0 µm to 1.7 µm with increasing energy in Figure 4.1 whereas the x90 decreases from 5.6 µm to 3.8 µm.

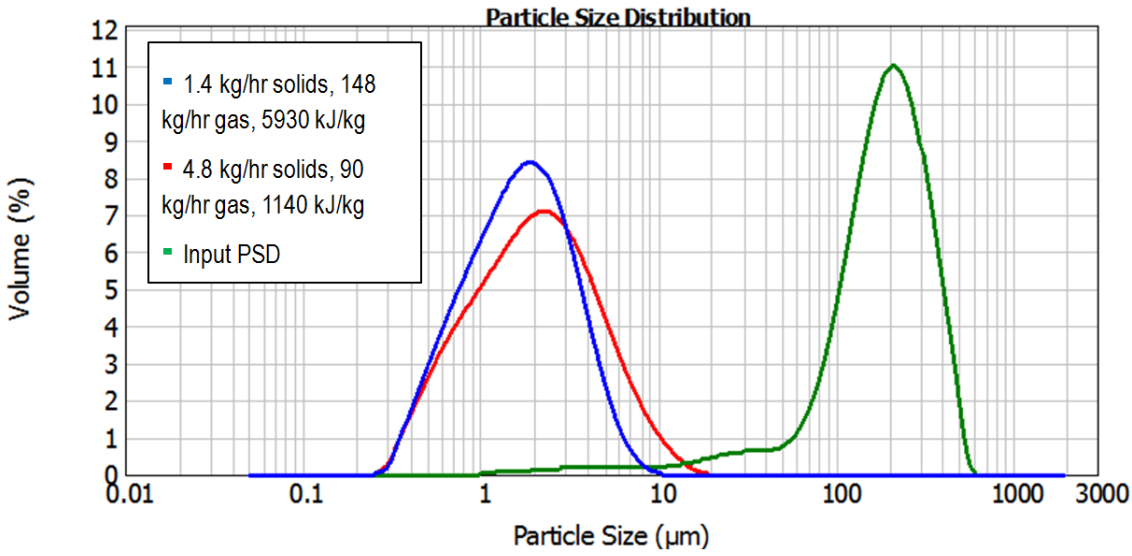

Figure 4.1 Product A PSD Plots (MacDonald *et al.* 2016)

Due to the presence of a persistent portion of fine particles, analysis of x50 will not give an accurate reflection of what is happening to the cut size for Product A. x90 is the assumed spherical particle diameter for which 90% (by volume of assumed spherical particles) of the PSD is of a smaller diameter. x90 will be assumed to be equivalent to the cut size for the subsequent analysis as it provides a better reflection of changes in cut size than x50 for product A.

The x90 measured for Product A micronised at a range of solids feed rates and gas mass flow rates with a fixed geometry is shown in Figure 4.2 for solids feed rate versus x90, and Figure 4.3 for specific energy (calculated as per Equation 2.3 using both feed and grind gas mass flow rate) versus x90, with the data grouped according to gas mass flow rate. As can be observed from Figure 4.3 there is a significant level of variability in the x90 obtained for a given specific energy depending on the gas mass flow rate.

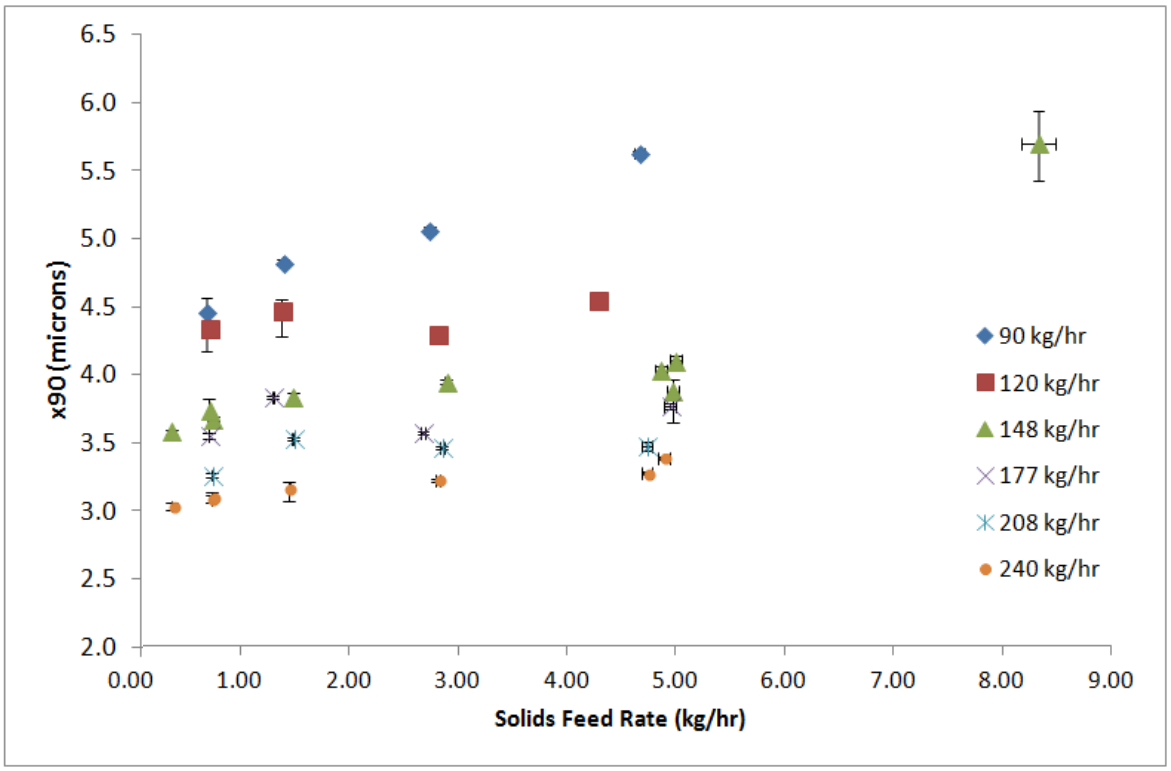

Figure 4.2 Solids Feed Rate against x90 for a Range of Constant Gas Mass Flow Rates (MacDonald *et al.* 2016)

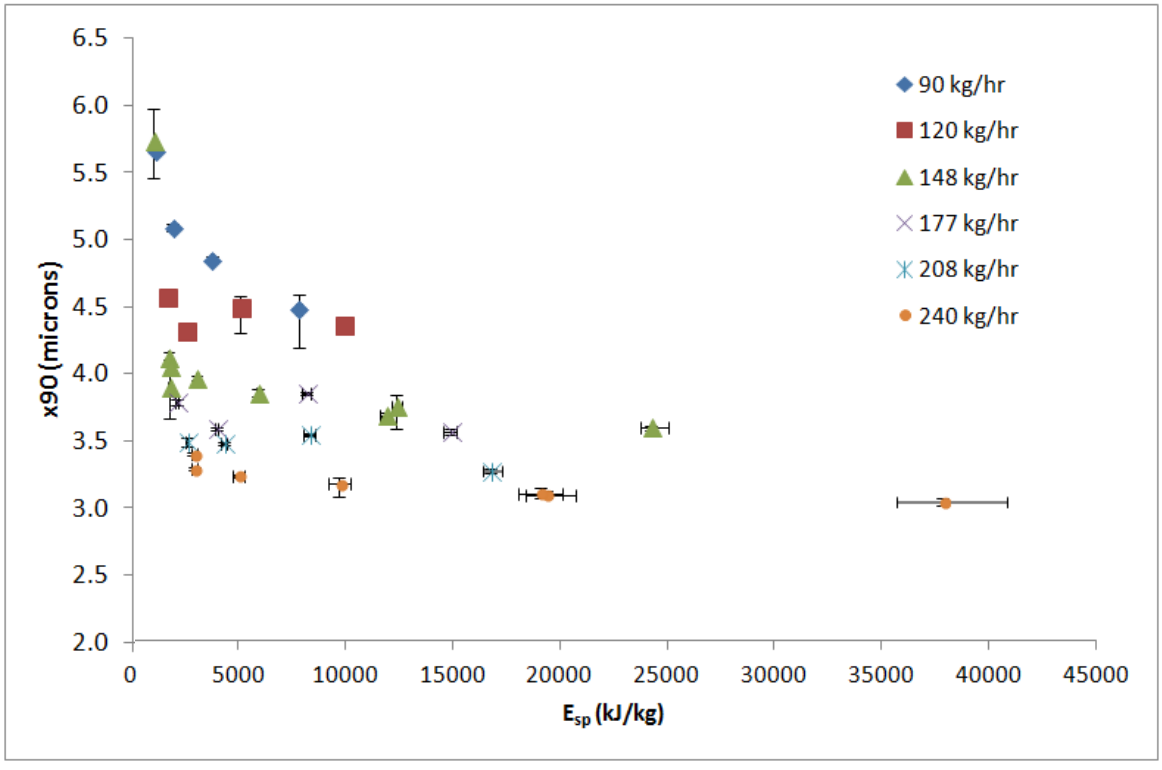

Figure4.3 E_{sp} against x90 for a Range of Constant Gas Mass Flow Rates (MacDonald *et al.* 2016)

4.2.2 Variation in Solids Feed Rate and Total Gas Mass Flow Rate

According to Equation 3.27 it is expected that a plot of $1/E_{sp}$ against x90 will give a relationship of the form "y = mx + c" depending on whether the solids feed rate or gas mass flow rate is held constant while the other varies. Figure 4.4 and Figure 4.5 are plots of $1/E_{sp}$ against x90 for set of data shown in Figure 4.1 and Figure 4.2, with the data grouped by gas mass flow rate and solids feed rate in Figure 4.4 and Figure 4.5 respectively. As can be seen from Figure 4.4 and Figure 4.5, straight lines are obtained which differ depending on whether the solids feed rate or gas mass flow rate is held constant. For ease of data presentation and analysis, have been removed from Figure 4.4 where the mill is likely to have been in a state of starvation.

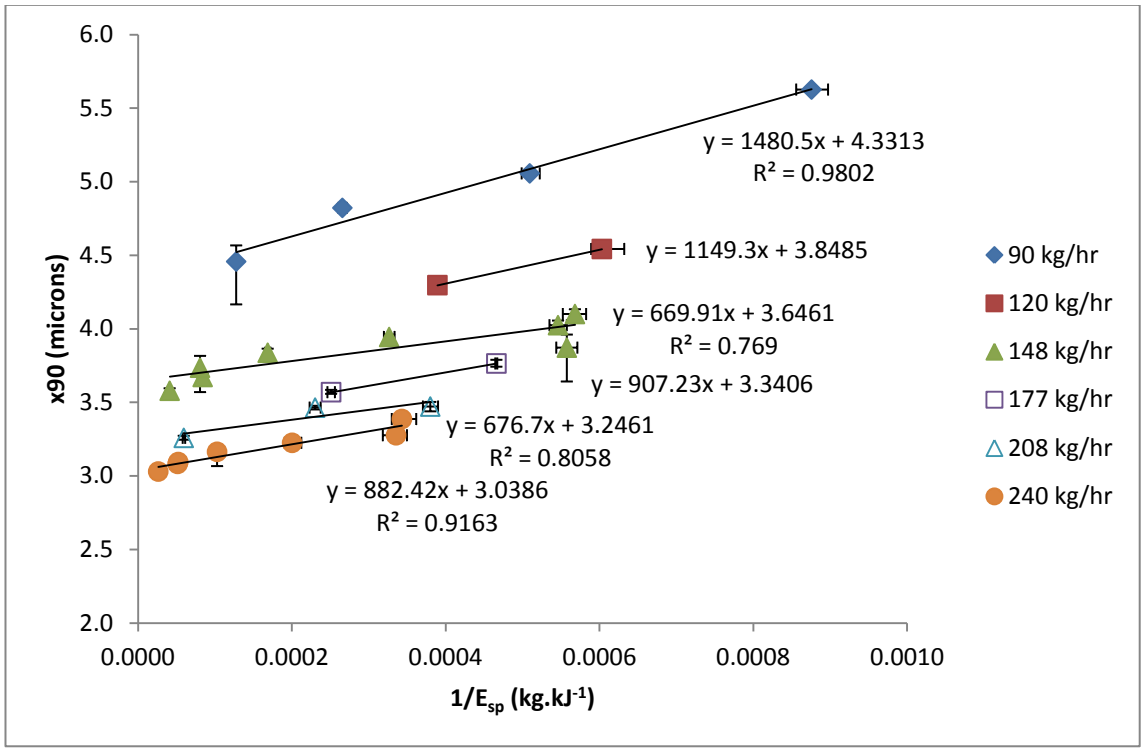

Figure 4.4 1/ E_{sp} against x90 for a Range of Constant Gas Mass Flow Rates (MacDonald *et al.* 2016)

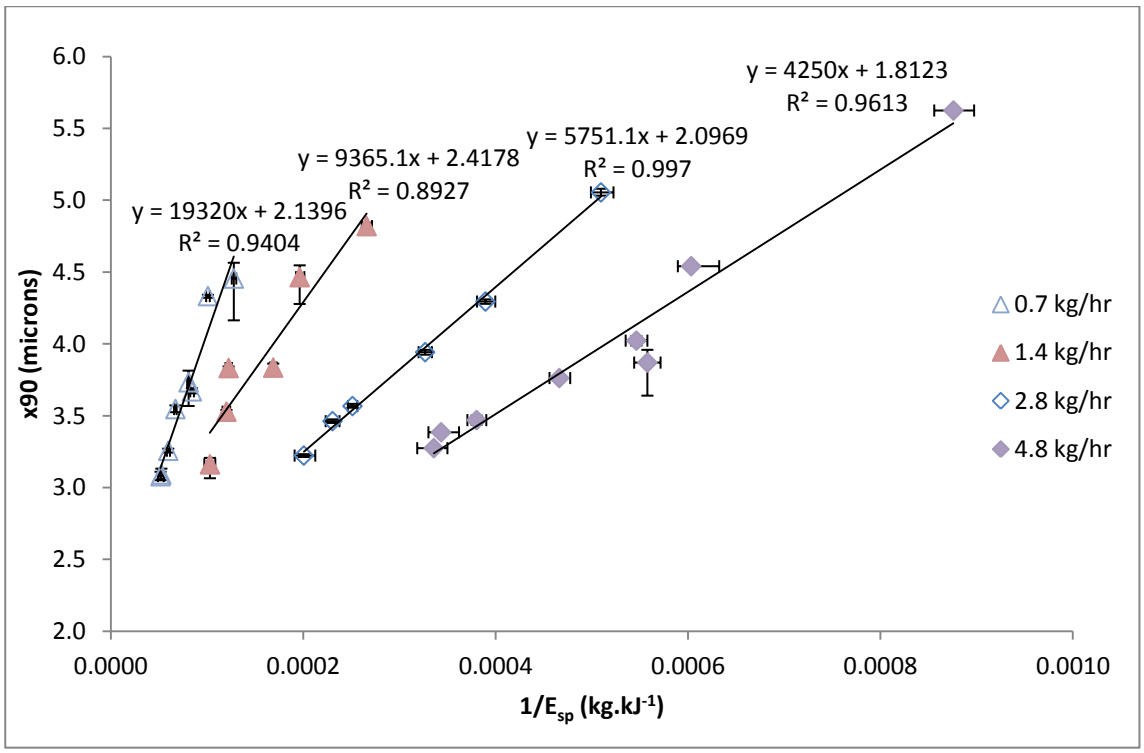

Figure 4.5 1/ E_{sp} against x90 for a Range of Constant Solids Feed Rates (MacDonald *et al.* 2016)

4.2.3 Variation in Classifier Geometry

Figure 4.6 shows $(h_2/h_1)^2$ against x90 for Product A for a fixed solids feed rate of 3.5 kg.hr^{-1} and gas mass flow rate of 177 kg.hr^{-1}.

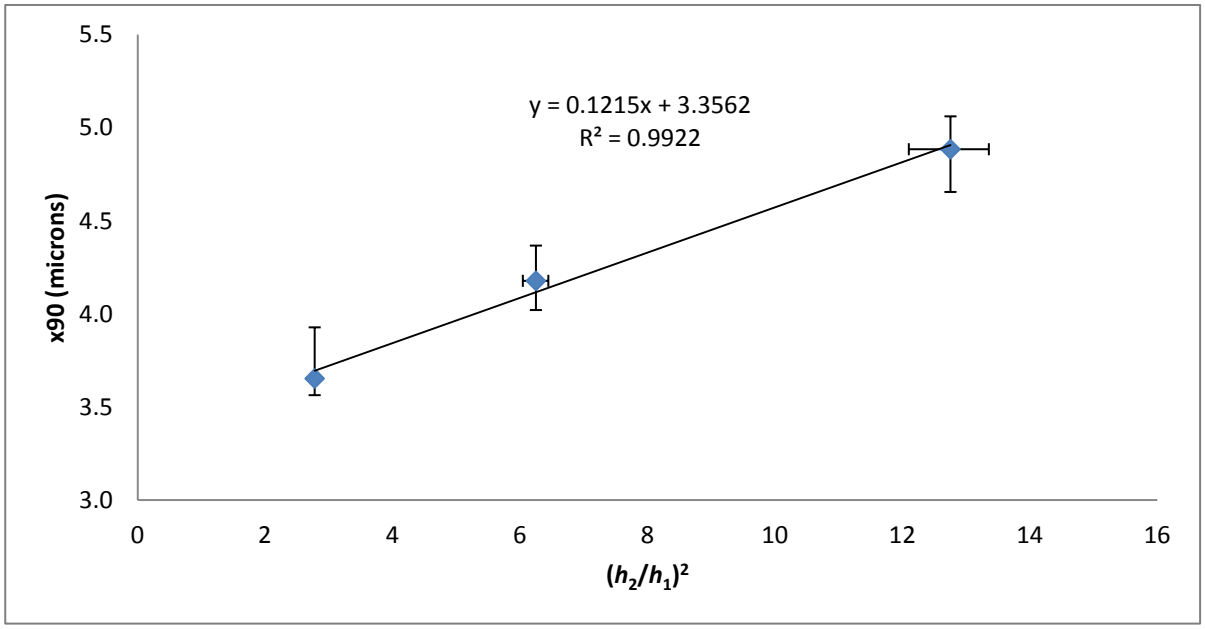

Figure 4.6 $(h_2/h_1)^2$ against x90 (MacDonald *et al.* 2016)

4.3 Analysis

The grinding limit, or *y*-intercepts from the linear regressions in Figure 4.4 and Figure 4.5, is of particular interest and is expected to take the form of either Equation 3.28 or Equation 3.29 respectively. Linear regression models with an R^2 value of less than 0.9 and derived from less than 10 data points are included in subsequent analysis as the data points are the means of four or more values and the linear regression models are, in most cases, within the error bars associated with measurement and process variability. According to Equation 3.28, the grinding limit obtained by solids feed rate reduction (cut size for zero solids feed rate) should be directly proportional to the reciprocal of the gas mass flow rate. This can be seen from Figure 4.7 where the reciprocal of the gas mass flow rate is plotted against the grinding limits obtained from the linear regression model reported in Figure 4.4.

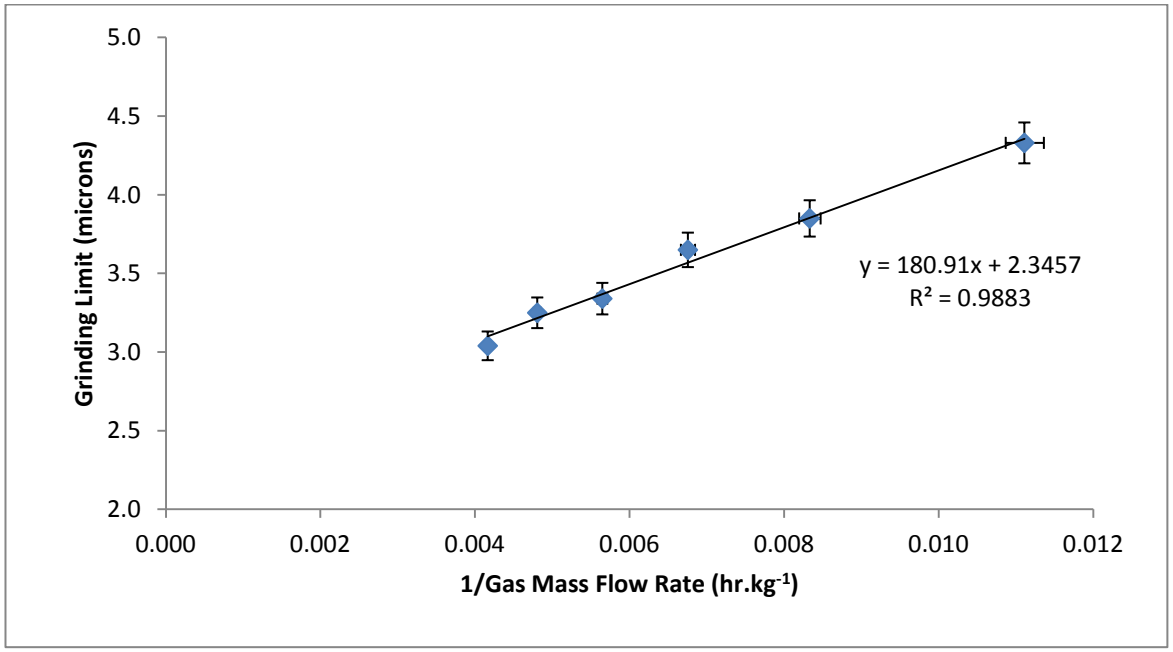

Figure 4.7 1/ Gas Mass Flow Rate against Feed Rate Reduction Grinding Limit (MacDonald *et al.* 2016)

The grinding limit approached by increasing gas mass flow rate (cut size for infinite gas mass flow rate) does not however behave as predicted by Equation 3.27 and Equation 3.29 as observed in Figure 4.8 where the solids feed rate is plotted against the grinding limits obtained from the linear regression model reported in Figure 4.5.

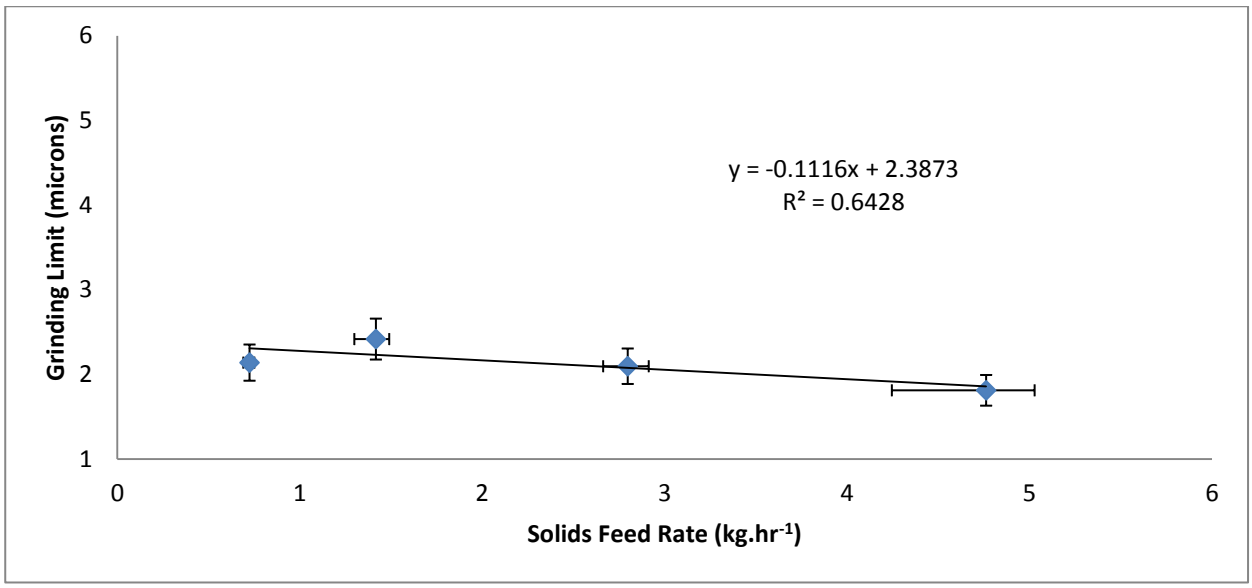

Figure 4.8 Solids Feed Rate against Gas Mass Flow Rate Increase Grinding Limit (MacDonald *et al.* 2016)

Although the reduction in grinding limit with increasing solids feed rate in Figure 4.8 is small, it may be a real effect. Both *y* intercepts from the linear regressions in Figure 4.7 and Figure 4.8 should by definition be equivalent as they are both the cut size for zero solids feed rate and infinite gas mass flow rate as per Equation 3.27. As can be seen from Figure 4.7 and Figure 4.8, the *y* intercepts are similar despite Figure 4.8 not matching the expected behaviour of Equation 3.29.

Equation 3.27 and Equation 3.29 have assumed that the mass fraction of collision fragments below the cut size, *b*, remains constant for varying solids feed rates. Collisions between large primary particles, which are likely to be better at retaining momentum following acceleration by grind nozzles, should be more energetic than collisions between smaller particles which will quickly lose their momentum as a result of fluid forces following exit from a nozzle jet. It would therefore be expected that larger input particles, although requiring more energy for surface area generation, may provide more energetic collisions as a result of their ability to retain momentum. It would therefore be expected that for increased solids feed rates the proportion of collision fragments below the cut size, *b*, may increase as a result of the average collision energy increasing. For input materials that are particularly sensitive to this effect, it could be possible to observe a reduction in particle size for increasing solids feed rates at a constant grind pressure. An increase in *b* with increasing solids feed rate is likely to be the cause

of the reduction in grinding limit with increasing solids feed rate. The close match in *y* intercepts between Figure 4.7 and Figure 4.8 is because the grinding limits in Figure 4.7 are by definition for zero solids feed rate.

The converse of the phenomenon of reduction in grinding limit, and potentially particle size, with increasing solids feed rate is that particle size will not reduce as expected with feed rate reduction. Some of the atypical results excluded from Figure 4.4 but included in Figure 4.5 are thought to be a result of the solids feed rate being so low such that the spiral jet mill was in a state of starvation whereby the grinding process becomes less effective due to the reduced particle concentration.

Although the grinding limit for infinite gas mass flow rate changes with solids feed rate in Figure 4.8, it is minimal when compared to changes seen in the grinding limit for zero solids feed rate with varying gas mass flow rate per Figure 4.7. If variation in the grinding limit as a result of differences in feed rate is considered insignificant, it is possible to determine some of the constants specific to Product A and its spiral jet mill by simple linear regressions. Figure 4.9 shows $1/E_{sp}$ against x90 minus the grinding limit obtained by reduction in feed rate. By rearranging Equation 3.27 and assuming $C_2\dot{m}_s/{k_3}^2 x_2$ to be insignificant, Equation 4.1 can be developed to describe the expected behaviour of Figure 4.7:

$$d_{cut} - \left(\frac{h_2}{h_1}\right)^2 \left(\frac{C_2}{{k_3}^2} + \frac{x_1 k_4}{{k_3}^2 d_{Reynolds} \dot{m}_g}\right) = \left(\frac{h_2}{h_1}\right)^2 \frac{x_1}{{k_3}^2 d_{Reynolds} x_2} \frac{1}{E_{sp}} \qquad (4.1)$$

As the *y* intercept is expected to be zero as per Equation 4.1, the *y* intercept of the linear regression in Figure 4.9 has been set as zero. The deviation from the expected *y* intercept of zero and poor linear fit in Figure 4.9 could either be a result of a small error from the previous fits to determine the grinding limit for zero solids feed rate or a result of $C_2\dot{m}_s/{k_3}^2 x_2$ not being truly insignificant.

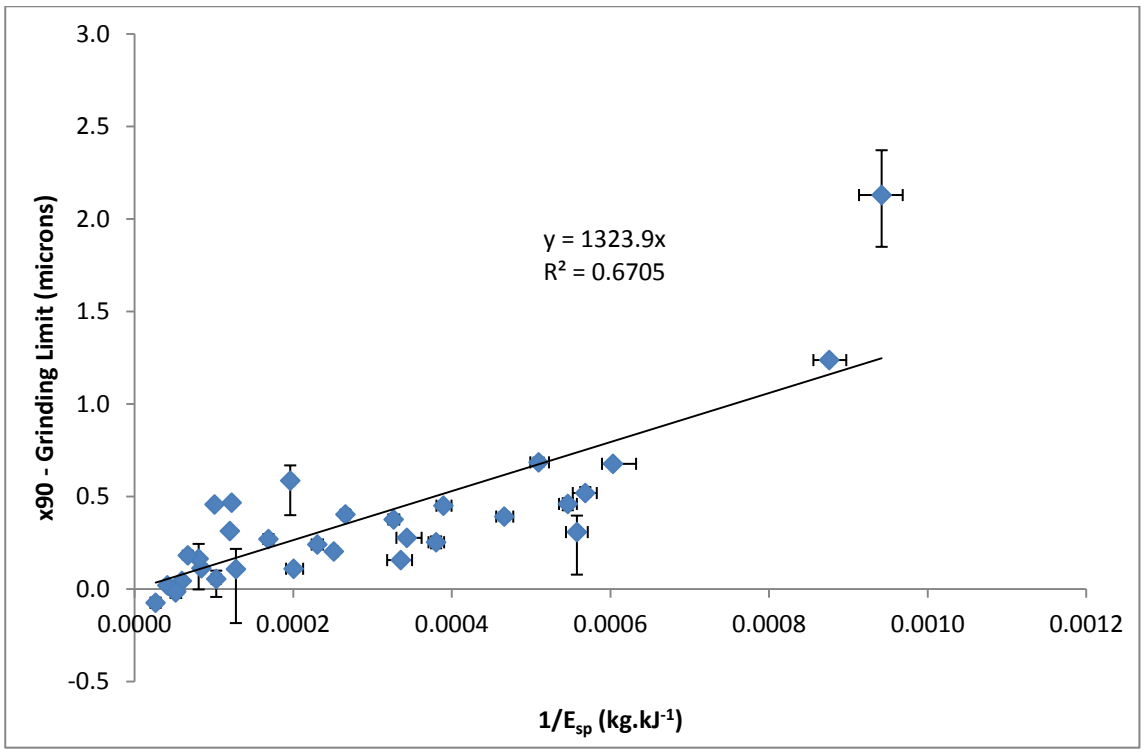

Figure 4.9 1/ E_{sp} against x90 – Reduction in Feed Rate Grinding Limit (MacDonald *et al.* 2016)

The slopes and intercepts obtained in Figure 4.7 and Figure 4.9 can be used to determine the milling constants for Product A and the industrial 8" spiral jet mill used during the trial as per Table 4.2.

$\frac{C_2}{{k_3}^2}$ (µm)	$\frac{x_1 k_4}{{k_3}^2 d_{Reynolds}}$ (µm.kg.hr^{-1})	x_2 (kg.hr^{-1})
0.375	28.9	6.10

Table 4.2 Milling Constants for Product A (MacDonald *et al.* 2016)

Based on the calculated value of x_2 and the magnitude of $d_{Reynolds}$, it is possible to see that the term $C_2\dot{m}_s/{k_3}^2 x_2$ is expected to be very small, and have a negligible impact on cut size. This explains why there is almost no variation in grinding limit observed in Figure 4.8.

A high x_2 value would suggest that Product A is relatively easy to micronise, meaning that the mill is operating at low values of hold up and close to its grinding limit. This means that the resultant cut size is much more sensitive to gas mass flow rate than solids feed rate. Product A, and similarly easy to micronise materials may therefore be approximated by:

$$d_{cut} = \left(\frac{h_2}{h_1}\right)^2 \left(\frac{C_2}{{k_3}^2} + \frac{x_1 k_4}{{k_3}^2 d_{Reynolds} \dot{m}_g} + \frac{x_1}{{k_3}^2 d_{Reynolds} x_2} \frac{1}{E_{sp}}\right) \quad (4.2)$$

Whereas, harder to micronise materials are likely to be better approximated by Equation 4.3 where the effect of variation in grinding limit with gas mass flow rate becomes negligible:

$$d_{cut} = \left(\frac{h_2}{h_1}\right)^2 \left(\frac{C_2}{{k_3}^2} + \frac{x_1}{{k_3}^2 d_{Reynolds} x_2} \frac{1}{E_{sp}}\right) \quad (4.3)$$

It is important to note that Equation 4.3, if b and D are assumed constant, is solely a function of specific energy. For investigations with difficult to micronise materials, or very high solids feed rates such that E_{sp} is small and $d_{Reynolds}$ is large, it is likely that the results will conform to Equation 4.3. This may explain why the relationship between particle size and specific energy has been a valid observation in previously reported data.

Equation 4.2 with empirically derived constants in Table 4.2 may be used to form a predictive model for x90 as per Figure 4.10. The error bars for predicted x90 are based on the accuracy of the solids feed rate and gas mass flow rate data used for the calculation.

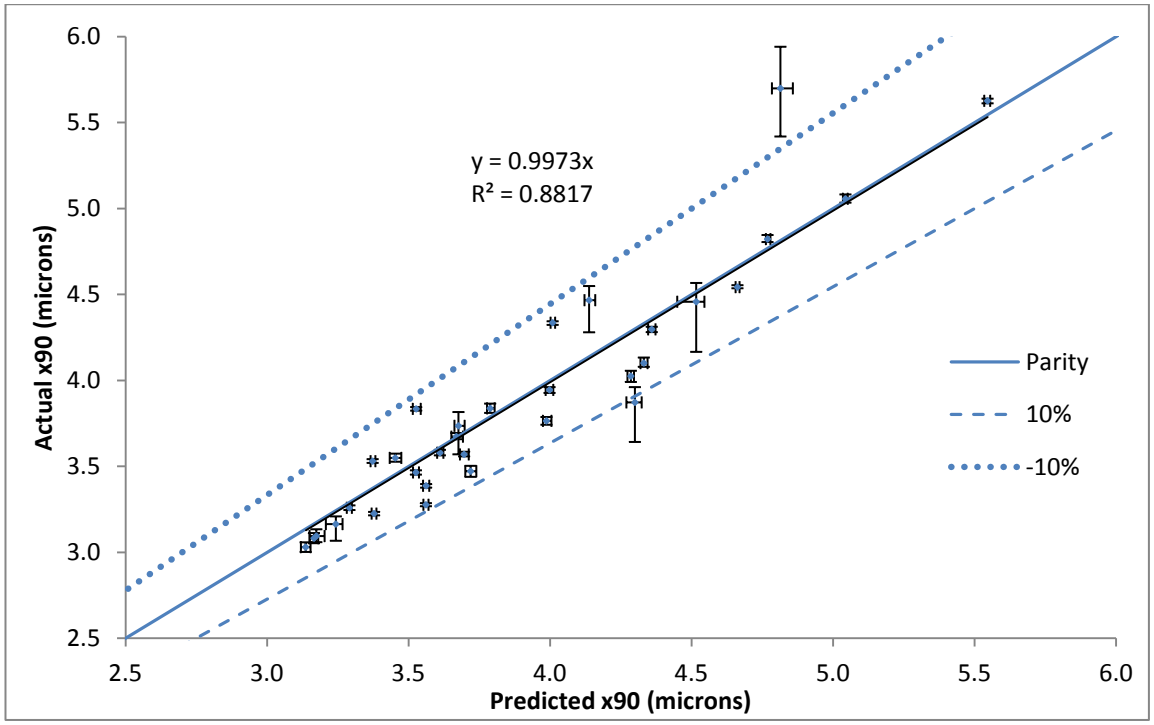

Figure 4.10 Predicted x90 against Actual x90 for Product A using Equation 4.2 (MacDonald *et al.* 2016)

As can be seen from Figure 4.10, the predicted x90 is within the maximum demonstrated experimental repeatability of approximately $\pm$ 10% as per Table 4.1.

The cut size equation has also been verified by Figure 4.6 as the observed change in cut size with classifier height fits with prediction as per Equation 3.27. It is expected that at either extreme of classifier height the relationship will breakdown. For a zero classifier height such that $h_2 = h_1$and $(h_2/h_1)^2$ is at its minimum possible value of 1, a coarser output is expected to be seen as the classifier no longer prevents larger particles escaping via a short cut route out of the grind chamber along the wall closest to the gas exit (Kozawa *et al.* 2012).

Variation in material specific constants b and C_1 within Equation 3.27 may explain why some materials conform better than others to a correlation with only specific energy (Equation 4.3). An investigation into different materials and their response to different spiral jet mills is recommended.

4.4 Conclusion

The results for Product A show good agreement with Equation 3.27 and its simplified form, Equation 4.2. This may confirm the validity of the assumptions required for the derivation of Equation 3.27.

Equation 4.3 and Equation 3.30 have been proposed as further simplified forms of Equation 3.27 for materials where b is particularly small, or cases where the solids feed rate to gas mass flow rate ratio is particularly high.

Chapter 5. CFD Spin Ratio Investigation for Varying Motive Gases

5.1 Rationale

As the constant spin ratio assumption is a crucial aspect in the derivation of Equation 3.27, it has been investigated for several motive gases using Computational Fluid Dynamics (CFD). The CFD investigation is to test the following hypotheses:

1. Constant spin ratio only applies to gas flow rates before sonic velocity is approached near the grind chamber exit.
2. The theoretical grinding limit will be coarsened for increases in gas flow rate beyond the critical point where constant spin ratio no longer applies (sonic velocity at classifier).

5.2 Investigation Details

5.2.1 Parameter Selection

Simulations were performed as per Table 5.1 with pressures set in the simulation to achieve a range of kinetic energy delivery rates. The exit pressure was set at a boundary condition of 1 bar absolute, and the pressure behind the nozzles was set at a gauge pressure relative to the exit pressure as per Table 5.1.

Gas	Desired Kinetic Energy Delivery Rate (kW)	Expected Grind Gas Mass Flow Rate ($kg.hr^{-1}$)	Nozzle Pressure Boundary Condition (bar gauge relative to exit)
Helium	1	25.2	0.47
Nitrogen	1	58.0	1.59
Air	1	59.7	1.61
Carbon Dioxide	1	99.9	2.29
Helium	5	126.0	2.34
Nitrogen	5	290.0	7.95
Air	5	298.3	8.06
Carbon Dioxide	5	499.5	11.44
Helium	12	84.0	5.60
Nitrogen	12	696.0	19.07
Air	12	715.8	19.34
Carbon Dioxide	12	1198.8	27.45

Table 5.1 Gases, Pressures and Mass Flow Rates for Investigation

5.2.2 CFD Model Details

Simplistic CFD simulations are performed with an academic version of ANSYS FLUENT 14.5 with a model according to Table 5.2.

Model Parameter	Setting
Viscous Model	k-epsilon (2 equation), Default Settings
Gas Density	Ideal Gas
Gas Viscosity	Constant, Fluent Database for Gas Investigated
Gas Thermal Conductivity	Constant, Fluent Database for Gas Investigated
Gas Specific Heat Capacity	Constant, Fluent Database for Gas Investigated

Table 5.2 CFD Model Settings

This model was selected over Large Eddy Simulation (LES) or a Reynolds Stress Transport Model (RSTM) as detailed information on flow of high accuracy is not required. This simplistic model is typically selected by GSK for their simulations as it converges reliably.

Analysis is performed on a spiral jet mill with geometry similar to that used by Rodnianski *et al.* (2013) as detailed in Table 5.3 and illustrated in Figure 5.1. This geometry was selected as the overall dimensions and number of nozzles were as per most of their simulations, and nozzle angle is within their simulation range and similar to other commercial spiral jet mills.

Parameter	Value
Number of Nozzles	12
Nozzle Diameter	2 mm
Nozzle Angle	19.3^{o}
Grind Chamber Height	8 mm
Grind Chamber Diameter	200 mm
Exit Diameter	32 mm

Table 5.3 Spiral Jet Mill Geometry for CFD Investigation

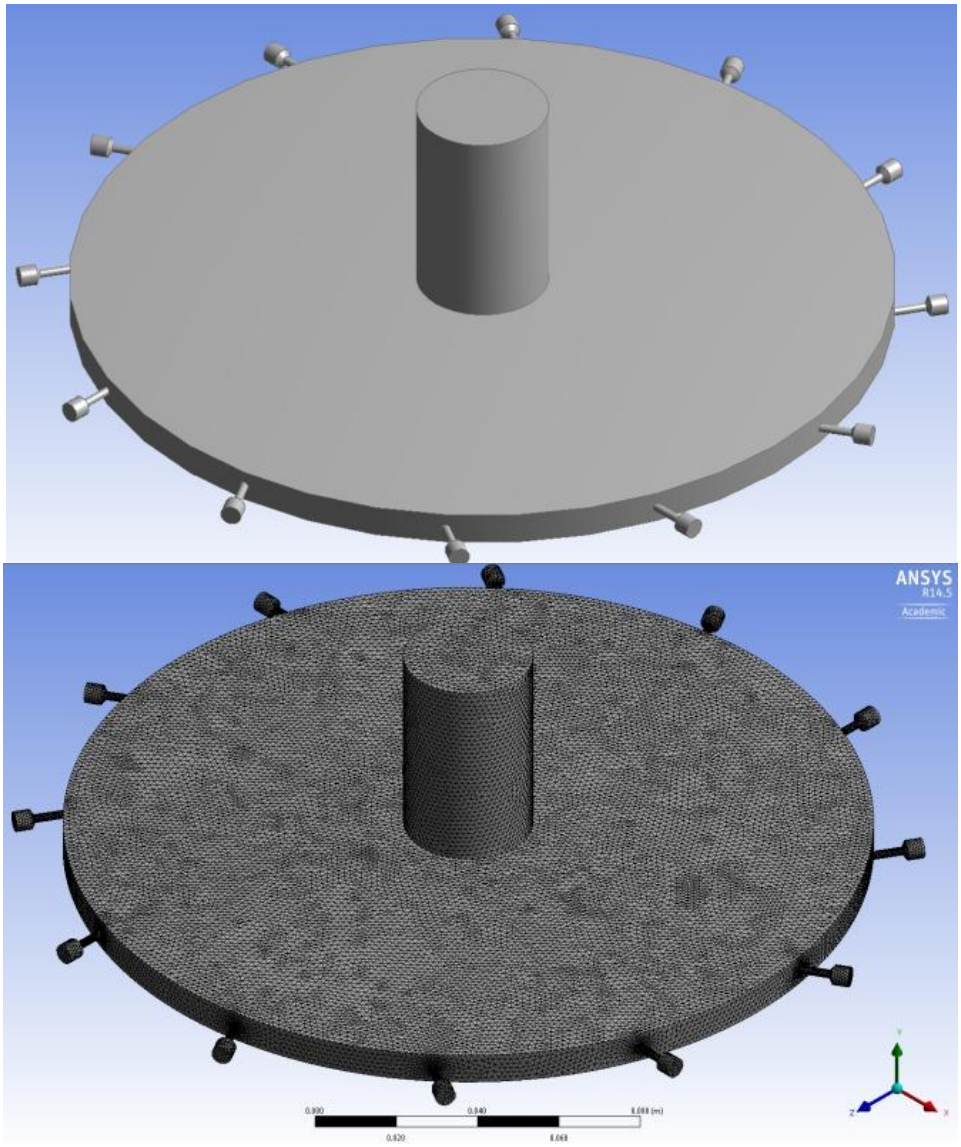

Figure 5.1 Spiral Jet Mill Geometry and Mesh Investigated

5.2.3 Informal Grid Independence Study

Rodnianski *et al.* (2013) in their previous CFD investigation only used between 150,000 and 250,000 cells in their mesh and provided no evidence of grid independence. To ensure that the results obtained in this analysis are reliable, an informal grid independence study is performed with air at a pressure of 3.0 bar as detailed in Table 5.4

Number of Cells	Mass Flow Rate ($g.s^{-1}$)	Gas Tangential Velocity at Exit			Gas Radial Velocity at Exit			Spin Ratio at Exit		
		2 mm Above Central Plane	Central Plane	2 mm Below Central Plane	2 mm Above Central Plane	Central Plane	2 mm Below Central Plane	2 mm Above Central Plane	Central Plane	2 mm Below Central Plane
171607	25.1	178.5	185.7	177.1	15.81	10.91	14.32	11.29	17.02	12.36
350302	26.6	191.2	193.1	189.9	17.20	10.98	15.33	11.12	17.59	12.39
501258	29.2	200.9	202.6	199.7	17.39	11.19	16.26	11.52	18.11	12.28
874317	30.6	207.0	208.4	207.0	17.65	11.68	16.34	11.72	17.84	12.66

Table 5.4 Informal Grid Independence Study

The predicted mass flow rate using a choked flow equation for the investigated geometry at 3 bar is 30.8 $g.s^{-1}$, and as can be seen the mass flow rate is tending towards this value with an increasing numbers of cells. This is likely to be a result of the nozzle outer edge becoming more circular and the total area available for flow becoming closer to the circular area used to predict mass flow rate. This convergence towards the theoretical prediction is shown in Figure 5.2

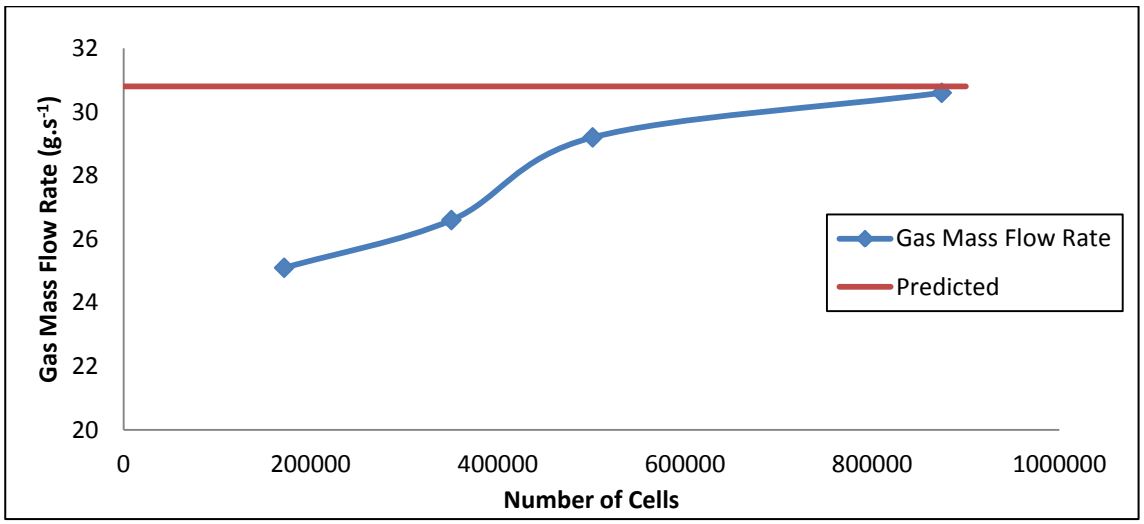

Figure 5.2 Informal Grid Independence Study

Interestingly Rodnianski *et al.*'s (2013) observation of approximately constant spin ratio across a range of mass flow rates is observed in Figure 5.3 for the gas mass flow rates over the range of the grid independence study.

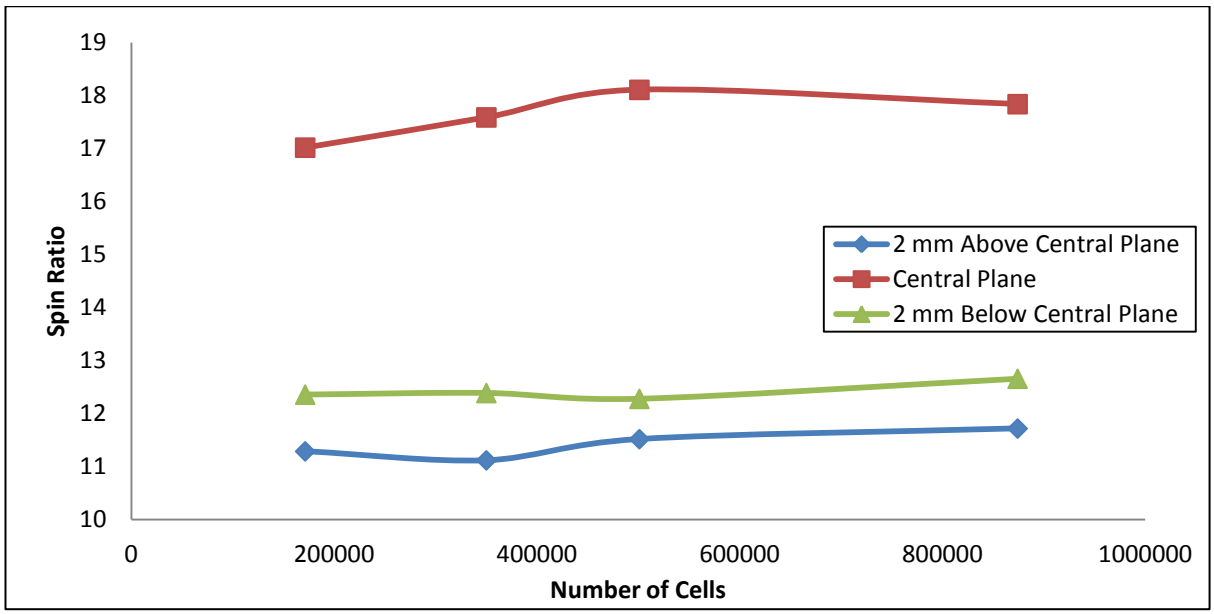

Figure 5.3 Spin Ratio at Exit

As the gas mass flow rate determined by CFD for 874,317 cells is close to theoretical prediction, this mesh size is progressed for further analysis.

5.3 CFD Results Obtained

The typical flow pattern observed along the central plane of the spiral jet mill may be found in Figure 5.4, 5.5, 5.6 and 5.7.

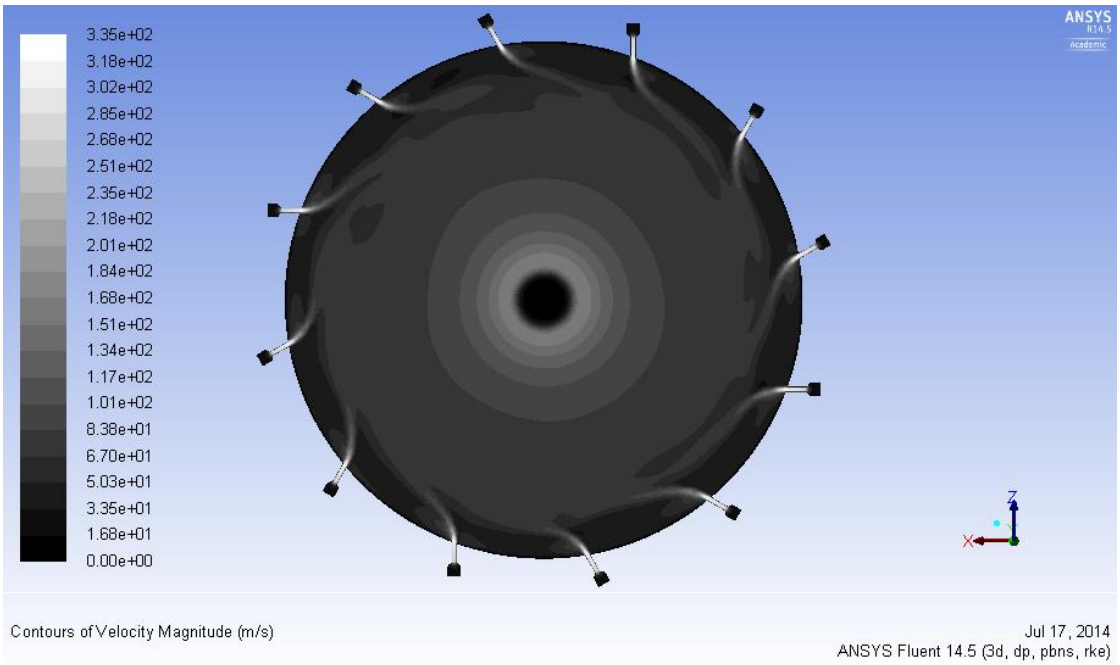

Figure 5.4 Velocity Magnitude along Central Plane

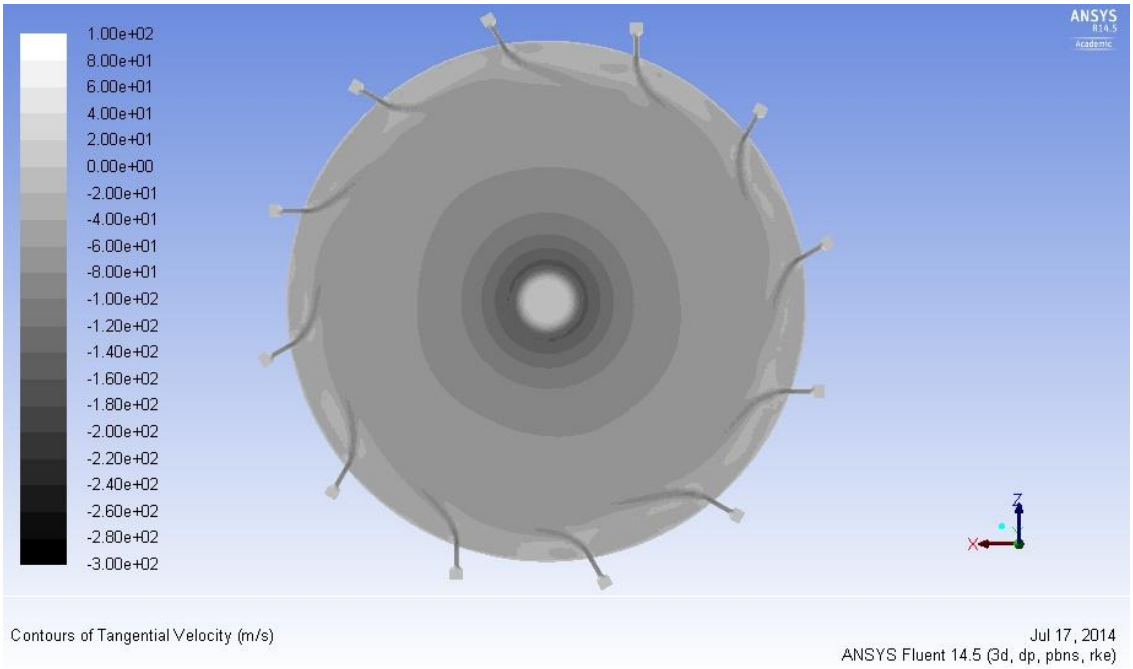

Figure 5.5 Tangential Velocity along Central Plane

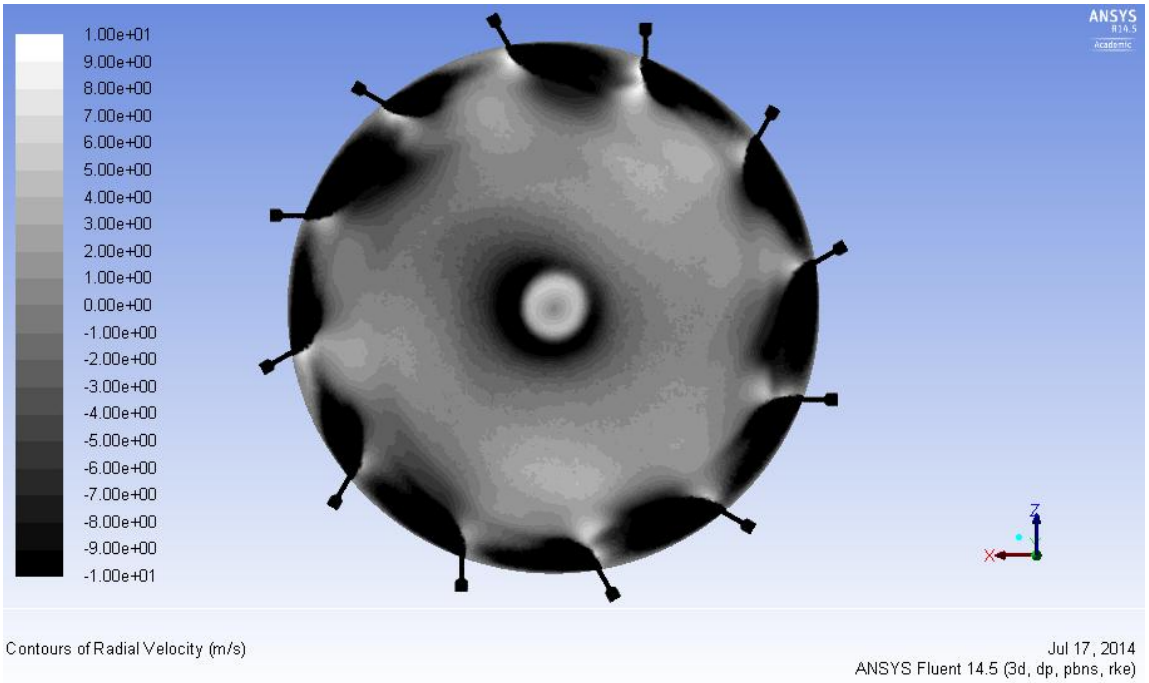

Figure 5.6 Radial Velocity along Central Plane

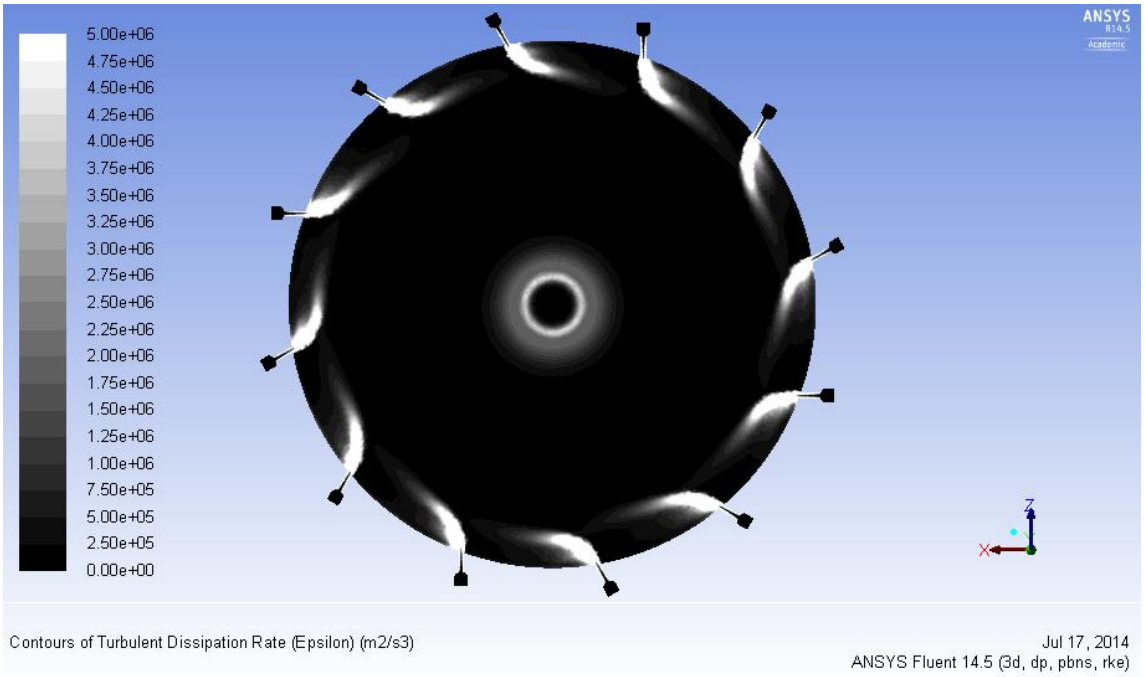

Figure 5.7 Turbulent Dissipation Rate along Central Plane

A comparison of the predicted mass flow rates and kinetic energy delivery rates to those actually obtained by CFD at the specified grind pressure is detailed in Table 5.5.

Gas	Pressure (bar gauge)	Predicted Grind Gas Mass Flow Rate ($g.s^{-1}$)	CFD Grind Gas Mass Flow Rate ($g.s^{-1}$)
Helium	0.47	1.9	3.7
Nitrogen	1.59	16.1	19.3
Air	1.61	16.6	19.8
Carbon Dioxide	2.29	27.7	30.4
Helium	2.34	9.7	9.8
Nitrogen	7.95	80.6	67.6
Air	8.06	82.9	69.6
Carbon Dioxide	11.44	138.7	115.6
Helium	5.60	23.3	19.6
Nitrogen	19.07	193.3	151.8
Air	19.34	198.8	156.4
Carbon Dioxide	27.45	333.0	264.2

Table 5.5 Predicted and CFD Mass Flow and Kinetic Energy Delivery Rates

The gas velocity as it exits the nozzle and enters the grind chamber was found to differ from the expected sonic velocity at the nozzle throat. Despite being abrupt nozzles, gas expansion still takes place following exit from the nozzle resulting in supersonic flow. Additionally, some heating of the gas may have occurred at the convergent section of the nozzle leading to higher gas velocities. The nozzle exit

velocities and subsequent adjusted kinetic energy delivery rates are detailed in Table 5.6

Gas	Pressure (bar gauge)	Sonic Velocity at 20°C ($m.s^{-1}$)	Nozzle Exit Velocity ($m.s^{-1}$)	Adjusted Kinetic Energy Delivery Rate (kW)
Helium	0.47	1014	579	0.62
Nitrogen	1.59	352	318	0.98
Air	1.61	347	318	1.00
Carbon Dioxide	2.29	269	277	1.16
Helium	2.34	1014	912	4.07
Nitrogen	7.95	352	402	5.46
Air	8.06	347	396	5.46
Carbon Dioxide	11.44	269	332	6.36
Helium	5.60	1014	1038	10.57
Nitrogen	19.07	352	412	12.86
Air	19.34	347	406	12.90
Carbon Dioxide	27.45	269	378	18.83

Table 5.6 Nozzle Exit Velocity and Adjusted Kinetic Energy Delivery Rates

The spin ratio is compared for the different gases and flow rates in Table 5.7. As expected, increasing the mass flow rate significantly beyond the range investigated by Rodnianski *et al.* (2013) resulted in the spin ratio decreasing.

Gas	Exit Velocity (Central Plane) ($m.s^{-1}$)	Exit Mach Number (Central Plane)	Spin Ratio (Central Plane)
Helium	208	0.20	22.3
Helium	495	0.49	16.7
Helium	680	0.67	14.9
Nitrogen	170	0.48	18.6
Nitrogen	300	0.85	14.8
Nitrogen	354	1.01	13.4
Air	159	0.46	17.0
Air	296	0.85	14.6
Air	344	0.99	12.0
Carbon Dioxide	164	0.61	18.1
Carbon Dioxide	266	0.99	14.4
Carbon Dioxide	271	1.01	8.9

Table 5.7 Spin Ratio at Exit for Varying Gas and Mass Flow Rate

With regards to Hypothesis 1, it can clearly be seen in Table 5.7 that as sonic velocity is approached, constant spin ratio no longer applies. The values obtained of greater than Mach 1 may be the result of an accrued error as the Mach number was calculated outside of ANSYS Fluent based on an average gas velocity across the classifier. It can also be seen that the spin ratio is not constant when changing

conditions, but actually varies with gas mass flow rate as per Figure 5.8 and classifier Mach number as per Figure 5.9.

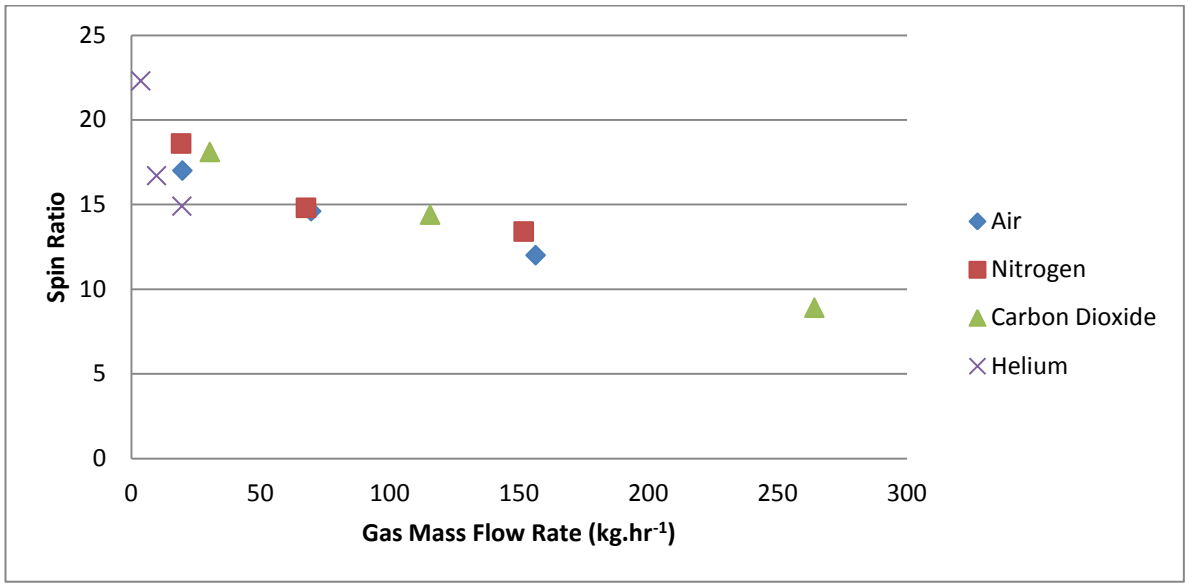

Figure 5.8 Gas Mass Flow Rate against Spin Ratio

As can be seen from Figure 5.9 the spin ratio appears to have an approximately linear relationship with the Mach number until Mach one at which point the relationship breaks down and further increases in flow rate result in a bigger reduction in spin ratio.

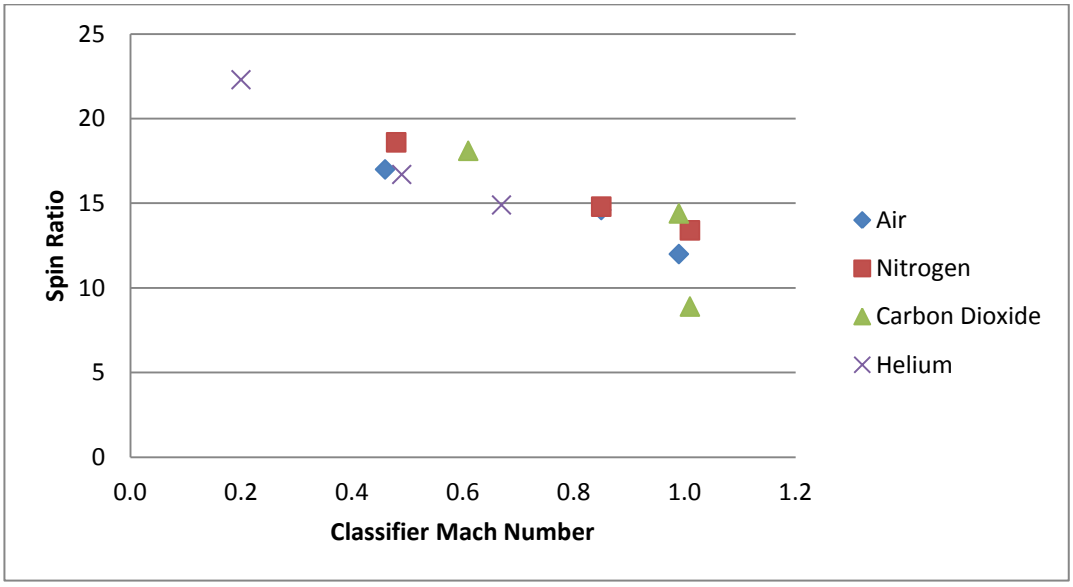

Figure 5.9 Classifier Mach Number against Spin Ratio

5.4 Conclusion

Although this investigation has shown that at the extremes of possible flow regimes the constant spin ratio assumption is no longer valid, it has also confirmed that it is approximately constant across a relatively wide range of flow rates. For example, as per Figure 5.8, tripling the gas mass flow rate from 50 $kg.hr^{-1}$ to 150 $kg.hr^{-1}$ results in a decrease of less than 10% in the spin ratio. Compared to the expected increase in particle Reynolds number and decrease in drag as per Chapter 3, this change is relatively insignificant.

Additionally, the grind chamber shape investigated was reduced in height compared to typical industrial spiral jet mills. Therefore, the total velocity of gas near the grind chamber exit will be higher for a given flow rate, resulting in unrealistically high Mach numbers. Therefore it is expected that the change in spin ratio with flow rate may be more pronounced for this test geometry than in typical spiral jet mill designs.

Although the constant spin ratio assumption should still be valid across a range of gas mass flow rates, it is necessary to be aware that at extremely high gas flow rates there will be a drop in spin ratio and milling efficiency.

Chapter 6. Cut Size Equation Validation

6.1 Industrial Development Data

To test the robustness of the cut size equation, data sets spanning several materials and spiral jet mills have been fitted to the cut size equation (Equation 3.27) and its most simplified form (Equation 3.30 / Equation 4.3). If either equation can be used to predict performance across the data set for a given material, it demonstrates the validity of the cut size equation. A discrepancy between the predictions of both equations suggests the material is highly friable and has a high x_2 value.

The constants determined for Equation 3.27 can be compared for different mills and materials to assess its utility for scale up and platform transfer.

For the sake of comparability with data for Product A, the x90 has been fitted for Products B-H rather than the x50. As the cut size is the largest possible particle that could escape, it theoretically relates to the x100. Due to the stochastic nature of the process some particles greater than the theoretical cut size will be able to escape the grind chamber, making the x90 a relevant PSD value for analysis with the cut size equation.

Additionally, as the classifier heights are not known for the Manufacturer C and D mills, the exit gap to grind chamber height ratio has been set as equal to the Manufacturer A 8" mill. As the resultant error will be systematic, the impact on the assessment of the utility of the cut size equation will be minimal. There may however be a subsequent incorrect offset in the mill specific parameter ($\frac{x_1 k_4}{{k_3}^2 d_{Reynolds}}$) and absolute grinding limit ($\frac{C_2}{{k_3}^2}$) as a result of this necessary assumption when comparing the Manufacturer C and D data to the rest of the data set.

The data from Product A has been re-analysed to determine the constants with a numerical solver for Equation 3.27 rather than graphically as per Chapter 4 for Equation 4.2. Fitting with a numerical solver has led to a discrepancy for the Product A constants compared to Chapter 4, but also an increase in the prediction accuracy.

Fitting reliable constants to the industrial data is challenging for the following reasons:

- The data sets can include a wide variety of input batches for a given material, leading to unpredictable variability.
- There is uncertainty regarding mass flow rate data as only pressure data is available without a corresponding temperature.
- A volumetric feeder was used in some cases, and as such the feed rate data may not be reliable as mass and time data for individual runs is not available.
- For Product D the x90 data was unavailable for the entire data set and so this had to be extrapolated from %<1 μm data based on the assumption of a uniform span across the data set.
- In many of the data sets the x90 values were rounded to 1 decimal place for reporting against release specifications. This reduces the accuracy of the data set as a whole.
- Information is not available on the accuracy or reliability of the data, and as such it is not possible to plot the information with error bars.
- The experiments were not designed to test the cut size equation, and so do not have sufficient variability in both solids feed rate and gas mass flow rate to accurately determine the milling constants.
- The contract Manufacturers who perform micronisation of Products B and C for GSK will not disclose any details on the geometry of their spiral jet mills other than the grind chamber diameter (8" or 4"), meaning that the classifier gap to grind chamber height ratio is unknown. This makes assessing the utility of Equation 3.27 for scale up challenging.

As the fitting process can get stuck on local minima/maxima, the fitting data from Product A was used as the initial iteration for the numerical solver function in Microsoft Excel for all other products. Once a material specific constant, such as x_2, is determined for a material it is then used as the initial guess during the constant fitting process for the next data set with that material.

The industrial development data may be found in Appendix 2. A summary of the milling constants for Products A-E across three spiral jet mills may be found in Table 6.1.

Product	Mill	$\frac{C_2}{{k_3}^2}$ (μm)	$\frac{x_1 k_4}{{k_3}^2 d_{Reynolds}}$ (μm.kg.hr^{-1})	x_2 (kg.hr^{-1})
A	Manufacturer A 8”	0.346	32.9	9.29
B	Manufacturer C 8”	0.505	16.5	6.80
B	Manufacturer D 8”	0.458	49.6	6.90
B	Manufacturer C 4”	0.087	17.0	6.51
C	Manufacturer C 8”	0.092	29.0	5.44
C	Manufacturer D 8”	0.383	141	253
C	Manufacturer A 4”	0.078	24.4	6.83
D	Manufacturer A 8”	0.335	32.7	13.90
E	Manufacturer A 8”	1.030	32.1	1.43
F	Manufacturer A 8”	0.341	32.9	25.80
G	Manufacturer A 8”	0.107	32.1	3.06
H	Manufacturer A 8”	0.369	31.5	17.10
H	Manufacturer A 4”	0.156	24.7	17.10

Table 6.1 Summary of Milling Constants

With the exception of the data for Products B and C which are micronised by a contract manufacturer, the summary of data in Table 6.1 shows that $\frac{x_1 k_4}{{k_3}^2 d_{Reynolds}}$ is strongly mill specific for varying materials at both 8” and 4” scale. According to the basis of the cut size equation, $\frac{x_1 k_4}{{k_3}^2 d_{Reynolds}}$ should remain constant for a given mill and motive gas. Furthermore, the adjustment of cut size for a given mill according to a change of motive gas may be estimated by adjustment of this constant based on the difference in gas physical properties as for Products A and D with air and nitrogen. The specificity of $\frac{x_1 k_4}{{k_3}^2 d_{Reynolds}}$ to spiral jet mill geometry and motive gas shows strong support for Equation 3.27. The reduction by approximately half of $\frac{C_2}{{k_3}^2}$ for Product H when moving from 8” scale to 4” scale also corresponds with the prediction of Equation 3.27 as C_2 is directly proportional to the classifier radius while also being a function of C_1, the drag coefficient as the Reynolds number tends

towards infinity. The expected reduction of C_2 with scale matches the prediction of Equation 3.27 and may also be a demonstration that C_1 remains constant as it should be material specific so long as the fragmentation process leads to similarly shaped particles across scales and spiral jet mills. If C_1 is found to remain constant across scales for a given material it will allow Equation 3.27 to be used for scale up of the spiral jet mill.

In further support of the structure of the derivation of the cut size equation, for the materials micronised with the 8" Manufacturer A mill, $\frac{C_2}{{k_3}^2}$ (function of C_1) correlates as it is expected to with particle shape (Product G is the most spherical, Product E is needle shaped and is the least spherical).

It also appears that for Products B and H, x_2 may be assumed as material specific as it remains approximately constant when changing mill manufacturer and scale. The identification of material specific constants is crucial to the development of a robust scale up methodology. To ascertain whether x_2 may truly be assumed as material specific, more data spanning multiple materials and spiral jet mills of differing grind angles is necessary. It is expected that this parameter will also vary depending on the collision angle and mass transport properties of the grind chamber, however for geometrically similar mills of varying scale it is likely to be constant for a given material. In the case of Product C, x_2 is approximately constant between the 8" Manufacturer D mill and the 4" Manufacturer A mill, but radically different for the 8" Manufacturer C mill. It may be the case that Product C is much more sensitive to differences in collision energy than Product B. A difference in grind angle between the Manufacturer D and Manufacturer C mills may have resulted in vastly different fragmentation for Product C, whereas for Product B the fragmentation remained similar. Although included in the analysis, the data gathered for Products B and C with the Manufacturer D mill was during Factory Acceptance Testing (FAT) with poorly controlled gas mass flow rates, making the data reliability questionable for the Manufacturer D mill.

6.2 Industrial Commercial Data

For safety reasons it was necessary to change the micronisation gas for Product A and Product D from air to nitrogen.

Although air and nitrogen are similar, they have different molecular weights and different viscosities. Both of these gas physical properties impact the constants in Equation 3.27 and therefore theoretically will have an impact on particle size.

Particle size data with Product A and Product D with both air and nitrogen confirm the validity of the cut size equation.

6.2.1 Change of Motive Gas for Product A

Particle size data for Product A micronised with both air and nitrogen may be found in Table 6.2.

Input Batch	Gas	Solids Feed Rate ($kg.hr^{-1}$ $\pm$ 0.2 $kg.hr^{-1}$)	Total Gas Mass Flow Rate ($kg.hr^{-1}$ $\pm$ 10 $kg.hr^{-1}$)	x50 (microns)	Actual Nitrogen x50 to Air x50 Ratio	Expected Nitrogen x50 to Air x50 Ratio*
1	Nitrogen	3.5	220	1.66	0.965	0.940 – 1.00
	Air	3.5	220	1.72		
2	Nitrogen	3.5	220	1.63	0.953	0.940 – 1.00
	Air	3.5	220	1.71		
3	Nitrogen	3.5	220	1.71	0.972	0.940 – 1.00
	Air	3.5	220	1.76		
Mean					0.963	0.970

*Equation 3.27 is used to estimate the ratio at the extremes of the solids feed rate and total gas mass flow rate process tolerances.

Table 6.2 Product A Commercial Air and Nitrogen Data

As can be seen from Table 6.2, there is a close match between the mean actual and predicted x50 ratio between air and nitrogen.

6.2.2 Motive Gas Change for Product D

Particle size data for Product D micronised with both air and nitrogen may be found in Table 6.3.

Input Batch	Gas	Solids Feed Rate ($kg.hr^{-1}$ $\pm$ 0.2 $kg.hr^{-1}$)	Total Gas Mass Flow Rate ($kg.hr^{-1}$ $\pm$ 10 $kg.hr^{-1}$)	x50 (microns)	Actual Nitrogen x50 to Air x50 Ratio	Expected Nitrogen x50 to Air x50 Ratio*
1a	Nitrogen	1.5	255	1.57	0.975	0.952 – 0.993
	Air	1.5	255	1.61		
1b	Nitrogen	1.5	255	1.58	0.969	0.952 – 0.993
	Air	1.5	255	1.63		
2a	Nitrogen	1.5	255	1.60	1.00	0.952 – 0.993
	Air	1.5	255	1.60		
2b	Nitrogen	1.5	255	1.63	0.988	0.952 – 0.993
	Air	1.5	255	1.65		
3a	Nitrogen	1.5	255	1.60	0.988	0.952 – 0.993
	Air	1.5	255	1.62		
3b	Nitrogen	1.5	255	1.64	0.994	0.952 – 0.993
	Air	1.5	255	1.65		
Mean					0.986	0.973

*Equation 3.27 is used to estimate the ratio at the extremes of the solids feed rate and total gas mass flow rate process tolerances.

Table 6.3 Product D Commercial Air and Nitrogen Data

As can be seen from Table 6.3, there is a close match between the mean actual and predicted x50 ratio between air and nitrogen.

6.4 Comparison with Data from Academic Literature

6.4.1 Zhao and Schurr (2002)

Zhao and Schurr (2002) performed micronisation with gases of differing molecular weight and showed that at high values of specific energy consumption, gases with a lower molecular weight give a smaller average particle size. An even more important observation is that at lower values of specific energy consumption, gases with a lower molecular weight give a larger average particle size.

Based on the assumption of similarity of grinding and similarity of spin ratio, Equation 4.3 may be used to investigate the impact of changing gas physical properties such as molecular weight, viscosity and ratio of specific heat capacities

on cut size as per Figure 6.1. The predicted response in Figure 6.1 shows a close match to previously reported data from Zhao and Schurr (2002) in Figure 2.8 which has been repeated in this chapter as Figure 6.2. These have not been overlaid as Figure 6.1 is for Product A whereas Figure 6.2 is for silica sand.

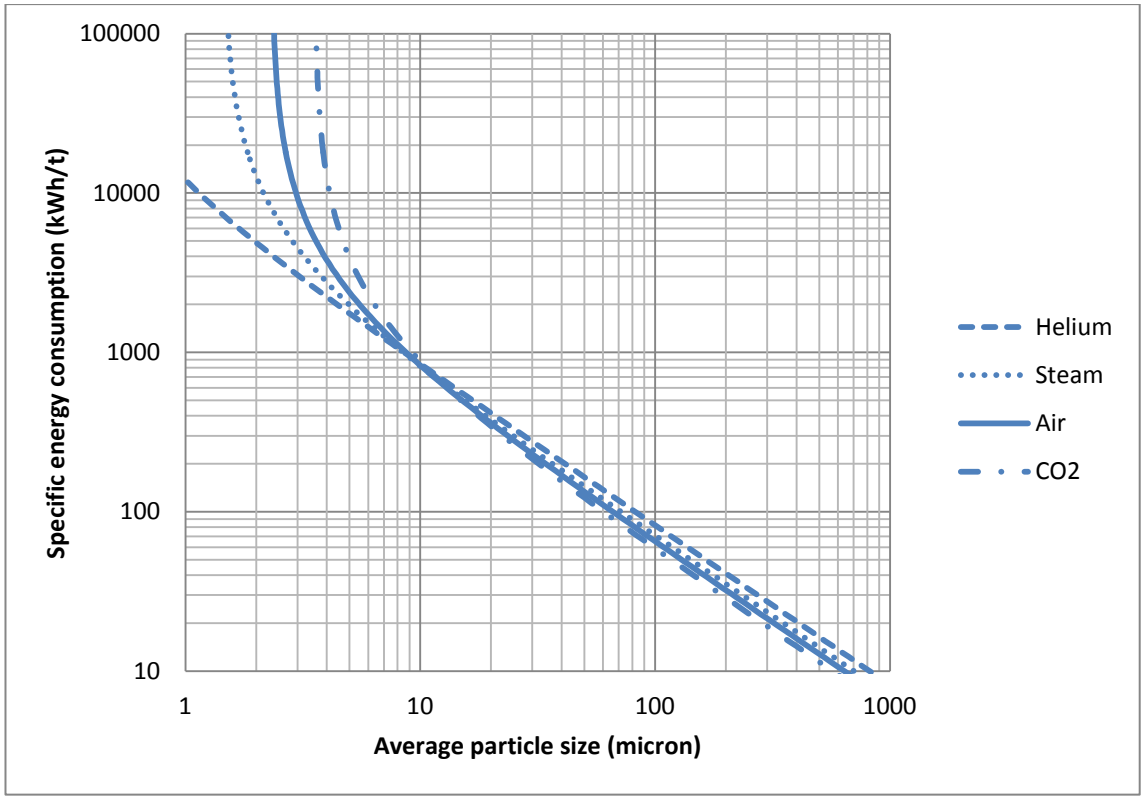

Figure 6.1 Predicted cut size against E_{sp} (MacDonald *et al.* 2016)

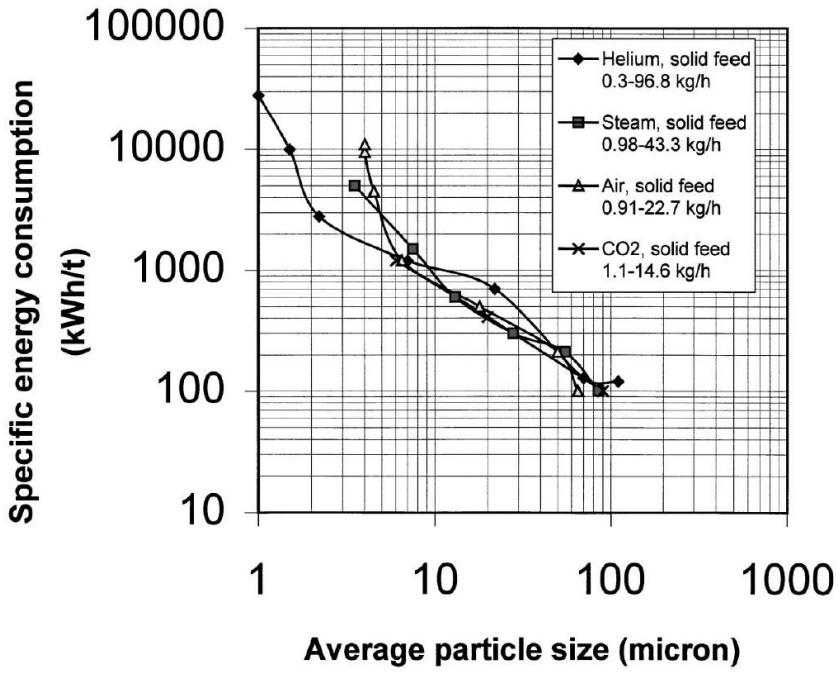

Figure 6.2 Experimental Particle Size against E_{sp} (Zhao and Schurr 2002)

Importantly, the cut size equation predicts that at higher values of E_{sp} gases of a lower molecular weight give smaller cut sizes and at lower values of E_{sp} give larger cut sizes. The smaller cut size at high values of E_{sp} is a result of the grinding limit being smaller for gases of a lower molecular weight, whereas the larger cut size at lower values of E_{sp} is a result of there being a lower gas mass flow rate for a given volumetric flow rate and hence greater deceleration of gas required to maintain a given quantity of hold up in circulation around the grind chamber.

6.4.2 Midoux et al. (1999)

In addition to the cut size equation matching experimental observations by Zhao and Schurr (2002), Equation 4.3 replicates the typical "transition" observed by Midoux *et al.* (1999) when plotting E_{sp} against changes in Specific Surface Area (SSA). Although the cut size equation cannot be used to predict changes in SSA, the cut size can be predicted across a range of values and the spherical SSA can be calculated based on the assumption that all particles are of the cut size diameter. Such an exercise is shown in Figure 6.3 which replicates the typical shape of data obtained by Midoux *et al.* (1999) in Figure 2.7 which has been repeated as Figure 6.4 in this chapter.

Figure 6.3 shows that the observed "transition" is not a result of a change in grinding process from fragmentation to attrition, but is a result of the cut size beginning to tend asymptotically towards the grinding limit as a result of the aerodynamic limitations of the system.

Importantly, the location of the asymptote will vary depending on the grind chamber flow conditions and the aerodynamic properties of the material being micronised. Operating within the asymptotic region is generally preferred from a process robustness perspective as the output PSD is insensitive to changes in solids feed rate. It would therefore be recommended to understand how the grinding limit varies with grind pressure and grind chamber geometry and adjust these such that the target x50/x90 can be attained while operating within this asymptotic region.

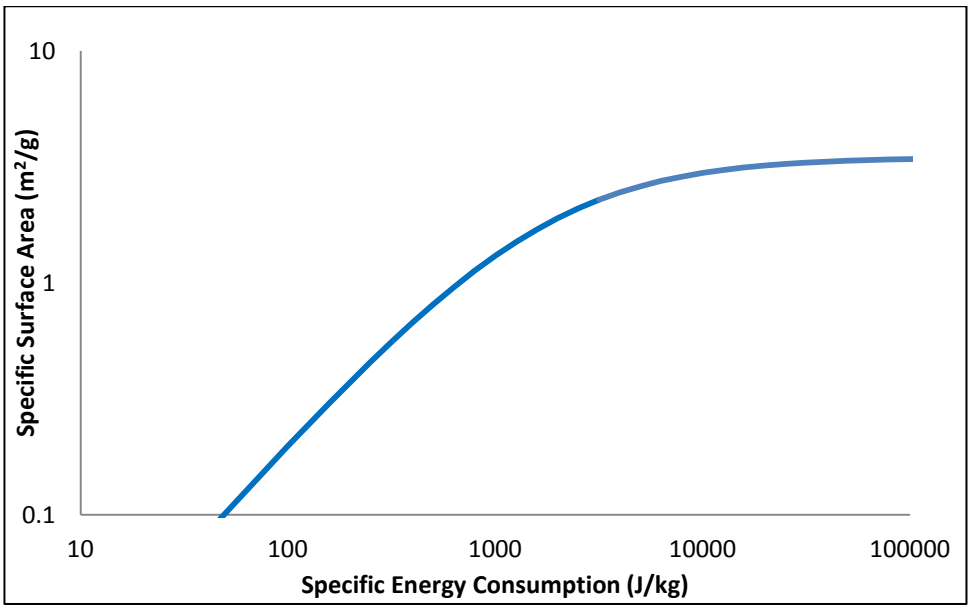

Figure 6.3 E_{sp} **against Spherical Specific Surface Area of Cut Size**

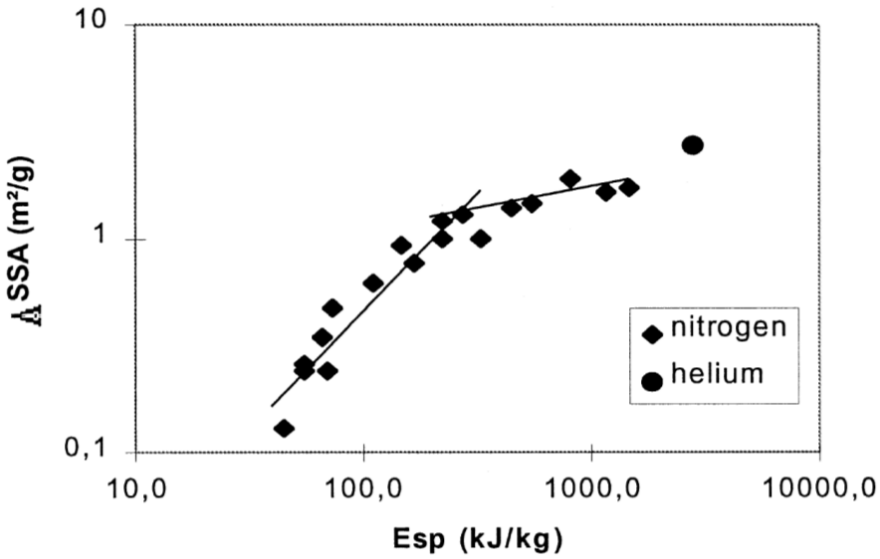

Figure 6.4 Change in SSA against E_{sp} (Midoux *et al.* 1999)

6.4.3 Tuunila & Nyström (1998)

In addition to the cut size equation matching previously reported data for variation in solids feed rate and gas mass flow rate, the variation in classifier geometry and grind chamber height also matches previously reported data in academic literature. Tuunila and Nyström (1998) showed that for a fixed grind chamber height, reduction in the gap h_1 results in a coarsening of the output PSD, matching the prediction of Equation 3.27 and experimental data for Product A.

6.4.4 Katz and Kalman (2007)

Katz and Kalman (2007) showed that variation in h_2 with no classifier resulted in no notable change in PSD, also matching the prediction of Equation 3.27.

6.5 Proposed Scale Up Methodology

As the cut size equation appears valid for the data investigated, a scale up methodology is proposed for a high value product:

1. Micronise at least two inexpensive surrogate materials at small scale and at least one at large scale at a wide range of solids feed rates and grind pressures so as to fully characterise the performance of both spiral jet mills and identify the material specific parameters C_1 and x_2 for both materials. This will allow mill specific parameters to be determined for both the small and large scale spiral jet mill.

2. Micronise the high value product at the small scale to determine its material specific parameters.

3. Combine the material specific constants for the high value product determined at small scale with the mill specific constants for the large scale mill so that Equation 3.27 can be used to describe the response of particle size to variation in solids feed rate and gas mass flow rate.

4. Identify which combination of solids feed rate and gas mass flow rate is necessary to robustly achieve a desired output particle size at increased scale.

6.6 Conclusion

In addition Equation 3.27 and its simplified form Equation 4.3 matching experimental data for Product A and industrial development data for Products B-H as per Table 6.1, it closely matches previously reported data from academic literature as per Section 6.4. It provides a succinct explanation for key observations such as the difference in grinding limit for different gases or change in cut size with classifier height.

Furthermore, the cut size equation provides a better explanation for the response of particle size to changes in parameters than previously reported papers on specific energy.

Industrial data spanning several spiral jet mills and scales has shown that Equation 3.27 may have potential applications for scale up, however more investigation is required to verify its utility.

Chapter 7. Cyclone Literature Review

7.1 Introduction

The cyclone and spiral jet mill share some key principles of operation, particularly as both classify particles aerodynamically. GSK currently use a number of bottom discharge spiral jet mills (cyclone directly placed at the bottom of the grind chamber) and experience a low yield for Product A as per Chapter 1. As with the spiral jet mill, it is necessary to understand what has led to the current academic literature on the cyclone to determine what next steps are required. This literature review is primarily chronological, taking the reader on a journey from invention of the cyclone through to modern computer aided techniques for design optimisation.

7.2 Invention

The cyclone, or dust collector, was originally patented by Daniel G. Reitz (1889). The cyclone uses centrifugal force to separate two phases by density as per Figure 7.1.

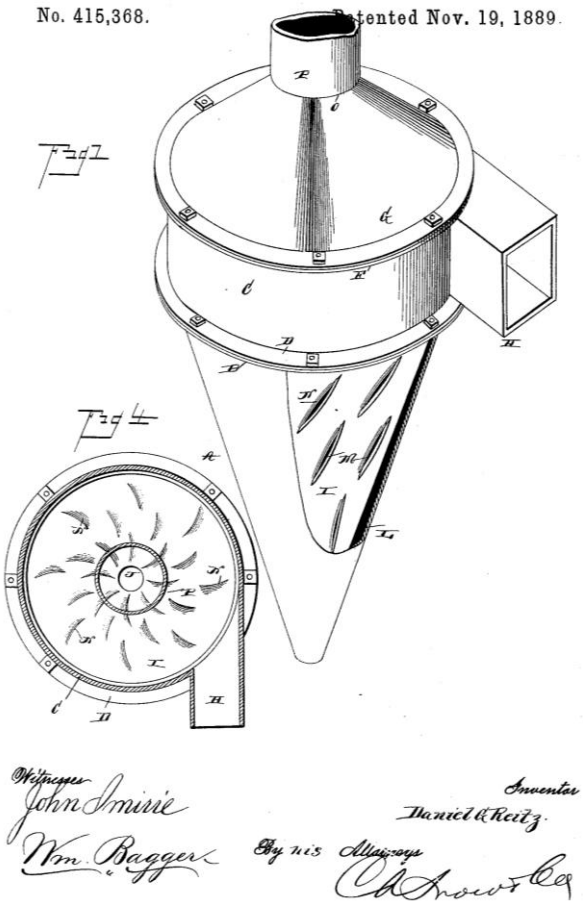

Figure 7.1 The Tangential Entry Cyclone (Reitz 1889)

The cyclone pictured in Figure 7.1 is a tangential entry reverse flow cyclonic separator, as the gas enters tangentially at the top of the device, flows to the bottom and reverses direction to exit centrally from the top. This tangential entry duct and cylindrical shape of the top of the device causes the gas to spin around the central axis of the cyclone. The gas then flows downwards in a spiral motion until it reverses back on itself and flows up the central axis towards the gas exit, or vortex finder. The diameter of the cyclone reduces along its length to create a conical shape. This reduction in radial position of the gas circulating around the central axis greatly increases the centrifugal force which pushes the denser phase against the walls of the cyclone. Similarly to the spiral jet mill, the cyclone will have a given cut size as a result of the balance between centrifugal force retaining the dense phase in the cyclone and drag force of exiting gas. Differently to the spiral jet mill however, the dense phase is subject to both radial and axial drag of gas exiting the system, with axial drag often being counteracted by gravity.

The axial entry cyclonic separator appears to have been first patented by John W. Newcombe (1922) as shown in Figure 7.2.

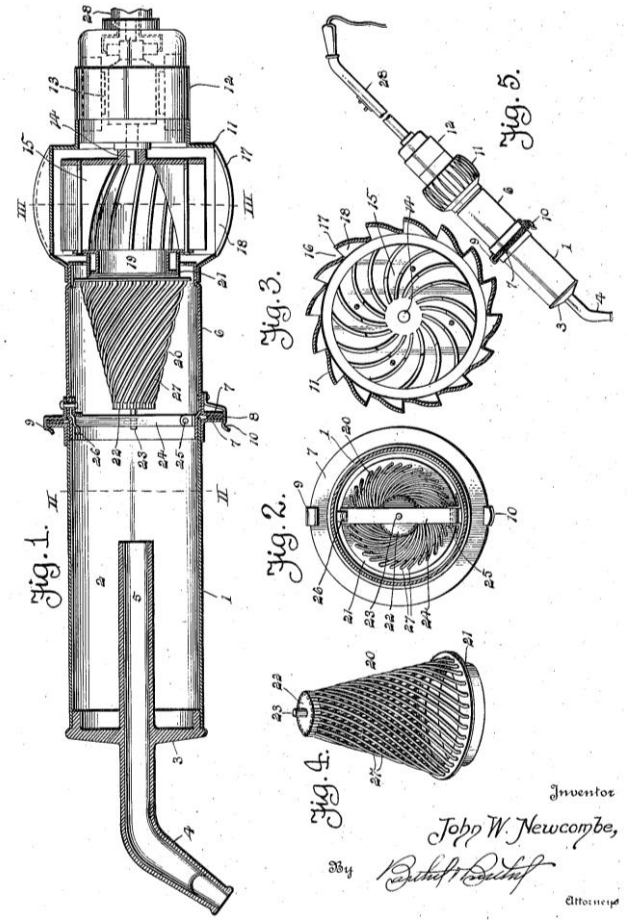

Figure 7.2 The Axial Entry Cyclone (Newcombe 1922)

The axial entry cyclone differs from the tangential entry as gas flows into the device axially (from the top in Figure 7.2). In the case of most axial entry cyclones the gas must be set into circulation by a series of angled vanes as per Figure 7.2. The device shown in Figure 7.2 is not a reverse flow cyclonic separator, as the gas flows out the opposite end to where it entered. The cyclone combined with the spiral jet mill design in Figures 1.3 and 2.2 is relatively unique as it is a vane-less axial entry reverse flow cyclonic separator. The high speed circulation within the spiral jet mill provides circulation in the cyclone, allowing the cyclone to function without vanes.

7.3 Early Investigation

The first detailed investigation into the flow pattern and pressure drop through a cyclone was published by Shepherd and Lapple (1939). Shepherd and Lapple (1939) investigated pressure drop and velocity for a range of different dimensions with a tangential entry reverse flow cyclonic separator. Following this investigation they were able to identify particular relationships between cyclone dimensions, flow velocity and pressure drop. Ter Linden (1949) published further data on the cyclone as a dust collector and the impact of guide vanes at the gas exit.

Lapple (1950) then subsequently developed a means of estimating the efficiency of a cyclone as a solids separation device. To perform this he assumed that the particle concentration was uniform at the inlet of the cyclone and that the particle size which travels from the centre of the inlet to the cyclone wall during its residence time in the cyclone would be collected with 50% efficiency.

Lapple's method (1950) is referred to as the "timed flight approach" as it is based the cut size on the particle which travels a given distance within the residence time of the cyclone. This cut size is selected to be the d_{50} as by its definition 50% of the particles of this size will not reach the cyclone wall during their residence time, and are therefore likely to exit with the lighter phase. The collection efficiency for a given particle size can then be estimated by Figure 7.3 following determination of the theoretical d_{50}. The predicted fractional collection efficiency can be determined by comparing the ratio of its diameter, d, to the d_{50} (x axis, d/d_{50}) and then looking up the corresponding fractional collection efficiency on the y axis.

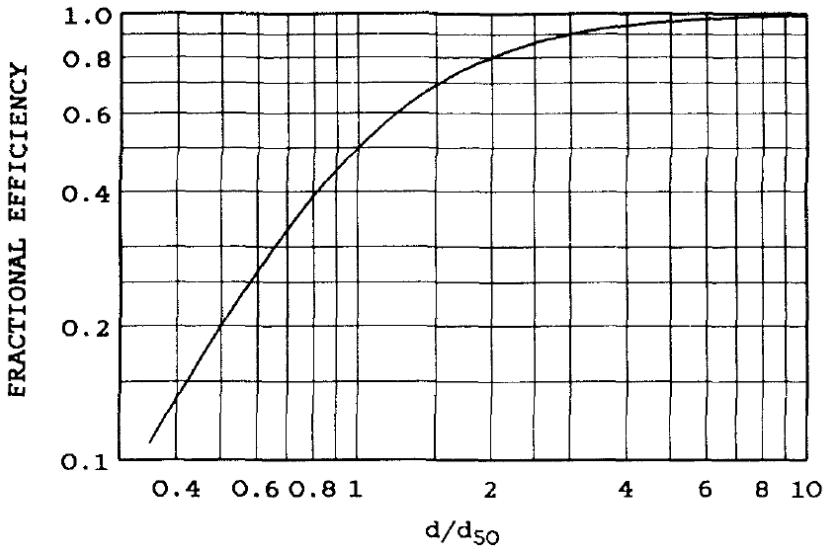

Figure 7.3 Lapple's Grade Efficiency Curve (Dirgo and Leith 1985)

Theoretically this approach has merit as it incorporates both the drag to centrifugal force balance acting on particles as well as physical and geometrical constraints such as the time and space available for solids separation. Unfortunately however, he assumed in all cases that the gas circulates five times around the central axis. This assumption of five circulations means that the estimation of both the residence time and the centrifugal force are greatly limited in their accuracy.

A detailed investigation was also performed by Stairmand (1949) which led to the renowned Stairmand high efficiency cyclone design (1951) as per Figure 7.4 and Table 7.1. To this date, the Stairmand high efficiency cyclone is still widely used and forms the basis of textbook cyclone design.

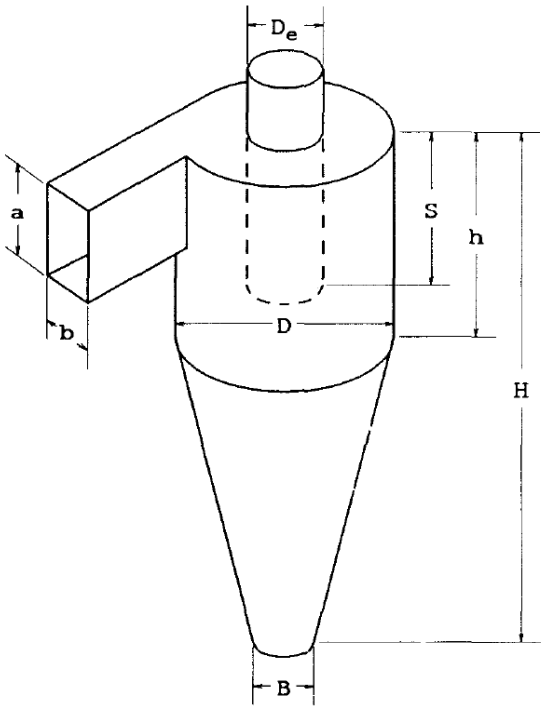

Figure 7.4 Stairmand High Efficiency Cyclone (Dirgo and Leith 1985)

Dimension	Dimension Ratio
Cyclone diameter, *D*	1:1
Gas outler diameter, D_e	1:2
Inlet height, *a*	1:2
Inlet width, *b*	1:5
Outlet duct length, *S*	1:2
Cyclone height, *H*	4:1
Cylinder height, *h*	3:2
Dust outlet diameter, *B*	3:8

Table 7.1 Stairmand High Efficiency Cyclone (Dirgo and Leith 1985)

A comparison of experimental data with theoretical predictions was performed by Dirgo and Leith (1985). The cyclone tends to become more efficient with higher gas velocities as a result of increased rotational speed and centrifugal force as per Figure 7.5.

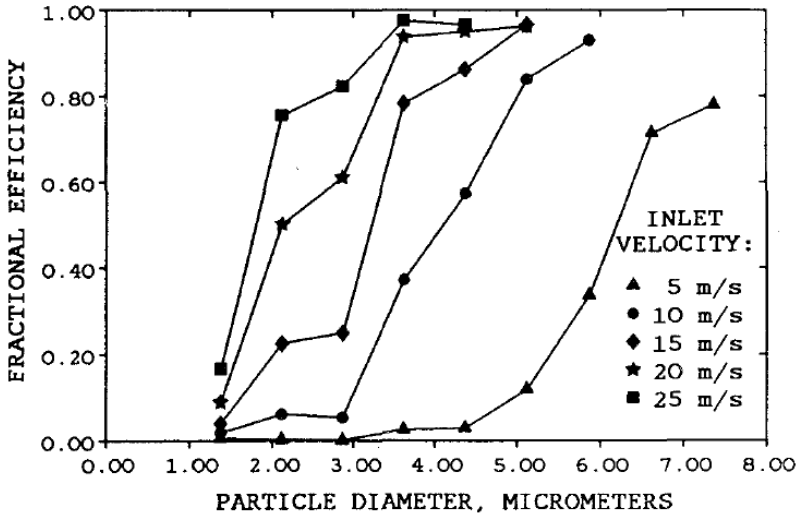

Figure 7.5 Stairmand High Efficiency Cyclone (Dirgo and Leith 1985)

Dirgo and Leith (1985) assessed the accuracy of theoretical models by how well they fitted the experimental data across a range of inlet velocities for a fixed cyclone geometry.

The most accurate theoretical model was found to be that of Barth (1956) as per Figure 7.6.

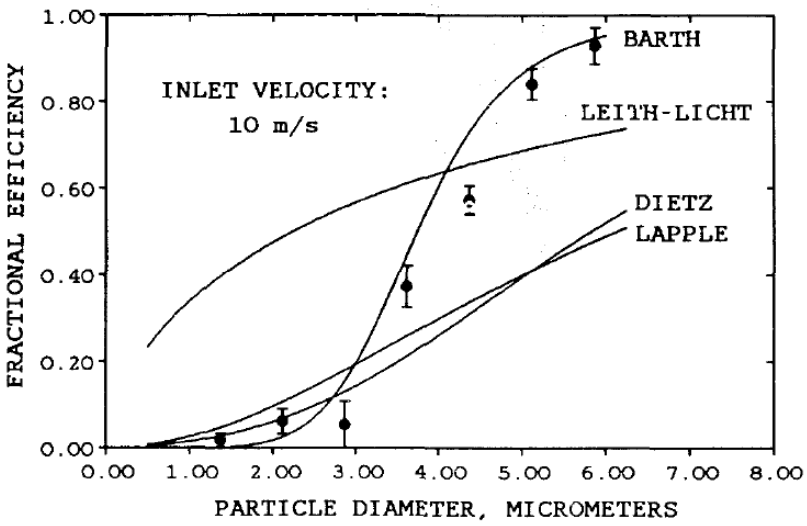

Figure 7.6 Compared Cyclone Theoretical Model (Dirgo and Leith 1985)

Barth's efficiency theory (1956) is based on a force balance approach, which defines a cut diameter based on a particle that would theoretically remain balanced between drag and centrifugal force within the cyclone. To perform this force balance an imaginary cylinder extending from below the gas outlet to the bottom of the cyclone or cone wall is defined. It is assumed that gas flows radially

through the outer walls of this cylinder to the central axis and that this radial velocity forms the basis of the drag to centrifugal force balance. An empirically derived formula is used to relate tangential velocity at the cyclone core to cyclone geometry, wall roughness and gas outlet velocity. An axial drag to gravitational balance is not considered.

The collection efficiency of any particle size other than that of the cut diameter is defined by the ratio of its settling velocity, v_{ts}, to the terminal settling velocity of the cut diameter particle, v_{ts}^*, as per Figure 7.7.

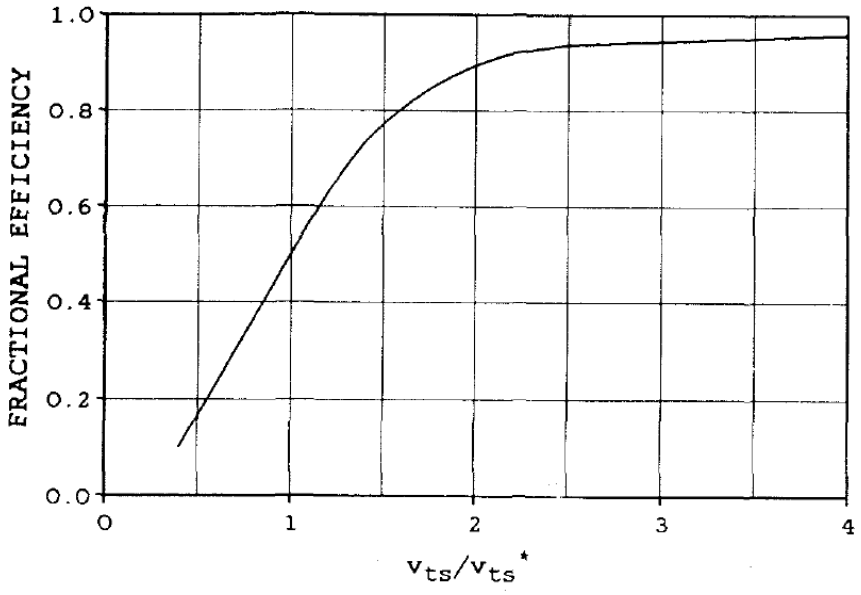

Figure 7.7 Barth's Grade Efficiency Curve (Dirgo and Leith 1985)

Although Barth's force balance (1956) gave the best match to experimental data in Dirgo and Leith's study (1985), it is very simplistic in nature and to fit the experimental data the settling velocity ratio had to be multiplied by a factor of four. Following this modification to Barth's model (1956) it provided the most accurate prediction of change in cut size with change in gas flow rate. In this study Lapple's timed flight approach (1950) did not match experimental data as a result of his assumption of five circulations being incorrect. The experimental data suggests that with varying gas flow rates the number of circulations and overall residence time within the cyclone changes. It must be noted that although Barth's modified model worked well, it cannot account for changes in collection efficiency with different solids loading (Dirgo and Leith 1985).

Barth's model was further developed by Muschelknautz (1970, 1972) and Meißner and Löffler (1978) to account for changes in dynamics with different solids loadings. Muschelknautz's modification (1972) gained popularity and formed the basis of textbook cyclone collection efficiency estimation (Hoffmann 2002). The means of estimating the tangential and radial velocity within the cyclone were also further developed by Ogawa (1984, 1997). Although the means of estimating velocities were further refined, the principle of the Barth's force balance (1956) still remained the basis of the theoretical modelling of cyclone collection efficiency.

Further experimental studies by Hoffmann *et al.* (1991) showed that collection efficiency increases with solids loading, but not in a manner predicted by concurrent theoretical models. The experimental evidence showed that agglomeration and particle-particle interactions are the likely cause of increased efficiency with greater solids loadings. This led to further development of the Muschelknautz method by Trefz and Muschelknautz (1992).

7.4 Experimental Geometry Optimisation

The cyclone which is combined with the spiral jet mill is a vane-less axial entry reverse flow cyclonic separator as per Figure 1.3, making a review of papers discussing optimisation of tangential entry inlet dimensions irrelevant with respect to the planned design optimisation. Additionally, due to footprint constraints of the project it is not possible to adjust the dimensions of the cone, also excluding research papers on optimisation of cone length and diameter. As a result of the specific constraints to the project, only modifications to the vortex finder are reviewed.

Moore and McFarland (1993) showed that reduction of the ratio between the vortex finder diameter and cyclone diameter results in a significant increase in recovery of finer particles. In most industrial applications the pressure drop is constrained, and as such rather than reducing the vortex finder diameter, the cyclone diameter is increased.

Lim *et al.* (2004) published a detailed experimental study which looked at varying diameters and shapes of vortex finder. In all cases it was found that a thinner vortex finder was able to recover smaller particles with greater efficiency.

7.5 Computational Geometry Optimisation

Computer simulations allow for more detailed optimisation with a great number of experiments, and, in some cases where CFD-DEM is used, allow the physical processes resulting in changes to performance to be investigated.

As the output of a spiral jet mill has a notable mass percentage of its output in the submicron range, literature regarding cyclonic separation of very fine particles is particularly relevant. A CFD and experimental study was published by Yoshida *et al.* (1991) which investigates size classification of submicron powder. They were able to find good agreement between experimental results and CFD simulation with calculated particle trajectories. Their results showed that loss of very small particles with exiting gas is primarily a result of the upward velocity component at the bottom of the cyclone.

The results from CFD were further confirmed by Slack *et al.* (2000) who compared the results of Large Eddy Simulation (LES) to laser Doppler anemometry measurements of gas flow at a number of locations in a Stairmand cyclone. LES was also used by Derksen and Van den Akker (2000) to investigate vortex core precession within a cyclonic separator. The study of Derksen and Van den Akker (2000) is particularly useful as it considers that the flow pattern within a cyclone is not entirely steady and that the core of gas flowing out of the cyclone can precess around the central axis. Vortex core precession is a known phenomenon, and therefore CFD studies into particle classification in cyclones should consider variation in flow pattern with time. Additionally, Cortes and Gil (2007) published a detailed review of modelling of cyclonic separation. The review covered numerous publications of evidence of vortex core precession in gas cyclones and hyrdocyclones with experimental evidence and CFD. It is noted that only LES and unsteady Reynolds-averaged Navier-Stokes (URANS) simulations appear capable of capturing the complexity of unsteady flow patterns inside a cyclonic separator.

With regards to CFD simulation of changes in vortex finder dimensions, the experimental study of Lim *et al.* (2004) was replicated using Reynolds stress transport model (RSTM) CFD and Discrete Phase Modelling (DPM) by Raoufi *et al.* (2008). The CFD study showed that increases in vortex finder diameter led to a

reduction in tangential velocity in the inner region of the cyclone, leading to lower separation efficiency.

CFD simulations can be used to perform a great number of simulated experiments, which can then lead to computer aided design optimisation. Elsayed and Lacor (2010) used CFD and the Muschelknautz method to optimise the design of a tangential entry cyclonic separator using a Nelder-Mead downhill simplex optimisation technique. Their computer aided optimisation led to a design close to the Stairmand high efficiency cyclone with a similar cut-off diameter but greatly reduced pressure drop. A similar exercise was published by Elsayed and Lacor (2013a) using a radial basis function neural network (RBFNN) and genetic algorithms for optimisation, yielding a similarly optimised cyclone design to their previous study (2010). Elsayed and Lacor (2013b) also published a study into varying the vortex finder length and diameter. It was shown that although reduction in vortex finder diameter leads to increased tangential velocity, it results in significant increases to the pressure drop.

The CFD studies so far presented have assumed that the solids concentration is sufficiently low that its effect on the gas flow may be ignored. It is however known from experimental evidence that solids loading can have a large effect on the collection efficiency. Combined gas flow and particle behaviour was initially simulated by Crowe and Pratt (1974). Their study showed that moment coupling of gas and particles results in increased efficiency with higher particle loading.

CFD-DEM allows for much more refined simulations of gas and particle systems by allowing gas-particle and particle-particle interactions to be simulated. Chu *et al.* (2010) performed a CFD-DEM simulation at varying solids loadings and showed good agreement with experimental observations of reduced pressure drop and increased collection efficiency with increased solids loading. However, their study assumed no cohesion between particles and was for large particle diameters.

Alves *et al.* (2015) published some of the CFD simulation and experimental basis for the Advance Cyclone Systems (ACS) proprietary Hurricane_MK design. Their model considered agglomeration within the cyclone, and that if smaller particles are encouraged to associate with larger particles the overall collection efficiency can be greatly improved. This model was then used to perform numerical

optimisation that led to the Hurricane_MK design, which cannot be fully disclosed by ACS for confidentiality reasons, although it is reported to have a narrow inlet and outlet and large cylindrical section prior to the cone.

7.6 Summary of Key Facts

- The collection efficiency of a cyclone may be approximately estimated by a force balance between centrifugal force and radial drag (Barth 1956).
    - This force balance suggests that increasing the length of the central core of gas within the cyclone will reduce the radial drag, and improve collection efficiency (Dirgo and Leith 1985).
    - This approach does not consider an axial drag to gravitational force balance (Dirgo and Leith 1985).
    - This approach does not consider the impact of solids loading on collection efficiency (Dirgo and Leith 1985).
- Loss of submicron particles is primarily a result of the upward (axial) component of velocity at the bottom of the cyclone (Yoshida 1991).
- Agglomeration and particle association are key processes in cyclonic separation (Hoffmann *et al.* 1991, Alves *et al.* 2015).
- Experimental evidence and CFD has shown that reduction in vortex finder diameter leads to an increase in collection efficiency and pressure drop (Moore and McFarland 1993, Lim *et al.* 2004, Raoufi *et al.* 2008, Alves *et al.* 2015).
- Increased solids loading and gas flow rate can increase the collection efficiency (Dirgo and Leith 1985, Hoffmann *et al.* 1991).

Chapter 8. Cyclone and Grind Chamber Optimisation Rationale

8.1 Product A Cyclonic Separation Data

Following micronisation of Product A, approximately 11% of the mass is lost during cyclonic separation as filter fines. A comparative frequency PSD can be seen in Figure 8.1 and cumulative undersize PSD in Figure 8.2 for filter fines (red) and collected product (green).

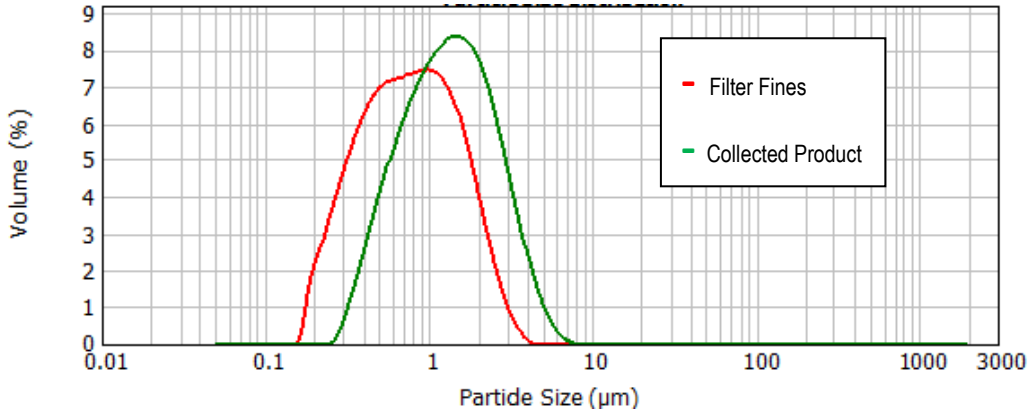

Figure 8.1 Product A Filter Fines and Collected Product Frequency PSD

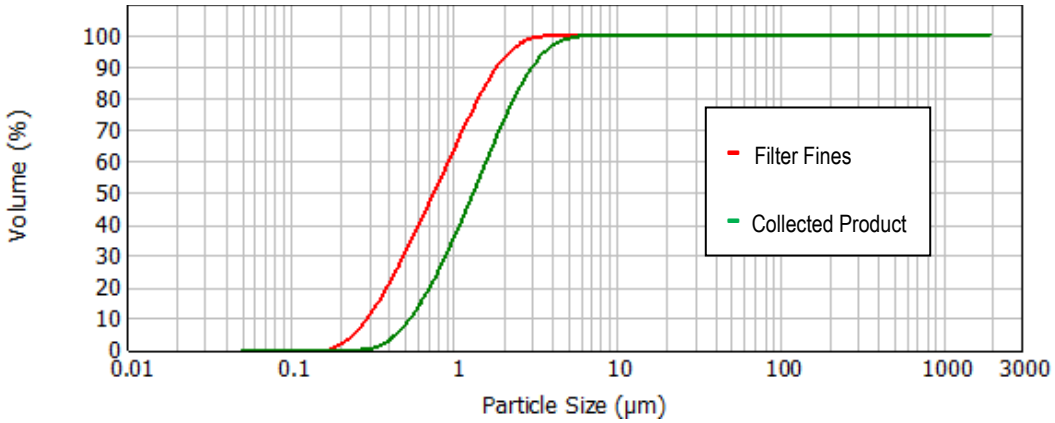

Figure 8.2 Product A Filter Fines and Collected Product Cumulative PSD

Mass balance data and PSD data is used to generate a collection efficiency curve for Product A and its current Manufacturer A cyclonic separator as shown in Figure 8.3.

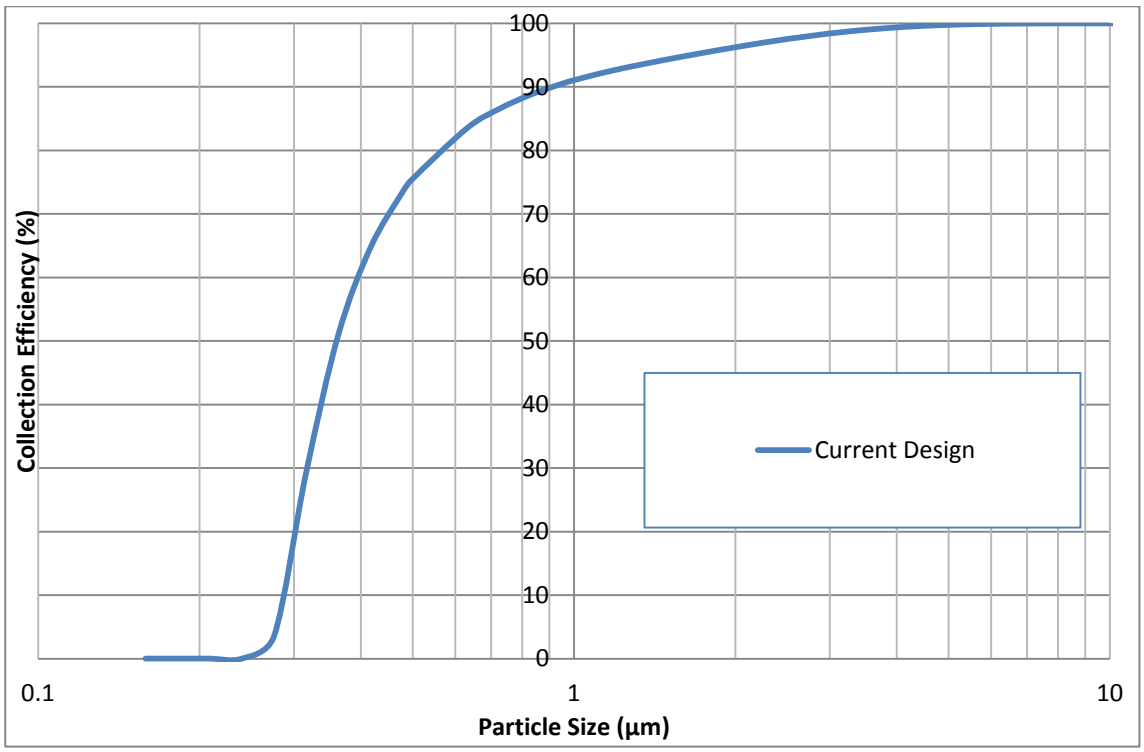

Figure 8.3 Product A Collection Efficiency Curve

Although there is a desire within GSK to increase the cyclonic separation yield for Product A, there is not an intention to recover 100% of the output material for an established API such as Product A if it means bringing the PSD outside of commercial knowledge space. It can be seen from Figure 8.2 that approximately 10% of the volume of the filter fines (when particle diameters are assumed spherical) are particles which are smaller than the smallest particles currently in Product A (0.3 microns). If these particles are not to be recovered such that the PSD remains within commercial knowledge space, then the maximum possible yield will be approximately 98.9%. Currently, around 70% of the assumed spherical volume of the filter fines is greater than 0.5 microns in diameter, meaning that a yield increase to 96.7% without any increase to the number of particles smaller than 0.5 microns is possible.

Although a yield increase while still removing very fine particles is possible, it will still result in a shift in the PSD that may impact the product performance of secondary formulations. Product A is used in several respiratory formulations which are sensitive to PSD. Therefore, it may still be necessary to modify the output of the grind chamber to increase the number of particles between 2 and 5 microns which are able to escape and form part of the product.

8.2 Low Yield Hypotheses

Other materials micronised by GSK with a similar PSD, such as Product D, have cyclonic separation yields of 99% or more. Understanding why Product A has a low cyclonic separation yield also requires understanding why Product D has a high yield.

8.2.1 Particle Shape

Comparative Scanning Electron Microscographs (SEM) of micronised Product A and Product D can be found in Figure 8.4, which shows 20,000x magnification on the left and 5,000x magnification on the right. Although in both cases the particles are agglomerated, the PSD measurement process ensures dispersion through the use of an appropriate liquid medium, surfactant and sonication. It is also believed that the highly turbulent conditions near the classifier of the spiral jet mill result in individual aerosolised particles being present in the gas initially entering the cyclone.

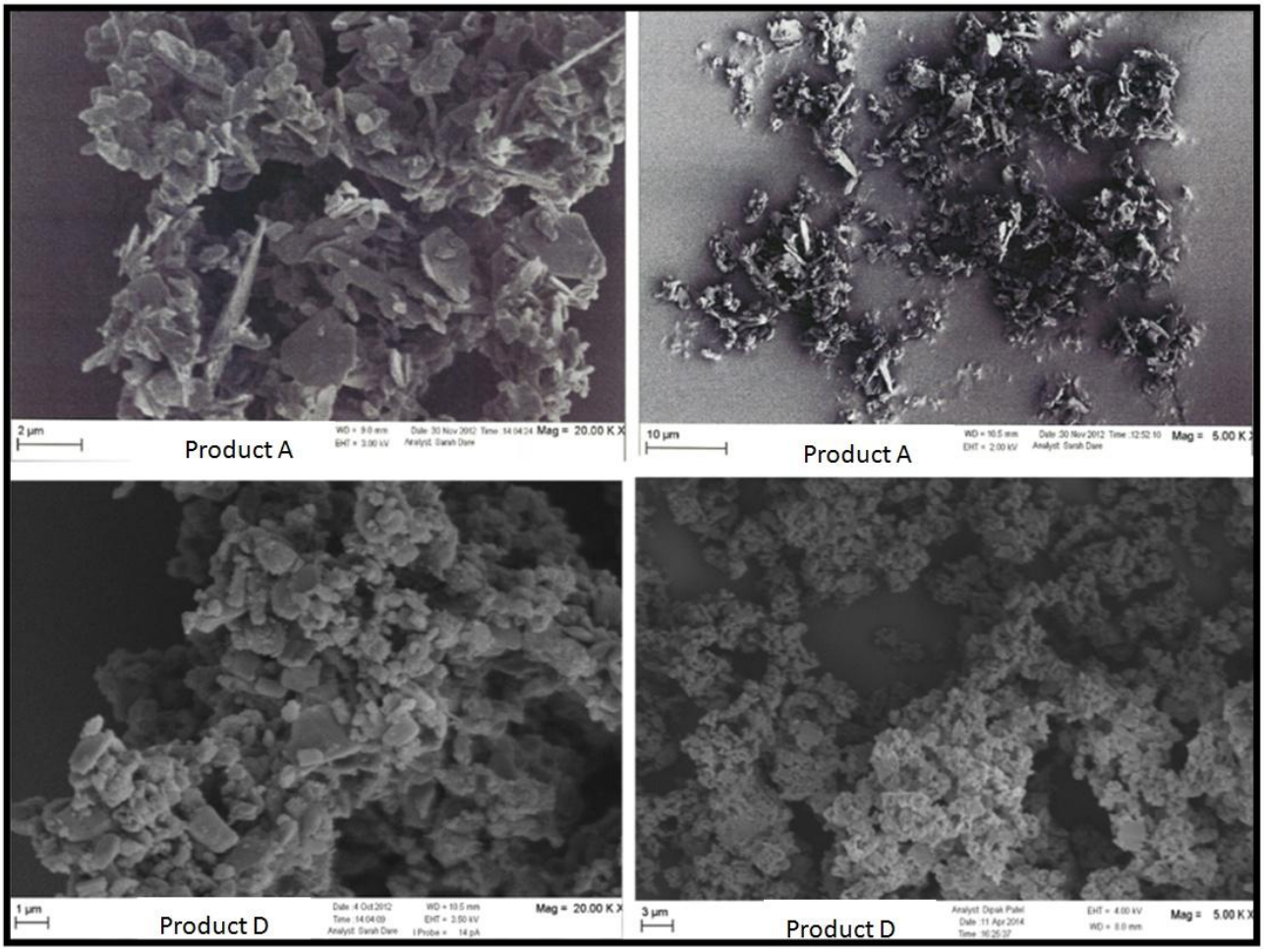

Figure 8.4 Comparative SEMs for Micronised Product A and Product D

As can be seen from Figure 8.4 there is a clear difference in particle shape between Product A and Product D. Although Product D is irregular and non-spherical, there do not appear to be many thin or elongated particles. Product A however appears to have a large number of flat and elongated particles. The difference in particle shape and surface properties is evident in the different Specific Surface Area (SSA) of the two products, as per Table 8.1.

Product	SSA range ($m^2.g^{-1}$)	x50 range (microns)
A	12.1 – 13.4	1.49 – 1.76
D	8.8 – 10.0	1.63 – 1.79

Table 8.1 Comparative SSA data for Product A and Product D

Although Product A is generally finer than Product D, the difference in particle size distribution does not account for the difference in SSA. Both the SEM and the SSA data for Product A and Product D suggest that there is a distinct difference in particle shape and roughness between the two materials.

It may be the case that, as Product A is much less spherical than Product D, it behaves aerodynamically as much smaller particles. Barth's static particle approach (1956) and collection efficiency curve is based on terminal settling velocity rather than actual particle diameter. It would be expected that thin and elongated particles with low settling velocities will be collected less effectively than irregular particles with high sphericity and high settling velocities. A comparison of Barth's static particle collection efficiency curve (1956) to the Product A collection efficiency curve can be found in Figure 8.5.

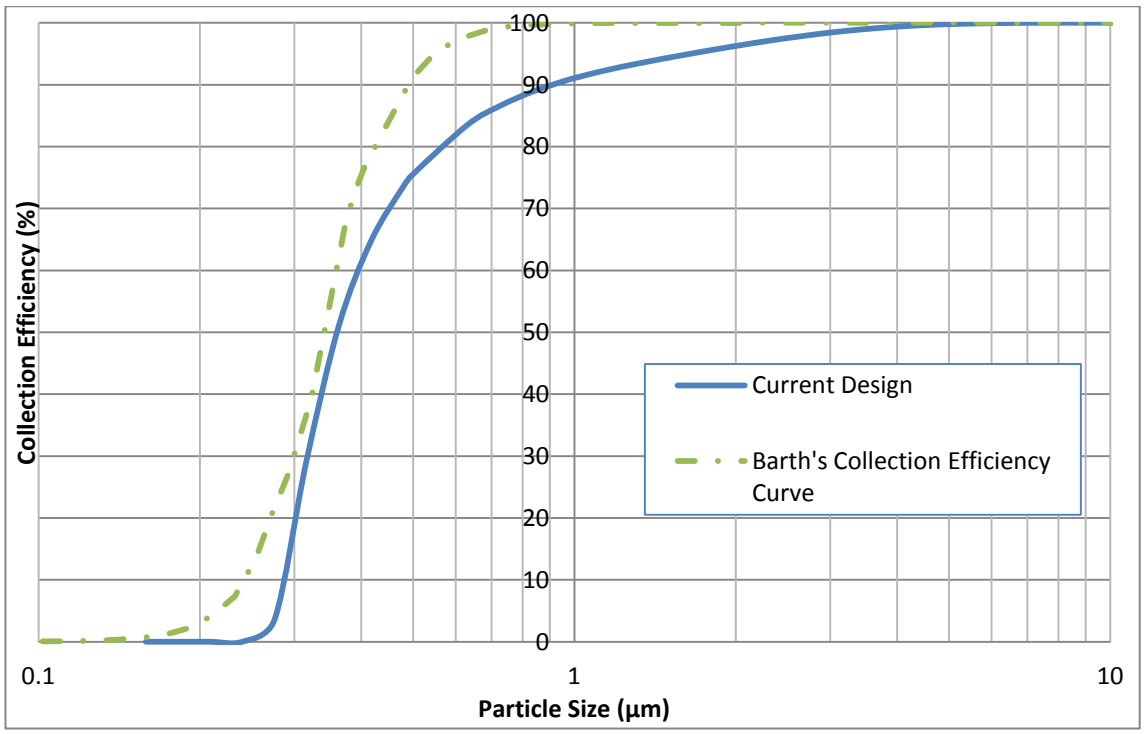

Figure 8.5 Barth's Static Particle Approach compared to Product A Data

The discrepancy between the theoretical collection efficiency curve and the actual collection efficiency data may be a result of the particle shape of Product A. The behaviour may actually conform to Barth's settling velocity curve (1956), as the Product A particles may have settling velocities equivalent to much smaller particles. For example, consider the difference in settling velocity of a rectangular prism of length, L, breadth, B, and height, H, compared to a sphere of diameter, D, as per Figure 8.6 (buoyancy is not included in the diagram as it is insignificant for a gas at low pressure).

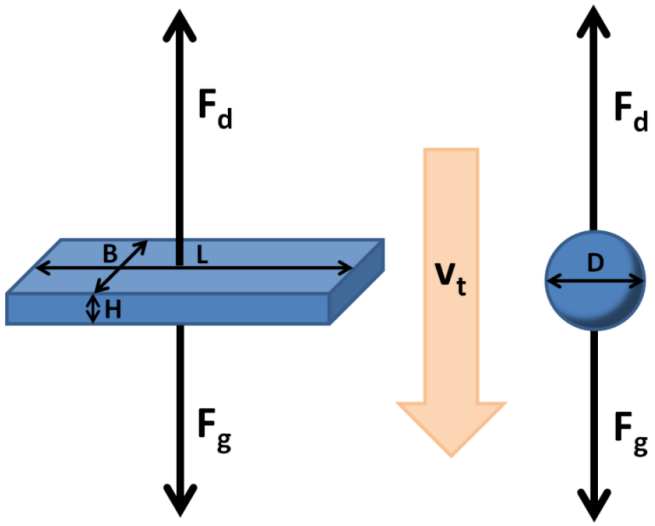

Figure 8.6 Dimensions to Define Settling Velocity of a Rectangular Prism

The terminal velocity, $v_{terminal}$, in a gas of low density for a particle is defined by Equation 8.1 and the drag coefficient number by Equation 8.2:

$$v_{terminal} = \sqrt{\frac{2mg}{\rho_g A C_d}} \tag{8.1}$$

$$C_d = \frac{24}{Re} \tag{8.2}$$

where g is gravitational acceleration, m is the mass of a particle and A is the particle projected area. If it is considered that the rectangular prism projected area which presents the greatest resistance to flow is LB and its Reynolds length scale is L, it is possible to determine the diameter, D, of a sphere with an equivalent settling velocity to the lowest settling velocity of prism LBH as per Equation 8.3:

$$D = \sqrt{\frac{3HL}{2}} \tag{8.3}$$

If a particle with a height of 0.15 μm and length 1.00 μm is considered, its equivalent sphere with the same terminal velocity is 0.47 μm in diameter. This corresponds approximately to Figure 8.5 where particles of 1.00 μm in diameter as measured by laser diffraction are collected with 86% efficiency rather than 100% efficiency.

In addition to particle shape influencing the radial drag to centrifugal force balance, it is also likely to impact the axial drag to gravitational force balance at the gas flow reversal point. Thin and elongated particles are more likely to be pulled upwards with exiting gas than irregular particles with high sphericity. Therefore, moving the vortex finder further away from the gas flow reversal point to reduce axial drag may recover more particles with lower settling velocities.

8.2.2 Agglomeration

The SEMs in Figure 8.4 show more than just a difference in particle shape between Product A and Product D, they also show a difference in particle association. Particularly at the 5000x magnification scale it is possible to see that the particle association for Product A is not continuous and that there are a significant number of voids between small agglomerates of particles. For Product D however, the particle association is relatively continuous with the particles being almost entirely interconnected with each other through mutual contact. The 20,000x

magnification images again show very few voids between particles of Product D and continuous mutual contact, whereas for Product A it can be seen that there are many voids.

The particle association and agglomeration properties may be important in defining behaviour during cyclonic separation, particularly for the “dropping out” process. Micronised particles have very low settling velocities, and as such for them to fall into the collection bag by gravity they need to associate with other micronised particles to form agglomerates that are capable of “dropping out”. As this drop out process must occur against an upward axial velocity, the settling velocity of the agglomerates needs to be greater than the upward component of velocity at the gas flow reversal point.

The difference in particle association between Product A and Product D indicate the following regarding their cyclonic separation behaviour:

- Product D may have a higher number of contact points between particles for a given agglomerate size due to the continuous nature of the particle association. This high level of contact area may make the agglomerate robust against shearing forces from gas within the cyclone.
- Product A may have a lower number of contact points between particles for a given agglomerate size due to the lack of continuous particle association. This low level of contact area may make the agglomerate fragile and likely to aerosolise as a result of shearing forces from gas within the cyclone.
- Product D may form dense agglomerates due to the continuous nature of the particle association and tight packing. This will increase the settling velocity of the agglomerates and aid the dropping out process.
- Product A may form agglomerates with low density as shown by the number of voids in SEM images. This will reduce the settling velocity of the agglomerates and hinder the dropping out process.
- Product D may form large agglomerates due to the continuous nature of the particle association seen in the SEM images. This will increase the settling velocity of the agglomerates and aid the dropping out process.
- Product A may form small agglomerates as seen in SEM images. This will reduce the settling velocity of the agglomerates and hinder the dropping out process.

If a lack of cohesion between particles and low agglomerate strength is the cause of poor cyclonic separation yields for Product A compared to Product D, any design changes that could reduce shearing forces and increase residence time for agglomeration are likely to increase yield.

8.3 Geometry Modification to Optimise Yield

Figure 8.7 shows four critical areas to performance of the cyclone of a bottom discharge spiral jet mill. The dimensions of these areas are critical as they define one of the components of gas velocity passing through them for a given volumetric flow rate.

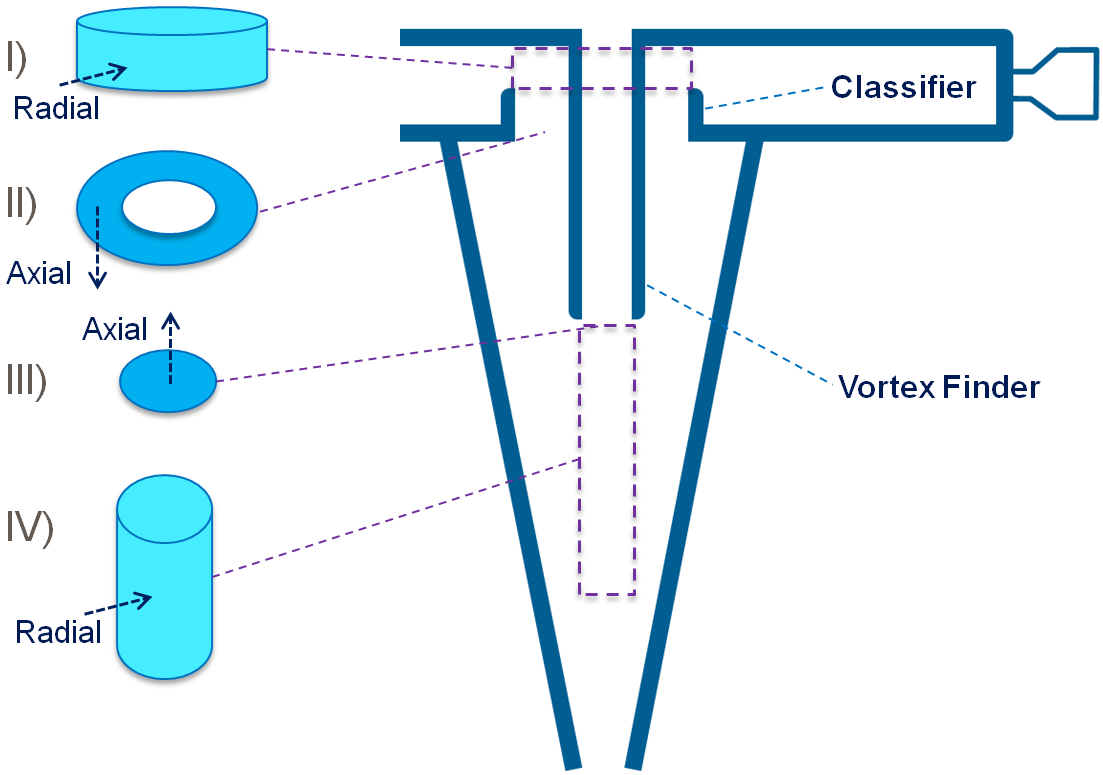

Figure 8.7 Critical Areas for Particle Classification in a Bottom Discharge Spiral Jet Mill

Means of increasing yield are likely to be:

- Reduce lower classifier height (I) to increase tangential velocity and centrifugal force by reducing the proportion of gas kinetic energy changed to radial velocity. This will bring particles together with more force on the cyclone wall and may improve particle association.

- Move upper classifier further away from the bottom of the cyclone (IV) to reduce radial exit velocity and drag force. Barth's theorem (1956) sees this area for radial gas flow as crucial to defining the balance between radial drag and centrifugal force. Moving the exit further from the gas flow reversal point may also reduce axial velocity pulling particles/agglomerates upwards and aid the drop out process.

- Increase cyclone entrance area (II) by vortex finder diameter reduction to reduce axial velocity towards the bottom of the cyclone and give particles more time to migrate towards the wall of the cyclone. This will also reduce the amount of kinetic energy converted to downwards axial velocity and increase the gas tangential velocity. The increase in residence time may also increase the level of particle association.

- Reduction in vortex finder diameter (III) to reduce the diameter of the central core and increase the distance between the cyclone wall and the central core of gas. This may reduce the shearing forces on agglomerates and prevent them from becoming re-aerosolised. Reduction in vortex finder diameter will also increase the centrifugal force at the interface between the central core of gas and outer section by reducing the radius on which the tangential velocity is acting.

8.4 Geometry Modification to Change PSD

Within the scope of this project the PSD may be modified in two ways:

1. Adjustment of classifier height.
    - If the output following yield increase is too fine, then increasing the classifier height can coarsen the output material.
    - If the output following a yield increase is too coarse (cyclone dynamics may interact with grind chamber in an unexpected way) then reducing the classifier height can make the output material finer.
2. Modification to grind chamber shape near the grind nozzles.
    - The introduction of geometry changes in the grind chamber, such as elliptical plates, may impact mass transport to the nozzles and collision process.

8.5 Discussion

There is a known difference in cyclonic separation performance between Product A and Product D which must be material specific as for identical gas flow rates and solids feed rates there is a more than 10% difference in yield. This may be a result of a difference in particle shape and/or agglomeration properties.

Although this particular cyclone design is unique, key areas for modification to improve yield have been identified. It may be possible to use Computational Fluid Dynamics (CFD) to assess which design changes will be more likely to improve yield. Due to the known discrepancy between CFD for a gas only system and the gas flows of a gas and powder system, experimentation will be required to identify the optimal cyclone design with respect to yield. Additionally, the combination of vortex finder shape and classifier height that delivers a yield increase while maintaining similarity of PSD may need to be found experimentally.

8.6 Conclusion

Based on the possible low yield mechanism for Product A, several possible design changes to increase yield have been identified for further design screening with CFD. Means of also changing the PSD to maintain similarity of PSD have also been identified for CFD design screening, but will require experimental investigation as the interactions between gas and powder will be challenging to predict.

Chapter 9. CFD Design Screening to Increase Cyclone Efficiency

9.1 Rationale

Although Computational Fluid Dynamics (CFD) alone will not be able to indicate the flow characteristics of a combined spiral jet mill and cyclone due to the effect of powder hold up on tangential velocity, it can aid the design process by giving an insight into flow patterns within the axial entry cyclone and grind chamber.

Discrete Phase Modelling (DPM) can be used to track particles through the spiral jet mill and cyclone. A count can be performed on the number of particles that are trapped in the product collection bin and the number that escape through the vortex finder to give a numerical measure as to changes in yield with geometry.

9.2 Investigation Details

9.2.1 CFD Model Details

As it is known that Computational Fluid Dynamics (CFD) alone will not be able to indicate the flow characteristics of a combined spiral jet mill and cyclone, a simplistic model is used to obtain approximate information on performance across the design space. CFD simulations are performed with an academic version of ANSYS FLUENT 14.5 with a model for nitrogen according to Table 9.1. A boundary condition of 20 ^{o}C and 8.0 bar absolute was set behind the grind nozzles, 20 ^{o}C and 10.0 bar absolute behind the feed nozzle, 20 ^{o}C and 1.0 bar absolute at the solids inlet and 1.0 bar absolute at the gas outlet.

Model Parameter	Setting
Viscous Model	k-epsilon (2 equation), Default Settings
Gas Density	Constant, Fluent Database
Gas Viscosity	Constant, Fluent Database
Gas Thermal Conductivity	Constant, Fluent Database
Gas Specific Heat Capacity	Constant, Fluent Database

Table 9.1 CFD Model Settings

This simplistic model was selected over Large Eddy Simulation (LES) or a Reynolds Stress Transport Model (RSTM) as it was necessary to perform a large number of simulations in a short space of time. Additionally, due to the expected

discrepancy between the gas and powder system and the gas only system, a detailed CFD model cannot be justified over a simplistic model as the results of any simulation will not be fully representative of the real system.
It is known that the selection of constant gas density will have resulted in the nozzle dynamics of the grind chamber being unrealistic. It is also known that assuming an incompressible gas in the cyclone will result in a notable discrepancy between simulated flow and actual flow. However, the selection of constant gas density allowed the simulation to converge repeatedly. It is expected that the region of optimal geometry for increasing collection efficiency will be similar for both compressible and incompressible gas.

DPM for spherical particles which do not interact with the fluid phase was performed once the simulation had converged. Due to some variability in the flow pattern even after convergence, the DPM simulations were repeated a number of times with several hundred fluid phase iterations between them.

A great number of varying geometries were assessed that were based on the tangential entry bottom discharge spiral jet mill in Figure 1.3 as per Figure 9.1.

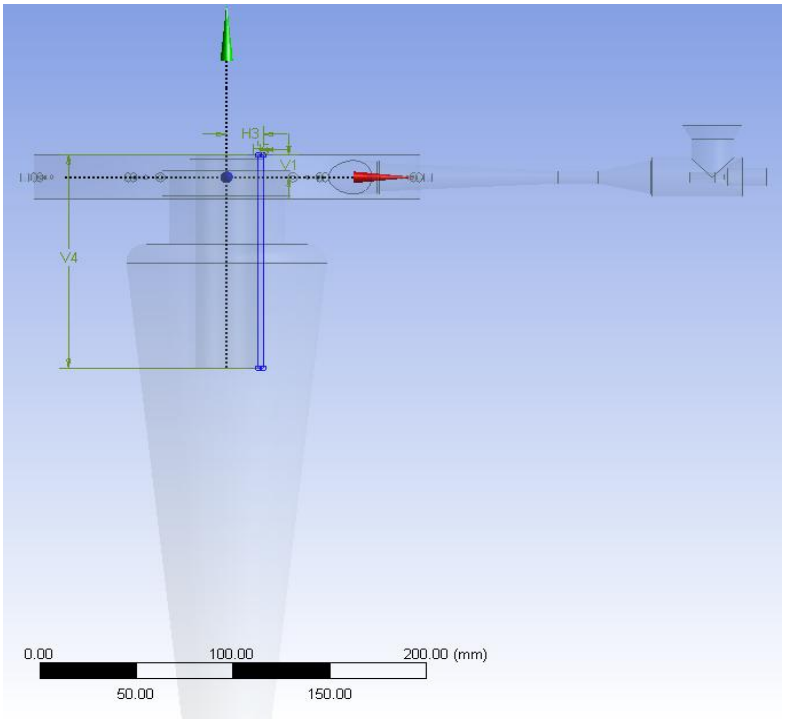

Figure 9.1 Spiral Jet Mill Geometry Investigated

9.2.2 Geometries Investigated

As part of initial screening, a number of geometry changes were investigated such as modification to the angle of the cyclone wall and cyclone diameter to even the introduction of fins and stabilisers. It was found that these geometry changes only had a negative impact on the ability of the cyclone to recover very fine particles when within the footprint constraints of the design project.

Modification of the vortex finder length and diameter, in addition to the classifier height were investigated in detail as these changes are feasible within the current footprint constraints and are capable of increasing yield and modifying PSD.

The range of geometries investigated may be found in Table 9.2.

Geometry Parameter	Range (mm)
Classifier Height	3 - 18
Vortex Finder Diameter	26 - 45
Vortex Finder Length	80 - 175

Table 9.2 Geometry Ranges for Detailed Investigation

9.3 Investigation Results

9.3.1 General Qualitative Observations

The first qualitative observation to note regarding the CFD results is that the flow pattern is not steady over time, and that following solution convergence there is vortex core precession around the central axis. This is shown in Figure 9.2 where the coloration has been set such that blue indicates a downwards axial velocity of greater than 1 $m.s^{-1}$ and red indicates an upwards axial velocity of greater than 1 $m.s^{-1}$.

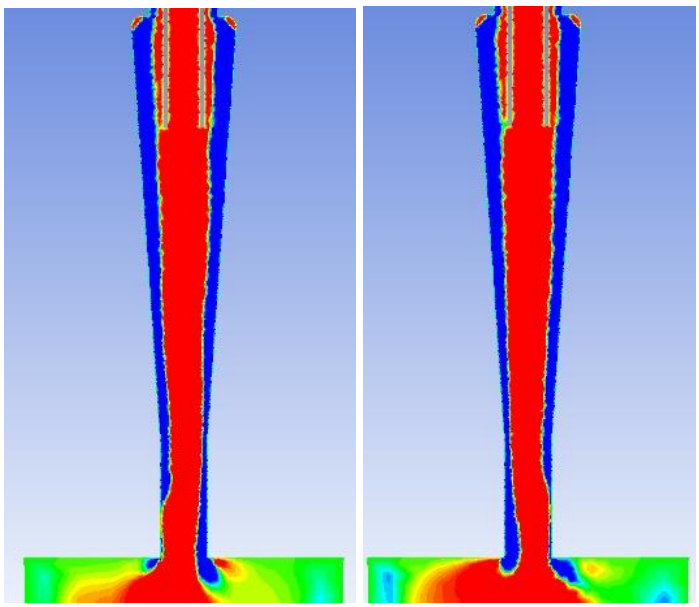

Figure 9.2 Vortex Core Precession

(left and right images are at different time points following solution convergence)

This vortex core precession may lead to poor cyclonic separation yields, and as such initial geometry modification was performed in an attempt to reduce precession. A number of design changes were tested, however only one was successful at removing vortex core precession. This involved inserting a perfectly stiff rod along the central axis. This reduced the turbulence and brought stability to the design as per Figure 9.3 where the standard case is on the left, and the stabilising rod is on the right.

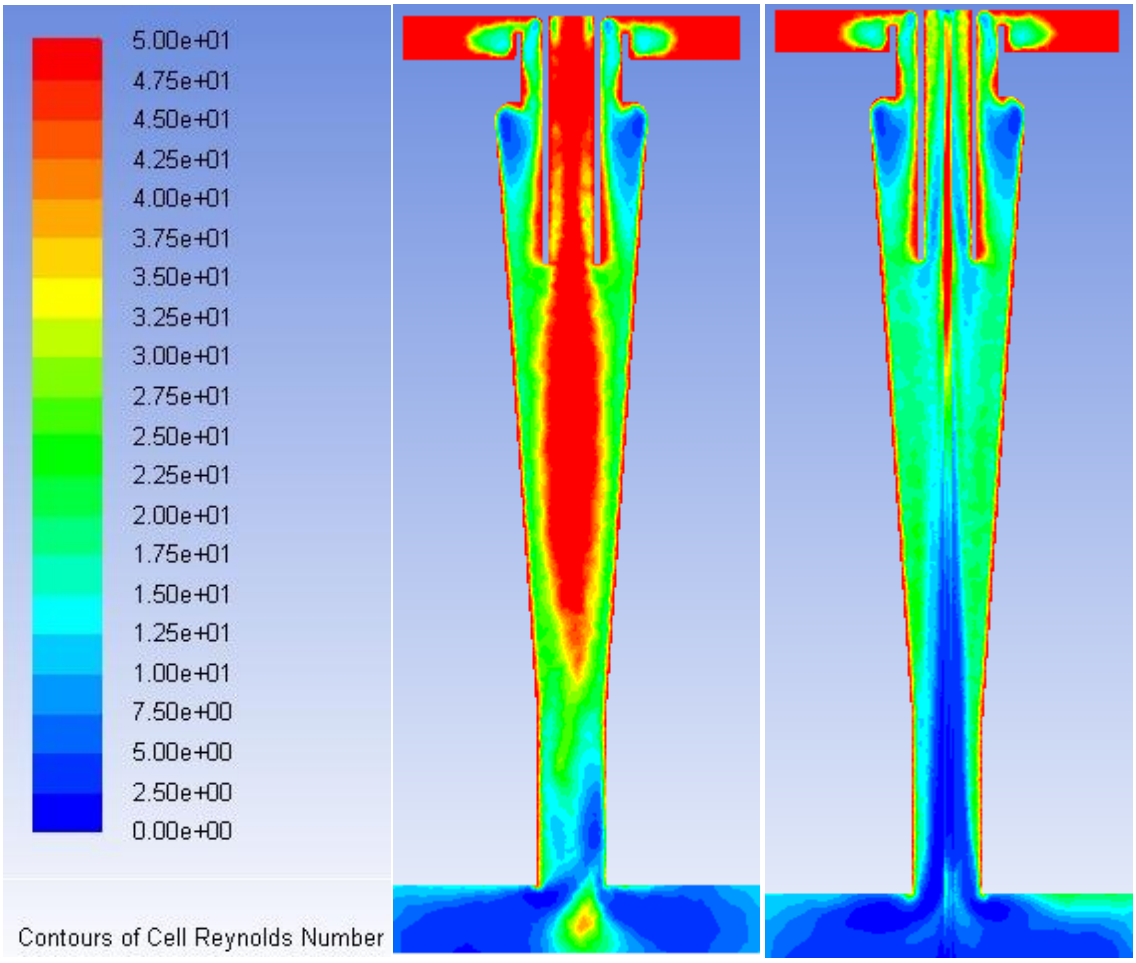

Figure 9.3 Turbulence in Vortex Core Precession Stabilisation (Standard = Left, Rod Stabilised = Right)

Unfortunately, the introduction of the stabilising rod also greatly increased the length of the central core of gas and moved the gas flow reversal point downwards and into the product collection bin. This can be seen from the axial velocity contour plot in Figure 9.4 where the standard case is on the left and the stabilised case is on the right.

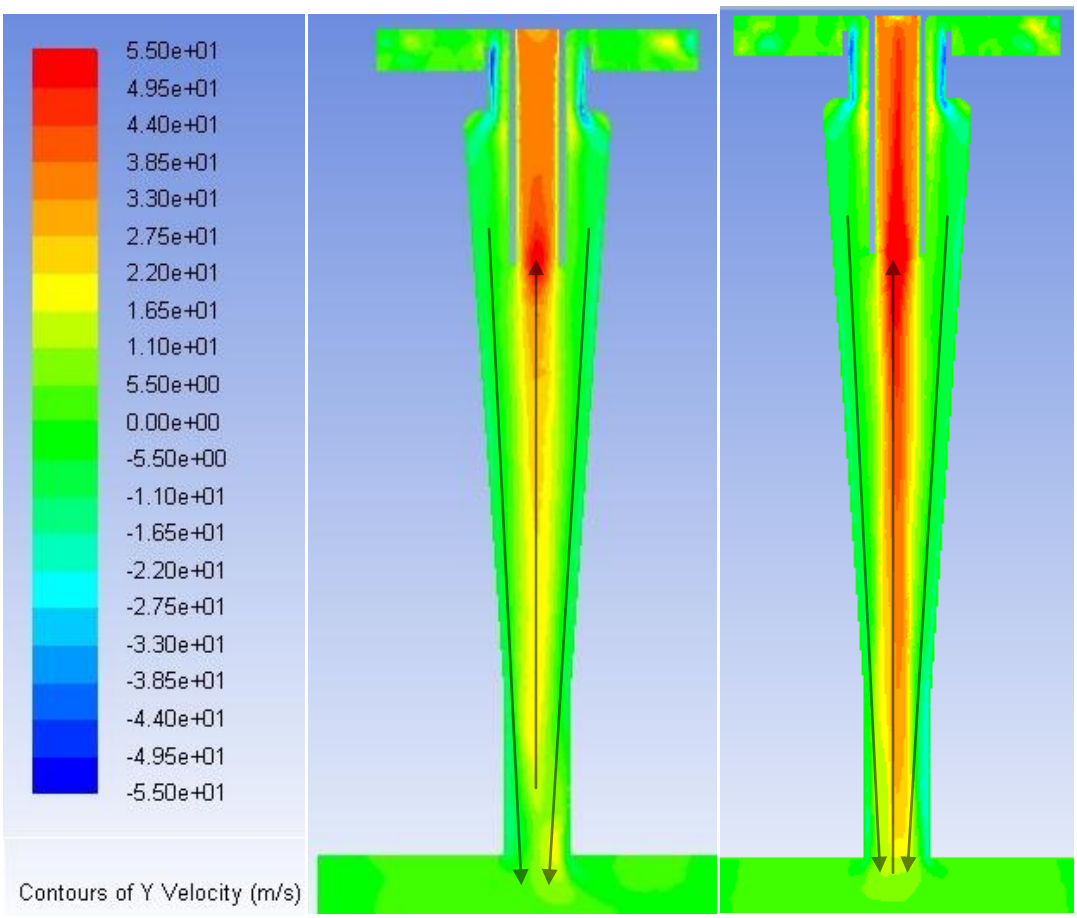

Figure 9.4 Axial Velocity in Vortex Core Precession Stabilisation (Standard = Left, Rod Stabilised = Right)

The increase in upwards axial velocity resulted in a marked reduction in recovery of smaller particles (50.5% recovery of 0.05 micron particles compared to 95.9%) and as such the stabilisation rod was no longer investigated.

Prior to obtaining numerical data, particle tracking by DPM was used to gain an understanding of how and where particles escape through the vortex finder. It was noted that particles that escape through the vortex finder travel the length of the cyclone first, enter the product collection bin and then are pulled back into the cyclone as per Figure 9.5.

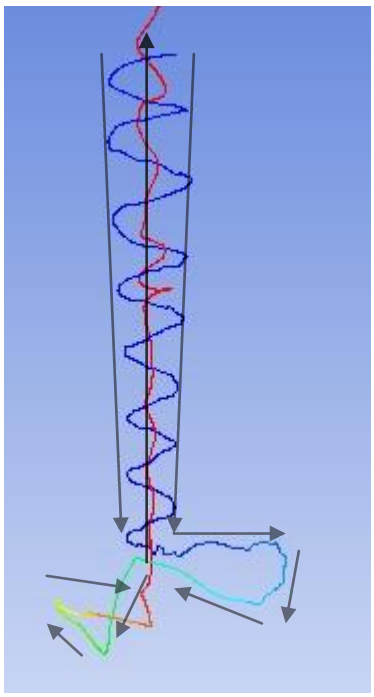

Figure 9.5 0.05 micron Particle Track
(Coloured by Residence Time, Blue = Start, Red = End)

Interestingly, it was also noted that particles travelling up the central core of gas are still subject to centrifugal force. The result of this effect is that in many cases gas solids separation can still take place as a particle travels upwards in the cyclone. In many cases particles are pulled upwards from the bin and then migrate from the central axis towards the wall of the cyclone where they meet the outer section of gas travelling back towards the bin. Examples of this secondary gas solids separation are shown in Figure 9.6.

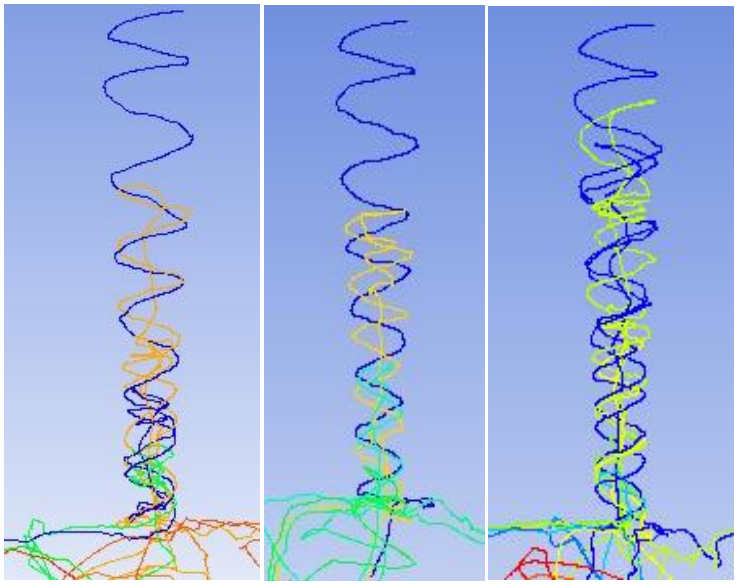

Figure 9.6 0.05 micron Particle Tracks
(Coloured by Residence Time, Blue = Start, Red = End)

9.3.2 Qualitative Observations for Vortex Finder Modification

Modification of the vortex finder diameter and length was shown in the literature review to be the change with the greatest likelihood of increasing yield, and as such this was investigated in detail using CFD. Although modification to the vortex finder resulted in notable differences in collection efficiency, the differences are less notable in comparative contour plots as per Figures 9.7 – 9.10.

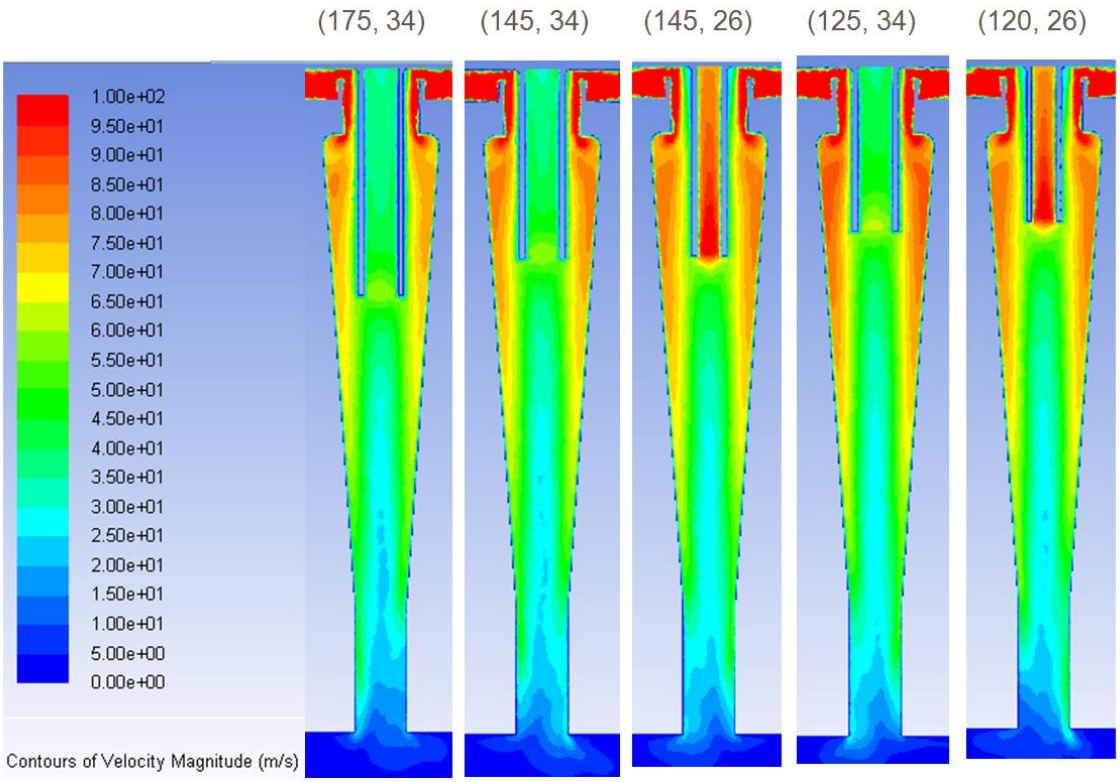

Figure 9.7 Velocity Magnitude Contour Plots (Length, Diameter)

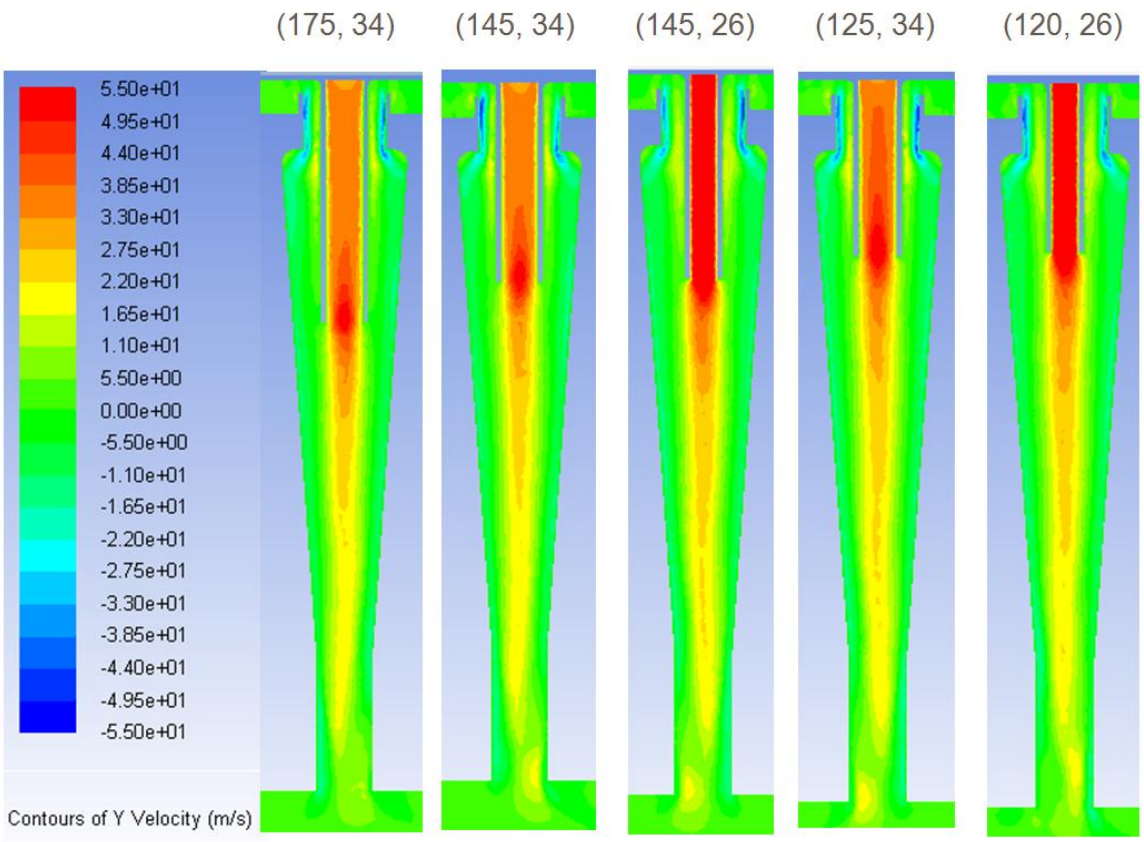

Figure 9.8 Axial Velocity Contour Plots (Length, Diameter)

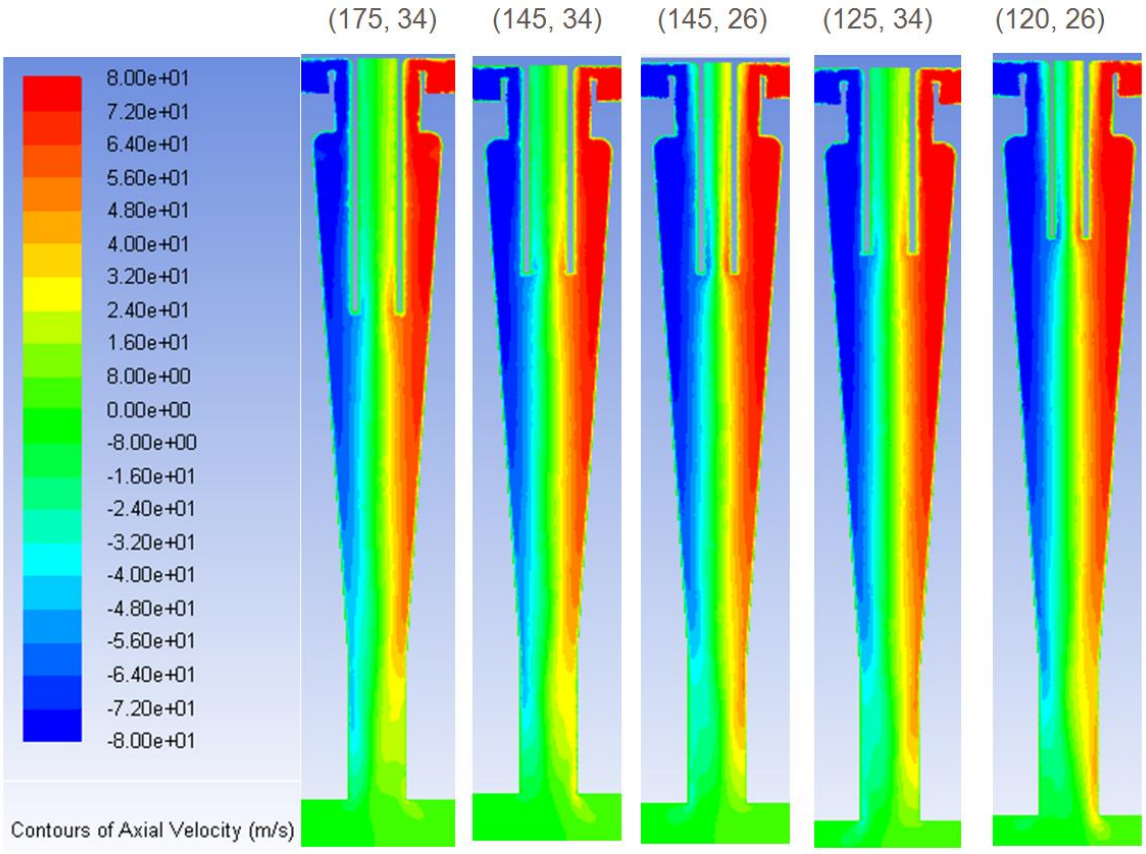

Figure 9.9 Tangential Velocity Contour Plots (Length, Diameter)

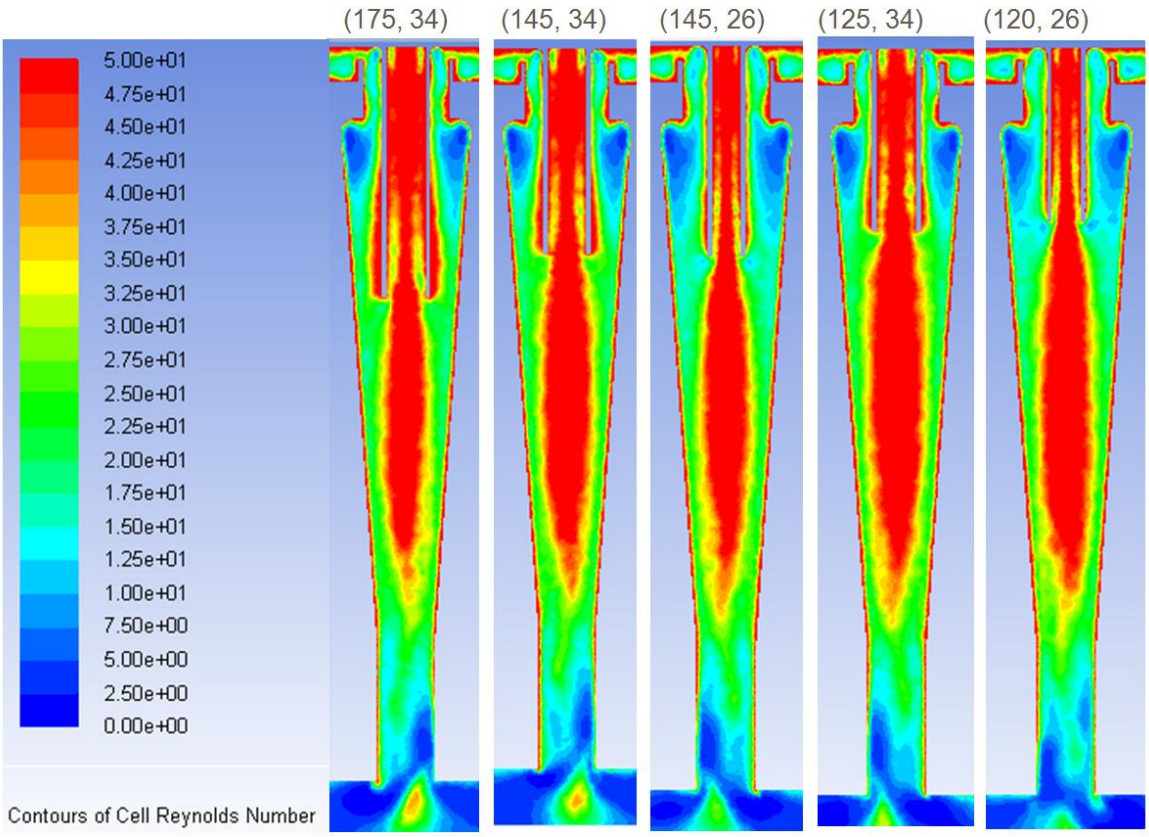

Figure 9.10 Tangential Velocity Contour Plots (Length, Diameter)

The only notable change as per contour plots in Figures 9.7 – 9.10 is that with a reduction in vortex finder length there is an increase in the length of the central core rather than a change in the gas reversal point. Additionally, it can be seen that reduced vortex finder diameters and reduced lengths result in a reduced turbulence around the vortex finder and at the interface between the cyclone and the product collection bin.

9.3.3 Quantitative Observations

To give quantitative data on the collection efficiency, a test particle diameter of 0.05 microns was used. This diameter was used as it was collected at a similar efficiency to the Product A particles. Between 12,500 and 13,600 particles were introduced to the cyclone and tracked using DPM individually, considering no interactions between particles. It was assumed that once a particle comes into contact with the wall of the product collection bin that it is collected as initial simulations without this condition appear unrealistic as with no adhesion force the particles are eventually pulled back out of the bin.

Due to vortex core precession a number of repetitions were required with each geometry to ensure reliability of the data. The geometries trialled, number of repetitions, mean results and percentage standard deviation may be found in Table 9.3. The current dimensions used are 145 mm, 34 mm and 15 mm for the vortex finder length (VFL), diameter (VFD) and classifier height (CH) respectively.

VFL (mm)	VFD (mm)	CH (mm)	Number of Repetitions	Standard Deviation (%)	Yield for Spheres of 0.05 micron Diameter (%)
100	26	15	8	0.21	96.63
120	26	15	9	0.21	96.10
145	26	15	11	0.77	95.11
80	34	15	15	0.23	96.44
90	34	15	9	0.20	96.70
100	34	15	9	0.35	97.35
110	34	15	9	0.77	97.10
120	34	15	13	0.16	96.82
125	34	15	11	0.28	97.05
145	34	15	13	0.52	95.85
155	34	15	6	0.55	93.93
175	34	15	9	0.56	93.92
145	34	10	5	0.20	96.26
145	34	18	5	0.19	95.49
80	38	15	17	0.40	96.96
90	38	15	11	0.17	98.04
100	38	15	11	0.18	97.55
110	38	15	11	0.20	97.55
120	38	15	8	0.23	96.73
135	38	15	6	0.26	96.41
90	42	15	11	0.18	97.71
100	42	15	15	0.16	98.18
110	42	15	10	0.17	97.73
100	45	15	6	0.36	96.55
110	45	15	10	0.13	97.51
100	26	7	12	0.30	96.69
100	34	7	17	0.49	96.94
100	38	7	16	0.24	97.58
145	34	7	11	0.27	96.13

Table 9.3 Yield Data for Varying Geometries

As expected, reduction in vortex finder length results in an increase in yield. An optimal region of 90 – 110 mm can be seen as per Figure 9.11 and as such vortex finder lengths of 90, 100 and 110 mm are investigated experimentally in Chapter

10. The trend line has been plotted on Figure 9.11 to illustrate where the local maximum point for collection efficiency may be.

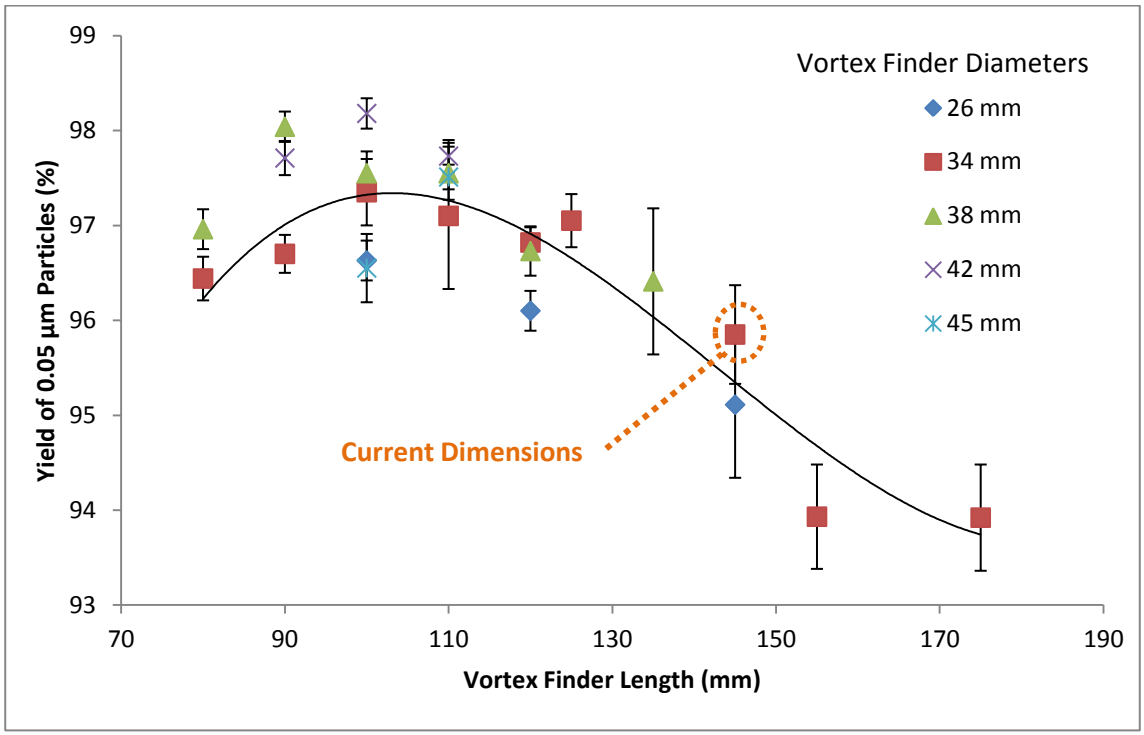

Figure 9.11 Vortex Finder Length against Yield of 0.05 Micron Particles, 15 mm Classifier

Surprisingly however, as can be seen from Figure 9.12, reduction in vortex finder diameter results in a reduction in yield.

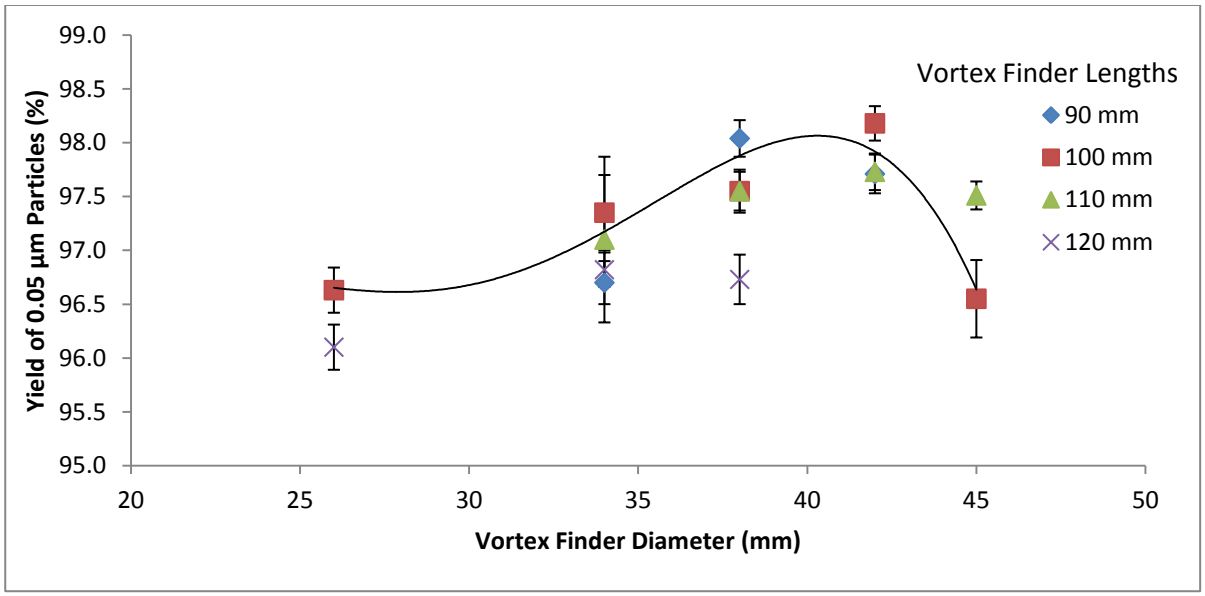

Figure 9.12 Vortex Finder Diameter against Yield of 0.5 Micron Particles, 15 mm Classifier

The results of Figure 9.12 are in direct contradiction to both previously reported experimental and CFD investigations. This may be because the design is significantly different to previously investigated tangential entry cyclones. However, this may also be a result of particles being excluded from the simulation once they hit the wall of the product collection bin. Increasing the vortex finder diameter increases the axial velocity of gas travelling down the cyclone, and increases the particles' axial velocity towards the bottom of the product collection bin. With greater axial velocity towards the bottom of the product collection bin, particles tracked for wider vortex finders may have been more likely to collide with the walls of the bin than those for thinner vortex finders. The unexpected results may therefore be a function of the way in which the DPM investigation was performed, rather than a true reflection of the solids separation process. To test whether this is a true prediction or an artefact of the DPM simulation, vortex finder diameters of 26, 34, 38 and 42 mm are investigated experimentally in Chapter 10.

Modification to the classifier height adjusted the yield of 0.05 micron particles as expected for reduction from 15 mm to 10 mm, and not as expected for further reduction. Reduction in classifier height led to increased recovery of fine particles until a maximum yield at 10 mm, after which point reduction in classifier height led to a reduction in yield as shown in Figure 9.13. Classifier heights of 10, 15 and 18 mm are selected for further experimental investigation in Chapter 10 as it is expected that reduction below 10 mm will be detrimental to PSD and yield.

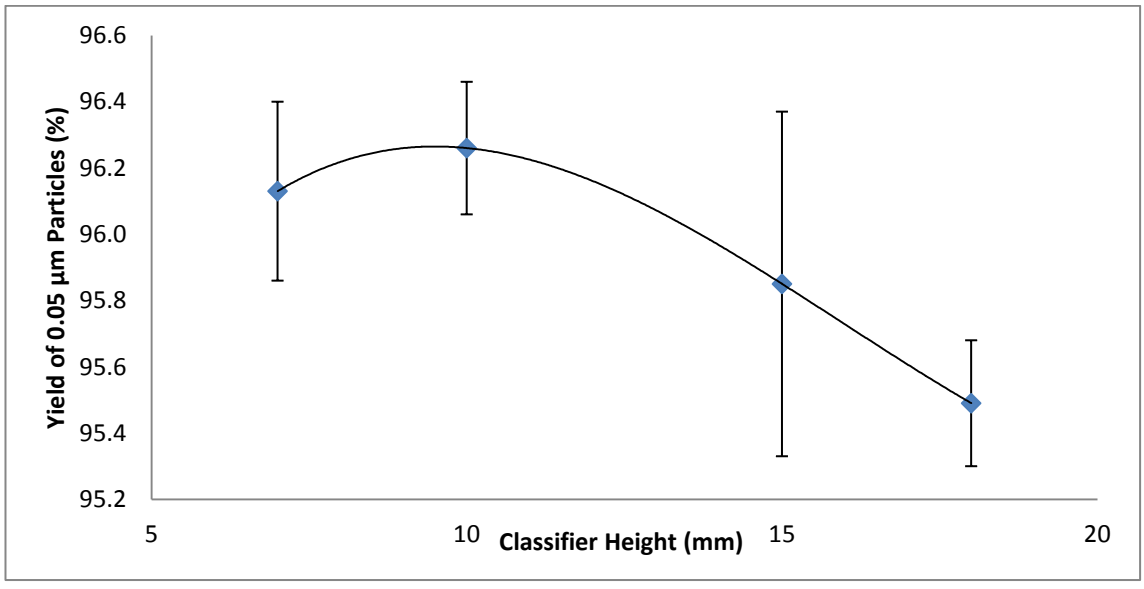

Figure 9.13 Yield of 0.5 Micron Particles, Vortex Finder with 145 mm Length and 34 mm Diameter

To gain some prior understanding of the impact of changing vortex finder dimensions and classifier dimensions on aerodynamic particle classification in the grind chamber, DPM was also performed. To assess changes to aerodynamic particle classification, 2000 particles of 0.3 microns in diameter were released at intervals of 0.01 mm from a 20 mm line crossing the central plane. This particle release line was placed 10 mm away from the classifier as per Figure 9.14.

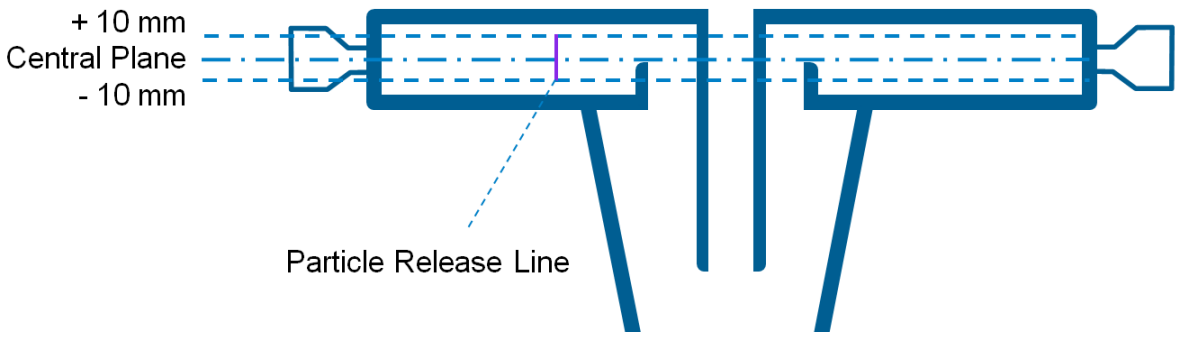

Figure 9.14 Classifier DPM Release Locations (Not to Scale)

The simulation was then allowed to simulate each particle's motion for 100,000 iterations for three separate time points within the simulation, and the number of particles which escape the grind chamber are recorded. The classifier height against percentage of particles escaped is shown in Figure 9.15.

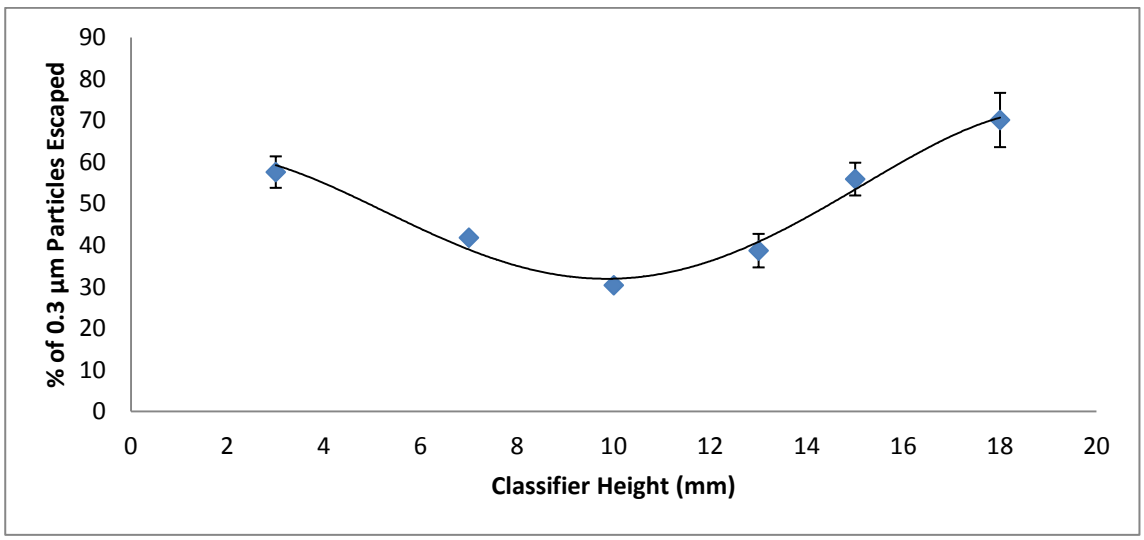

Figure 9.15 Grind Chamber Exit Rate for Varying Classifier Height

As expected from Equation 3.27 and experimental data in Figure 4.4, a reduction in lower classifier height leads to greater fineness and a reduced rate of escape of particles from the grind chamber as per Figure 9.15. However, it is also noted that

reduction in classifier height below 10 mm leads a similar performance to the current classifier height of 15 mm. These results concur with Kozawa *et al.* (2012).

The same simulation technique is then used to assess the impact of changing vortex finder diameter as per Figure 9.16 for a fixed classifier height of 15 mm and vortex finder length of 100 mm.

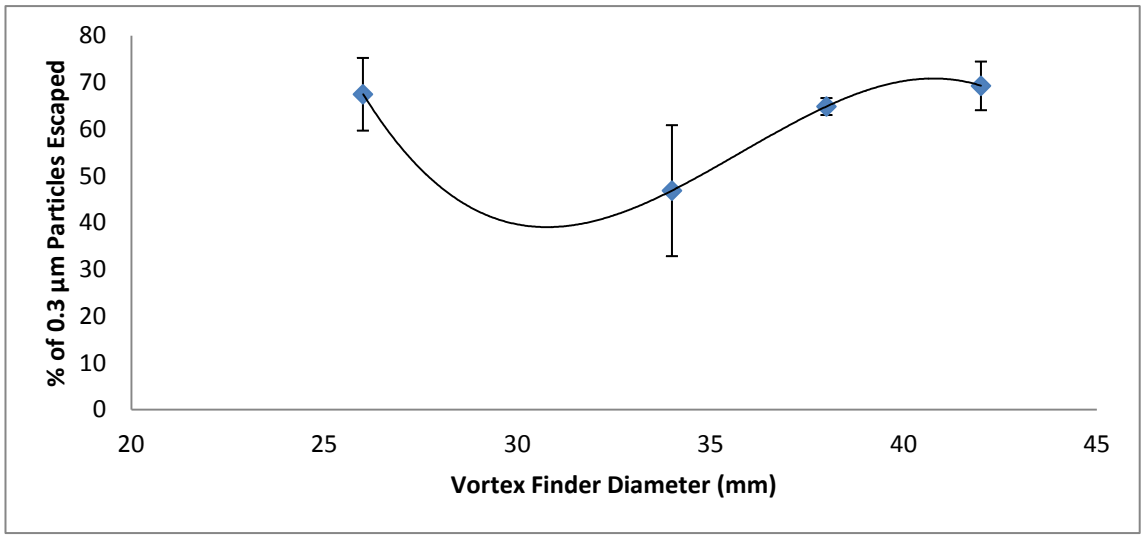

Figure 9.16 Grind Chamber Exit Rate for Varying Vortex Finder Diameter

9.4 Recommendations of CFD Investigation

The CFD investigation has reliably shown that reduction in vortex finder length from 145 mm to 100 mm can lead to significant increases in yield. As such, experimental investigation of the length range 90 – 110 mm is performed in Chapter 10.

In contradiction to academic literature (Moore and McFarland 1993, Lim *et al.* 2004, Raoufi *et al.* 2008, Alves *et al.* 2015), increases in vortex finder diameter lead to increases in yield rather than reduction. The particular cyclone investigated (vaneless axial entry reverse flow) is relatively unique and may have a different response to varying geometry than previously reported academic literature. As such an investigation into increases in vortex finder diameter from 34 mm to 42 mm is performed as this may lead to an increase yield if the CFD simulations are accurate.

Although reduction in vortex finder diameter from 34 mm to 26 mm led to a reduction in yield for a given length, it is still capable of delivering an increase

compared to the base case when coupled with length reduction from 145 mm to 100 mm. Therefore, diameter reduction is also investigated experimentally as it is reported in academic literature to be very successful at delivering yield increases. From Figure 9.9 it can be seen that vortex finder diameter reduction may reduce the turbulence at the bottom of the cyclone, which could lead to a reduction in re-aerosolisation of agglomerates and improve the drop out process. Additionally, the reduction in axial velocity towards the bottom of the cyclone will increase particle residence time and aid the agglomeration process. Unfortunately the CFD-DPM simulations performed in this chapter are not capable of modelling complex particle-particle interactions.

The CFD results for reduction in classifier height confirm theoretical expectations in the 10 mm to 18 mm range, and as such an investigation is performed into reduction in classifier height to increase yield.

The CFD results for modification of aerodynamic particle classification in the grind chamber by classifier height modification match previous CFD analysis, academic literature (Kozawa *et al.* 2012) and experimental evidence with Product A in Figure 4.4.

It is important to note that the CFD analysis of grind chamber dynamics indicate that increases or reduction in vortex finder diameter lead to an increase in the rate of escape of particles from the grind chamber. It may be the case that certain modifications to the cyclone to increase yield may inadvertently also coarsen the output of the spiral jet mill. Due to this effect, the classifier height may need to be reduced to prevent a coarsening of the output material following adjustment to the vortex finder diameter. This may be beneficial in terms of yield optimisation as both are expected to increase yield.

Additionally, due to the interaction between the classifier and vortex finder for both yield and PSD it is recommended to perform a multivariate DOE or full factorial experiment so that interactions can be fully understood.

9.5 Conclusion

CFD has provided several insights into this design optimisation problem:

- It is possible for secondary particle classification to occur in the central core of gas exiting the spiral jet mill.
- An optimal vortex finder length of between 90 mm and 110 mm has been identified for the cyclone geometry.
- It has been confirmed that reduction in classifier height can improve the performance of the cyclone.

Problematically, the results for vortex finder diameter contradict previously reported CFD and experimental data. This may be a result of particles being excluded from the simulation the moment they hit the wall of the product collection bin. Increasing the vortex finder diameter increases the axial velocity of gas travelling down the cyclone, and increases the particles' axial velocity towards the bottom of the product collection bin. With greater axial velocity towards the bottom of the product collection bin, particles tracked for wider vortex finders may have been more likely to collide with the walls of the bin than those for thinner vortex finders. The unexpected results may therefore be a function of the way in which the CFD investigation was performed, rather than a true reflection of the solids separation process. Experimental investigation is detailed in Chapter 10 which tests the predictive capability of the CFD simulations described in this chapter.

Chapter 10. Cyclone and Grind Chamber Design Modification with Product A

10.1 Materials and Methods

To optimise the yield for Product A while maintaining similarity of Particle Size Distribution (PSD), experiments were performed with a number of different geometries as recommended in Chapter 9 and with the current commercial geometry to serve as a control.

A single input batch of Product A was micronised with nitrogen on an industrial 8" spiral jet mill with tangential powder entry and eight grinding nozzles. The feed and grind gas pressures were controlled to a validated set point. The gas mass flow rate was measured by a coriolis flow meter. The screw speed was set for a volumetric feeder and the average solids feed rate was determined by measurement of input mass and the time taken for the feeder to fully discharge. The feed rate of powder was maintained within Product A's validated range. Process data was collected in the same manner as described in Chapter 4.

Powder was collected by a vaneless axial entry reverse flow cyclonic separator that is attached directly below the grind chamber exit. As it was not possible to sample from a moving stream during micronisation with the available equipment, sampling was performed at the end of each 1 kg micronisation run. Four samples were taken for particle size analysis, one of material adhered to the bin collar, one from the top of the bag, one from the bottom and one from multiple locations in the bag following tumbling.

Each 1 g sample was then tumbled prior to taking two smaller 35.0 mg aliquots. Tumbling was performed to minimise the effect of particle size segregation within the sample. Each aliquot was then subject to duplicate particle size analysis with a Malvern Mastersizer 2000 following sonication in a Hydro 2000S sample handling unit as per the method described in Chapter 4.

It is assumed that there is the same particle size measurement repeatability and experimental repeatability as demonstrated in Chapter 4.

10.2 Results

10.2.1 Control Micronisation Qualitative Observations

The current spiral jet mill used for commercial manufacture is constructed of stainless steel, resulting is some powder adhesion and deposition. The patterns of deposition left on the stainless steel are informative of flow patters within the spiral jet mill. It can be seen from Figure 10.1 that the powder deposition patterns correspond to Figure 2.4 and highlight where nozzle jets intersect with the grind chamber.

Figure 10.1 Product A Deposition, Top Plate and Vortex Finder

Additionally, it can be seen that there is a small zone of no deposition behind the grinds nozzles as per Figure 10.2, potentially as a result of the nozzle jet shielding the region of the grind ring behind it from particles circulating around the chamber.

Figure 10.2 Product A Deposition, Grind Ring Nozzle

10.2.2 Optimisation Trials Qualitative Observations

In addition to increasing yield, the optimisation project for Product A involves the introduction of polytetrafluoroethylene (PTFE) surfaces to prevent aggregation that currently takes place on stainless steel surfaces. Parts were fabricated out of PTFE by a precision engineering company (Manufacturer B) for the experimental optimisation trial.

The initial design utilised a PTFE vortex finder, however it was found that this vibrated with the high gas velocities. This meant that a planned Box-Behnken Design of Experiments (DOE) could not be performed, and instead a targeted set of experiments were completed to quickly identify the optimal configuration.

It was also found that less isolator air was drawn into the process for the smallest diameter vortex finder, and due to a fault with the process oxygen analyser this prevented the process from operating at 7.0 barg grind pressure during the initial trial with a PTFE vortex finder.

A subsequent trial with a steel vortex finder, and rescaled oxygen analyser output, allowed the process to run successfully at 7.0 barg grind pressure.

All experiments for the geometry optimisation trial were performed at the validated solids feed rate for Product A.

10.2.3 Quantitative Results

The yield and particle size data obtained for Product A with the current commercial equipment is compared to the optimisation trial in Table 10.1 where

VFD is the vortex finder diameter, VFL is the vortex finder length and CH is the classifier height.

Mill	VFD (mm)	VFL (mm)	CH (mm)	Vortex Finder Material	Grind Pressure (barg, ± 0.1 barg)	Yield (%, ± 0.5%)	Mean x10 (µm, ±1%)	Mean x50 (µm, ±1%)	Mean x90 (µm, ±1%)
A	34	145	15	Steel	7.0	89.3	0.56	1.44	3.35
A	34	145	15	Steel	7.0	89.4	0.55	1.44	3.42
A	34	145	15	Steel	7.0	88.2	0.55	1.45	3.38
A	34	145	15	Steel	7.0	89.0	0.53	1.37	3.29
B	34	145	15	PTFE	7.0	77.9*	0.56	1.41	3.37
B	42	90	18	PTFE	7.0	90.0	0.57	1.56	4.05
B	34	145	10	PTFE	7.0	90.4	0.59	1.57	3.79
B	38	100	15	PTFE	7.0	91.3	0.57	1.57	3.94
B	42	100	10	PTFE	7.0	91.4	0.58	1.58	3.95
B	38	100	15	PTFE	7.0	92.2	0.56	1.50	3.85
B	34	100	10	PTFE	7.0	92.7	0.56	1.45	3.48
B	34	100	18	PTFE	7.0	92.8	0.57	1.58	4.14
B	26	100	10	PTFE	5.0	96.1	0.58	1.53	3.69
B	26	100	15	PTFE	5.0	95.4	0.56	1.62	4.18
B	26	100	18	PTFE	5.0	94.7	0.58	1.75	4.88
B	26	100	15**	PTFE	7.0	95.1	0.57	1.61	3.96
B	26	90	10	Steel	7.0	84.1*	0.56	1.46	3.57
B	26	100	10	Steel	7.0	92.6	0.58	1.56	3.87
B	26	110	10	Steel	7.0	96.9	0.57	1.45	3.49
B	26	100	15**	Steel	7.0	90.2	0.59	1.63	3.99

Table 10.1 Summary of Experimental Results for Geometry Modification

*Low yields obtained due to the initial start up of the mill being aborted due to an aerosolised powder leak.

**Elliptical bottom plate investigated.

Some of the results obtained from the experimental investigation are compared to the results obtained by CFD in Chapter 9 in Figures 10.3 – 10.5. Please note that different scales are used on the *y* axes for the CFD results compared to the experimental results as the data in both charts is not directly comparable. The *x*

axes are however the same, and as can be seen in Figures 10.3 – 10. 5, the locations of local minima and maxima occur at almost identical regions of geometry.

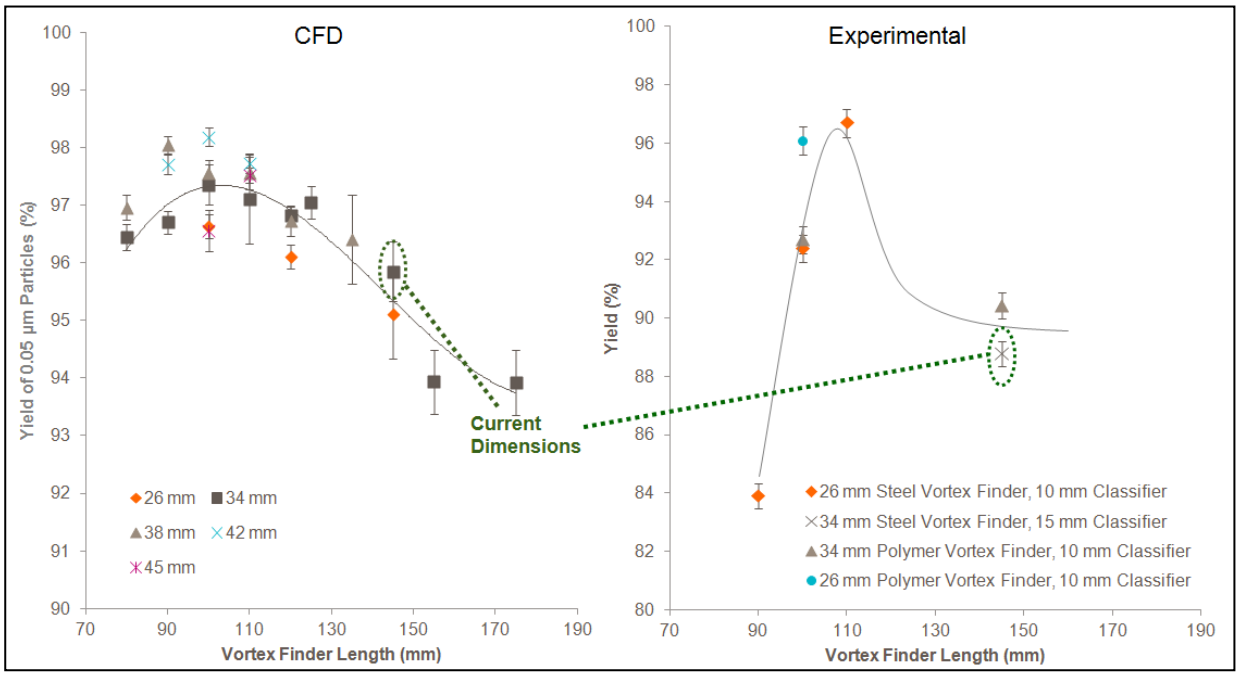

Figure 10.3 CFD and Experimental Vortex Finder Length Data

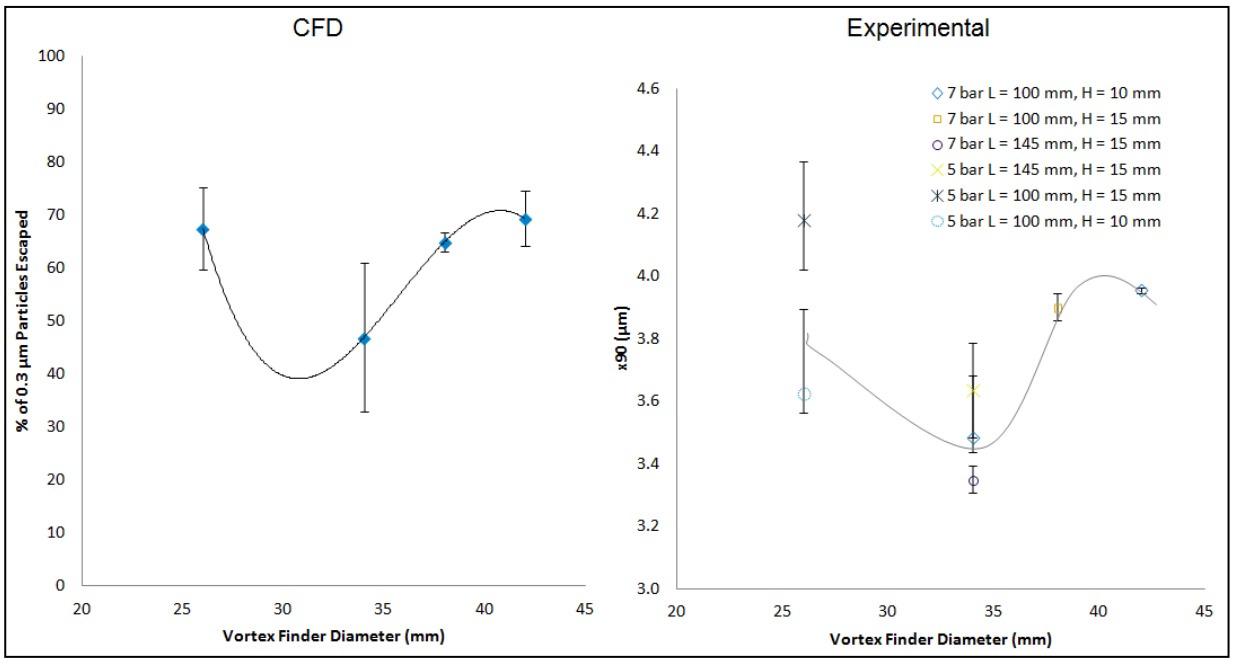

Figure 10.4 CFD and Experimental Vortex Finder Diameter Data

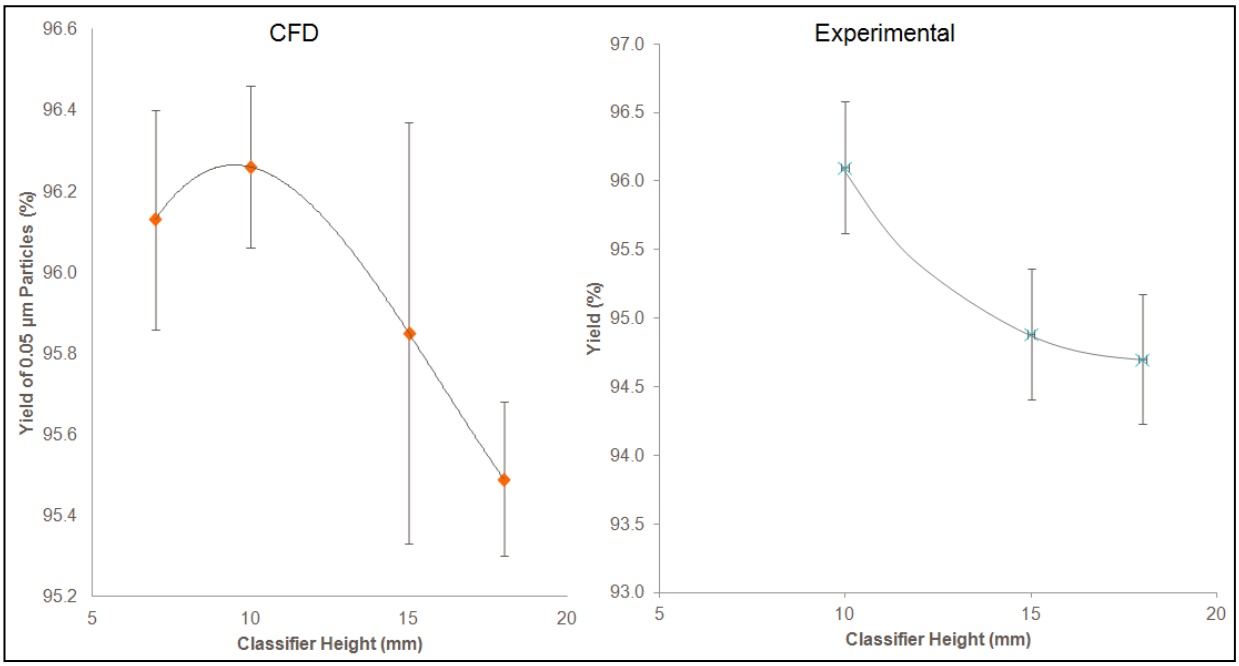

Figure 10.5 CFD and Experimental Classifier Height Data

As can be seen from Figure 10.3, there is a good agreement between the CFD determined optimal vortex finder length and the experimental data. The optimal experimental length for vortex finder could potentially be between 100 and 110 mm or 110 mm and 145 mm, however it is likely to be closer to 110 mm than 145 mm based on the CFD data.

Although the response of yield to vortex finder diameter was not as per CFD prediction, the response of x90 correlates well with CFD data as shown in Figure 10.4. Different scales are used on the *y* axis as accurate estimation of x90 by CFD is not possible, whereas the probability of a particle of a given size escaping the mill is possible. This probability of a particle of 0.3 µm escaping correlates with the grinding limit of Equation 3.27 as it has been determined for the gas only system.

Figure 10.5 also shows again that the simplistic CFD model correlates with experimental observation as the yield increased with classifier height reduction. The error bars appear particularly large for Figure 10.5 as the plotted range is relatively narrow compared to Figure 10.3. As discussed in Chapter 9, there is some variability in the CFD results due to vortex core precession. Due to the high cost of Product A, it was not possible to increase the experimental size beyond 1 kg during experimentation and the combined accuracy of the balance and tare pack led to a 0.005 kg uncertainty in the measurement.

The response of x90 to modification of the classifier height was also as per the prediction of the cut size equation as shown in Figure 10.6 (Featured in Chapter 4 as Figure 4.6).

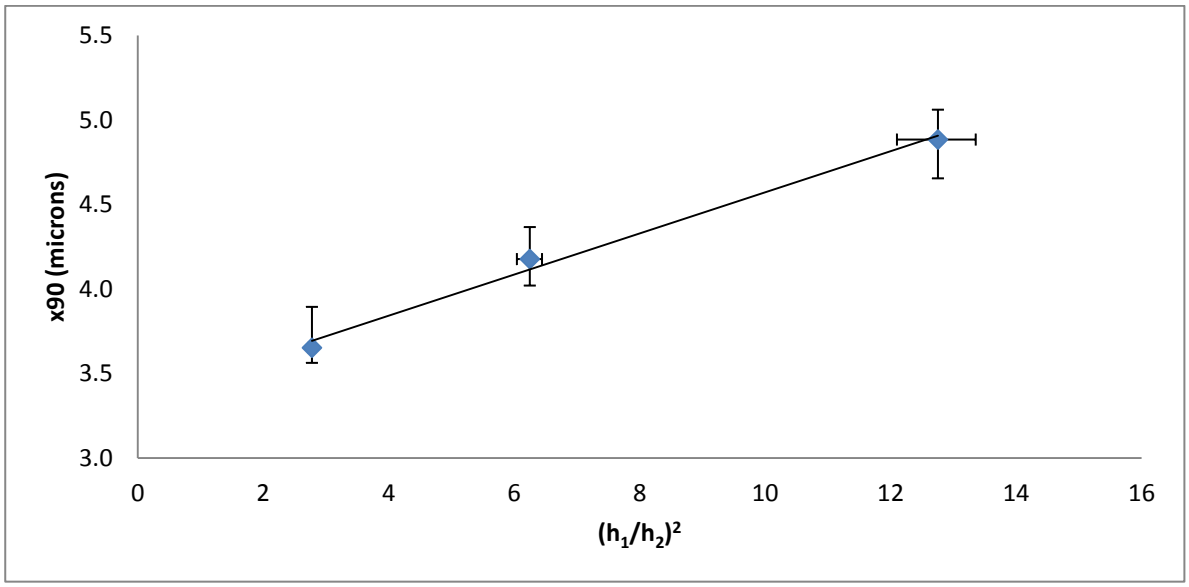

Figure 10.6 $(h_1/h_2)^2$ against x90 for Product A (MacDonald *et al.* 2016)

The PSD of the highest yield geometry at 7 bar grind pressure compared to the control batch at 7 bar grind pressure may be found in Figure 10.7 and Table 10.2. Although there is a slight discrepancy in PSD, it is within acceptable limits. Crucially, the comparative PSD shows no increase in fine particles despite a significant increase in yield.

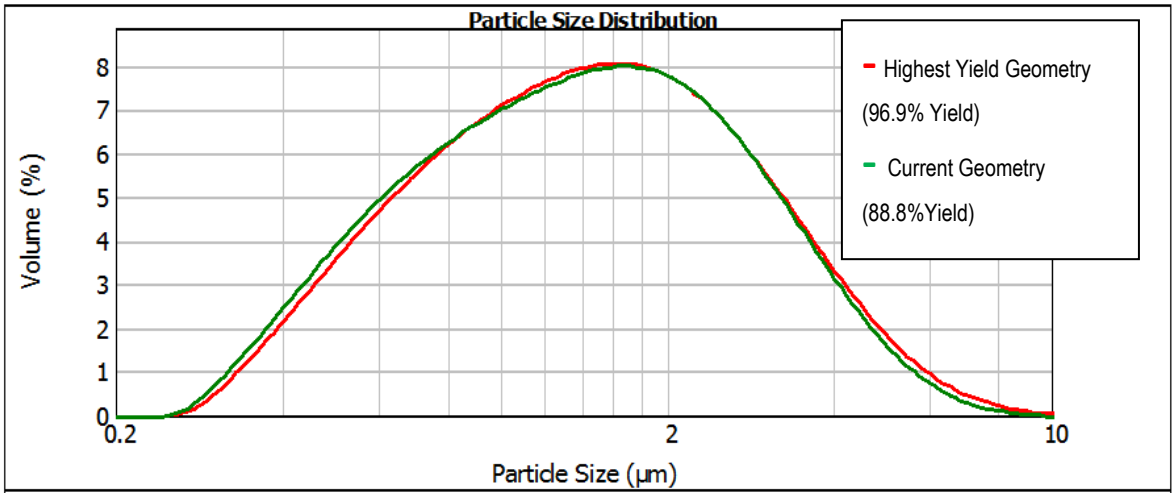

Figure 10.7 Comparative Frequency PSD for Control and Optimised Mill

Spiral Jet Mill	Mean x10 (µm, ±1%)	Mean x50 (µm, ±1%)	Mean x90 (µm, ±1%)	SSA($m^2.g^{-1}$, ±0.05 $m^2.g^{-1}$)
Current	0.55	1.41	3.36	13.9
Highest Yield Modified Design	0.57	1.45	3.49	13.7

Table 10.2 Comparative PSD and SSA for Control and Optimised Mill

Figure 10.8 plots the collection efficiency data for the current geometry (old design) and highest yield modified design (new design).

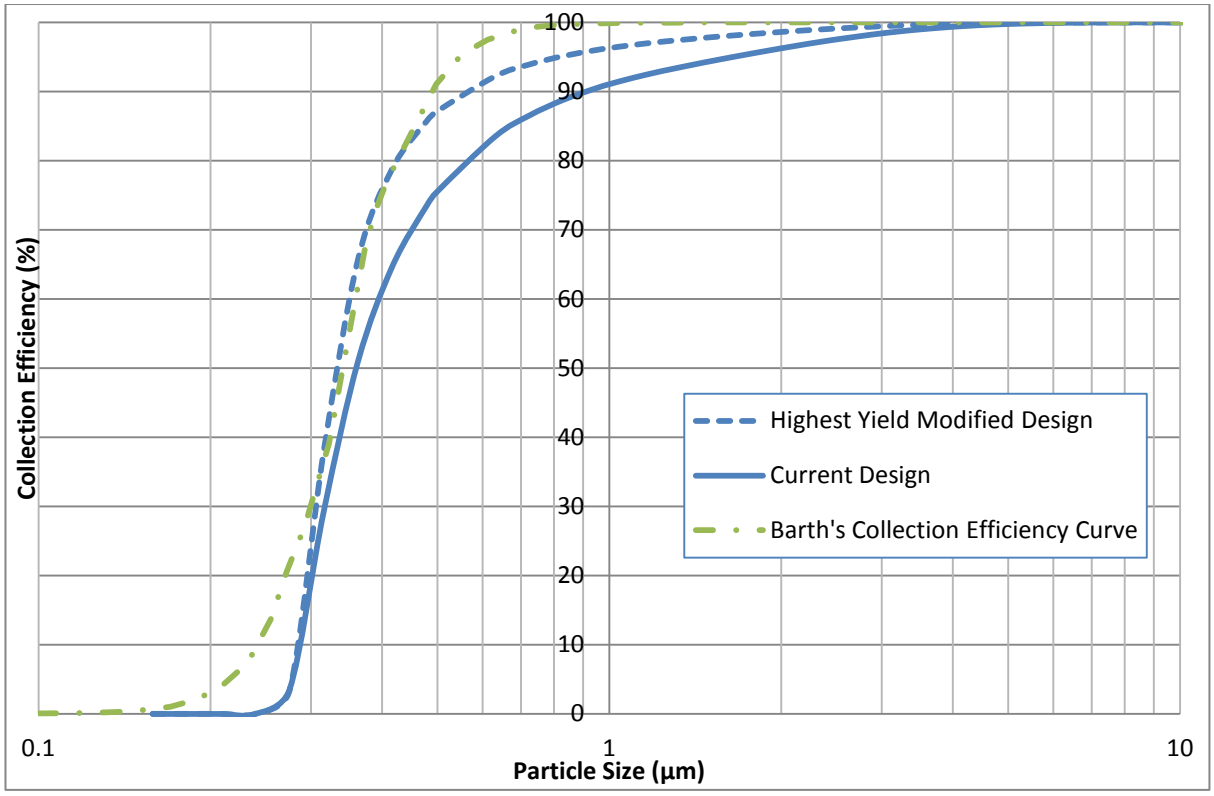

Figure 10.8 Comparative Collection Efficiency Data

The modified vortex finder provides a much sharper separation of very fine particles and micronised Product A. As there has not been an increase in the number of very fine particles collected as product, the increase in yield may be a result of a change to the agglomeration process within the cyclone.

The clear difference in performance of the two cyclones can be seen by the comparative frequency PSD of the filter fines collected with the optimised geometry and current geometry as shown in Figure 10.9. No particles greater than 3 µm are present in the filter fines for the modified geometry, the second population of particles greater than a micron in diameter is reduced and the

primary population of particles less than 0.5 microns in diameter is increased. The shift in the PSD of the filter fines suggests that some change has occurred to the cut off point of the cyclone.

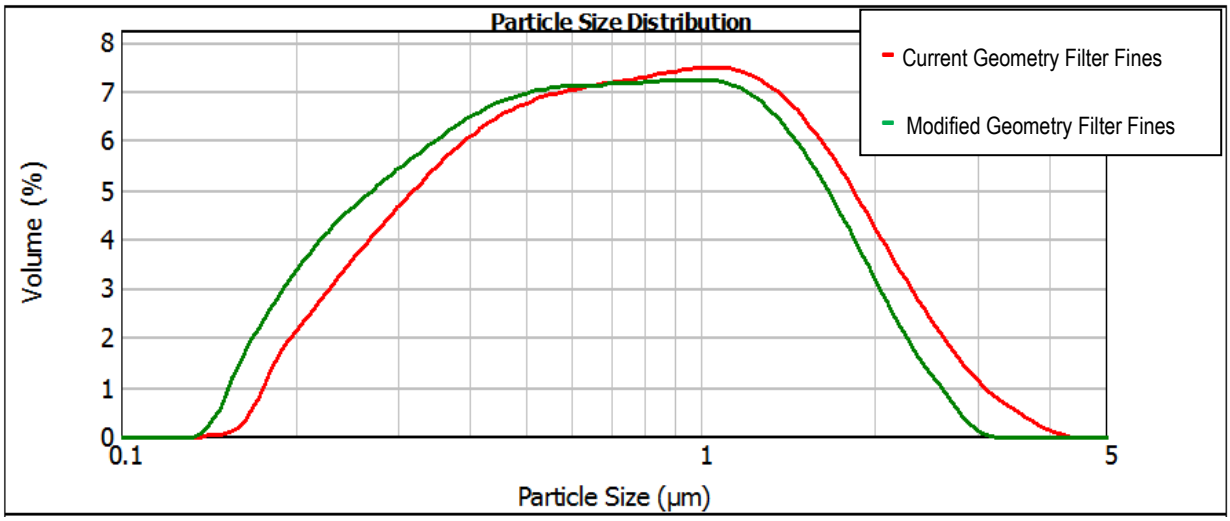

Figure 10.9 Comparative Frequency PSD of Filter Fines

10.3 Discussion

Despite the CFD-DPM data for changes in vortex finder diameter being incorrect, all other data was concordant with experimental data despite the simplistic and basic nature of the simulations. The incorrect yield data for changes in vortex finder diameter may have been a result of the way in which the DPM was performed rather than the actual gas flow data being incorrect. The DPM simulations defined a particle as collected after having come into contact with a surface of the product collection bin, and increasing the vortex finder diameter may have increased the axial velocity towards the bin and increased the number of particles collected in a way that is not representative of the actual collection process.

The similarity between experimental results and CFD for all other aspects demonstrates that very simplistic CFD simulations can still be value adding, particularly when used as a tool to suggest regions of geometry for further experimental investigation rather than a surrogate for experimentation itself.

The experimental data has shown that a significant yield increase is possible while maintaining the PSD within commercial knowledge space. The new design has met

its acceptance criteria and is in the process of implementation at GSK for Product A and is under investigation for other APIs with low cyclonic separation yields.

10.4 Conclusion

It is recommended that CFD-DPM screening of bottom discharge spiral jet mills be performed to optimise their performance with respect to both yield and particle size. As demonstrated for Product A, significant yield increases are possible, and as such the bottom discharge spiral jet mill should be considered for large scale micronisation. A large scale bottom discharge system could have a reduced capital cost compared to top discharge as less equipment is required, and there may be a lower operating cost as there are fewer parts to maintain and fewer surfaces to clean.

Chapter 11. Critical Analysis and Further Work

11.1 Limitations of the Cut Size Equation

11.1.1 Grind Chamber Starvation

The cut size equation does not apply to when the spiral jet mill is starved of powder. As shown in Figure 2.5, for low solids feed rates the powder grinding process is less effective such that increases in solids feed rate result in a finer output material. Due to the assumptions made in the cut size equation regarding b and D, it only describes behaviour after the starving condition where increases in solids feed rate for a constant gas mass flow rate always result in an increase in hold up and an increase in cut size. Although Equation 3.27 provided a reasonable approximation to the behaviour of Product F in Chapter 6, it was micronised under starved conditions such that increases in solids feed rate actually led to a slight reduction in particle size. The starving condition and the observed discrepancy between actual behaviour and predictions of the cut size equation is likely to be for one of the following two following reasons:

1) The collision energy between large primary particles may be considerably higher than the collision energy between small collision fragments as a result of their larger mass and momentum allowing them to retain their velocity against fluid forces. Therefore, the mass fraction of collision fragments below the cut size, b, may change depending on the PSD of particles colliding. For a low solids feed rate with a low collision rate, small collision fragments above the cut size may be generated and not further reduced in size. This situation will lead to an accumulation of small particles which are difficult to micronise (low b value due to their low momentum for a given velocity) but too large to escape the mill. This hold up of small particles will continue to increase until a steady state condition is reached where the output rate of micronised particles below the cut size equals the solids feed rate. This increase in hold up of smaller particles results in a coarsened cut size and output material. Increases in solids feed rate from the starved state will then result in more collisions between primary particles and the overall b value increasing, allowing the rate of generation

of particles below the cut size to increase, the hold up to reduce and the corresponding cut size to reduce.

2) Particles slightly greater than the cut size may be able to escape the grind chamber when given enough time. For low solids feed rates and low rates of collisions, collision fragments above the cut size are able to escape the grind chamber as the probability of escaping the grind chamber is greater than the probability of a successful collision and further size reduction. Increases in solids feed rate beyond this point result in an increase in the probability of successful collision and an increase in the rate of generation of particles below the cut size, such that the comparative rate of escape of particles above the cut size reduces and the overall PSD of the output material becomes finer.

As the starving condition is known to occur at different solids feed rates and gas mass flow rates for different materials, it would be recommended to determine the region of the operating space at small scale where starving behaviour is seen. If required, an empirical correlation to adjust b for low feed rates could be determined for a given material. However, it would be recommended to simply ensure that the spiral jet mill does not operate in this region as it is undesirable from an efficiency perspective.

11.1.2 Grind Chamber Flooding

The cut size equation is also incapable of predicting performance at the other extreme of solids concentration; flooding. Beyond a critical solids feed rate the spiral jet mill will not be able to generate enough particles below the cut size to allow the output rate to equal the solids feed rate. This will lead to an excessive accumulation of hold up until either the gas circulation collapses permitting large input particles to escape or a blockage occurs that prevents further solids entry to the grind chamber. It would be recommended to investigate at small scale the solids concentration required for flooding of the grind chamber so that it can be avoided at increased scale.

11.1.3 Reynolds Length Scale

One key assumption of the cut size equation is that the changes in cut size resulting from changing micronisation settings are small enough that changes in particle

diameter (Reynolds length scale) have a negligible impact on the drag coefficient. Assuming the Reynolds length as constant was necessary to develop an analytical solution and easy to use equation for modelling of the response of cut size to micronisation parameters. Although it appears from the datasets in Chapter 4 and Chapter 6 that this is a valid assumption, further investigation may be required. It is recommended to assess using an iterative solver for the cut size equation where the Reynolds length scale varies with cut size.

11.1.4 Mass Fraction of Collision Fragments below the Cut Size

Another key assumption of the cut size equation is that the changes in cut size resulting from changing micronisation settings are small enough that the mass fraction of collision fragments below the cut size does not vary significantly with cut size. It is known that the mass fraction of collision fragments below the cut size will, by its own definition, vary with cut size. Similarly to the Reynolds length scale, for the sake of an analytical solution it was necessary to assume this to be constant, and again from the datasets in Chapter 4 and Chapter 6 this is likely to be a valid assumption. Solving this iteratively may prove more problematic than variation in Reynolds length scale, as the response of mass fraction of collision fragments below the cut size to variation in cut size will depend greatly on the material breakage properties and therefore each material may require a different mathematical expression.

11.1.5 Variation in Spin Ratio

As shown by CFD in Chapter 5, the spin ratio does change with classifier Mach number and can only be assumed constant across a range of values. Although it was shown in Chapter 5 that the variation in spin ratio is relatively small, this can still have an impact on the cut size. CFD could be used to obtain a relationship for the response of spin ratio to classifier Mach number, and allow the cut size equation to be modified accordingly if necessary. Again, as before, the datasets in Chapter 4 and Chapter 6 do suggest that the assumption of constant spin ratio is valid for the ranges of gas mass flow rate investigated. The assumption may also be valid as the effect of solids hold up on spin ratio may completely outweigh any effect of classifier Mach number.

11.1.6 Grind Chamber Geometry

Despite the cut size equation having utility for predicting variation in particle size with classifier geometry, it offers almost no predictive capability for changes in nozzle angle, number, diameter and separation distance for a given mass flow rate and solids feed rate. Although the cut size equation does not offer predictive data for changing some aspects of grind chamber geometry, analysis of milling data allows the new mill specific constants to be determined and for the impact on performance to be understood. Experimentation with a cheaper surrogate material can be used to determine mill specific parameters.

11.1.7 Input Material Physical Properties

The cut size equation on its own cannot predict changes in particle size for known changes in input material physical properties, and therefore some experimentation at small scale is required to determine any changes to material specific constants. There is some uncertainty as to how applicable the small scale determined x_2 value will be at industrial scale.

In the case of Product B, the small scale determined x_2 appeared to work across scales and spiral jet mill designs. However, in the case of Product C, the x_2 value was radically different for the Manufacturer C mill compared to the Manufacturer A and Manufacturer D mills. This difference for Product C may be a result of it being more sensitive than Product B to changes in collision energy, but could equally be a result of a manufacturing deviation at the third party micronisation facility. Predicting variation in x_2 for materials of varying collision energy sensitivity is likely to be complicated, and could make scale up challenging. Maintaining similarity of nozzle angle, diameter and separation distance across scales to maintain similarity of collision dynamics may allow x_2 to be assumed constant for a given material during scale up.

For variability in physical properties of a given input material, there may be variability in output particle size following micronisation with a spiral jet mill. This is particularly clear for some of the industrial data in Chapter 5 for products D, E and F where notable variability in particle size for a fixed solids feed rate and gas mass flow rate can be seen as the data was gathered during stretching of input material physical properties. Changes to the crystalline form such that its

mechanical properties change (Young's modulus, yield strength, hardness, fracture toughness *etc.*) are likely to result in notable differences in performance, whereas changes in input material particle size are unlikely to result in large changes in output particle size (Ramanujam *et al.* 1969, Katz and Kalman 2007).

It could be possible during stretching of crystallisation in early API development to correlate physical properties as measured following crystallisation to the material specific parameters x_2 and C_1. This could allow the milling parameters at industrial scale to be adjusted for each input batch so as to minimise variability in output material.

11.1.8 Gas and Powder Slip

The cut size equation assumes a no slip condition between the powder and gas in the tangential component of velocity. For particularly high solids concentrations at the periphery of the grind chamber, some slip could occur. Slip between the hold up and the gas responsible for particle classification could actually lead to apparent increases in efficiency as the gas kinetic energy would not be wasted on maintaining un-micronised particles in high speed circulation. In the event of slip occurring, notable deviation from predicted behaviour would be likely to occur.

11.2 Recommendations for Further Investigation into Spiral Jet Mill Scale up and Optimisation

11.2.1 Classifier Radius and Height

The cut size equation (Equation 3.27) focuses on the classification process, and as such it would be recommended to further test the robustness of the equation by varying the classifier radius and height. Reduction in classifier radius would be expected to increase the centrifugal force and could result in cut size reduction if the increase is in centrifugal force is greater than the corresponding increase in radial velocity associated with reduced area for flow. Some of the data in Table 6.1 appears to support this as reduced scale, and subsequent reduction in r appears to result in lower values of C_2.

If scale up/down experiments were performed for several materials on different spiral jet mills of similar geometry but varying scale, it would be possible to determine whether C_2 varies as expected with r or not. Furthermore, it would also

be a means of verifying that C_1 may be used as a material specific constant as predicted by its definition.

A simple investigation into variation in milling constants with scale for several materials would be a valuable test of Equation 3.27 and the scale up approach detailed in Chapter 6.

11.2.2 Collision Angle, Nozzle Separation Distance, Grind Chamber Shape and Scale Up

As it is expected that the mass transport properties to the grind nozzles (D), the mass fraction of collision fragments below the cut size (b) and the spin ratio (k_3) will all vary with grind chamber geometry, it is recommended to perform a detailed experimental investigation to determine how they vary with geometry and scale.

Such an investigation would have two primary goals:

1) Demonstration that by maintaining similarity of some geometry features across scale it is possible to assume that D, b and k_3 will remain constant with scale up.
2) Geometry optimisation to maximise all three parameters and reduce energy consumption.

Such an investigation would require looking at the following key geometrical parameters:

a) Nozzle angle (collision angle)
b) Nozzle separation distance
c) Nozzle diameter
d) Number of Nozzles
e) Scale (grind chamber diameter)
f) Grind chamber shape (chamfered edges, standard cylinder, asymmetric elliptical)

It is expected that, by maintaining similarity of both collision angle and nozzle separation distance across scales, it will be possible to maintain similarity of the grinding parameter b. It would also be expected that by maintaining similarity of

grind chamber shape and a similar ratio of grind chamber volume to nozzle intersection volume, the parameter D should remain constant with scale.

Changes in nozzle angle to increase the momentum exchanged during collisions would be likely to optimise the parameter b and increase the mass fraction of collision fragments below the cut size. However, changing the angle to be further from tangential and towards the centre of the mill would be likely to have a negative impact on the spin ratio and subsequent classification performance of the spiral jet mill. Previous optimisation exercises have found a 45º angle to be the most efficient (Katz and Kalman 2007).

The nozzle separation distance has not been investigated but would also be likely to impact the collision energy and parameter b. It is expected that there will be an optimal separation distance for maximal collision energy. If the nozzles are too far apart, fine particles will decelerate on exit from the nozzle jets prior to collision with other fine particles in the next jet. If the nozzles are too close together the particles may not have enough time to accelerate prior to collision. Additionally, if the nozzles are too close together the full length of the nozzle jet will not be available for accepting particles and accelerating them for collisions, resulting in a reduction to the parameter D.

Changes in grind chamber shape to aid mass transport to the grind nozzles would be likely to increase the parameter D and result in increases in energy efficiency.

11.2.3 Experimentally Determined Breakage Parameter

It is recommended to assess the use of a Scirocco and Malvern Mastersizer 2000 (Bondakar *et al.* 2016) to determine $\alpha H/K_c^2$ and whether this can be correlated to b, the mass fraction of collision fragments below the cut size. If some assumptions can be made about the particle shape, this could lead to a predictive model for spiral jet mill performance at any scale based on experimentation with several grams of powder or less.

11.2.4 Grinding Limit Determination with CFD

As the grinding limit is by definition the cut size for zero hold up, it should be possible for it to be determined by CFD alone. Additionally, CFD combined with DPM should be capable of determining more detailed information than just the cut

size. It should be possible to release a population of particles of varying size and determine the probability of them escaping the grind chamber within a given time period. Such information could allow for optimisation of classification performance.

The previously recommended scale up approach in Chapter 6 involved using a surrogate material to determine the mill specific constants at increased scale. With CFD-DPM it should be possible to verify and optimise a model at small scale with a given high value material, such that the mill specific parameters and variation in grinding limit with gas mass flow rate can be reliably predicted with CFD. By maintaining similarity of collision angle and nozzle separation distance (which could also be investigated with CFD-DPM) it may be possible to assume that x_2 will remain constant with increasing scale. CFD-DPM could then be used to determine the mill specific parameters and variation in grinding limit with gas mass flow rate at increased scale. This approach could allow the cut size equation to be used without the need for a surrogate material.

With CFD-DPM it would also be possible to perform a detailed optimisation of the grind chamber and classifier shape to maximise the collision rate, collision energy and spin ratio. A similar optimisation to that of Elsayed and Lacor (2010, 2013a) could be performed by using computer aided optimisation techniques.

11.3 Spiral Jet Mill CFD-DEM

The end goal of academic study of the spiral jet mill is to allow industry to improve efficiency, scale up processes and ensure product critical needs are met such as narrow PSD and low amorphous content. With increasing computational capability it will be possible to numerically simulate spiral jet milling in 3-D with CFD-DEM. This will allow a greater understanding of the interaction between particle breakage and classification to be developed. This could lead to precise optimisation of the grind chamber shape and nozzle arrangement to meet specific needs whether it be maximal efficiency, precise aerodynamic particle classification or gentler collisions for easily friable materials. Performing accurate simulations however requires accurate models and data. Advances in characterisation of powders with nano-indentation (Zügner *et al.* 2006) should make it possible for future CFD-DEM simulation of pharmaceutical powders.

With current computational capabilities, 3-D CFD-DEM simulations can only be performed if fine particles are immediately excluded from the simulation upon creation (Brosh *et al.* 2014). This can allow hold up and its impact on gas velocity to be approximated, but cannot accurately simulate output PSD as it will simply be a reflection of the predefined exclusion size. It is proposed that the gas tangential and radial velocity profile from a CFD-DEM simulation could be used to determine a variable exclusion size for the simulation, such that it will adjust depending on the level of hold up in the grind chamber. This type of simulation would allow the interaction between particle breakage rate, hold up and particle classification to be simulated to estimate cut size for a given powder feed rate, powder properties, gas flow rate, gas physical properties and spiral jet mill geometry. This proposed mechanistic model could allow scale up and process optimisation of the spiral jet mill with current computational capabilities.

The power of the cut size equation (Equation 3.27) is that is allows difficult to measure mechanical properties to be summarised in one single constant based on experimental data for a given material. The equation lends itself to fitting to experimental data, and once these constants are determined at small scale it is expected they could then be applied at large scale. Given how challenging finding reliable mechanical properties for CFD-DEM simulations can be, it would be recommended to take a similar approach to CFD-DEM as that used for the cut size equation. A CFD-DEM model could be created for a given small scale geometry across a range of gas mass flow rates and solids feed rates, and then the input material mechanical properties could be fitted and adjusted until the simulation data provides an accurate reflection of experimental data. With knowledge of the mechanical properties of the material as required for CFD-DEM simulation, it would then be possible to either model scale up or perform computer aided optimisation on the design to precisely tailor the PSD as per industrial requirements.

Furthermore, if CFD-DEM could be used to also simulate agglomeration properties of a given material, steps could be taken to minimise deposition of material within the spiral jet mill and ensure that during product collection the particles form loose agglomerates rather than tightly bound aggregates.

11.4 Limitations of Cyclonic Separation Optimisation

11.4.1 Limitations of CFD

Due to the expected discrepancy between CFD of a gas only system to experimental results with a complicated gas and powder system, the CFD simulations were purposefully simple. Although simplified, the CFD simulations were able to identify the optimal classifier height and vortex finder length with respect to yield.

The CFD simulations performed were limited in their accuracy, particularly for the predictions of changing vortex finder diameter for the following reasons:

1) The gas density was treated as a constant.
2) Only gas flow was investigated for the combined spiral jet mill and cyclone, meaning that tangential velocities will be much higher for the CFD simulations than in reality.
3) Only particles of a single size (0.05 μm) were tracked.
4) Particles were excluded from the simulation following contact with the product collection bin wall.
5) Particle agglomeration and the drop out process could not be modelled as only single particle tracking was performed.
6) Not enough geometries were trialled.
7) The optimisation was a manual iterative process, and not a computer aided optimisation.

The limitations of the CFD simulation in Chapter 9, particularly the means by which particles were removed following impact with the product collection bin wall, were apparent following experimentation in Chapter 10. The experimental data matched academic literature (Moore and McFarland 1993, Lim *et al.* 2004, Raoufi *et al.* 2008, Alves *et al.* 2015), further confirming that the CFD study was incorrect with respect to its predictions for variation in vortex finder diameter. It must also be noted however, that in all other cases the CFD predictions were accurate and this contributed to the development of an optimised design.

11.4.2 Limitations of Experimental Study

The experimental study was limited in terms of the number of experiments performed and the number of geometries trialled. It was intended to perform a structured DOE to gather information on the interaction between the parameters

and then select the optimal geometry configuration based on the optimal point on a response surface. Unfortunately design and material constraints forced the study to be manually iterative; however this led to a faster optimisation as the interactions between the cyclone and mill were less complex than expected. Although the true optimum geometry may be several millimetres away from the selected geometry, further optimisation will not be performed as the current design has met its requirements in terms of yield or PSD.

The optimised geometry has also only been shown to work for just one product. If another low yield product, such as Product E or Product F, were to be micronised with the optimised geometry found in Chapter 10, there is a possibility that there would not be equivalence of PSD or that the yield increase would not be maximised without further optimisation for those particular products. Differences in performance could occur for different materials due to either particle shape and/or true density impacting aerodynamic behaviour in the cyclone, cohesion characteristics changing the level of agglomeration or material specific breakage properties changing the circulation rate in the grind chamber and cyclone.

Furthermore, only PSD and SSA have so far been analysed in the equivalence study between the current geometry and the optimised geometry for Product A. As the difference in yield may be due to differences in particle shape, the larger particles that are no longer exiting the cyclone through the vortex finder and are now collected as product could actually be significantly less spherical. Changes to particle shape are particularly important to identify, as the material recovered from the filter and now collected as product could behave very differently in respiratory formulations if they have a low sphericity and behave aerodynamically as small particles. Additionally, other attributes such as surface energy or amorphous content could change with an increase in recovery of particles that had historically been removed by the cyclone.

The optimised geometry for Product A is being progressed for implementation within GSK. An equivalency study is being performed looking at the stability of PSD, SSA and surface energy as per GSK change control processes. If the material meets stringent acceptance criteria it will still likely require development formulation assessments to confirm that the aerodynamic particle size distribution of Product A in the respiratory formulation is unchanged.

11.5 Recommendations for Further Work on Cyclone Optimisation

The process itself to improve cyclone design was a manual iterative process, rather than a systematic optimisation. The CFD optimisation could have benefitted from automation in a similar manner to Elsayed and Lacor (2010) whereby an optimisation algorithm such as that of the Nelder-Mead method could be used to find the local maxima. The experimental work could have then benefitted from the utilisation of a response surface model to identify the combination of vortex finder and classifier that give the highest yield while within an acceptable range for PSD.

Chapter 12. Conclusion and Summary of Contributions to Industry and Academia

12.1 Cut Size Equation

Although simplistic and based on assumptions only known to be true for a particular window of operation, the derivation of the cut size equation brings a significant advancement to the understanding of the spiral jet mill. It provides a reliable explanation for the observed response of cut size to changes in solids feed rate, gas mass flow rate, mill geometry, gas physical properties and material properties. Although the equation cannot be used in its raw form, and requires empirical determination of constants, some of these constants may be scale independent. Although not yet demonstrated, this has the potential to lead to cost savings when scaling up the micronisation of high value materials.

For the academic community, the cut size equation (MacDonald *et al.*, 2016), provides a novel insight into the interactions between grinding and aerodynamic particle classification in a spiral jet mill. It provides a worthwhile demonstration that in an age of numerical simulation and Multivariate Analysis (MVA), there is still a time and place for first principles derivations and classical approaches to process modelling.

The cut size equation is more than just a tool for scale up, it can be the basis for targeted optimisation with respect to energy efficiency. Fine grinding is particularly energy intensive, and as such any change which can reduce the specific energy required to attain a given particle size could result in significant energy savings. By publishing the derivation, the wider academic and industrial community should benefit, and eventually energy reductions may be made globally through the development and eventual spread of higher efficiency spiral jet mills.

Crucially, the cut size equation has addressed the industrial problem statement of "lack of mechanistic process understanding".

12.2 Optimised Bottom Discharge Spiral Jet Mill

The CFD-DPM optimisation and subsequent experimental investigation into the bottom discharge spiral jet mill is an industry and academia first, and similarly to

the cut size equation is a valid demonstration that simple techniques can work well. Although there may have been discrepancies between the predicted and experimental data due to the simplistic nature of the model, it still provided enough information for a highly targeted and successful experimental optimisation with a conservative quantity of API.

Optimisation of the bottom discharge spiral jet mill has met an industry need, addressed the problem statement of "low cyclonic separation yield", and will eventually deliver financial benefits to GSK when implemented across its portfolio.

With regards to energy efficiency, the energy required to make high value products can be significant, and as such design changes that increase yield will also have a subsequent effect of reducing the overall energy consumption of industries using the bottom discharge spiral jet mill. The optimised bottom discharge spiral jet mill developed in Chapter 10 will eventually reduce the carbon foot print of some GSK products by reducing the amount of API required as yield losses will be significantly reduced.

12.3 Summary of Contributions to the Spiral Jet Mill Body of Knowledge

The original research presented in this thesis has made the following significant contributions to the body of knowledge on the spiral jet mill:

- The spiral jet mill cut size equation (MacDonald *et al.* 2016).
    - Semi-empirical mechanistic model for process modelling.
    - Most detailed experimental investigation in literature regarding variation of solids feed rate and gas mass flow rate for the spiral jet mill.
- Spin ratio CFD investigation with varying motive gases.
    - Demonstration of break-down of constant spin ratio at Mach 1.
    - Validation that the assumption of a constant spin ratio is acceptable for a range of flow rates.
- Simultaneous Optimisation of a Cyclone and Spiral Jet Mill.
    - First CFD observation of solids separation in the inner core of gas within a cyclone.
    - First ever simultaneous optimisation of a cyclone and spiral jet mill to maintain similarity of PSD while increasing yield.

12.4 Conclusion

Fluid particle systems are often complex and challenging to model analytically, and as such the academic community has responded to industry needs with either empirical correlations or with numerical simulations with CFD-DEM. Both techniques are an equally valid approach, with empirical correlations providing highly reliable models for measurable output characteristics and CFD-DEM providing insights into the un-measurable processes driving output characteristics. The spiral jet mill is however a structured and ordered fluid particle system that can be modelled analytically as shown in this thesis. The work undertaken not only contributes to the body of knowledge on the spiral jet mill, but is a valid demonstration of first principles chemical engineering science to an important unit operation.

The simultaneous optimisation of a spiral jet mill grind chamber and cyclone with CFD-DPM is an example of a situation where numerical simulation was necessary and provided an effective and useful output. Although the model was simplistic, it greatly reduced the quantity of API used for experimental optimisation and led to an improved design.

The work carried out as part of this Engineering Doctorate (EngD) has not only contributed significantly to the body of knowledge of the subject of investigation as per the requirements of doctoral research, but has also delivered successful solutions to problems faced by industry. Aspects of the recommended further work are intended to be completed at GSK, and as such further benefits will be delivered to industry and academia beyond this EngD project.

Appendix 1 – Chapter 4 Experimental Data

Feeder Screw Speed (RPM ± 1 RPM)	Grind Gas Pressure Set Point (barg ± 0.1 barg)	Feed Gas Pressure Set Point (barg ± 0.1 barg)	Feeder Input Mass (kg ± 0.001 kg)	Feeding Time (Minutes:Seconds ± 2 Seconds)	Feed Gas Mass Flow Rate (kg/hr ± 1 kg/hr)			Feed Gas Temperature (°C ±1 °C)			Grind Gas Mass Flow Rate (kg/hr ± 1 kg/hr)			Grind Gas Temperature (°C ±1 °C)			x50 (µm ± 1%)			x90 (µm ± 1%)		
					Mean	Max	Min	Mean	Max	Min	Mean	Max	Min	Mean	Max	Min	Mean	Max	Min	Mean	Max	Min
50	2.0	2.8	0.250	21:42	19.3	19.7	18.9	18.1	19.0	17.7	71.1	72.1	70.3	17.1	18.0	16.7	1.96	1.99	1.89	4.46	4.57	4.17
100	2.0	2.8	0.250	10:44	19.2	19.6	18.8	20.0	21.4	19.0	68.1	69.0	67.4	18.5	19.8	17.7	2.03	2.04	2.03	4.82	4.85	4.80
200	2.0	2.8	0.250	05:29	19.3	19.7	18.9	19.1	19.7	18.7	70.1	71.2	69.4	18.1	18.9	17.7	2.03	2.04	2.02	5.06	5.08	5.03
350	2.0	2.8	0.250	03:13	19.3	19.6	19.0	19.1	19.5	18.8	69.4	70.2	68.7	18.0	18.6	17.8	2.00	2.01	1.99	5.63	5.64	5.61
50	3.0	4.0	0.250	21:01	25.5	26.0	25.0	18.2	19.5	17.5	92.8	93.9	91.7	17.2	18.5	16.4	1.88	1.88	1.87	4.33	4.34	4.32
100	3.0	4.0	0.250	10:51	25.4	26.0	25.0	17.9	19.9	16.7	92.6	93.7	91.6	16.0	18.5	14.9	1.94	1.96	1.92	4.47	4.55	4.28
200	3.0	4.0	0.250	05:20	25.4	25.9	24.9	18.6	20.2	17.4	95.3	96.6	94.4	16.7	18.5	15.3	1.77	1.78	1.75	4.30	4.31	4.28
350	3.0	4.0	0.250	03:30	25.5	29.0	25.1	17.3	18.1	16.7	93.7	94.7	92.8	15.8	16.5	15.2	1.78	1.78	1.77	4.54	4.55	4.54
25	4.0	5.3	0.250	41:05	32.2	32.8	31.7	15.4	18.0	14.4	117.2	120.1	115.5	14.1	16.8	13.1	1.56	1.57	1.55	3.58	3.60	3.56
50	4.0	5.3	0.250	20:01	33.3	33.9	32.8	17.2	19.8	15.9	115.9	117.6	114.4	15.9	18.7	14.6	1.58	1.61	1.57	3.67	3.69	3.66
50	4.0	5.3	0.250	21:02	32.2	32.7	31.7	17.5	19.2	16.4	115.6	116.7	114.3	16.5	18.1	15.1	1.64	1.66	1.62	3.73	3.82	3.57
100	4.0	5.3	0.250	10:06	32.2	32.8	31.8	16.0	17.8	15.0	116.2	117.5	114.8	14.4	16.0	13.2	1.66	1.68	1.65	3.84	3.86	3.81
200	4.0	5.3	0.250	05:11	32.2	32.6	31.7	17.9	18.8	17.1	116.1	117.4	115.0	16.5	17.6	15.4	1.67	1.69	1.66	3.94	3.96	3.93
350	4.0	5.3	0.250	03:01	33.3	33.8	32.9	18.8	19.7	17.9	115.4	116.4	114.4	17.3	18.7	16.3	1.60	1.62	1.57	3.87	3.96	3.64
350	4.0	5.3	0.250	03:05	33.2	33.6	32.8	18.3	18.7	17.9	115.4	116.5	114.6	17.3	17.7	17.1	1.61	1.62	1.60	4.02	4.06	3.99
400	4.0	5.3	0.250	03:00	32.1	32.4	31.7	19.4	20.6	18.2	114.6	115.7	113.4	17.6	19.0	15.8	1.61	1.62	1.60	4.10	4.13	4.08
600	4.0	5.3	0.250	01:48	32.2	32.5	31.8	17.9	18.6	17.2	115.9	116.8	114.9	16.3	16.8	15.8	1.83	1.87	1.80	5.70	5.94	5.42
50	5.0	6.5	0.250	21:09	38.4	39.0	37.9	16.8	18.0	16.1	139.1	140.9	136.5	15.5	16.6	15.0	1.54	1.56	1.52	3.55	3.57	3.53
100	5.0	6.5	0.250	11:31	38.2	39.1	37.7	19.2	21.0	16.7	139.2	141.4	137.2	17.5	20.1	14.8	1.64	1.65	1.63	3.83	3.84	3.82
200	5.0	6.5	0.250	05:36	39.8	40.3	39.3	19.4	20.6	18.2	137.8	139.1	136.7	17.8	19.1	17.0	1.54	1.55	1.52	3.57	3.58	3.56
350	5.0	6.5	0.250	03:02	38.3	38.7	37.9	19.4	20.2	18.9	138.3	139.7	137.2	18.2	19.2	17.5	1.55	1.57	1.54	3.76	3.79	3.74
50	6.0	7.8	0.250	20:20	46.3	47.0	45.7	16.0	18.2	15.1	162.4	166.3	159.0	14.1	16.3	13.7	1.42	1.43	1.41	3.26	3.27	3.25
100	6.0	7.8	0.250	10:06	45.1	45.6	44.5	16.0	18.7	14.8	163.2	167.1	158.7	14.6	16.9	13.1	1.52	1.53	1.51	3.53	3.54	3.52
200	6.0	7.8	0.221	04:39	45.0	45.5	44.5	18.8	21.1	17.0	161.6	164.6	159.2	17.3	19.5	14.4	1.49	1.50	1.48	3.46	3.48	3.45
350	6.0	7.8	0.250	03:10	45.1	45.6	44.6	18.6	18.9	18.3	162.7	165.3	160.4	17.6	18.0	17.4	1.46	1.48	1.44	3.47	3.50	3.44
25	7.0	9.0	0.250	40:07	51.6	52.5	50.6	14.7	18.2	13.9	187.7	202.8	175.9	13.6	16.5	12.7	1.32	1.34	1.30	3.03	3.06	3.00
50	7.0	9.0	0.250	20:21	52.9	54.2	52.1	15.9	18.0	15.1	187.6	200.8	177.6	14.6	16.7	13.9	1.35	1.37	1.34	3.08	3.11	3.05
50	7.0	9.0	0.250	20:12	51.5	52.1	50.8	16.3	19.5	13.8	186.7	196.0	176.8	15.0	18.4	12.7	1.35	1.38	1.32	3.09	3.13	3.06
100	7.0	9.0	0.250	10:21	51.4	52.3	50.4	16.0	18.3	14.4	186.2	195.8	176.1	14.0	16.7	12.8	1.37	1.40	1.34	3.16	3.21	3.07
200	7.0	9.0	0.250	05:20	51.3	52.3	50.6	16.7	18.3	15.6	184.4	195.6	176.8	15.2	16.6	14.1	1.41	1.42	1.40	3.22	3.23	3.21
350	7.0	9.0	0.250	03:10	51.2	51.7	50.7	19.8	20.4	19.1	183.2	190.1	175.2	18.8	19.3	18.0	1.40	1.41	1.39	3.28	3.29	3.27
350	7.0	9.0	0.250	03:04	51.2	51.8	50.8	18.6	19.0	18.4	186.1	196.1	180.5	18.0	18.5	17.9	1.44	1.45	1.43	3.39	3.40	3.38

Table A1.1 Chapter 4 Experimental Data Summary

Appendix 2 – Chapter 6 Industrial Development Data

A2 Industrial Development Data

A2.1 Product A – 8" Manufacturer A Mill

A plot of specific energy, E_{sp}, in Megajoules per kg (MJ.kg^{-1}) against x90 may be found for product A with an 8" Manufacturer A mill in Figure A2.1, and 1/ E_{sp} against x90 in Figure A2.2.

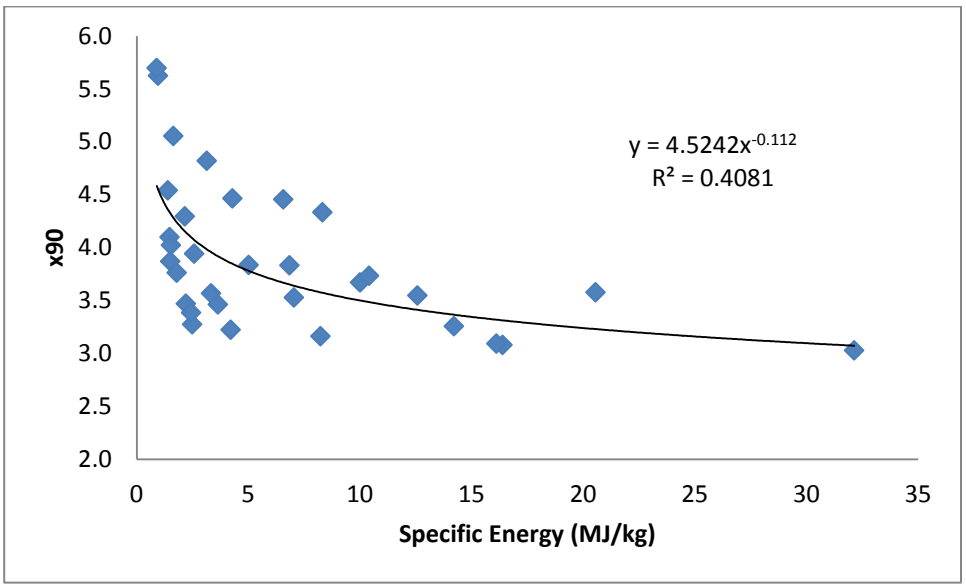

Figure A2.1 **E_{sp} against x90, Product A, 8" Manufacturer A Mill**

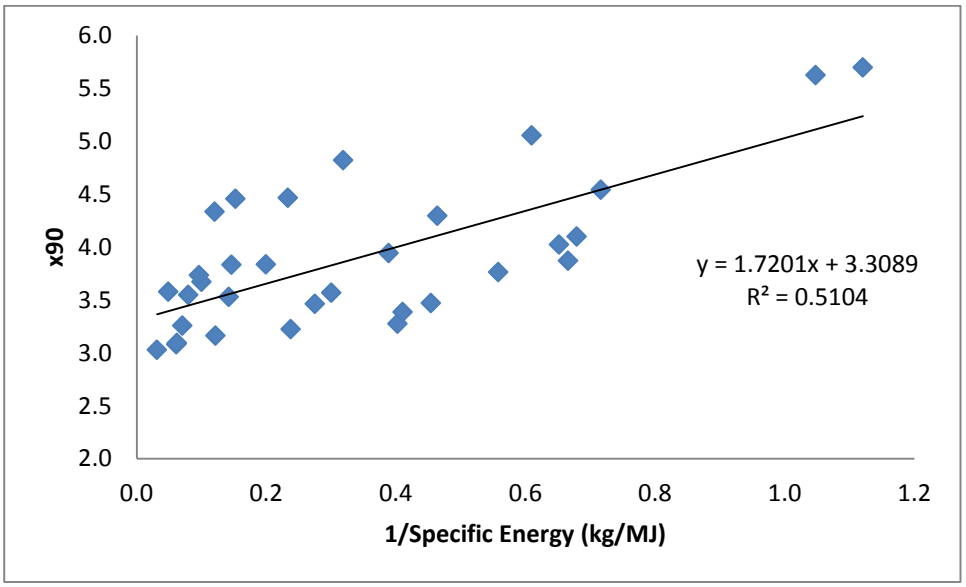

Figure A2.2 **1/E_{sp} against x90, Product A, 8" Manufacturer A Mill**

The milling constants for Product A with an 8" Manufacturer A mill may be found in Table A2.1.

$\frac{C_2}{{k_3}^2}$ (µm)	$\frac{x_1 k_4}{{k_3}^2 d_{Reynolds}}$ (µm.kg.hr^{-1})	x_2 (kg.hr^{-1})
0.346	32.9	9.29

Table A2.1 Milling Constants for Product A, 8" Manufacturer A Mill

A comparison between the prediction accuracy of Equation 3.27 compared to its simplified form, Equation 4.3, may be found in Table A2.2 and Figure A2.3.

$\sum(actual - predicted)^2$ Equation 3.27	$\sum(actual - predicted)^2$ Equation 4.3
1.67	7.32

Table A2.2 Prediction Comparison, Product A, 8" Manufacturer A Mill

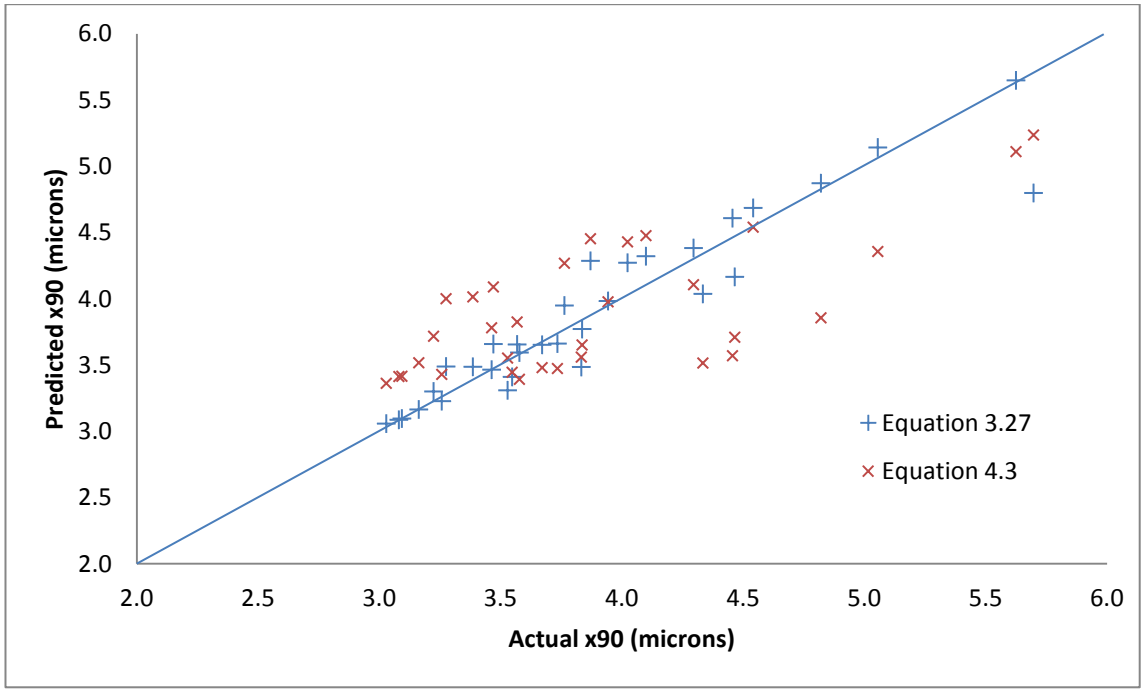

Figure A2.3 Prediction Accuracy, Product A, 8" Manufacturer A Mill

A2.2 Product B – 8" Manufacturer C Mill

A plot of specific energy, E_{sp}, against x90 may be found for product B with an 8" Manufacturer C mill in Figure A2.4, and 1/ E_{sp} against x90 in Figure A2.5.

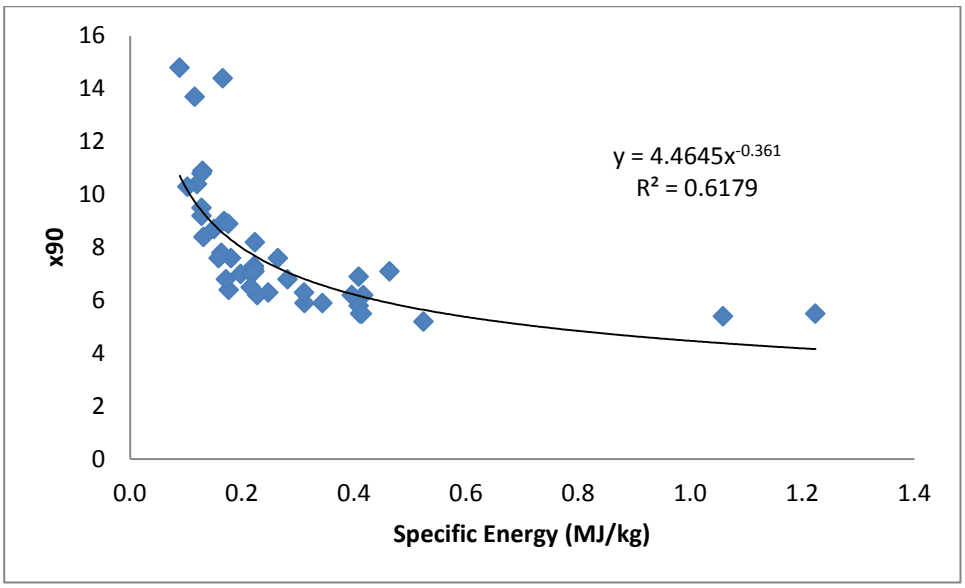

Figure A2.4 E_{sp} **against x90, Product B, 8" Manufacturer C Mill**

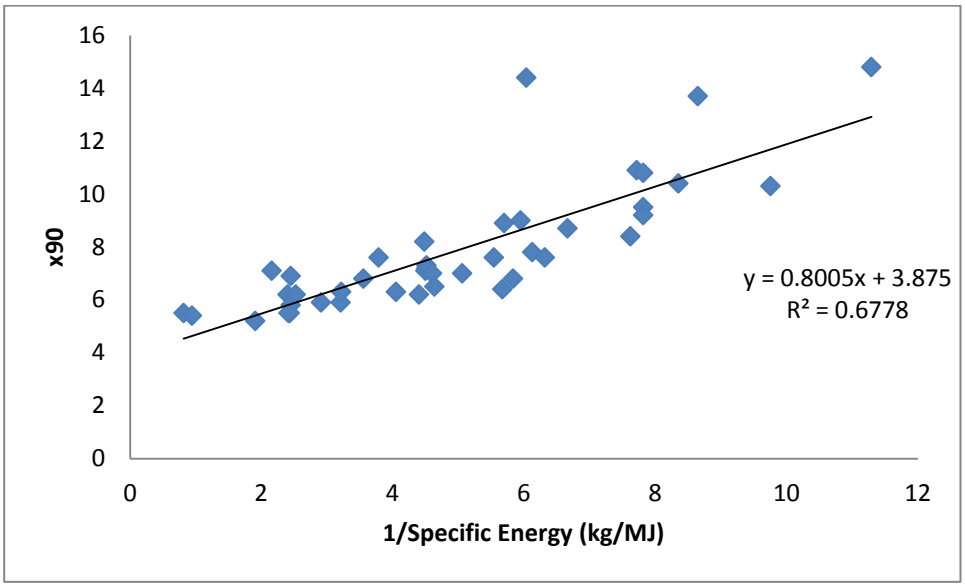

Figure A2.5 $1/E_{sp}$ **against x90, Product B, 8" Manufacturer C Mill**

The milling constants for product B with an 8" Manufacturer C mill may be found in Table A2.3.

$\frac{C_2}{{k_3}^2}$ (µm)	$\frac{x_1 k_4}{{k_3}^2 d_{Reynolds}}$(µm.kg.hr^{-1})	x_2 (kg.hr^{-1})
0.505	16.5	6.80

Table A2.3 Milling Constants for Product B, 8" Manufacturer C Mill

A comparison between the prediction accuracy of Equation 3.27 compared to its simplified form, Equation 4.3, may be found in Table A2.4 and Figure A2.6.

$\sum(actual - predicted)^2$ Equation 3.27	$\sum(actual - predicted)^2$ Equation 4.3
72.1	73.8

Table A2.4 Prediction Comparison, Product B, 8" Manufacturer C Mill

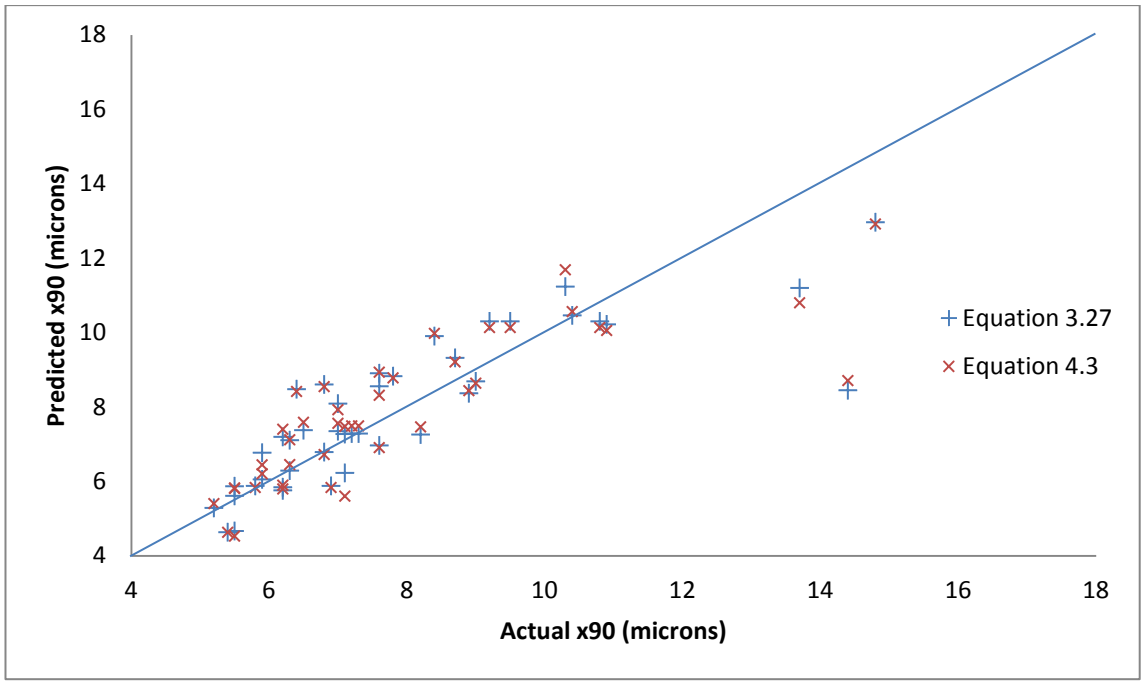

Figure A2.6 Prediction Accuracy, Product B, 8" Manufacturer C Mill

A2.3 Product B – 8" Manufacturer *D Mill*

A plot of specific energy, E_{sp}, against x90 may be found for product B with an 8" Manufacturer D mill in Figure A2.7, and 1/ E_{sp} against x90 in Figure A2.8.

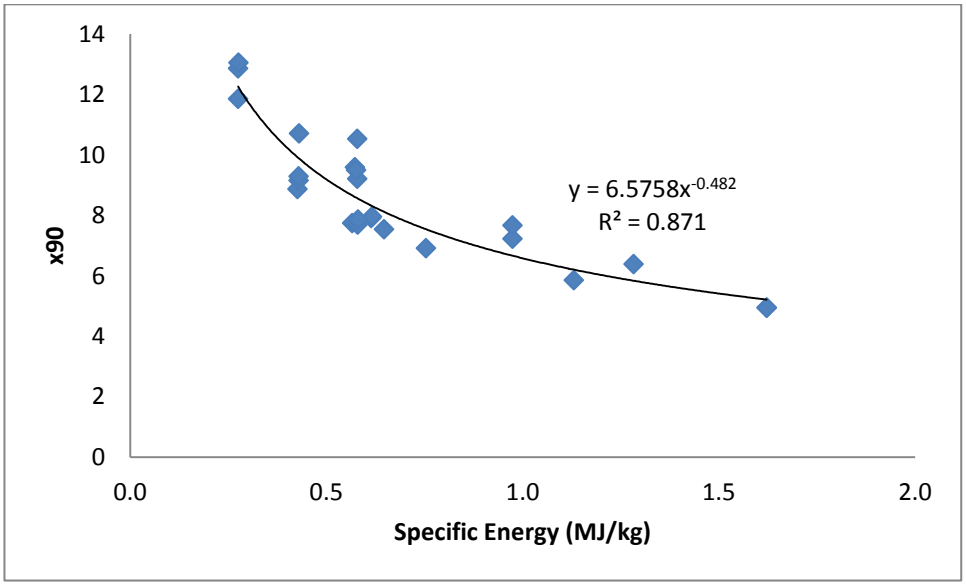

Figure A2.7 E_{sp} against x90, Product B, 8" Manufacturer D Mill

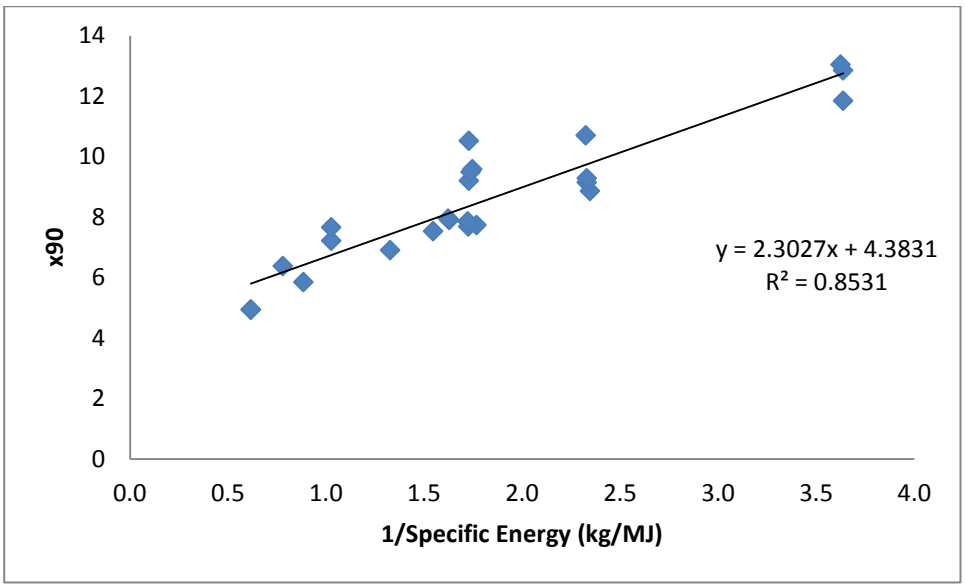

Figure A2.8 **$1/E_{sp}$ against x90, Product B, 8" Manufacturer D Mill**

The milling constants for product B with an 8" Manufacturer D mill may be found in Table A2.5.

$\frac{C_2}{{k_3}^2}$ (µm)	$\frac{x_1 k_4}{{k_3}^2 d_{Reynolds}}$(µm.kg.hr^{-1})	x_2 (kg.hr^{-1})
0.458	49.6	6.90

Table A2.5 **Milling Constants for Product B, 8" Manufacturer D Mill**

A comparison between the prediction accuracy of Equation 3.27 compared to its simplified form, Equation 4.3, may be found in Table A2.6 and Figure A2.9.

$\sum(actual - predicted)^2$ Equation 3.27	$\sum(actual - predicted)^2$ Equation 4.3
7.36	15.9

Table A2.6 **Prediction Comparison, Product B, 8" Manufacturer D Mill**

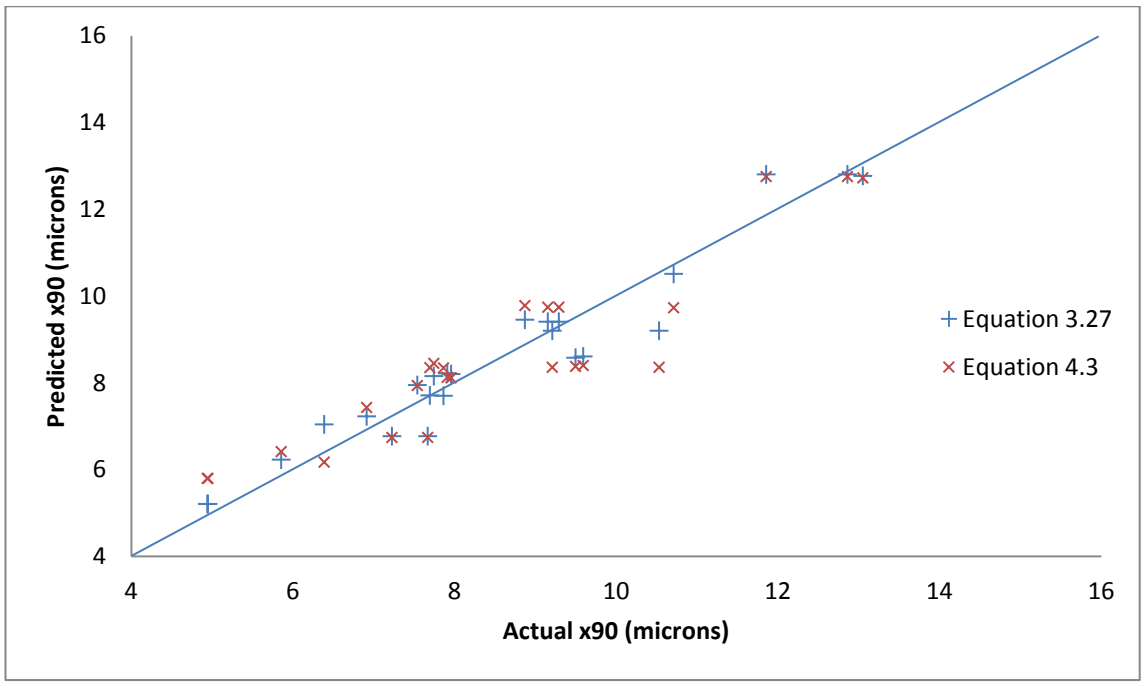

Figure A2.9 **Prediction Accuracy, Product B, 8" Manufacturer D Mill**

A2.4 Product C – 8" Manufacturer C Mill

A plot of specific energy, E_{sp}, against x90 may be found for product C with an 8" Manufacturer C mill in Figure A2.10, and 1/ E_{sp} against x90 in Figure A2.11.

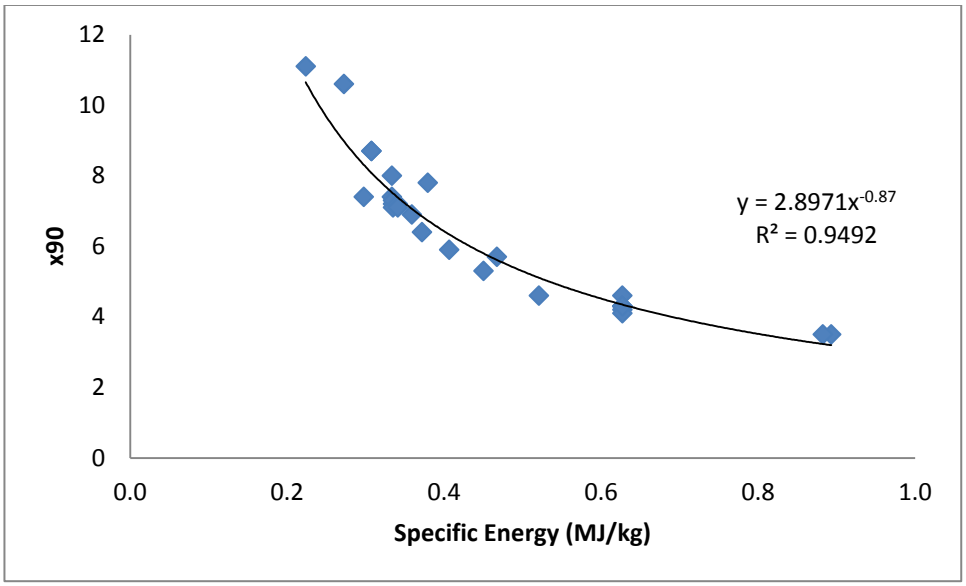

Figure A2.10 **E_{sp} against x90, Product C, 8" Manufacturer C Mill**

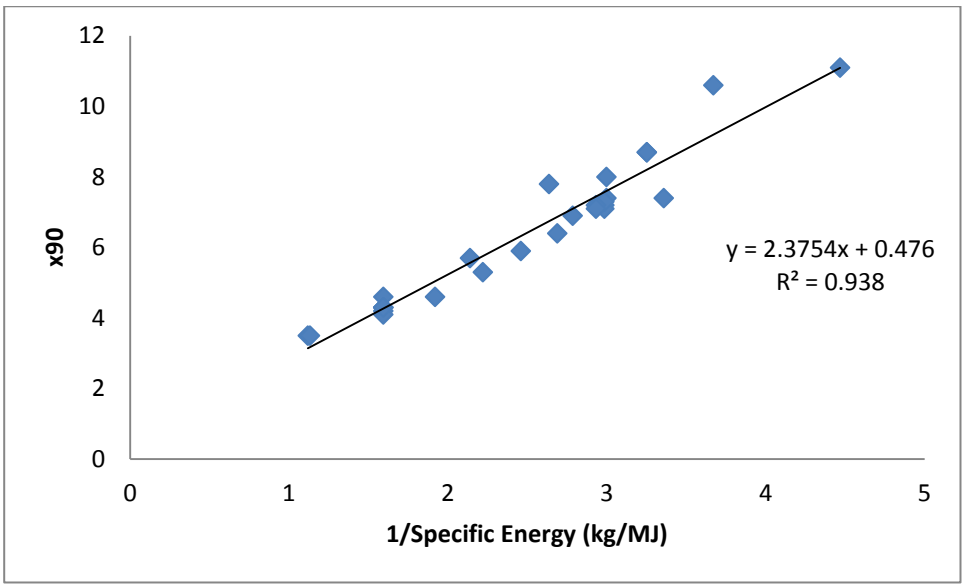

Figure A2.11 $1/E_{sp}$ against x90, Product C, 8" Manufacturer C Mill

The milling constants for product C may be found in Table A2.7

$\frac{C_2}{{k_3}^2}$ (μm)	$\frac{x_1 k_4}{{k_3}^2 d_{Reynolds}}$(μm.kg.hr^{-1})	x_2 (kg.hr^{-1})
0.092	29.0	5.44

Table A2.7 Milling Constants for Product C, 8" Manufacturer C Mill

A comparison between the prediction accuracy of Equation 3.27 compared to its simplified form, Equation 4.3, may be found in Table A2.8 and Figure A2.12.

$\sum(actual - predicted)^2$ Equation 3.27	$\sum(actual - predicted)^2$ Equation 4.3
5.07	6.74

Table A2.8 Prediction Comparison, Product C, 8" Manufacturer C Mill

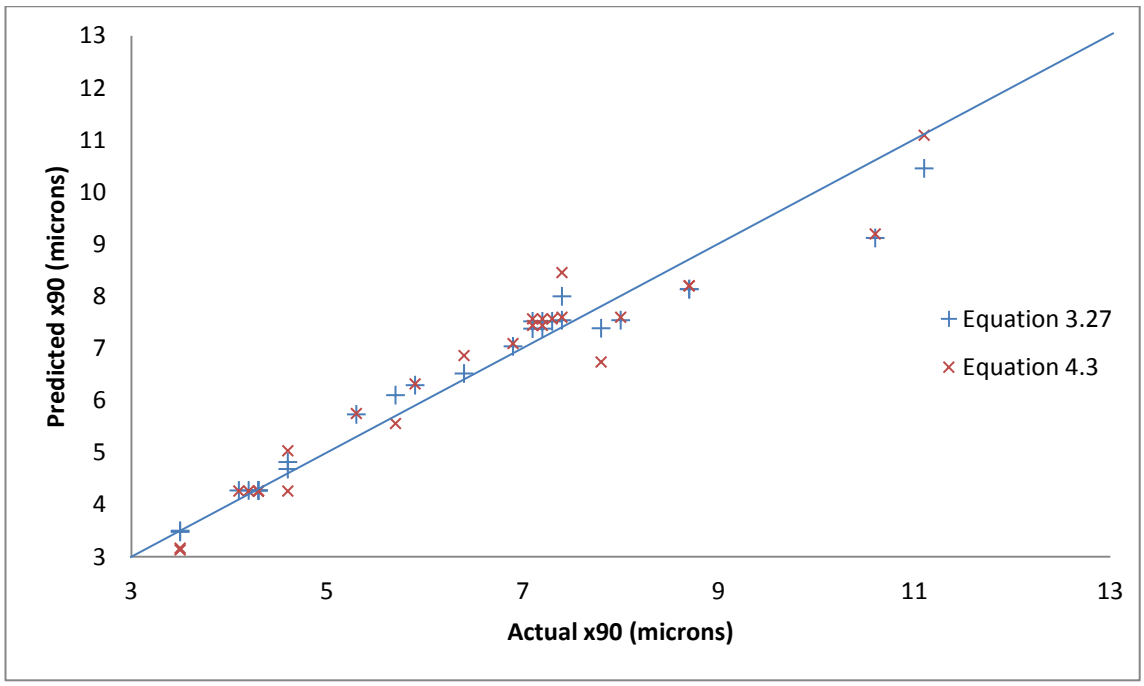

Figure A2.12 Prediction Accuracy, Product C, 8" Manufacturer C Mill

A2.5 Product C – 8" Manufacturer D Mill

A plot of specific energy, E_{sp}, against x90 may be found for product C with an 8" Manufacturer D mill in Figure A2.13, and 1/ E_{sp} against x90 in Figure A2.14.

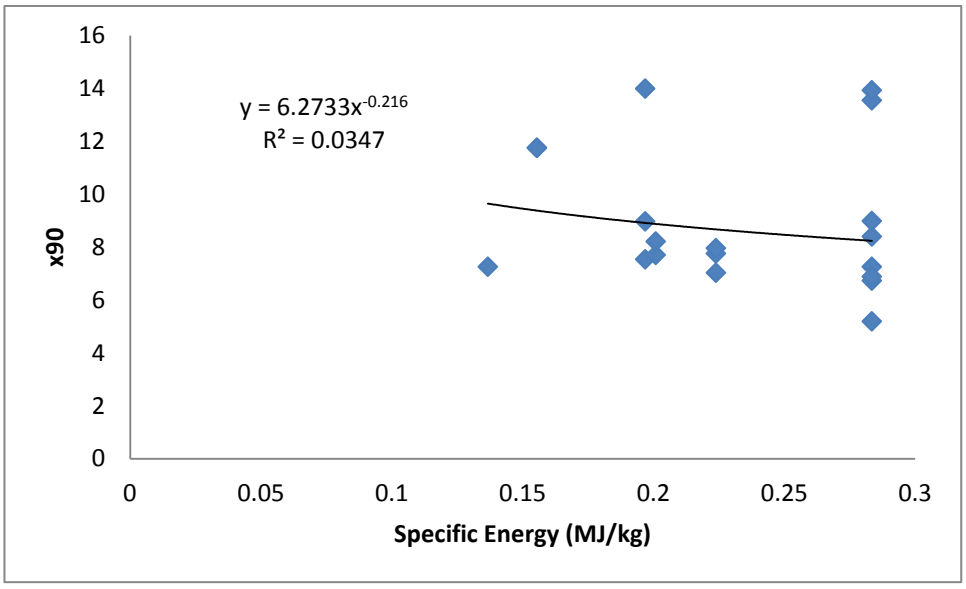

Figure A2.13 E_{sp} against x90, Product C, 8" Manufacturer D Mill

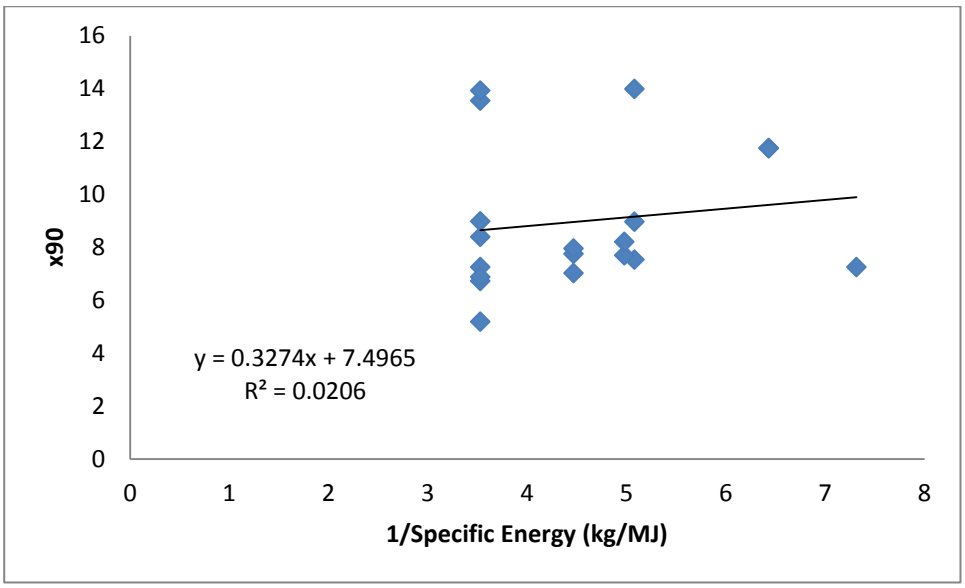

Figure A2.14 $1/E_{sp}$ against x90, Product C, 8" Manufacturer D Mill

The milling constants for product C may be found in Table A2.9

$\frac{C_2}{{k_3}^2}$ (µm)	$\frac{x_1 k_4}{{k_3}^2 d_{Reynolds}}$(µm.kg.hr^{-1})	x_2 (kg.hr^{-1})
0.383	141	253

Table A2.9 Milling Constants for Product C, 8" Manufacturer D Mill

A comparison between the prediction accuracy of Equation 3.27 compared to its simplified form, Equation 4.3, may be found in Table A2.10 and Figure A2.12.

$\sum(actual - predicted)^2$ Equation 3.27	$\sum(actual - predicted)^2$ Equation 4.3
20.8	124

Table A2.10 Prediction Comparison, Product C, 8" Manufacturer D Mill

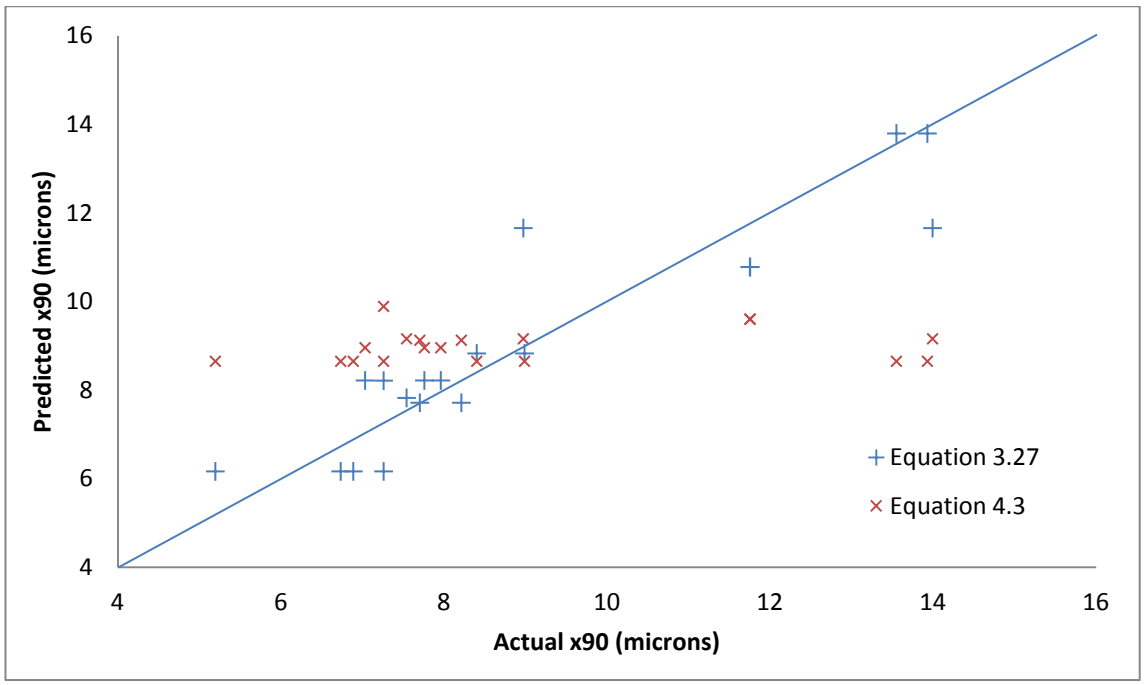

Figure A2.15 Prediction Accuracy, Product C, 8" Manufacturer D Mill

A2.6 Product C – 4" Manufacturer A Mill

A plot of specific energy, E_{sp}, against x90 may be found for product C with a 4" Manufacturer A mill in Figure A2.16, and $1/E_{sp}$ against x90 in Figure A2.17.

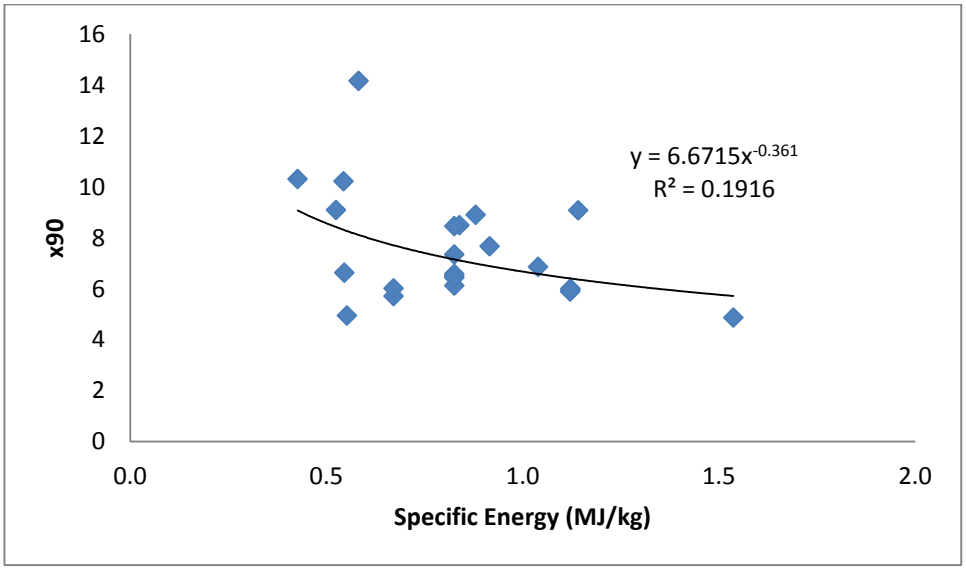

Figure A2.16 E_{sp} against x90, Product C, 4" Manufacturer A Mill

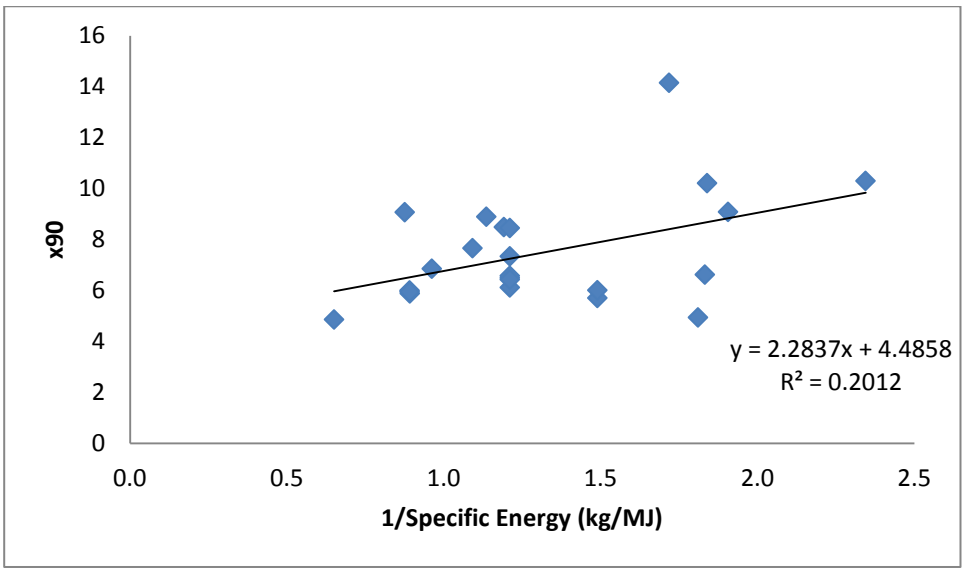

Figure A2.17 $1/E_{sp}$ against x90, Product C, 4" Manufacturer A Mill

The milling constants for product C may be found in Table A2.11

$\frac{C_2}{{k_3}^2}$ (µm)	$\frac{x_1 k_4}{{k_3}^2 d_{Reynolds}}$(µm.kg.hr^{-1})	x_2 (kg.hr^{-1})
0.0779	24.4	6.83

Table A2.11 Milling Constants for Product C, 4" Manufacturer A Mill

A comparison between the prediction accuracy of Equation 3.27 compared to its simplified form, Equation 4.3, may be found in Table A2.12 and Figure A2.18.

$\sum(actual - predicted)^2$ Equation 3.27	$\sum(actual - predicted)^2$ Equation 4.3
66.0	80.4

Table A2.12 Prediction Comparison, Product C, 4" Manufacturer A Mill

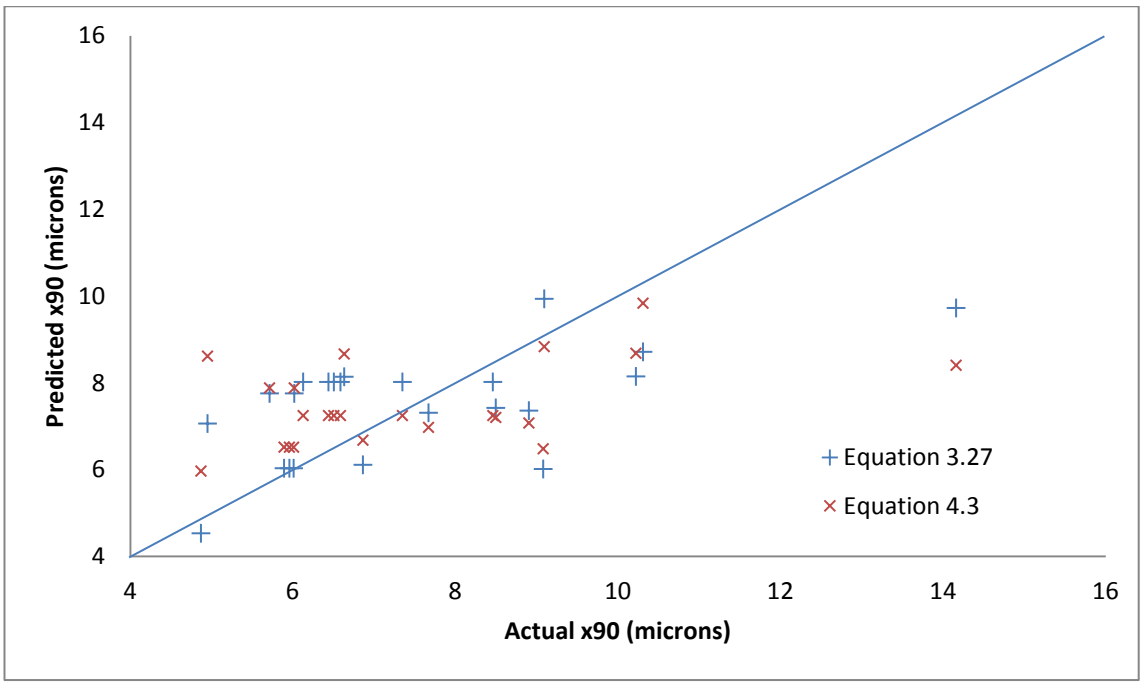

Figure A2.18 Prediction Accuracy, Product C, 8" Manufacturer A Mill

A2.7 Product D – 8" Manufacturer A Mill

A plot of specific energy, E_{sp}, against x90 may be found for product D with a 8" Manufacturer A mill in Figure A2.19, and 1/ E_{sp} against x90 in Figure A2.20.

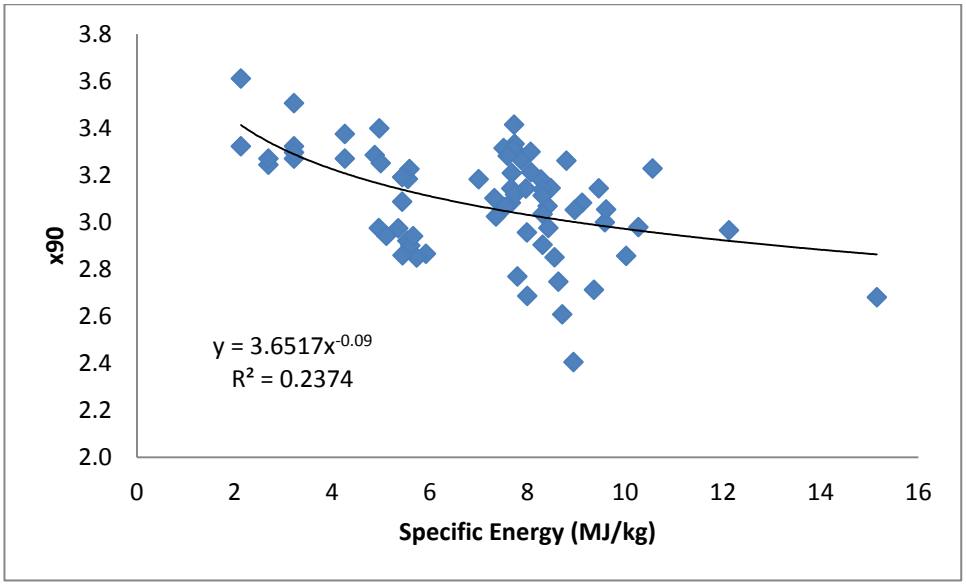

Figure A2.19 E_{sp} against x90, Product D, 8" Manufacturer A Mill

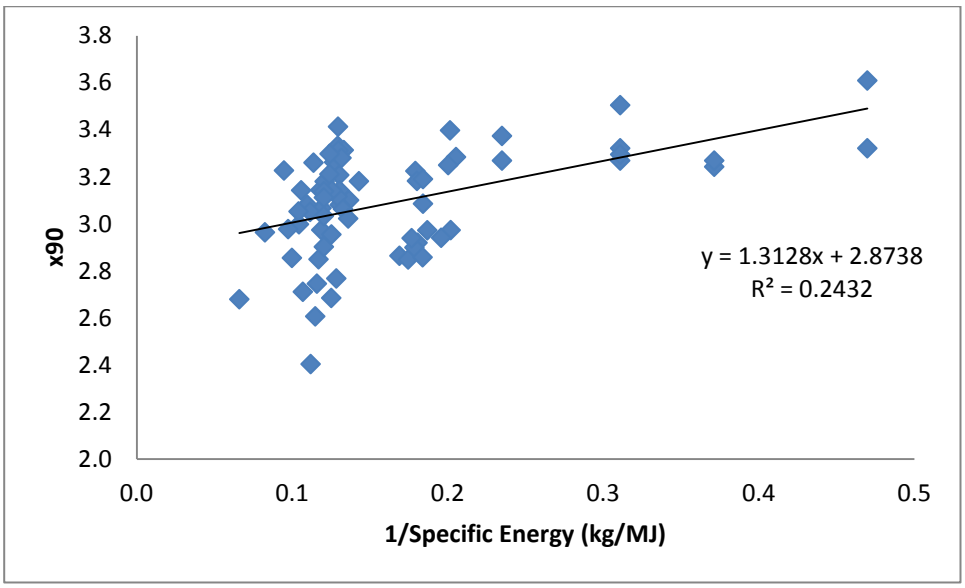

Figure A2.20 **$1/E_{sp}$ against x90, Product D, 8" Manufacturer A Mill**

The milling constants for product D may be found in Table A2.13

$\frac{C_2}{{k_3}^2}$ (µm)	$\frac{x_1 k_4}{{k_3}^2 d_{Reynolds}}$ (µm.kg.hr^{-1})	x_2 (kg.hr^{-1})
0.335	32.7	13.9

Table A2.13 **Milling Constants for Product D, 8" Manufacturer A Mill**

A comparison between the prediction accuracy of Equation 3.27 compared to its simplified form, Equation 4.3, may be found in Table A2.14 and Figure A2.21.

$\sum(actual - predicted)^2$ Equation 3.27	$\sum(actual - predicted)^2$ Equation 4.3
2.52	2.57

Table A2.14 **Prediction Comparison, Product D, 8" Manufacturer A Mill**

Almost no correlation is observed for Product D at its target settings as the variability in particle size is primarily a result of stretching of crystalline properties.

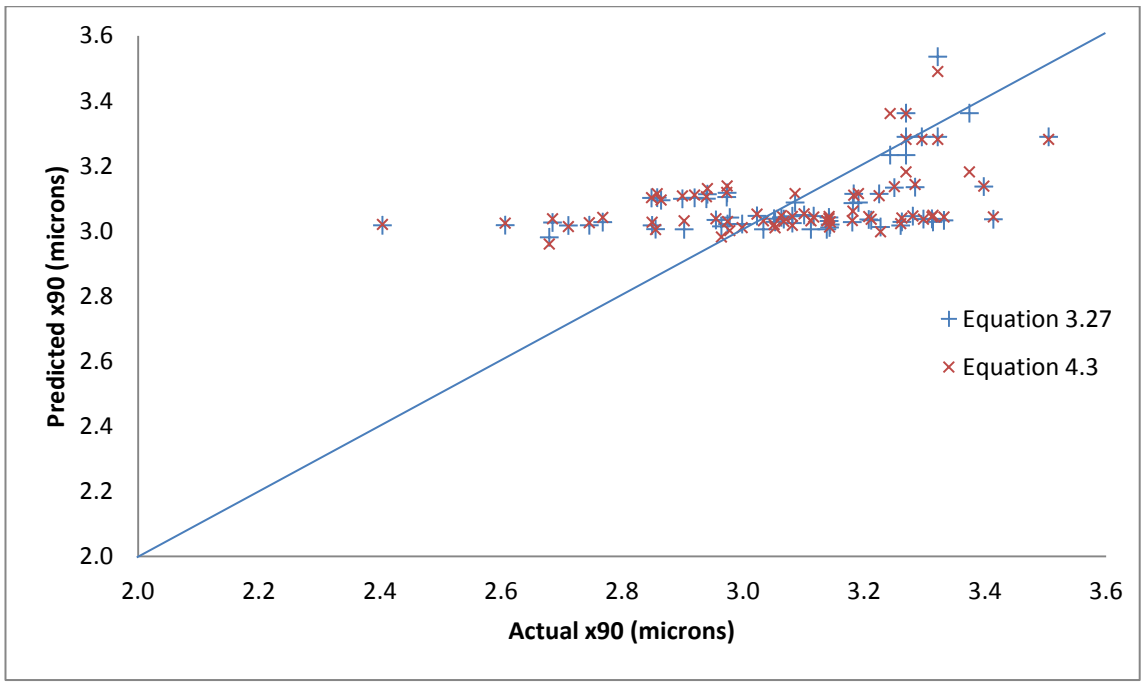

Figure A2.21 Prediction Accuracy, Product D, 8" Manufacturer A Mill

A2.8 Product E – 8" Manufacturer A Mill

A plot of specific energy, E_{sp}, against x90 may be found for product E with a 8" Manufacturer A mill in Figure A2.22, and 1/ E_{sp} against x90 in Figure A2.23.

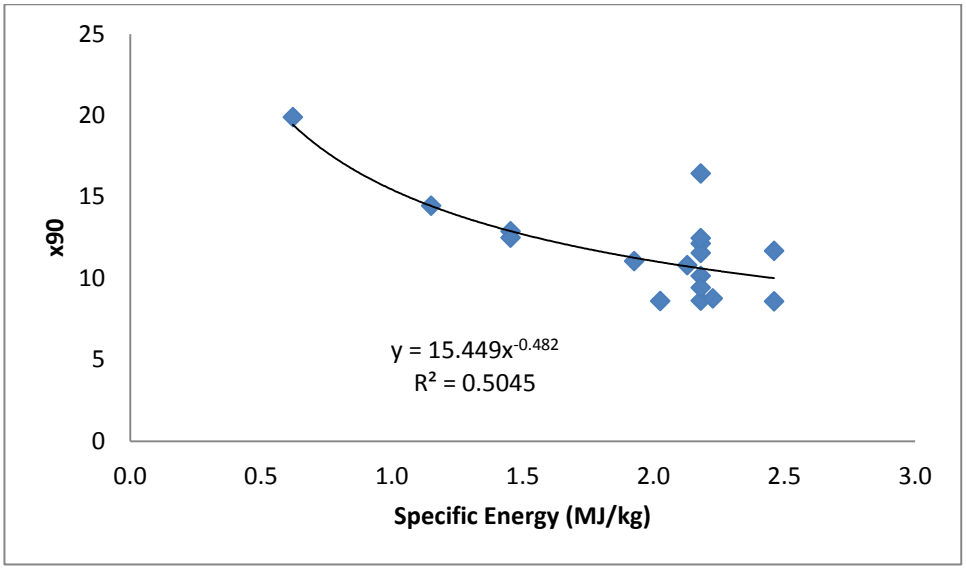

Figure A2.22 E_{sp} against x90, Product E, 8" Manufacturer A Mill

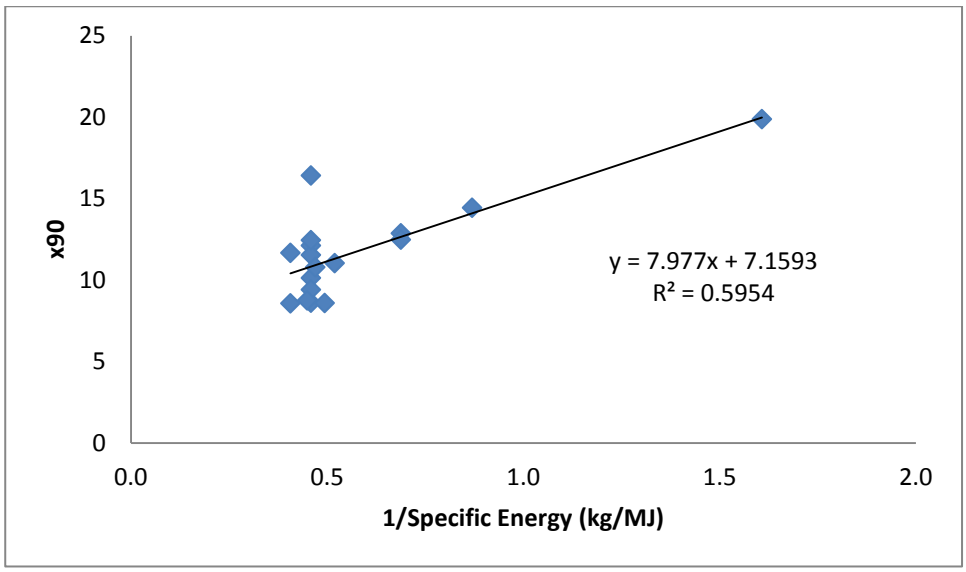

Figure A2.23 $1/E_{sp}$ against x90, Product E, 8" Manufacturer A Mill

The milling constants for product E with an 8" Manufacturer A mill may be found in Table A2.15.

$\frac{C_2}{{k_3}^2}$ (µm)	$\frac{x_1 k_4}{{k_3}^2 d_{Reynolds}}$ (µm.kg.hr^{-1})	x_2 (kg.hr^{-1})
1.03	32.14	1.43

Table A2.15 Milling Constants for Product E, 8" Manufacturer A Mill

A comparison between the prediction accuracy of Equation 3.27 compared to its simplified form, Equation 4.3, may be found in Table A2.16 and Figure A2.24.

$\sum(actual - predicted)^2$ Equation 3.27	$\sum(actual - predicted)^2$ Equation 4.3
59.1	59.1

Table A2.16 Prediction Comparison, Product E, 8" Manufacturer A Mill

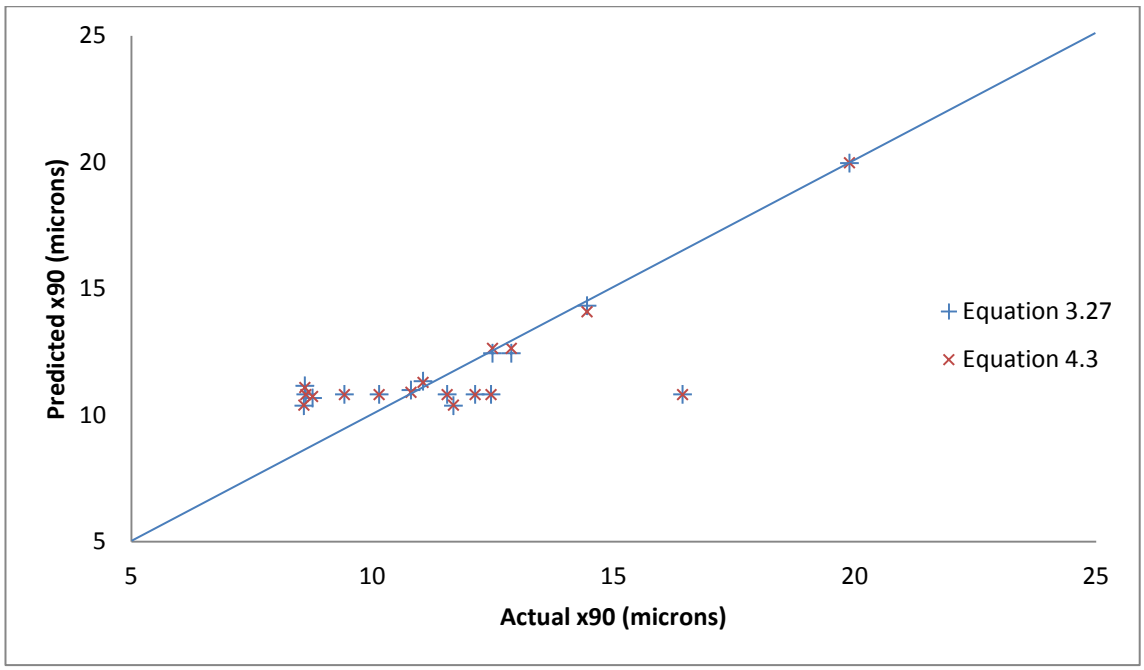

Figure A2.24 **Prediction Accuracy, Product E, 8" Manufacturer A Mill**

A2.9 Product B – 4" Manufacturer C Mill

A plot of specific energy, E_{sp}, against x90 may be found for product B with a 4" Manufacturer C mill in Figure A2.25, and 1/ E_{sp} against x90 in Figure A2.26.

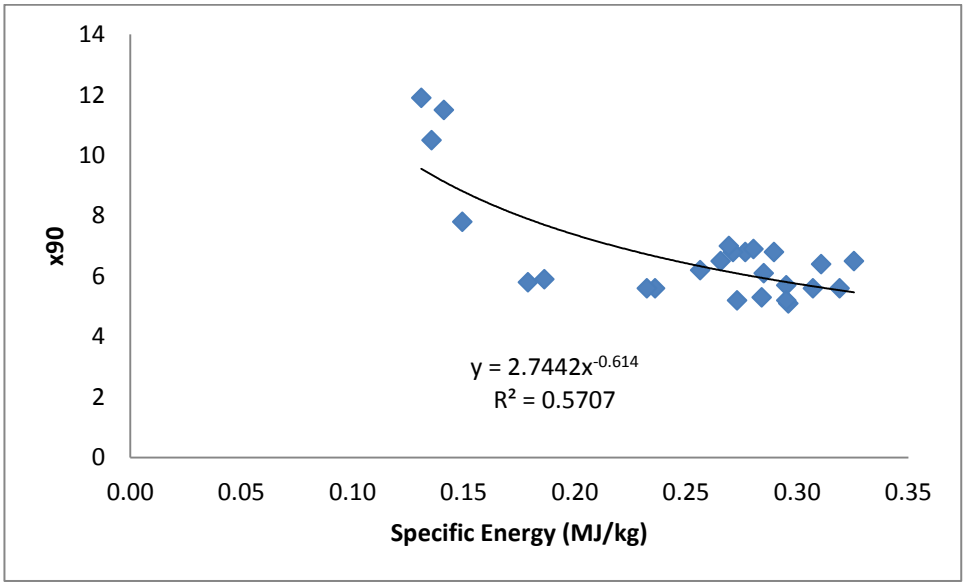

Figure A2.25 **E_{sp} against x90, Product B, 4" Manufacturer C Mill**

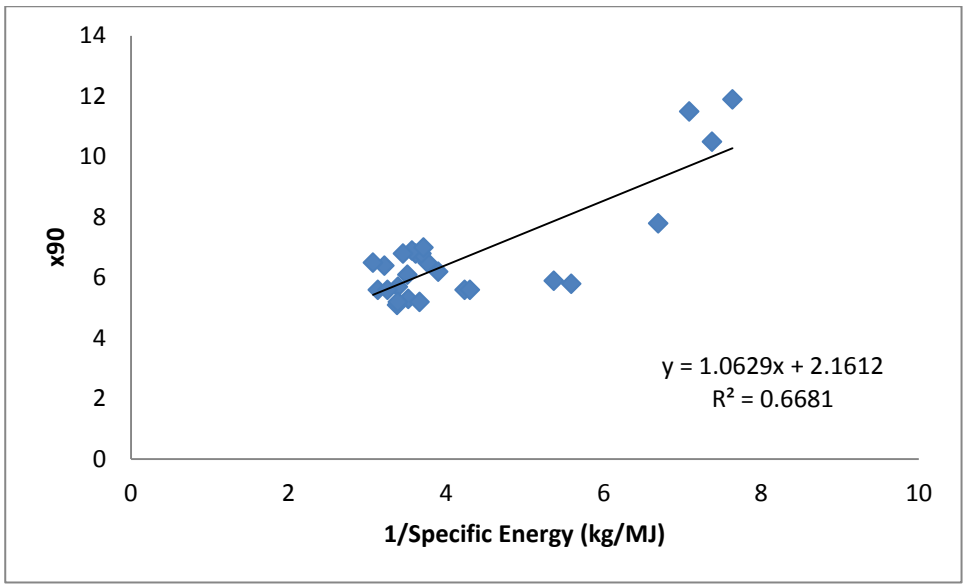

Figure A2.26 $1/E_{sp}$ against x90, Product B, 4" Manufacturer C Mill

The milling constants for product B with a 4" Manufacturer C mill may be found in Table A2.15

$\frac{C_2}{{k_3}^2}$ (µm)	$\frac{x_1 k_4}{{k_3}^2 d_{Reynolds}}$ (µm.kg.hr^{-1})	x_2 (kg.hr^{-1})
0.087	17.0	6.51

Table A2.17 Milling Constants for Product B, 4" Manufacturer C Mill

A comparison between the prediction accuracy of Equation 3.27 compared to its simplified form, Equation 4.3, may be found in Table A2.16 and Figure A2.27.

$\sum(actual - predicted)^2$ Equation 3.27	$\sum(actual - predicted)^2$ Equation 4.3
29.3	27.5

Table A2.18 Prediction Comparison, Product B, 4" Manufacturer C Mill

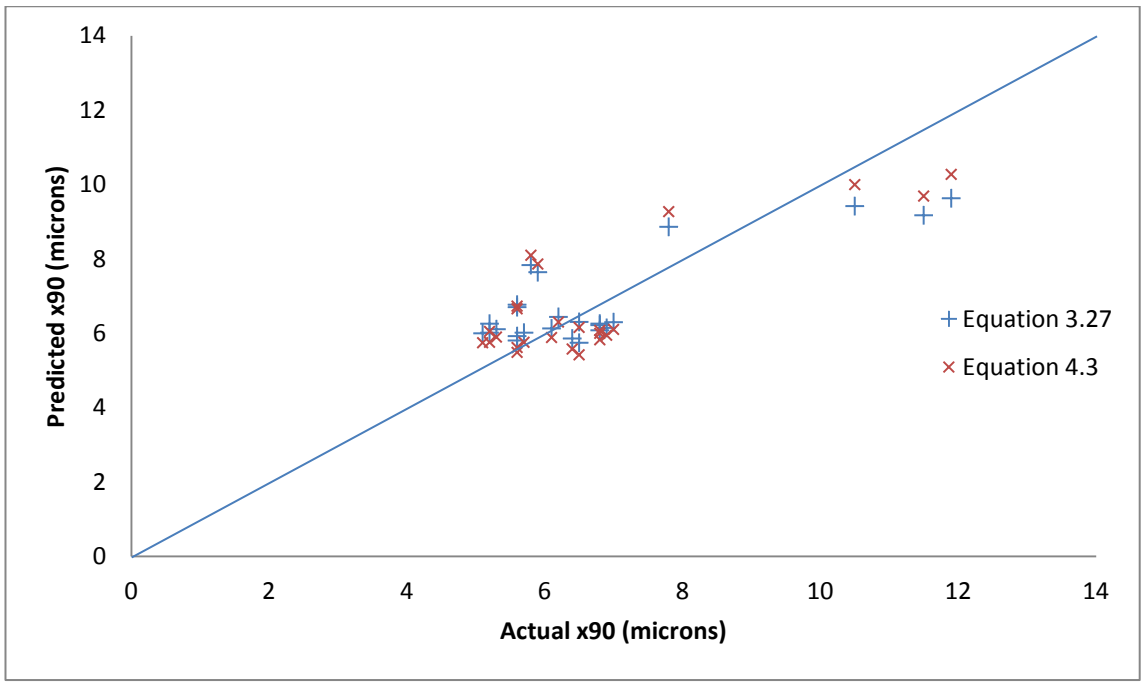

Figure A2.27 Prediction Accuracy, Product B, 4" Manufacturer C Mill

A2.10 Product F – 8" Manufacturer A Mill

A plot of specific energy, E_{sp}, against x90 may be found for product F with an 8" Manufacturer A mill in Figure A2.28, and 1/ E_{sp} against x90 in Figure A2.29.

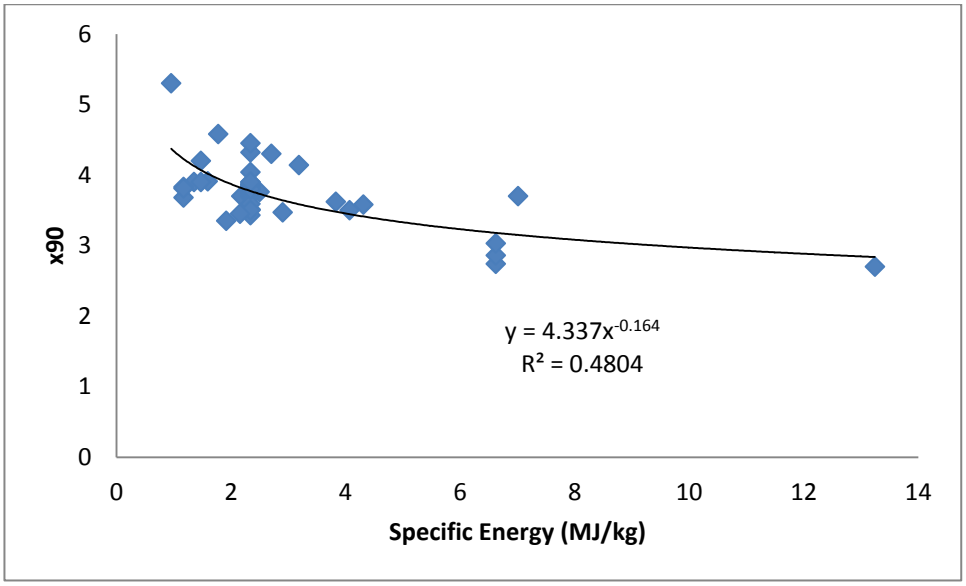

Figure A2.28 E_{sp} against x90, Product F, 8" Manufacturer A Mill

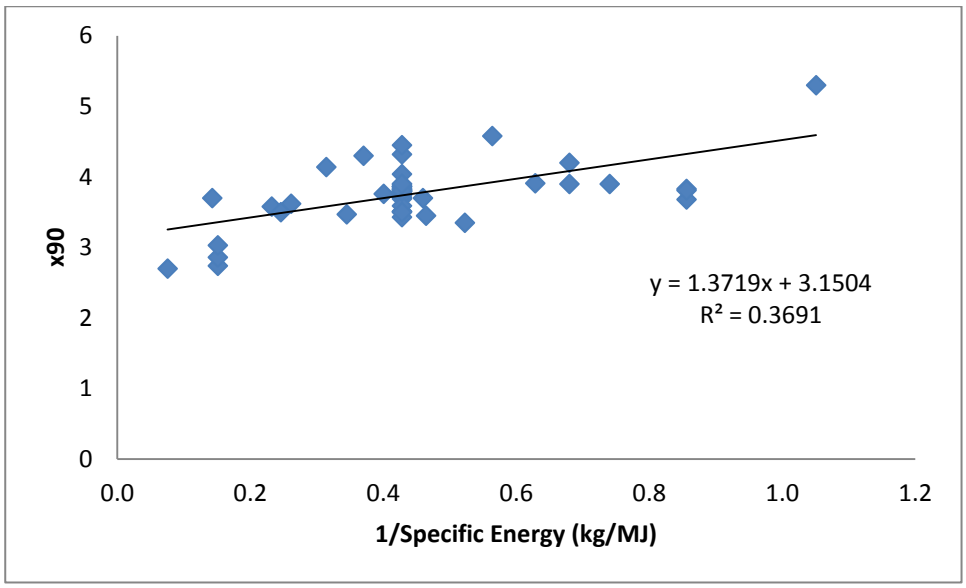

Figure A2.29 $1/E_{sp}$ against x90, Product F, 8" Manufacturer A Mill

The milling constants for product F with an 8" Manufacturer A mill may be found in Table A2.19

$\frac{C_2}{{k_3}^2}$ (µm)	$\frac{x_1 k_4}{{k_3}^2 d_{Reynolds}}$ (µm.kg.hr^{-1})	x_2 (kg.hr^{-1})
0.341	32.9	25.8

Table A2.19 Milling Constants for Product F, 8" Manufacturer A Mill

A comparison between the prediction accuracy of Equation 3.27 compared to its simplified form, Equation 4.3, may be found in Table A2.20 and Figure A2.30.

$\sum(actual - predicted)^2$ Equation 3.27	$\sum(actual - predicted)^2$ Equation 4.3
2.47	5.71

Table A2.20 Prediction Comparison, Product F, 8" Manufacturer A Mill

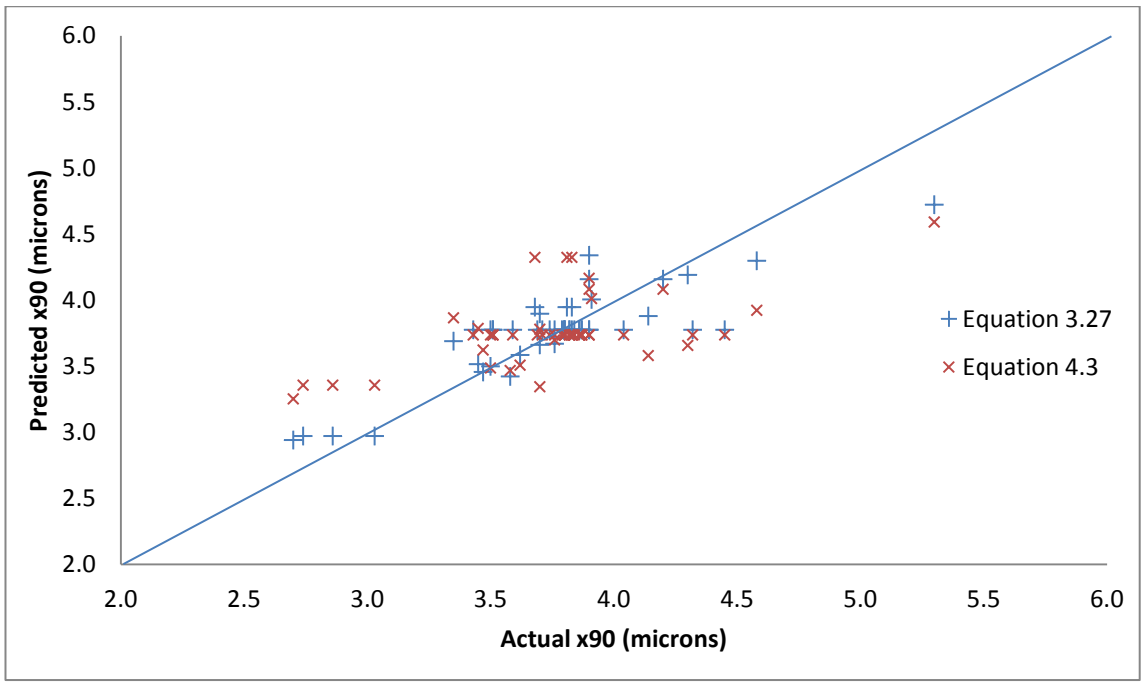

Figure A2.30 Prediction Accuracy, Product F, 8" Manufacturer A Mill

A2.11 Product G – 8" Manufacturer A Mill

A plot of specific energy, E_{sp}, against x90 may be found for product G with an 8" Manufacturer A mill in Figure A2.31, and 1/ E_{sp} against x90 in Figure A2.32.

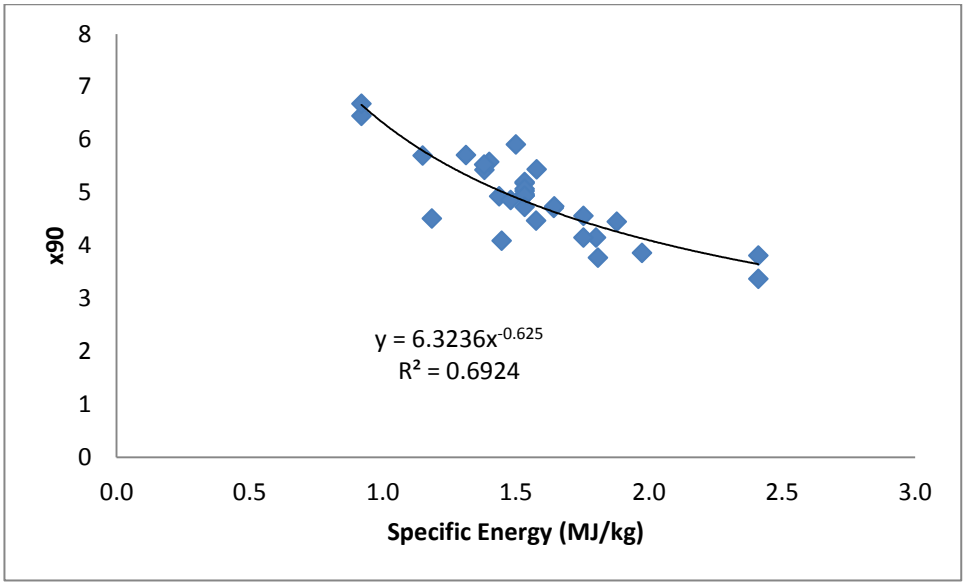

Figure A2.31 E_{sp} against x90, Product G, 8" Manufacturer A Mill

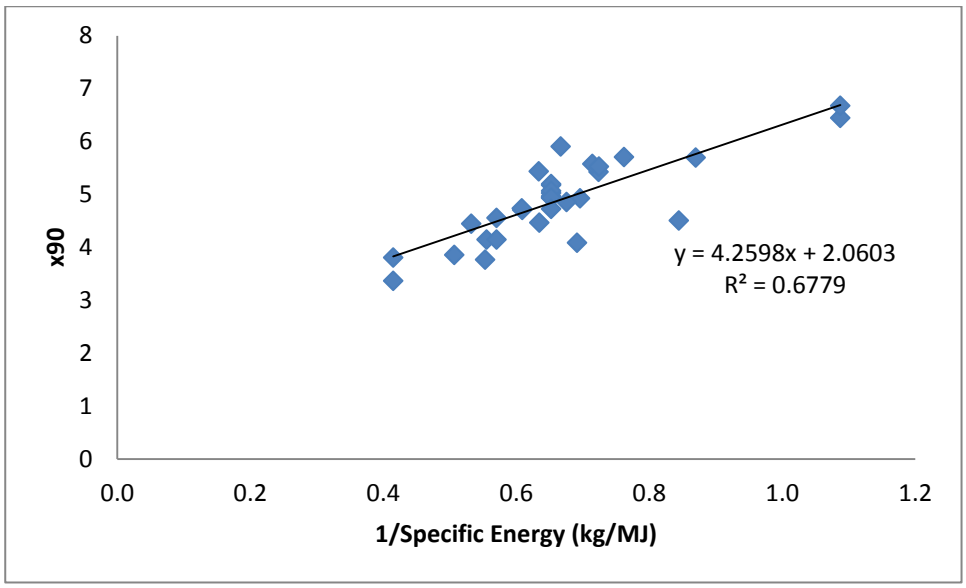

Figure A2.32 $1/E_{sp}$ against x90, Product G, 8" Manufacturer A Mill

The milling constants for Product G with an 8" Manufacturer A mill may be found in Table A2.21

$\frac{C_2}{{k_3}^2}$ (µm)	$\frac{x_1 k_4}{{k_3}^2 d_{Reynolds}}$ (µm.kg.hr^{-1})	x_2 (kg.hr^{-1})
0.107	32.1	3.06

Table A2.21 Milling Constants for Product G, 8" Manufacturer A Mill

A comparison between the prediction accuracy of Equation 3.27 compared to its simplified form, Equation 4.3, may be found in Table A2.22 and Figure A2.33.

$\sum(actual - predicted)^2$ Equation 3.27	$\sum(actual - predicted)^2$ Equation 4.3
2.03	5.78

Table A2.22 Prediction Comparison, Product 8, 8" Manufacturer A Mill

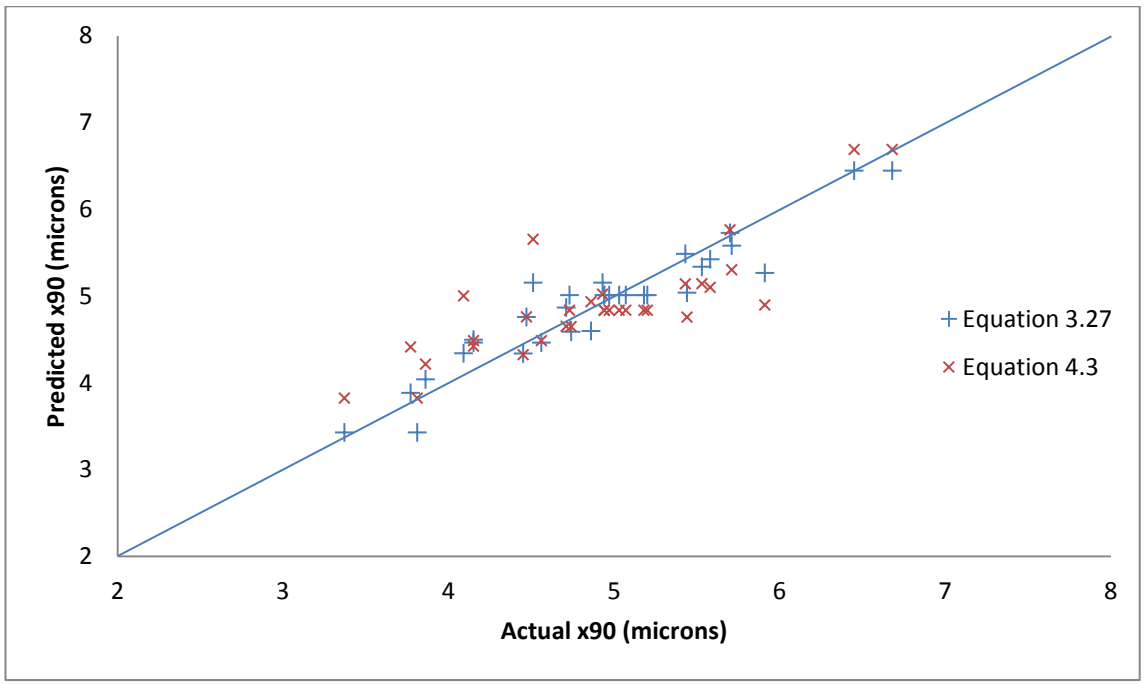

Figure A2.33 Prediction Accuracy, Product G, 8" Manufacturer A Mill

A2.12 Product H – 8" Manufacturer A Mill

A plot of specific energy, E_{sp}, against x90 may be found for product H with an 8" Manufacturer A mill in Figure A2.34, and 1/ E_{sp} against x90 in Figure A2.35.

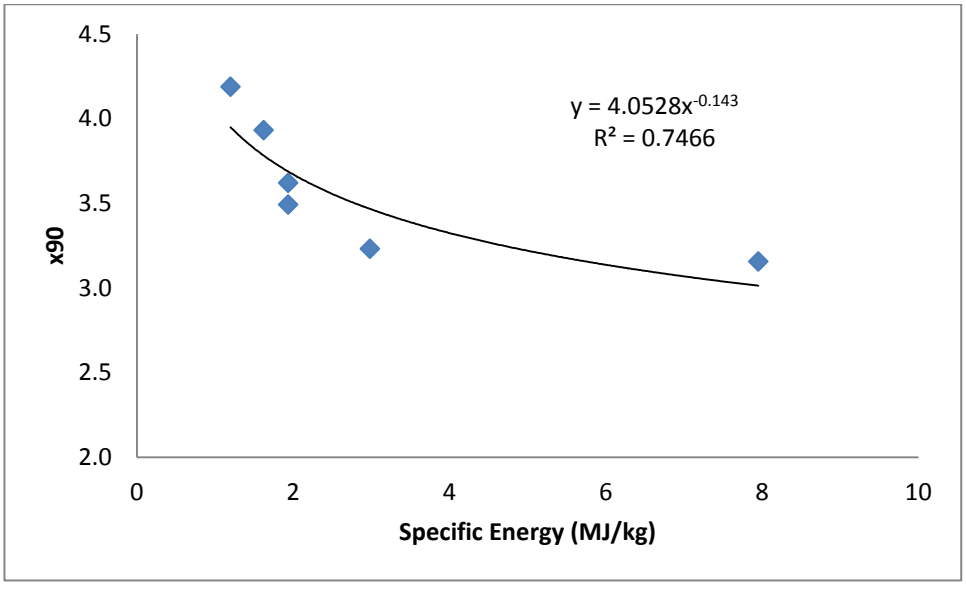

Figure A2.34 E_{sp} against x90, Product H, 8" Manufacturer A Mill

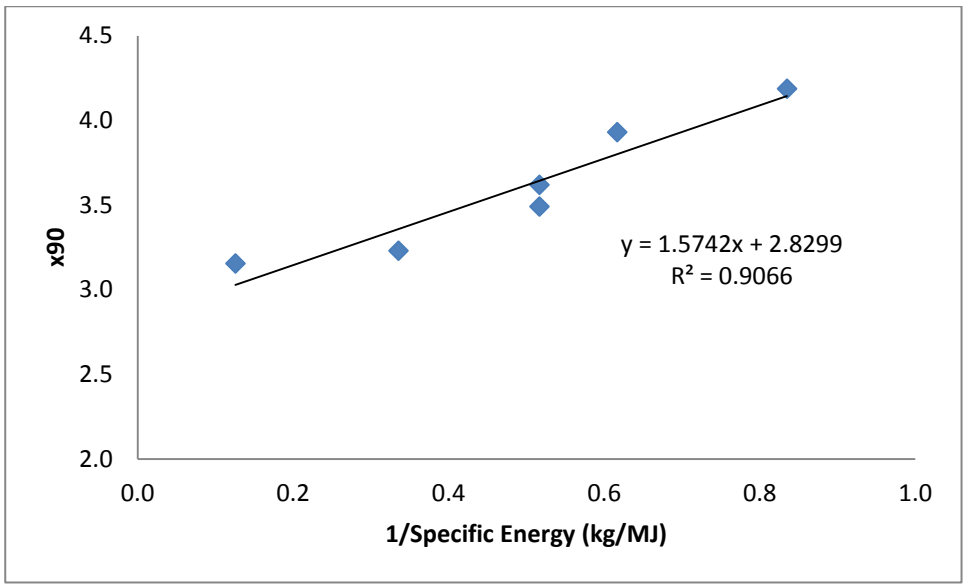

Figure A2.35 $1/E_{sp}$ against x90, Product H, 8" Manufacturer A Mill

The milling constants for product H with an 8" Manufacturer A mill may be found in Table A2.23.

$\frac{C_2}{{k_3}^2}$ (µm)	$\frac{x_1 k_4}{{k_3}^2 d_{Reynolds}}$ (µm.kg.hr^{-1})	x_2 (kg.hr^{-1})
0.369	31.52	17.1

Table A2.23 Milling Constants for Product G, 8" Manufacturer A Mill

A comparison between the prediction accuracy of Equation 3.27 compared to its simplified form, Equation 4.3, may be found in Table A2.24 and Figure A2.36.

$\sum(actual - predicted)^2$ Equation 3.27	$\sum(actual - predicted)^2$ Equation 4.3
0.0592	0.0749

Table A2.24 Prediction Comparison, Product H, 8" Manufacturer A Mill

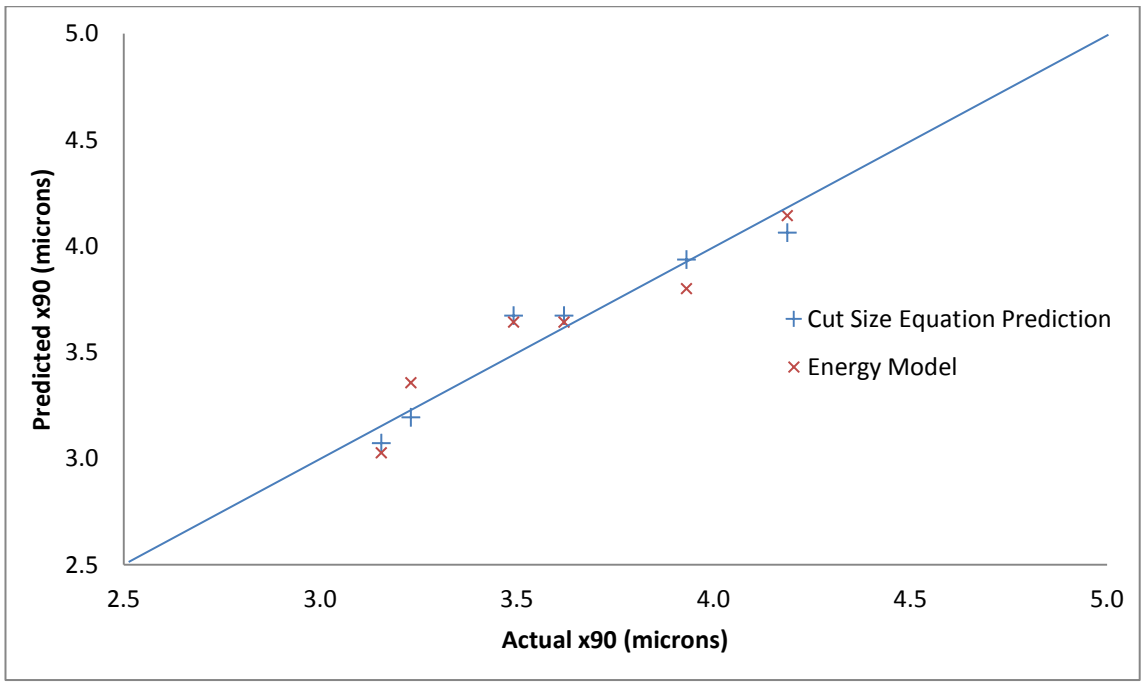

Figure A2.36 Prediction Accuracy, Product H, 8" Manufacturer A Mill

A2.13 Product H – 4" Manufacturer A Mill

A plot of specific energy, E_{sp}, against x90 may be found for product H with an 4" Manufacturer A mill in Figure A2.37, and 1/ E_{sp} against x90 in Figure A2.38.

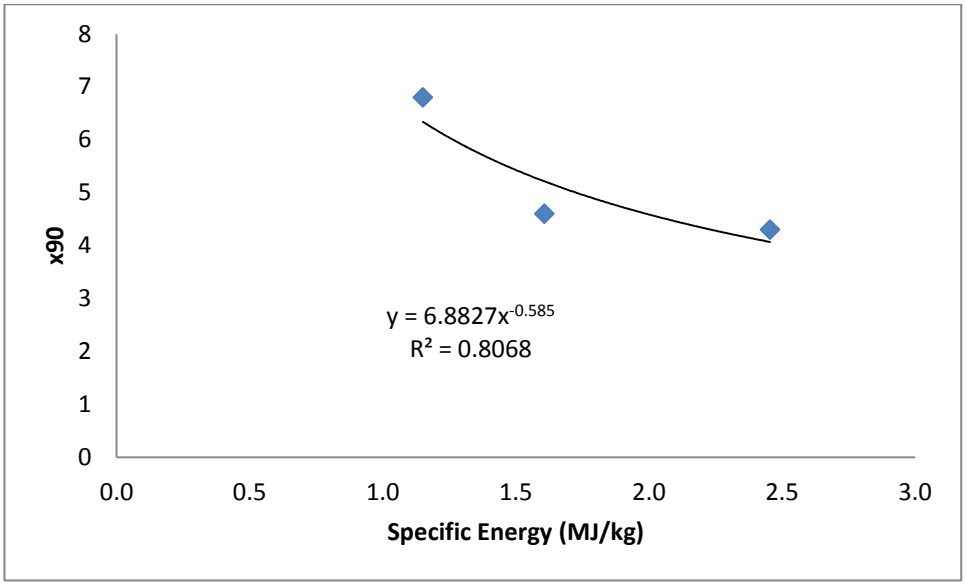

Figure A2.37 E_{sp} against x90, Product H, 4" Manufacturer A Mill

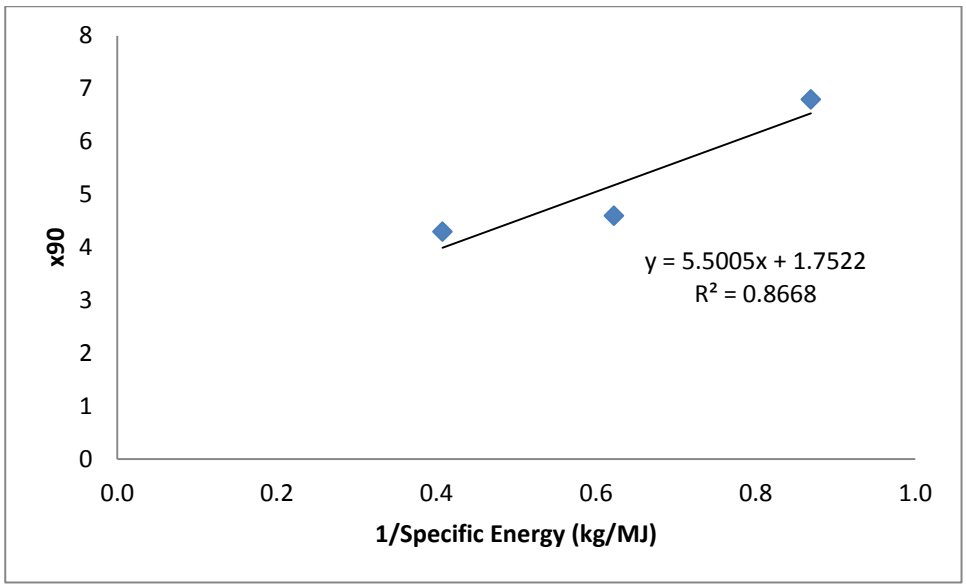

Figure A2.38 $1/E_{sp}$ against x90, Product H, 4" Manufacturer A Mill

The milling constants for product H with an 8" Manufacturer A mill may be found in Table A2.25.

$\frac{C_2}{{k_3}^2}$ (µm)	$\frac{x_1 k_4}{{k_3}^2 d_{Reynolds}}$ (µm.kg.hr^{-1})	x_2 (kg.hr^{-1})
0.156	24.7	17.1

Table A2.25 Milling Constants for Product G, 4" Manufacturer A Mill

A comparison between the prediction accuracy of Equation 3.27 compared to its simplified form, Equation 4.3, may be found in Table A2.26 and Figure A2.39.

$\sum(actual - predicted)^2$ Equation 3.27	$\sum(actual - predicted)^2$ Equation 4.3
1.22	1.76

Table A2.26 Prediction Comparison, Product H, 4" Manufacturer A Mill

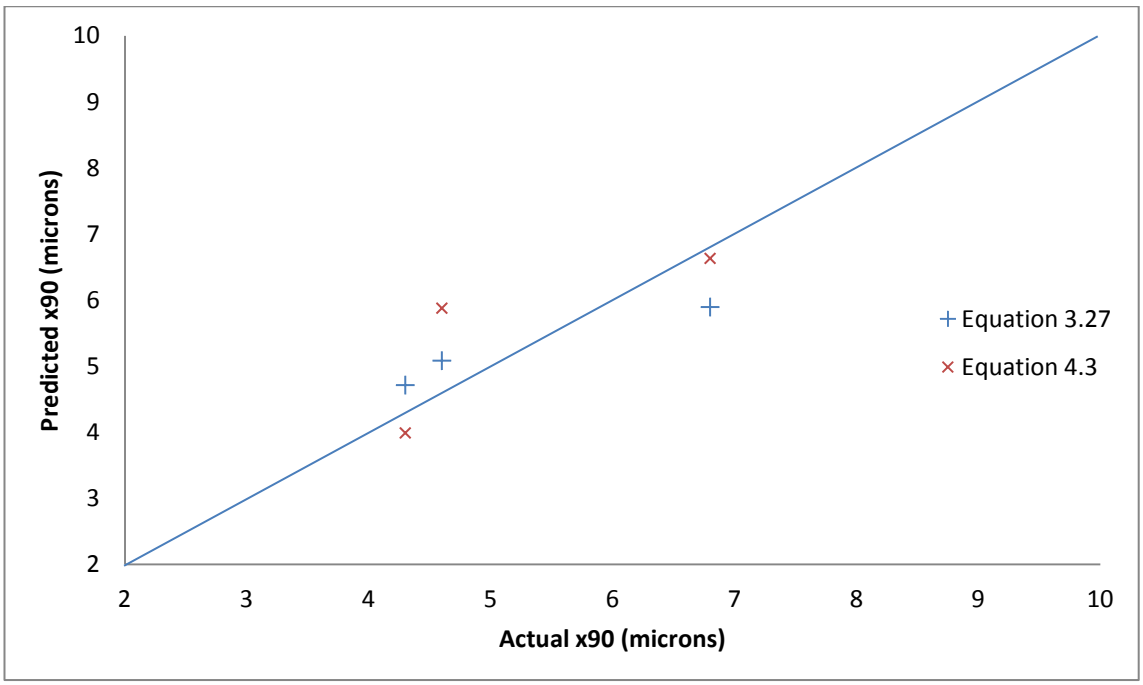

Figure A2.39 Prediction Accuracy, Product H, 4" Manufacturer A Mill

Nomenclature

Symbol	Description	Units
A	Particle Projected Area	m^2
B	Time Averaged Mass Fraction of Collision Fragments Below the Cut Size	N/A
B	Particle Breadth (Equation 8.3 only)	m
$B(x,y)$	Breakage Distribution Function for Coal	N/A
C_1	Drag Coefficient as the Reynolds Number Tends Towards Infinity	N/A
C_2	$3C_1\rho_g r/4\rho_p$	m
C_D	Drag Coefficient of Particle	N/A
d_{cut}	Diameter of Particle Balanced by Radial Drag and Centrifugal Force at Classifier	m
$d_{Reynolds}$	Length Scale of Particles at the Grind Chamber Exit	m
d_{limit}	Diameter of Particle Obtained as the Specific Energy Consumption Tends Towards Infinity	m
D	Mass Transfer Coefficient	$m^3.s^{-1}$
D	Diameter of Sphere with Equivalent Settling Velocity to Rectangular Prism LBH (Equation 8.3 only)	m
E_{sp}	Specific Energy Consumption	$J.kg^{-1}$
$\dot{E}_k$	Kinetic Energy Delivery Rate	W
$\dot{E}_{exit\ (gas\ only)}$	Kinetic Energy of Gas Exiting Grind Chamber for Gas Only System	W
$\dot{E}_{exit}$	Kinetic Energy of Gas and Powder Exiting Grind Chamber for Gas and Powder System	W
$\dot{E}_{loss}$	Rate of Energy Loss due to Particle Collisions and Friction	W
H	Height of Gap for Radial Gas Flow	M
h_1	Height of Grind Chamber Exit	M
h_2	Height of Grind Chamber	M
H	Particle Hardness	Pa
H	Particle Height (Equation 8.3 only)	m
K	Rate Constant for a Bi-Particular Collisions	$m^6.kg^{-1}.s^{-1}$
K_c	Fracture Toughness	$N.m^{-3/2}$
K	Ratio of Specific Heat Capacities	N/A
k_1	$3C_D\rho_g r/4\rho_p$	m
k_2	$T/T_{throat}\pi rhkP$	$m.J^{-1}$
k_3	Gas Spin Ratio, v_t/v_r	N/A
k_4	$2/v_{sonic}^2$	$m^{-2}.s^2$
l	Length Dimension of Particle	m
L	Particle Length (Equation 8.3 only)	m
M	Breakage Constant (Brown 1941)	N/A
$\dot{m}_g$	Gas Mass Flow Rate	$kg.s^{-1}$
$\dot{m}_s$	Solids Feed Rate	$kg.s^{-1}$
m_h	Total Solids Hold Up in Grind Chamber	kg
$\dot{m}_h$	Theoretical Rate of Powder Hold Up, $\dot{V}m_h/V_{grind}$	$kg.s^{-1}$
$\dot{m}_{collide}$	Rate of Particle Collisions	$kg.s^{-1}$
$\dot{m}_{nozzles}$	Rate of Mass Transfer of Solids to Grind Nozzles	$kg.s^{-1}$
$\dot{m}_{below\ cut\ size}$	Rate of Generation of Particles Below the Cut Size	$kg.s^{-1}$
M_W	Gas Molecular Weight	$kg.mol^{-1}$
P	Grind Chamber Pressure	Pa

Symbol	Description	Units
r	Radial Position	m
R	Specific Gas Constant	$J.K^{-1}.mol^{-1}$
Re	Reynolds Number, $\rho vd/\mu$	N/A
T	Gas Temperature	K
T_{throat}	Gas Temperature at the Nozzle Throat for Choked Flow $(2\,T/k{+}1)$	$m.s^{-1}$
v	Velocity	$m.s^{-1}$
$v_{r(general)}$	Gas Radial Velocity for Radial Flow Through Circular Gap	$m.s^{-1}$
v_r	Gas Radial Velocity	$m.s^{-1}$
v_t	Particle Tangential Velocity	$m.s^{-1}$
$v_{t\,(gas)}$	Gas Tangential Velocity	$m.s^{-1}$
$v_{t\,(gas\ only)}$	Gas Tangential Velocity for Gas Only System	$m.s^{-1}$
$v_{t\,(particle)}$	Particle Tangential Velocity	$m.s^{-1}$
$v_{p(radial)}$	Radial Velocity of Particles Exiting Grind Chamber	$m.s^{-1}$
v_{sonic}	Gas Sonic Velocity	$m.s^{-1}$
$v_{terminal}$	Particle Terminal Velocity	$m.s^{-1}$
$\dot{V}$	Gas Volumetric Flow Rate	$m^3.s^{-1}$
V_{grind}	Grind Chamber Volume	m^3
x	Output Size for Breakage Distribution Function (Brown 1941)	m
x_1	$18\mu h_1 r/\rho_p k_2$	$m.kg.s^{-1}$
x_2	$DbPM_w/RT$	$kg.s^{-1}$
x10	Particle Size that 10% of the Volume of Powder is Less Than	µm
x50	Particle Size that 50% of the Volume of Powder is Less Than	µm
x90	Particle Size that 90% of the Volume of Powder is Less Than	µm
x100	Particle Size that 100% of the Volume of Powder is Less Than	µm
y	Input Size for Breakage Distribution Function (Brown 1941)	m
z	Gas Compressibility Factor	N/A
α	Breakage Proportionality Constant	N/A
ξ	Fractional Loss per Impact	N/A
η	Dimensionless Attrition Propensity Parameter	N/A
ρ_g	Gas Density	$kg.m^{-3}$
ρ_p	True Particle Density	$kg.m^{-3}$
μ	Gas Viscosity	Pa.s

References

Spiral Jet Mill

Austin, L. G., 1971, Introduction to the mathematical description of grinding as a rate process, Powder Technology, Vol. 5, pp 1-17

Austin, L.G., 1973, A commentary on the Kick, Bond and Rittinger laws of grinding, Powder Technology, Vol. 7, pp 315-317

Berry, C. E., 1946, Modern Machines for Dry Size Reduction in Fine Size Range, Industrial & Engineering Chemistry, Vol. 38, pp 672-678

Berthiaux, H., Chiron, C., Dodds, J., 1999, Modelling fine grinding in a fluidized bed opposed jet mill: part II: continuous grinding, Powder Technology, Vol. 106, pp 88-97

Berthiaux, H., Dodds, J., 1999, Modelling fine grinding in a fluidized bed opposed jet mill: Part I: Batch grinding kinetics, Powder Technology, Vol. 106, pp 78-87

Bonakdar, T., Ali, M., Dogbe, S., Ghadiri, M., Tinke, A., 2016, A method for grindability testing using the Scirocco disperser, International Journal of Pharmaceutics, Vol. 501, pp 65-74

Brodka-Pfeiffer, K., Langguth, P., Graβ, P., Häusler, H., 2003, Influence of mechanical activation on the physical stability of salbutamol sulphate, European Journal of Pharmaceutics and Biopharmaceutics, Vol. 56, pp 393-400

Brosh, T., Kalman, H., Levy, A., 2014, Accelerating CFD–DEM simulation of processes with wide particle size distributions, Particuology, Vol. 12, pp 113-121

Brosh, T., Kalman, H., Levy, A., Peyron, I., Ricard, F., 2014, DEM–CFD simulation of particle comminution in jet-mill, Powder Technology, Vol. 257, pp 104-112

Brown, R. L., 1941, Broken coal-3. Generalized law of size distribution, Journal of the Institute of Fuel, Vol. 14, pp 129-134

Burnett, D.J., Thielmann, F., Booth, J., 2004, Determining the critical relative humidity for moisture-induced phase transitions, International Journal of Pharmaceutics, Vol. 287, pp 123-133

Djokić, M., Djuriš, J., Solomun, L., Kachrimanis, K., Djurić, Z. and Ibrić, S., 2014, The influence of spiral jet-milling on the physicochemical properties of carbamazepine form III crystals: Quality by design approach, Chemical Engineering Research and Design, Vol. 92, pp 500-508

Dobson, B., Rothwell, E., 1969, Particle Size Reduction in a Fluid Energy Mill, Powder Technology, Vol. 3, pp 213-217

Dotson, J.M., 1962, Extending the Range of Jet Mills, Industrial and Engineering Chemistry, Vol. 54, pp 62-65

Epstein, B., 1948, Logarithmico-normal distribution in breakage of solids, Industrial & Engineering Chemistry, Vol. 40, pp 2289-2291

Eskin, D., Voropayev, S., Vasilkov, O., 1999, Simulation of jet milling, Powder Technology, Vol. 105, pp 257-265

Fischer-Cripps, A.C., 2000, Introduction to Contact Mechanics, Springer, New York

Geller, M. J., 2010, Ancient Babylonian medicine: theory and practice, John Wiley & Sons, Chichester

Ghadiri, M., Zhang, Z., 2002, Impact attrition of particulate solids, Part 1: a theoretical model of chipping, Chemical Engineering Science, Vol. 57, pp 3659-3669

Grimsey, I. M., Feeley, J. C., York, P., 2002, Analysis of the surface energy of pharmaceutical powders by inverse gas chromatography, Journal of Pharmaceutical Sciences, Vol. 91, pp 571-583

Haider, A.,Levenspiel, O., 1989, Drag coefficient and terminal velocity of spherical and nonspherical particles, Powder Technology, Vol. 58, pp 63-70

Han, T., Kalman, H., Levy, A., 2002, DEM Simulation of Particle Comminution in Jet Milling, Particulate Science and Technology, Vol. 20, pp 325-340

Heng, J.Y., Thielmann, F., Williams, D.R., 2006, The effects of milling on the surface properties of form I paracetamol crystals, Pharmaceutical Research, Vol. 23, pp 1918-1927

Herbst, J. A., Fuerstenau, D. W., 1980, Scale-up procedure for continuous grinding mill design using population balance models, International Journal of Mineral Processing, Vol. 7, pp 1-31

Herzfeld, A., 1896, Ball Grinding Mill, U.S. Patent 569,828

Ito, H., 1987, Scale-up theory of single track jet mill, 2nd Korean-Japan Powder Technology Seminar, Pusan Korea

Katz, A., Kalman, H., 2007, Preliminary Experimental Analysis of a Spiral Jet Mill Performance, Particle & Particle Systems Characterisation, Vol. 24, pp 332-338

Konno, H., Saito, S.J., 1969, Pneumatic conveying of solids through straight pipes, Chemical Engineering in Japan, Vol. 2, pp 211-217

Kozawa, K., Seto, T., Otani, Y., 2012, Development of a spiral-flow jet mill with improved classification performance, Advanced Powder Technology, Vol. 23, pp 601-606

Kürten, H., Rink, N., Rumpf, H., 1970, Strömung und Zerkleinerung beim Stoß zweier Gas-Festoff-Strahlen, Powder Technology, Vol. 4, pp 221-231

Kürten, H., Rumpf, H., 1966, Zerkleinerungsuntersuchungen mit tribolumineszierenden Stoffen, Chemie Ingenieur Technik, Vol. 38, pp 331-342

Lloyd, D.R., Ward, T.C., Schreiber, H.P., 1989, Inverse Gas Chromatography, American Chemical Society, Washington DC

Lucas, A., 2006, Wind, Water, Work: Ancient and Medieval Milling Technology (Vol. 8), Brill, Leiden

Luckenbach, F. A., Wolfenden, J., 1881, Method of and Apparatus for Pulverizing Mineral and other Substances, U.S. Patent 238,044

MacDonald, R., Rowe, D., Martin, E., Gorringe, L., 2016, The spiral jet mill cut size equation, Powder Technology, Vol. 299, pp 26-40

Mercader, J., 2009, Mozambican grass seed consumption during the Middle Stone Age, Science, Vol. 326, pp 1680-1683

Midoux, N., Hošek, P., Pailleres, L., Authelin, J. R., 1999, Micronization of pharmaceutical substances in a spiral jet mill, Powder Technology, Vol. 104, pp 113-120

Mohanty, B., Narasimhan, K. S., 1982, Fluid energy grinding, Powder Technology, Vol. 33, pp 135-141

Müller, F., Polke, R., Schädel, G., 1996, Spiral jet mills: hold up and scale up, International Journal of Mineral Processing, Vol. 44, pp 315-326

Nadel, D., Piperno, D. R., Holst, I., Snir, A., Weiss, E., 2012, New evidence for the processing of wild cereal grains at Ohalo II, a 23 000-year-old campsite on the shore of the Sea of Galilee, Israel, Antiquity, Vol. 86, pp 990-1003

Nair, P. B R., 1999, Breakage parameters and the operating variables of a circular fluid energy mill: Part I. Breakage distribution parameter, Powder Technology, Vol. 106, pp 45-53

Nair, P.B. R., Ramanujam, M., 1991, Classification function in fluid energy grinding, Powder Technology, Vol. 68.1, pp 79-84

Norwood, H. A., 1936, Method of and Apparatus for Providing Material in Finely Divided Form, U.S. Patent 2,023,827

Ostwald, H., 1912, Ball-mill, U.S. Patent 1,043,349

Rader, D., 1990, Momentum slip correction factor for small particles in nine common gases, Journal of Aerosol Science, Vol. 21, pp 161-168

Ramanujam, M., Venkateswarlu, D., 1969, Studies in fluid energy grinding, Powder Technology, Vol. 3, pp 92-101

Rautiainen, A., Stewart, G., Poikolainen, V., Sarkomaa, P., 1999, An experimental study of vertical pneumatic conveying, Powder Technology, Vol. 104, pp 139-150

Rodnianski, V., Krakauer, N., Darwesh, K., Levy, A., Kalman, H., Peyron, I., Ricard, F., 2013, Aerodynamic classification in a spiral jet mill, Powder Technology, Vol. 243, pp 110-119

Rumpf, H., 1973, Physical aspects of comminution and new formulation of a law of comminution, Powder Technology, Vol. 7, pp 145 – 159

Schurr, G. A., Zhao, Q. Q., 1994, Fluid mechanic considerations for fine grinding in a fluid energy mill, 8th European Symposium on Comminution, Stockholm, Sweden

Stephanoff, N. N., 1943, Method and apparatus for comminuting or drying materials, U.S. Patent 2,325,080

Tanaka, T., 1972, Scale-up theory of jet mills on basis of comminution kinetics, Industrial & Engineering Chemistry Process Design and Development, Vol. 11, pp 238-241

Teng, S., Wang, P., Zhang, Q., Gogos, C. G., 2011, Analysis of fluid energy Mill by gas-solid two-phase flow simulation, Powder Technology, Vol. 208, pp 684-693

Teng, S., Wang, P., Zhu, L., Young, M., Gogos, C. G., 2010, Mathematical modeling of fluid

energy milling based on a stochastic approach, Chemical Engineering Science, Vol. 65, pp 4323-4331

Tuunila, R., Nyström, L., 1998, Effects of Grinding Parameters on Product Fineness in Jet Mill Grinding, Minerals Engineering, Vol. 11, pp 1089-1094

Vemuri, N. M., Brown, A. B., Authelin, J. R. and Hošek, P., 2003, Milling process for the production of finely milled medicinal substances, U.S. Patent 6,641,063

Venkataraman, K. S., Fuerstenau, D. W., 1984, Application of the population balance model to the grinding of mixtures of minerals, Powder Technology, Vol. 39, pp 133-142

Vogel, L., Peukert, W., 2003, Breakage behaviour of different materials—construction of a mastercurve for the breakage probability, Powder Technology, Vol. 129, pp 101-110

Vogel, L., Peukert, W., 2003, Modelling of grinding in an air classifier mill based on a fundamental material function, KONA Powder and Particle Journal, Vol. 21, pp 109-120

Walker, C., 1847, Mill for grinding mustard, U.S. Patent 5,262

Yoon, S. H., 1994, Scale-up method for a horizontal-type jet mill, Advanced Powder Technology, Vol. 5, pp 53-59

Zhang, Z., Ghadiri, M., 2002, Impact attrition of particulate solids. Part 2: experimental work, Chemical Engineering Science, Vol. 57, pp 3671-3686

Zhao, Q. Q., Schurr, G., 2002, Effect of motive gases on fine grinding in a fluid energy mill, Powder Technology, Vol. 122, pp 129-135

Zügner, S., Marquardt, K., Zimmermann. I., 2006, Influence of nanomechanical crystal properties on the comminution process of particulate solids in spiral jet mills, European Journal of Pharmaceutics and Biopharmaceutics, Vol. 62, pp 194-201

Cyclone

Alves, A., Paiva, J., Salcedo, R., 2015, Cyclone optimization including particle clustering, Powder Technology, Vol. 272, pp 14-22

Barth, W., 1956, Design and layout of the cyclone separator on the basis of new investigations, Brennstoff Warme Kraft, Vol. 8, pp 1-9

Chu, K. W., Wang, B., Xu, D. L., Chen, Y. X., Yu, A. B., 2011, CFD–DEM simulation of the gas–solid flow in a cyclone separator, Chemical Engineering Science, Vol. 66, pp 834-847

Cortes, C., Gil, A., 2007, Modeling the gas and particle flow inside cyclone separators, Progress in Energy and Combustion Science, Vol. 33, pp 409-452

Crowe, C. T., Pratt, D. T., 1974, Analysis of the flow field in cyclone separators, Computers & Fluids, Vol. 2, pp 249-260

Derksen, J. J., Van den Akker, H. E. A., 2000, Simulation of vortex core precession in a reverse-flow cyclone, AIChE Journal, Vol. 46, pp 1317-1331

Dirgo, J., Leith, D., 1985, Cyclone collection efficiency: comparison of experimental results with theoretical predictions, Aerosol Science and Technology, Vol. 4, pp 401-415

Elsayed, K., Lacor, C., 2010, Optimization of the cyclone separator geometry for minimum pressure drop using mathematical models and CFD simulations, Chemical Engineering Science, Vol. 65, pp 6048-6058

Elsayed, K., Lacor, C., 2013, CFD modeling and multi-objective optimization of cyclone geometry using desirability function, artificial neural networks and genetic algorithms, Applied Mathematical Modelling, Vol. 37, pp 5680-5704

Elsayed, K., Lacor, C., 2013, The effect of cyclone vortex finder dimensions on the flow pattern and performance using LES, Computers & Fluids, Vol. 71, pp 224-239

Hoffmann, A. C., Arends, H., Sie, H., 1991, An experimental investigation elucidating the

nature of the effect of solids loading on cyclone performance, Filtration & Separation, Vol. 28, pp 188-193

Hoffmann, A. C., Stein, L. E., 2002, The Muschelknautz Method of Modeling, Gas Cyclones and Swirl Tubes, Springer, Berlin

Lapple, C. E., 1950, Gravity and centrifugal separation, American Industrial Hygiene Association Quarterly, Vol. 11, pp 40-48

Lim, K. S., Kim, H. S., Lee, K. W., 2004, Characteristics of the collection efficiency for a cyclone with different vortex finder shapes, Journal of Aerosol Science, Vol. 35, pp 743-754

Meißner, P., Löffler, F., 1978, Zur berechnung des strömungsfeldes im zyklonabscheider, Chemie Ingenieur Technik, Vol. 50, pp 471-471

Moore, M. E., McFarland, A. R., 1993, Performance modeling of single-inlet aerosol sampling cyclones, Environmental Science & Technology, Vol. 27, pp 1842-1848

Muschelknautz, E., 1970, Auslegung von Zyklonabscheidern in der technischen Praxis, Staub-Reinhalt Luft, Vol. 30, pp 187-195

Muschelknautz, E., 1972, Die berechnung von zyklonabscheidern für gase, Chemie Ingenieur Technik, Vol. 44, pp 63-71

Newcombe, J. W., 1922, Centrifugal dust separator, U.S. Patent 1,420,665

Ogawa, A., 1984, Separation of particles from air and gases, CRC Press, Boco Raton

Ogawa, A., 1997, Mechanical separation process and flow patterns of cyclone dust collectors, Applied Mechanics Reviews, Vol. 50, pp 97-130

Raoufi, A., Shams, M., Farzaneh, M., Ebrahimi, R., 2008, Numerical simulation and

optimization of fluid flow in cyclone vortex finder, Chemical Engineering and Processing: Process Intensification, Vol. 47, pp 128-137

Reitz, D. G., 1889, Dust-collector, U.S. Patent 415,368

Shepherd, C. B., Lapple, C. E., 1939, Flow pattern and pressure drop in cyclone dust collectors, Industrial & Engineering Chemistry, Vol. 31, pp 972-984

Slack, M. D., Prasad, R. O., Bakker, A., Boysan, F., 2000, Advances in cyclone modelling using unstructured grids, Chemical Engineering Research and Design, Vol. 78, pp 1098-1104

Stairmand, C. J., 1949, Pressure drop in cyclone separators, Engineering, Vol. 168, pp 409-412

Stairmand, C. J., 1951, The design and performance of cyclone separators, Transactions of the Institute of Chemical Engineers, Vol. 29, pp 356-383

Ter Linden, A. J., 1949, Investigations into cyclone dust collectors, Proceedings of the Institution of Mechanical Engineers, Vol. 160, pp 233-251

Trefz, M., Muschelknautz, E., 1993, Extended cyclone theory for gas flows with high solids concentrations, Chemical Engineering & Technology, Vol. 16, pp 153-160

Yoshida, H., Saeki, T., Hashimoto, K., Fujioka, T., 1991, Size classification of submicron powder by air cyclone and three-dimensional analysis, Journal of Chemical Engineering of Japan, Vol. 24, pp 640-647